LUND UNIVERSITY

Towards single Ce ion detection in a bulk crystal for the development of a single-ion qubit readout scheme

Yan, Ying

2013

LUND UNIVERSITY

ISBN 978-91-7473-699-1
ISSN 0281-2762

YING YAN

TOWARDS SINGLE CE ION DETECTION IN A BULK CRYSTAL FOR THE DEVELOPMENT OF A SINGLE-ION QUBIT READOUT SCHEME 2013

TOWARDS SINGLE CE ION DETECTION IN A BULK CRYSTAL FOR THE DEVELOPMENT OF A SINGLE-ION QUBIT READOUT SCHEME

YING YAN

DEPARTMENT OF PHYSICS
FACULTY OF ENGINEERING
LUND UNIVERSITY

Towards single Ce ion detection in a bulk crystal for the development of a single-ion qubit readout scheme

Ying Yan

Doctoral Thesis
2013

Lund University

Towards single Ce ion detection in a bulk crystal for the development of a single-ion qubit readout scheme

Printed in Sweden by Media-Tryck, Lund, 2013

Division of Atomic Physics
Department of Physics
Faculty of Engineering, LTH
Lund University
P.O. Box 118
SE–221 00 Lund
Sweden

http://www.atom.fysik.lth.se

ISSN 0281-2762
Lund Reports on Atomic Physics, LRAP-479

ISBN 978-91-7473-699-1 978-91-7473-700-4

To my father

Abstract

The work presented in this thesis was concerned with investigating the relevant spectroscopic properties of Ce ions randomly doped in an Y_2SiO_5 crystal at low temperatures (around 4 K), in order to develop a technique and an experimental set-up to detect the fluorescence photons emitted by a single Ce ion. The aim of the work was to determine whether a single Ce ion (referred to as the readout ion) can be used as a local probe to sense the quantum state of a neighbouring single-ion qubit via a state-selective interaction between the readout and qubit ion. More precisely, if the qubit ion is in state $|1\rangle$ or $|0\rangle$ state, the single Ce ion will, or will not, emit fluorescence photons. This single ion readout concept is a key step towards single-rare-earth-ion quantum computing, which is believed to be a promising approach for a scalable quantum computer.

Rare-earth ion based quantum computing is an attractive scheme for several reasons. Firstly, the qubit coherence time can be on the timescale of a minute while the optical coherence time can be on the millisecond timescale, despite the fact that the ions are in a solid (crystal), which means that more than 10000 optical pulses could be implemented before the system decoheres. Secondly, any sub-ensemble of ions in a frequency interval equal to or larger than the homogeneous linewidth within the inhomogeneously broadened absorption line can be used as a frequency-selectively addressed qubit. The proof of principle of the qubit-qubit interaction has been previously demonstrated. Thirdly, no special material engineering is required, and the crystal is commercially available. Ways of initializing a sub-ensemble of Pr ions as a qubit in the random system, manipulating the quantum state of the ions in a controlled way, and characterizing the quantum state created are presented.

In order to achieve better scalability, the idea of letting a single rare-earth ion represent a qubit was investigated. The fidelity of the single-ion readout scheme was briefly studied. The influence of the energy transfer process between two neighbouring ions on quantum computing is discussed.

A readout ion should possess a number of specific spectroscopic properties. Therefore, the position and the linewidths of the zero-phonon line of Ce ions were measured using an external cavity diode laser (at 371 nm) as the excitation source. The difference in the permanent dipole moment of the ground and excited states of Ce ions was measured in a photon echo experiment on Pr ions in a Ce-Pr co-doped Y_2SiO_5 crystal.

The last and most important task was to realize single Ce ion detection. Fluorescence of Ce ions has been detected from a crystal, where there is on average 1 ion within 4.6 μm^3 interacting with the excitation laser at a time. Estimates were made of the number of ions contributing to an observed signal. A trial experiment to investigate whether the signal was emitted by a single Ce ion was carried out, but was unsuccessful. Potential reasons why the experiment failed are presented.

Popular science description

At the beginning of 20th century, scientists started to realize that atoms exhibited the discrete behaviour, e.g. the energies of bond electrons were not continuously distributed, but had discrete values. Light is also transmitted as discrete packages (called photons). These phenomena can not be explained by classical physics, which has been accepted as the law of describing the nature for hundreds of years, and a new theory, called quantum mechanics, was born.

Quantum mechanics has already made great changes to our lives. Two important applications are lasers and and transistors. Lasers are now used in many fields, for example in industry (laser cutting and laser lithography), in daily life (laser printers and DVD players), and in medicine (eye surgery, laser cosmetology and laser diagnosis). Transistors are the elementary electronic devices used for the logic gates in a computer, which can have one of two binary output values: 0 or 1. The invention of the transistor allowed the first general-purpose electronic computer, the Electronic Numerical Integrator and Computer, which weighed 30 tons, to be replaced by a modern computer weighing only a few kilograms. Transistor-based computers also have other advantages: they are faster, more reliable, cheaper to produce and consume less energy. Computers have become more and more compact, due to the decreasing size of transistors. However, there is a limit on the reduction in size of transistors, and the next step is to use single atoms.

The performance of computers based on single atoms will be determined by quantum mechanics. A so-called quantum computer will make use of the quantum properties of atoms to carry out computations. The primary information carrier is the quantum bit (called a qubit), which is a coherent superposition of two classical bits (i.e. it can have values of 0 and 1 at the same time). This allows computation to be vastly speeded up. For example, a two-qubit state can be in all four states: 00, 01, 10 and 11 simultaneously (with different probabilities), so a computational process using these two qubits can be implemented simultaneously on all four states at once. Using the classical two-bit computer, the same task has to be carried out four times. This so-called quantum par-

allelism may allow certain types of problems, which are currently difficult or almost impossible to solve on a conventional computer, to be easily solved on a quantum computer. For instance, factorizing a 300-digit integer to two prime numbers would take a conventional computer with a THz clock speed 150 000 years, even using the best algorithm, but this could potentially be done in less than 1 second on a large quantum computer. The RSA encryption algorithm, which is used, for example, to ensure security of online shopping using credit cards, is based on the presumed difficulty of factoring large integers, and the advent of quantum computers would thus render this algorithm useless. However, quantum computers are still confined to the realms of the research laboratory. As is the case with any new invention, it is difficult to predict how or when quantum computers will make an impact on the world.

The work described in this thesis is focused on developing a single-ion qubit readout scheme, with which a quantum computer with a large number of qubits could potentially be constructed. The 'hardware' investigated consists of rare-earth ions (praseodymium or europium) doped in a transparent crystal. The qubit is represented by two of the hyperfine levels in the ground state of the ions. The electron population of these two states can be manipulated by optical laser pulses, using the excited state as an intermediate state. An arbitrary superposition state of a single qubit has been demonstrated. However, in this scheme each qubit consists of millions of ions, and all the ions in one qubit can not interact strongly with all the ions in another qubit, which imposes restrictions on the maximum number of qubits that can be used. Therefore, the use of a single ion as a qubit has been proposed, and simulations have shown that it is possible to construct a long chain of qubits using this scheme. However, it is necessary to develop a means of reading out the quantum state of a single-ion qubit.

The method currently being investigated in our group is co-doping another kind of rare-earth ion (cerium) into the same crystal as the qubit ions, and using a single Ce ion as a sensor (this can be pictured as a light bulb) to tell us which state the qubit ion (Pr) occupies via a controllable interaction between these two ions. If the Pr ion is in state 1, the 'light bulb' will be turned on, sending out light (fluorescence). If the Pr ion is in state 0, the bulb will be turned off so no light will be seen.

List of Publications

This thesis is based on the following papers, which will be referred to by their roman numerals in the text.

I **Experimental quantum state tomography of a solid state qubit**
L. Rippe, B. Julsgaard, A. Walther, Y. Ying and S. Kröll.
Phys. Rev. A **77**, 022307 (2008).

II **Extracting high fidelity quantum computer hardware from random systems**
A. Walther, B. Julsgaard, L. Rippe, Y. Ying, S. Kröll, R. Fisher and S. Glaser.
Phys. Scr. **T137**, 014009 (2009).

III **Measurement of linewidths and permanent electric dipole moment change of the Ce 4f-5d transition in Y_2SiO_5 for qubit readout scheme in rare-earth ion based quantum computing**
Y. Yan, J. Karlsson, L. Rippe, A. Walther, D. Serrano, D. Lindgren, M. E. Pistol, S. Kröll, Ph. Goldner, L. Zheng and Jun Xu.
Phys. Rev. B **87**, 184205 (2013).

IV **High fidelity readout scheme for rare-earth solid state quantum computing**
A. Walther, L. Rippe, Y. Yan, J. Karlsson, D. Serrano, S. Bengtsson and S. Kröll.
Manuscript in preparation , (2013).

V **Energy transfer mechanisms in Ce^{3+}-Pr^{3+} and Ce^{3+}-Eu^{3+} codoped Y_2SiO_5 and their impact on single-ion based quantum computing**
D. Serrano, Y. Yan, J. Karlsson, L. Rippe, A. Walther and S. Kröll.
Manuscript in preparation , (2013).

Abbreviations

AOM	Acousto-optical modulator
CCD	charge-coupled device
CNOT	Conditional not
CTE	Coefficient of thermal expansion
ECDL	External cavity diode laser
EOM	Electro-optical modulator
FWHM	Full width at half maximum
FSR	Free spectral range
GHZ	Greenberger-Horne-Zeilinger
PDH	Pound-Drever-Hall
PZT	Piezo electric transducer
RE	Rare-earth
RF	Radio frequency
STED	stimulated emission depletion
SNR	Signal-to-noise ratio
TEC	Thermoelectric cooler
ULE	Ultra-low-expansion
ZPL	Zero-phonon line

Contents

Papers

Chapter 1

Introduction

The objective of the work described in this thesis was to investigate some of the spectroscopic properties of Ce^{3+} ions doped in a bulk crystal of Y_2SiO_5 , and to develop the capability of detecting the fluorescence photons emitted by a single Ce ion in this crystal. These studies were driven by the aim of using the a single Ce ion as a microscopic sensor to probe the quantum state of a neighbouring qubit ion via a controllable ion-ion interaction between them. The interaction is initiated in such a way that the fluorescence emission (on/off) of the readout ion is correlated with the hyperfine state of the qubit ion ($|1\rangle/|0\rangle$).

Quantum computing

Quantum computing relies on a computational mechanism governed by quantum mechanics, which is in stark contrast to the way in which conventional computers work. The fundamental element is the qubit (quantum bit), which can be an arbitrary superposition of two discrete states, e.g. the vertical and horizontal polarization state of a photon, two electronic or hyperfine states of a trapped ion, or the clockwise and anticlockwise current in a superconducting circuit [1, 2]. A few quantum algorithms (e.g. Deutsch's algorithm, Shor's algorithm and Grover's database search algorithm) have been developed exploiting this so-called quantum parallelism to speed up the calculations required for certain types of problems that are difficult for a conventional computer to solve, e.g. factorization of large integers [3]. However, the coherence of a quantum system, on which this tremendous computational ability depends, is fragile and is susceptible to environmental disturbances. So far, no quantum computer has been shown to outperform a conventional computer. Nevertheless, learning how to communicate with

and manipulate a quantum system in a controlled way will enrich our knowledge on the nature of the microscopic world.

Why is single-ion readout required?

In the rare-earth(RE)-ion based quantum computing scheme, the qubit is defined as two of the hyperfine levels of the lowest crystal field level of the ground state of the RE ions, e.g. Pr^{3+} or Eu^{3+}. The long coherence times of both the hyperfine transitions (e.g. 0.9 s for Pr ions in an Y_2SiO_5 crystal [4]) and the optical transitions (e.g. 152 µs for Pr^{3+} $^3H_4 \rightarrow ^1 D_2$ transition) make the RE ions suitable for quantum information processing [5, 6]. Qubit-qubit interactions and arbitrary single qubit rotations have been carried out on a qubit represented by an ensemble of ions, whose optical transition frequencies has a narrow frequency distribution (e.g. 170 kHz) [7, 8]. However, the permanent dipole-dipole coupling between the qubits scales with the distance, r, between the two ions as $\propto 1/r^3$. This spatially dependent coupling, together with the random positioning of the ions in each qubit, makes it difficult to develop a large number of interacting qubits with reasonable dopant concentrations, where each ion in one qubit can control one ion in the other qubits. Because of this problem of scalability, the single-ion qubit approach has been proposed, in which the qubit is instead represented by a single RE ion, e.g. a Pr^{3+} or Eu^{3+} ion. However, it is difficult to read out the quantum state of a single-ion qubit. Direct hyperfine-state-selective fluorescence measurements are not possible (the reasons why will be presented in Chapter 6). It has therefore been suggested that a different species of RE ion from the qubit ion could be co-doped into the crystal, serving as a probe, and called the readout ion. Ce is the candidate under investigation in this work.

Single molecule/ion detection

Single molecule/ion detection reveals the microscopic behaviour of an individual emitter which is normally masked by an ensemble [9, 10]. It can also serve as a tool to study the nanometre scale environment of individual emitters [11]. It is also a very useful technique in chemical and biological analysis.

Research on single molecule/ion detection started in the late 1970s, and can be divided into three types according to the host environment: single molecules in a liquid solvent [12–14], a free single ion in a trap [15–17], or a single molecure/ion in a transparent solid, such as a thin film [18], a nanocrystal [19] or a bulk crystal [20–22]. Two difficulties are encountered when studying ions in a bulk crystal, which is the case in the work described here. One is that it is necessary to establish accessibility to a single ion among

the thousands to billions of ions within the resolved volume of the objective lens. The number of ions can be reduced either by using an ultra-pure crystal, or by making use of spectral selectivity, providing the linewidth of the excitation source is much narrower than that of the ion transition frequency. The other difficulty is suppressing the noise from the background fluorescence originating from unavoidable redundant dopants (e.g. ions in another site), or the Raman scattering of the substance on the surfaces, etc.

In the present work, Y_2SiO_5 crystals doped with Ce^{3+} at dopant concentrations as low as 10^{-7} relative to Y ions were used. The number of ions physically available is about 2000 ions per μm^3 on average. This number can be further reduced by four orders of magnitude by using spectral selectivity.

Experiments intend to identify whether the signal indeed originated from a single Ce ion usually take a few hours. Within this period of time, the frequency of the exciting laser should be sufficiently stable to obtain a good signal to noise ratio (SNR). An active frequency stabilization system was built, and trial experiments were carried out on single ion detection.

Outline of this thesis

Chapter 2 describes the coherent light-matter interaction in terms of the optical Bloch equations, and introduces the basic concepts of fluorescence emission, the techniques used for single molecule/ion detection and the properties and characterization of single molecule/ion emission.

The spectroscopic properties of RE ions doped into a crystal relevant for quantum computing are described in Chapter 3, focusing on the inhomogeneous and homogeneous linewidth broadening mechanisms and the methods used to probe the linewidths. The properties of the widely used host Y_2SiO_5 , and spectroscopic data for Pr^{3+} and Eu^{3+} in an Y_2SiO_5 crystal are summarized.

Chapter 4 describes the two different experimental systems used for the work presented in this thesis. One system was designed for the quantum control experiments and the other for the single Ce ion detection.

Chapter 5 summarizes the Pound-Drever-Hall (PDH) locking technique, and presents the design of the frequency stabilization system of the external cavity diode laser (ECDL) and the experimental set-up of the system.

Chapter 6 introduces the two approaches considered for RE ion quantum computing. In the ensemble qubit approach, the experimental demonstration of qubit initialization, arbitrary single qubit rotations and quantum tomography is presented. In the single-ion qubit approach, the concept of of single ion readout is discussed, the fidelity of the single-ion readout scheme is analysed

and the potential energy transfer process between the neighbouring ions is discussed.

Chapter 7 presents the spectroscopic investigations of the Ce ions with regard to the readout ion requirements. The inhomogeneous and homogeneous linewidths of the zero-phonon line (ZPL) were measured and the Ce-Pr ion-ion interaction was demonstrated, from which the difference in the permanent dipole moment between the ground and excited states were calculated.

Chapter 8 outlines the experimental progress made towards detecting a single Ce ion. Trial experiments were carried out in an attempt to turn the fluorescence signal of a single ion on and off scanning the excitation laser frequency across its resonance line. Unfortunately the signal does not seems to from a single ion. Potential reasons for the failure of the experiment are presented, and suggestions made on the improvements.

Chapter 2

Light-matter interaction and single-molecule detection

This chapter provides a brief introduction to some fundamental aspects of light-matter interaction. This maybe a coherent process (e.g. Rabi oscillations) or an incoherent process, which can be seen in daily life, such as the fluorescent digits on a watch, or the fluorescent strips on a policeman's clothes. First, the optical Bloch equation, which describes the coherent response of matter to irradiation by coherent light, will be introduced (Section 2.1). Then, the basics of an incoherent process, fluorescence emission, will be presented (Section 2.2), followed by a short description of single-molecule/ion detection techniques and the characterization of a single emitter (Section 2.3).

2.1 Bloch sphere representation of a two level atomic system interacting with a laser radiation

The optical Bloch equations are an analogue of the Bloch equation developed for nuclear magnetic resonance [23] in the optical frequency regime. They describe the time evolution of an atomic state during its interaction with an external coherent light field in the semiclassical regime, where the atom is quantized as a discrete two-level system, the external light field is treated as a classical electromagnetic wave described by the Maxwell equations, and the interaction energy between them is described in the electric dipole approximation.

The derivation of the optical Bloch equations for an ideal system without relaxation is quite straightforward starting from Schrödinger equation, as shown e.g. by C. J. Foot [24]. For a real system, however, the relaxation terms must be taken into account.

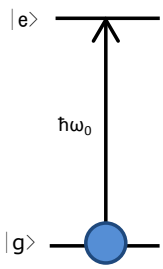

Figure 2.1. *A simple two-level system with a transition frequency of ω_0, an excited state lifetime of T_1, and optical coherence time of T_2. The two eigenstates are denoted as $|g\rangle$ (ground state) and $|e\rangle$ (excited state).*

A transparent way of doing this is illustrated by M. O. Scully et.al. [25], who introduced a phenomenological decay term into the Liouville or Von Neumann equation of motion for the density matrix.

2.1.1 The density matrix

The density matrix of a system is defined as

$$\rho = |\psi\rangle\langle\psi|, \tag{2.1}$$

where $|\psi\rangle$ is the wavefunction of the system in Dirac notation. For a two-level system, as illustrated in Figure 2.1, an arbitrary state $|\psi\rangle$ can be viewed as a superposition of the ground state ($|g\rangle$) and an excited state ($|e\rangle$) as

$$|\psi\rangle = C_g(t)|g\rangle + C_e(t)|e\rangle, \tag{2.2}$$

where $|C_{g,e}(t)|^2$ is the probability of the system being in the ground or excited state at time t. In the basis formed by these two eigenstates, the density matrix ρ is given in the matrix representation by:

$$\rho = \begin{bmatrix} \rho_{gg} & \rho_{ge} \\ \rho_{eg} & \rho_{ee} \end{bmatrix} = \begin{bmatrix} |C_g(t)|^2 & C_g(t)\cdot C_e^*(t) \\ C_g^*(t)\cdot C_e(t) & |C_e(t)|^2 \end{bmatrix}, \tag{2.3}$$

where $\rho_{ij} = \langle i|\rho|j\rangle$ is the matrix element of ρ and $|i,j\rangle$ refers to the $|g\rangle$ or $|e\rangle$ state. The diagonal terms in Equation (2.3) denote the population of the system in the ground (or excited) state, and the off-diagonal terms describe the atomic polarization.

2.1.2 The optical Bloch equations

The Liouville equation describes the system evolution thoroughly but it is so compact that it is not easy to get an intuitive picture of the light-matter interaction. For that purpose, three new real quantities based on density matrix elements have been defined as follows:

$$\begin{aligned} u(t) &= \rho_{ge}e^{-i\omega t} + c.c., \\ v(t) &= -i\rho_{ge}e^{-i\omega t} + c.c., \\ w(t) &= \rho_{ee} - \rho_{gg}, \end{aligned} \tag{2.4}$$

where ω is the angular frequency of the external electromagnetic field and *c.c.* stands for the complex conjugate. u and v represent the atomic polarizations, and w is the population difference between the two transition states. It is worth noting that $|u|^2 + |v|^2 + |w|^2 = 1$, which will be used in a later discussion.

Taking the time derivative of these equations, making use of the equation of motion for the density matrix elements obtained from

the Liouville equation and using the rotating wave approximation [25], gives the optical Bloch equations:

$$\begin{aligned}\dot{u} &= -\frac{1}{\mathrm{T}_2}u - \Delta v + \Omega_{\mathrm{Im}} w,\\ \dot{v} &= \Delta u - \frac{1}{\mathrm{T}_2}v + \Omega_{\mathrm{Re}} w,\\ \dot{w} &= -\Omega_{\mathrm{Im}} u - \Omega_{\mathrm{Re}} v - \frac{1}{\mathrm{T}_1}(w+1).\end{aligned} \tag{2.5}$$

The above equations are valid for a system initially in the ground state ($w = -1$). T_1 and T_2 are the lifetime of the excited state and the coherence time of the optical transition, respectively. They will be further discussed in Section 3.3. Δ denotes the frequency detuning between the external light frequency (ω) and the atomic transition (ω_0). Ω_{Re} and Ω_{Im} are the real and imaginary parts of the complex Rabi frequency (Ω), which describes the coupling between the external electromagnetic field and the atom as follows:

$$\Omega(t) = \frac{\mu \cdot \mathcal{E}(\mathbf{t})}{\hbar}, \tag{2.6}$$

where μ is the transition dipole moment of the material ($\mu = \langle g|qr|e\rangle$, where q is the charge on an electron), and $\mathcal{E}(\mathbf{t})$ is the complex amplitude of the external electromagnetic field.

The advantage of using u, v and w is not yet apparent, this will become clear in the next section.

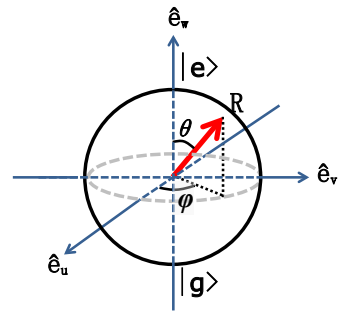

Figure 2.2. *An arbitrary Bloch vector* $\mathbf{R}$ *on the Bloch sphere.*

2.1.3 The Bloch sphere

u, v and w as expressed above, Equation (2.5), can be seen as three components of another vector, $\mathbf{R}$, which is defined in a three-dimensional space by three orthogonal unit vectors, $\hat{\mathbf{e}}_\mathbf{u}$, $\hat{\mathbf{e}}_\mathbf{v}$ and $\hat{\mathbf{e}}_\mathbf{w}$ as follows:

$$\mathbf{R} = u\hat{\mathbf{e}}_\mathbf{u} + v\hat{\mathbf{e}}_\mathbf{v} + w\hat{\mathbf{e}}_\mathbf{w}. \tag{2.7}$$

Figure 2.2 shows an arbitrary Bloch vector characterized by the angles θ and φ on a unit sphere (the so-called Bloch sphere). The corresponding state is

$$|\phi\rangle = e^{i\varphi}\sin\frac{\theta}{2}|g\rangle + \cos\frac{\theta}{2}|e\rangle. \tag{2.8}$$

It is clear that a vector pointing straight down (or up) refers to the $|g\rangle$ (or $|e\rangle$) state. A vector in the equatorial plane represents an equal superposition of the $|g\rangle$ and $|e\rangle$ states, the phase factor ($e^{i\varphi}$) describes the coherence property between the ground and excited state.

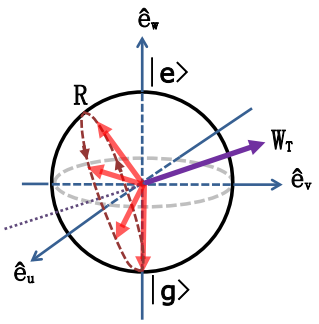

Figure 2.3. *Time evolution of the Bloch vector under light illumination. The movement of* $\mathbf{R}$ *constitutes a cone with its axis being the vector* $\mathbf{W_T}$.

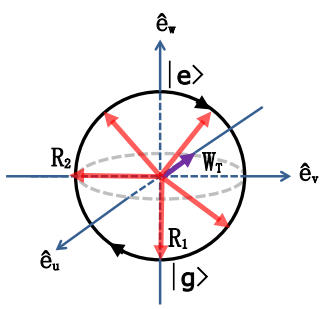

Figure 2.4. *Under continuous wave excitation, the Bloch vector (initially in ground state* $\mathbf{R_1}$*) will rotate clockwise in the* $\hat{\mathbf{e}}_\mathbf{v} - \hat{\mathbf{e}}_\mathbf{w}$ *plane. Red arrows denote the instant Bloch vector positions.*

Bloch equations (2.5) can be represented by the Bloch vector in a very compact form as:

$$\dot{\mathbf{R}} = \mathbf{W_T} \times \mathbf{R} - (\frac{1}{\mathrm{T}_2}u, \frac{1}{\mathrm{T}_2}v, \frac{1}{\mathrm{T}_1}(w+1)), \tag{2.9}$$

where $\mathbf{W_T} = (-\Omega_{\mathrm{Re}}, \Omega_{\mathrm{Im}}, \Delta)$ represents the coupling between the light and atoms.

To visualize the movement of the Bloch vector on the Bloch sphere, we neglect the relaxation terms in Equation (2.9) for simplicity, and consider a short period of time where $\mathbf{W_T}$ is constant, which gives

$$\frac{d}{dt}(\mathbf{R} \cdot \mathbf{W_T}) = 0. \tag{2.10}$$

The above equation shows that the projection of $\mathbf{R}$ onto $\mathbf{W_T}$ is constant, which means that $\mathbf{R}$ describes a cone around $\mathbf{W_T}$, see Figure 2.3. It is possible to engineer the external light field to obtain a certain Bloch vector rotation, as was done in the study described in Paper **I**.

Pulse area

During on-resonant continuous wave irradiation (for simplicity assuming $\Omega_{\mathrm{Im}} = 0$), the Bloch vector rotates clockwise in the $\hat{\mathbf{e}}_\mathbf{v} - \hat{\mathbf{e}}_\mathbf{w}$ plane, see Figure 2.4. The resulting variations along $\hat{\mathbf{e}}_\mathbf{w}$ are called Rabi oscillations, i.e. the atomic state is varying continuously between in the $|g\rangle$ and $|e\rangle$ state. In general, light pulses can be used to obtain a specific final state. The pulse area (Θ) is used to quantify the amount of Bloch vector rotation, which is defined as:

$$\Theta(t) = \int_0^t \Omega_{\mathrm{Re}}(t^{'})\, dt^{'} \tag{2.11}$$

Ω_{Re} is governed by the specific pulse type, e.g. it is constant for a square pulse, a Gaussian function for a Gaussian pulse, and a hyperbolic secant function for a hyperbolic secant pulse, as was used in the study presented in Paper **I**. Thus, a pulse is often named according to its pulse area, for instance, a $\pi/2$ pulse means that the Bloch vector will be rotated by 90° during the interaction with pulse. If the initial vector is in the $|g\rangle$ state (denoted $\mathbf{R_1}$ in Figure 2.4), it will end up in the equatorial plane ($\mathbf{R_2}$).

2.2 Fluorescence emission

Light-matter interactions can be manifested as light absorption by the material or as radiative light emission by the material. As an illustration let us consider a two-level free atom interacting with

an external field, as shown in Figure 2.5. If the light frequency matches the energy separation between the levels, the atom will be pumped into the higher state $|e\rangle$ (Figure 2.5a) by absorbing one photon from the external field. As excited state has a natural lifetime, this excited atom will eventually spontaneously decay back to the lower energy state, i.e. the ground state $|g\rangle$ (Figure 2.5b). When this happens a photon will usually be emitted. This radiative emission is called luminescence. Luminescence is common in our daily life, e.g. glow sticks and luminous watches.

Luminescence is often divided into two categories, fluorescence and phosphorescence. The difference between them lies in the timescale. Fluorescence typically has a lifetime in the ns range, whereas phosphorescence is a much slower process, in the millisecond to second range. In this thesis only fluorescence is of interest.

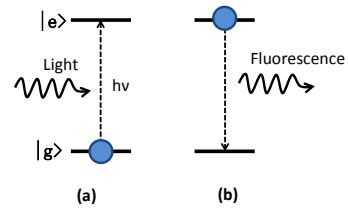

Figure 2.5. *Illustration of light-matter interactions. The ground state atom absorbs a photon from the external light source and is pumped to an excited state $|e\rangle$ (a). As time elapses the atom will spontaneously decay to the ground state $|g\rangle$, emitting a fluorescence photon (b).*

2.2.1 Fluorescence characterization

The spectroscopic characteristics of the fluorescence emitted by a material provides some information on the intrinsic properties of the material. In this section some of these characteristic parameters will be briefly reviewed.

(i) The emission spectrum

A two-level system such as that illustrated in Figure 2.5 is an idea model to obtain a reasonable understanding of light-matter interactions. But in reality, there are many energy levels in both the lower and higher energy states. An excited atom may spontaneously decay to any of the lower levels, while emitting a photon with an energy corresponding to the energy separation between these two states. Thus, the emission wavelength is not a single wavelength, but spreads over a range, creating a so-called emission spectrum. The emission spectrum may consist of discrete lines or a continuous band. Examples of the former are: the emission from molecules in a gas phase, and the emission from the 4f-4f transitions of a RE ion in a crystal [26–28]. Examples of continuous bands are the emission from molecules in a solvent and from the 4f-5d transitions of a RE ion in a solid matrix.

(ii) The excitation spectrum

Contrary to the emission spectrum mentioned above, which is observed by recording the emission wavelength following excitation at a specific wavelength, the excitation spectrum shows the spread of excitation wavelength to obtain a constant emission wavelength. This spectrum can reveal the structure of the excited state levels where only non-radiative relaxation takes place between them.

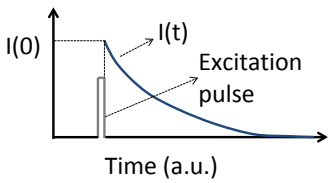

Figure 2.6. *Illustration of the excitation pulse and fluorescence signal of a time resolved fluorescence measurement. The intensities of the pulse and fluorescence signal are not to scale.*

(iii) Stokes shift
The Stokes shift is the name given to the energy difference between the maximum of the emission spectrum and the maximum of the absorption spectrum. Usually the emission spectrum is red-shifted, corresponding to a non-zero Stokes shift. In most cases, the loss of energy is caused by the non-radiative relaxations due, for example, to the interaction with the environment.

(iv) Fluorescence lifetime
The fluorescence lifetime is defined as the time that has elapsed when the fluorescence intensity has fallen to ∼37% of its maximum. In a time-resolved fluorescence measurement, a laser pulse is used to pump the atoms into their excited state, and the intensity of the fluorescence emission $I(t)$ is recorded as a function of time, see Figure 2.6. For a two level system an exponential decay curve is obtained, described by the following equation:

$$I(t) = I(0)e^{-t/\tau}, \tag{2.12}$$

where $I(0)$ refers to the fluorescence intensity immediately after the excitation pulse and τ is the fluorescence lifetime.

The exponential decay expressed in Equation (2.12) essentially originates from the finite lifetime of the excited state (T_1), which contains two contributions: the lifetime of the non-radiative decay process (T_{nrad}) and that of the radiative decay (T_{rad}). The relation between them is:

$$\frac{1}{T_1} = \frac{1}{T_{rad}} + \frac{1}{T_{nrad}}. \tag{2.13}$$

It is straightforward to prove that the fluorescence lifetime τ defined in Equation (2.12) is in fact the natural lifetime T_1 in Equation (2.13) although the fluorescence emission only results from the radiative decay process. This can be qualitatively understood as: the presence of the non-radiative decay modulates the population in the excited state so that the overall fluorescence intensity decays faster than the radiative lifetime.

(v) The quantum yield (or quantum efficiency) of the fluorescence
This refers to the ratio of the number of fluorescence photons emitted to the number of excitation photons absorbed. For a system in which the non-radiative decay is negligible, the quantum yield is unity.

2.2.2 Fluorescence quenching

There are a number of processes that can decrease the intensity of fluorescence emission. This is called fluorescence quenching. Only

the processes that are relevant to the detection of the fluorescence from a single Ce ion will be discussed here. One of these processes involves the energy transfer from an excited atom (called the donor) to a nearby atom (called the acceptor), which is in ground state. This transfer results in the donor decaying to the ground state without emitting a fluorescence photon, and the acceptor is promoted to its excited state. Another process is decay of the excited ion to a relatively long-lived intermediate state (called the trapping state), other than the state it was excited from. Short descriptions of the principles of these two processes are given below.

Energy transfer

Energy transfer is a transition dipole-transition dipole interaction, where two ions are treated as two transition dipoles with specific orientations, and the mutual interaction between the electric fields from each dipole creates the interaction. The energy transfer strength depends on the spatial separation r between the two dipoles as $1/r^6$, which is significant when r is in the subnanometre range.

Figure 2.7 illustrates the energy transfer process. Initially, both the donor and acceptor are in the ground state. An external field then pumps the donor into the excited state without affecting the acceptor, Figure 2.7a. While the donor is in its excited state, there is a probability that the energy will be transferred from the donor to the acceptor and, as a result, the donor will end up in the lower energy ground state with no photon emission, and the acceptor is pumped to the excited state by the transferred energy, Figure 2.7b. The theory of energy transfer has been well developed, for example [29]. This process creates an additional decay channel to the donor, which decreases the donor's excited-state lifetime from its natural lifetime T_1 to a shorter value T_1^{ET}.

The energy transfer rate k_{ET} is used to describe the part of the decay rate caused by the energy transfer process, and is defined as:

$$k_{ET} = \frac{1}{\mathrm{T}_1} \cdot \left(\frac{R_0}{r}\right)^6, \tag{2.14}$$

where R_0 is called the Förster distance, at which the energy transfer rate k_{ET} is equal to the undisturbed decay rate T_1^{-1}. This means that an excited donor has an equal probability of decaying without interacting with the acceptor, as if it were not present, or as a result of the energy transfer to the acceptor. In this case, the fluorescence intensity decreases to half. The Förster distance is an intrinsic parameter determined by the donor-acceptor system, and depends mainly on the spectral overlap between the donor emission spectrum and the acceptor absorption spectrum. The exact formulation is given, for example, by J. R. Lakowicz [30].

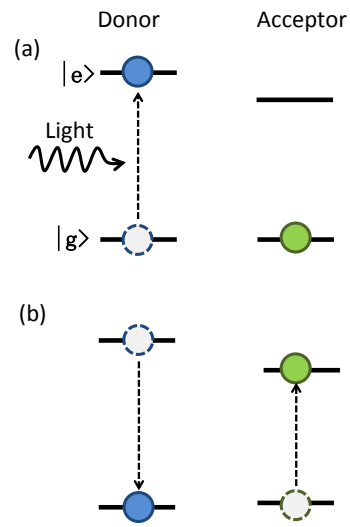

Figure 2.7. *Illustration of the energy transfer process. The donor is pumped to the excited state by an external field and the nearby acceptor is not affected (a). The dashed circles denote the initial state of the electron. As a result of the energy transfer process, the donor ends up in the ground state but not emitting a fluorescence photon, and the acceptor gained the transferred energy and jumped to its excited state (b).*

The fraction of the decay rate caused by the energy transfer process is described by the energy transfer efficiency η_{ET}. It can also be understood as the fraction of excited donors that decays through the energy transfer channel. The mathematical expression of η_{ET} is:

$$\begin{aligned}\eta_{ET} &= \frac{k_{ET}}{\mathrm{T}_1^{-1} + k_{ET}} \\ &= \frac{R_0^6}{r^6 + R_0^6} \\ &= \frac{\mathrm{T}_1 - \mathrm{T}_1^{ET}}{\mathrm{T}_1},\end{aligned} \tag{2.15}$$

where $1/\mathrm{T}_1^{ET} = 1/\mathrm{T}_1 + k_{ET}$ is used. At a 50% energy transfer efficiency, the excited-state lifetime of the donor is reduced to half its original value.

Trapping state

For an ion with multiple ground state levels, which may be crystal splitting levels, or fine or hyperfine structure levels, decay could take place from the excited state to any of the ground state levels. If the ground states have a long lifetime, then the decayed ion is trapped there until relaxation occurs, or, in other words, the ion is lost in the sense that it is not available to be excited from its ground state for a certain period of time. The fluorescence intensity is then decreased. When detecting the fluorescence of a single Ce ion, it is important to know if there is such a trapping level. That was part of the purpose of the spectral hole-burning experiment described in Paper **III**.

2.3 Single-molecule/ion detection

Single-molecule/ion detection is of interest as it would allow us to technically explore the ultimate detection limit. It is also of scientific value because it opens up a way of investigating the microscopic behaviour of an individual emitter, instead of observing the average effect of an ensemble of molecules or ions [9, 10]. Single-molecule/ion detection also serves as a tool to study the nanometre scale environment of individual emitters [11]. The purpose of this work was to detect a single Ce ion in a Pr:Ce:Y_2SiO_5 or Eu:Ce:Y_2SiO_5 crystal in such a way that the fluorescence state (ON or OFF) of this single Ce ion is able to tell us the hyperfine state of a neighbouring qubit ion (Pr or Eu). This scheme will be described in detail in Chapter 6.

The technical requirements for detecting a single emitter (molecules or ions) vary with the environment, and are related to the possibility of having only one single emitter in the focal volume

interacting with the irradiation, and suppression of the background signal from sources other than the emitter under investigation.

A single emitter can be detected by observing the fluorescence emission, or by monitoring its absorption spectrum. For example in a study by Moerner et al., a single molecule absorption spectrum was recorded, using frequency modulation spectroscopy to increase the signal to noise ratio (SNR) to a level at which single molecules could be detected [18]. Detecting the the absorption from a single emitter is more difficult than detecting the fluorescence, as the weak absorption may be concealed by the noise from the strong transmitted light. But this is not a problem for the fluorescence detection because the fluorescence spectrum is often red-shifted respective to the excitation wavelength. The SNR of fluorescence detection can be improved by accumulating the fluorescence photons for a longer period of time. The detection of fluorescence from a single emitter is discussed below.

2.3.1 Challenges in single-emitter detection

The fluorescence signal from a single emitter is so weak that it is often below the noise level of the background signal (any other light signal than the signal of interest, e.g. fluorescence emission from the host or ambient light, etc.). It is thus necessary to increase the SNR. On the signal side, signal losses before reaching the photodetector should be minimized. This can be done using a fluorescence detection system with high collection efficiency, high-transmission optics (lenses, filters etc.), and high quantum efficiency photodetector (e.g. avalanche photodiodes, photomultiplier tubes or CCD cameras). On the noise side, low noise photodetector should be used, and the noise level of the background signal, should be suppressed as far as possible, e.g. by reducing the excitation volume.

To achieve single-emitter detection with a reasonable SNR the following two conditions must be fulfilled.

(i) An environment must be created in which only one molecule/ion actively interacts with the macroscopic laser field in the excitation volume.
This condition imposes no restrictions on the single ion in a electromagnetic trap, and can also be easily achieved for the molecules in a solvent simply by diluting the sample sufficiently. But it is not trivial to fulfil this condition in condensed matter, especially in a bulk crystal, as the atomic number density is comparatively high. For instance, the number density of cerium ions in a $Ce{:}Y_2SiO_5$ crystal with a dopant concentration as low as $1{\times}10^{-7}$ relative to Y ions is $\sim$2000 ions/μm^3. However the transition frequencies of these ions spread out inhomogeneously over tens of GHz range because of the different local lattice strain experienced by each

ion. This frequency span is about four orders of magnitude larger than the intrinsic transition linewidth of an individual ion (measurement presented in Paper **III**). This line broadening provides us with the possibility of spectrally singling out one ion at a specific absorption frequency. By tuning the excitation laser frequency into the wing of the inhomogeneous line profile, which may mean tens of inhomogeneous linewidths away from the line centre, it is possible to find a single ion on resonance with the laser frequency (assuming the laser linewidth is not much broader than the homogeneous linewidth of the ion), although thousands of ions are physically present. This method was used in [18] to achieve single-molecule detection in a crystal.

Another way to accomplish this condition is to use an ultra-pure crystal, which means that the dopant concentration of the ions of interest is so low that there is only one ion present in the excitation/observation volume, as has been achieved for some crystals, e.g. an ultra-pure YAG crystal [21, 22].

(ii) The fluorescence signal from a single emitter must be higher than the overall noise of the system, which includes the quantum noises of the signal being studied and the disturbing background signal, and the electronic noise from the detection equipments.
The background signal may originate from other sources than the single emitter under study, as well as dark current in the detector, which is an important factor in the choice of photo detectors. Examples of the former case are fluorescence emission from impurities resulting from the sample preparation process, or from the host ions, Raman scattering from the host, or autofluorescence from optics (such as the substrate mirrors or lenses, or spectral filters). Autofluorescence can be significantly suppressed significantly by choosing the correct optics, but the background fluorescence emitted by impurities and Raman scattering is difficult to suppress. However they can be reduced by restricting the excitation volume, as the background signal strength is proportional to the number of impurities or number of host ions available in the excitation volume. Methods of restricting the excitation/observation volume are discussed below.

2.3.2 Restricting the excitation/observation volume

A number of techniques used to confine the excitation/observation volume are described in this section.

Confocal microscope

A schematic illustration of a confocal microscope set-up is shown in Figure 2.8. Its working principle has been well described in the literature e.g. [31].

In a confocal microscope, the excitation laser is focused to the sample by an objective lens and a fraction of the fluorescence photons emitted by the molecules/ions under illumination is collected by the objective lens, then passed through the dichroic beam splitter and an optical filter to eliminate the excitation light. Finally, they are focused by lens L_p onto a pinhole, located in the image plane of P_{obj} (the focal plane of the objective lens). Each point on plane P_{obj} is imaged to a specific point on the pinhole plane. The fluorescence originating from the points (such as point A and B in Figure 2.8) out of the focal point (point O) will be rejected by the pinhole. Benefiting from the confocal geometry, both the axial and lateral resolution decrease to approximately 70% of the corresponding resolution of the objective lens [32, 33]. In Rayleigh criterion, the lateral resolution of the objective lens is $0.61\lambda/NA$ [34], and the axial resolution is $2\lambda n/(NA)^2$, where λ and n denote the emission wavelength, and the refractive index of the sample, respectively.

The axial resolution can be improved by several folders in a 4Pi confocal microscope [35, 36], where two objective lenses are located face to face collinearly around the sample. They can both focus the excitation laser and collect the fluorescence signal. The interference of two counter-propagating beams, which may be the excitation beams or fluorescence beams or both, further increases the axial resolution.

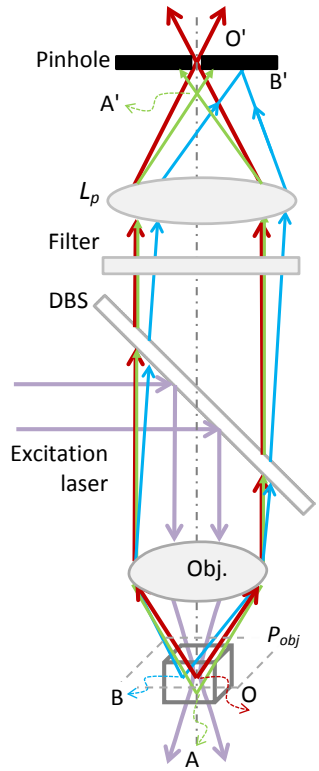

Figure 2.8. *The working principle of a confocal microscope. A pinhole and the focal plane P_{obj} of the objective lens constitute the image planes of the lens system. Points O', A' and B' are the respective image point of O, A and B in plane P_{obj}. The fluorescence signal from the out-of-focus points such A and B are rejected by the pinhole.*

Total internal reflection

Contrary to a confocal microscope which restricts the observation volume, total internal reflection can be used to confine the excitation volume by using an evanescent field for illumination. A schematic set-up is shown in Figure 2.9. In this scheme the illumination beam enters the sample indirectly after first passing through a high refractive index prism, then propagating into the sample with an incidence angle, θ_i, which is larger than the critical angle θ_c of the interface, where θ_c is determined by the refractive indices of the sample and prism from: $\theta_c = \arcsin(n_{smp}/n_{prism})$ $(n_{smp} < n_{prism})$. Under this illumination condition $(\theta_i > \theta_c)$, total internal reflection occurs, which means that the incident energy is totally reflected from the interface in a stationary state [37]. However, an electric field (evanescent wave) penetrates into the sample close to the boundary, and the intensity of this electric field decreases exponentially along the z axis as:

$$I_z = I_0 e^{-z/d}, \tag{2.16}$$

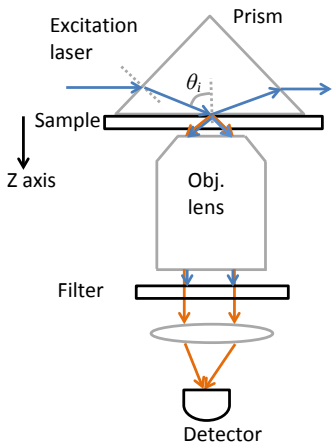

Figure 2.9. *Evanescent field illumination to restrict the excitation volume. The light impinged to the sample has a incidence angle θ_i larger than the critical angle θ_c. So the incident beam is totally reflected in a stationary state. Only the penetrating evanescent field excites the sample, which limits the excitation depth to hundreds of nanometer range.*

where I_0 is the intensity at the interface and d is the penetration depth, which depends on the illumination wavelength (λ_{vac}), the refractive indices of the prism and the sample, and the angle of incidence as [37]:

$$d = \frac{\lambda_{vac}}{4\pi\sqrt{n_{prism}^2 \sin^2\theta_i - n_{smp}^2}}. \tag{2.17}$$

The penetration depth is $\sim$ 60 nm for a 370 nm laser with an incidence angle of 75°, using a prism with $n_{prism} = 1.9$ and a sample with $n_{smp} = 1.8$. For a incident beam spot of 20 µm diameter, which can be obtained from a 1 mm wide beam using a 50 mm lens , the excitation volume is approximately 20 µm^3.

Evanescent field illumination restricts the excitation volume to the subwavelength range in only one dimension (that normal to the interface) , whereas confinement is possible in all three dimensions using a confocal microscope.

Other methods

Other techniques have also been used such as two-photon excitation e.g. [21, 38–40], and stimulated emission depletion (STED) e.g. [41–43] to confine the excitation volume.

Two-photon excitation is a third-order nonlinear process, localized to the vicinity of the focal point as the fluorescence intensity depends on the square of the incident beam intensity, which indicates that along the optical axis the fluorescence signal scales with the distance (between the observation plane to the focal plane) to the fourth power. Also, the fluorescence signal is free from background, which is a considerable improvement, especially for ultra-violet excitation, but it places high demands on the excitation laser power.

STED is an elegant technique to achieve a fluorescence spot, the size of which is not restricted by the diffraction limit. However, a sophisticated experimental system is required, including two lasers at different wavelengths. One of them (the so-called STED laser) must be sufficiently intense enough for the depletion rate to overcome the excitation rate. Furthermore the STED beam must have a specific intensity distribution, where the intensity goes sharply to zero at the focal point of the excitation laser and intense elsewhere else.

2.3.3 Characterization of single molecule/ion detection

In the previous sections methods of acquiring a signal from a single emitter were presented. The next issue is to determine under what circumstances it is possible to claim that the faint signal detected indeed originates from a single emitter.

Turning the fluorescence signal on and off

A simple way of characterizing single-photon emission is to record the fluorescence signal as a function of the excitation laser frequency across the homogeneous absorption line of the single emitter. The fact that the fluorescence can be turned on and off indicates that the emission originates from a single emitter. This is one of the earliest methods used to characterize single-molecule emission [44] and it is also the method we have tried to detect the single Ce ion, as will be discussed in detail in Chapter 8.

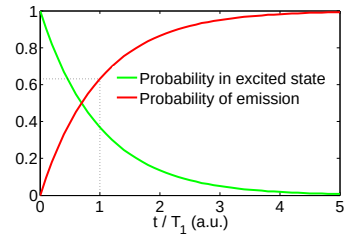

Figure 2.10. *The probability of a single emitter being in the excited state and the probability of single-photon emission as a function of elapsed time. The dashed line indicates the emission probability at time $t = T_1$, which is 63%.*

Photon antibunching

Fluorescence emission can be regarded as an electromagnetic wave in classical wave optics, as well as a stream of quantized energy packages (photons) in the quantum optics perspective. Photon bunching and antibunching effects describe how the stream of photons is distributed in the time domain: randomly (coherent light), bunched (thermal light or discharge lamps), or antibunched (single-photon sources).

In the case of an excited single emitter, there is only one photon emitted at a time. However decay is a probabilistic process, as shown in Figure 2.10, and at time T_1 (excited state lifetime) the probability of a fluorescence photon being emitted is 63%. At a shorter time scale $t \simeq T_1$, the probability of the excitation-decay cycle happening twice is much lower than that at a longer time scale when $t \gg T_1$.

This photon antibunching effect can be described by the second order correlation function $g^{(2)}(\tau)$, which is defined as:

$$\begin{aligned} g^{(2)}(\tau) &= \frac{\langle \mathcal{E}^*(\mathbf{t})\mathcal{E}^*(\mathbf{t}+\tau)\mathcal{E}(\mathbf{t}+\tau)\mathcal{E}(\mathbf{t})\rangle}{\langle \mathcal{E}^*(\mathbf{t})\mathcal{E}(\mathbf{t})\rangle\langle \mathcal{E}^*(\mathbf{t}+\tau)\mathcal{E}(\mathbf{t}+\tau)\rangle} \\ &= \frac{\langle I(t)I(t+\tau)\rangle}{\langle I(t)\rangle\langle I(t+\tau)\rangle}. \end{aligned} \tag{2.18}$$

where $\mathcal{E}(t)$ and $I(t)$ denote the time-dependent amplitude and intensity of the electric field. $\langle ... \rangle$ refers to the average value of the quantities over a long period of time, and τ is the time interval between two successive measurements. In the photon representation, Equation (2.18) reduces to [45]

$$g^{(2)}(\tau) = \frac{\langle N(t)N(t+\tau)\rangle}{\langle N(t)\rangle\langle N(t+\tau)\rangle}, \tag{2.19}$$

where $N(t)$ is the number of photons emitted at time t and its values is either 0 or 1 for a single emitter, as will be explained later.

A typical experimental set-up to measure the dependence of $g^{(2)}$ on time delay τ is shown in Figure 2.11, where a 50/50 beam

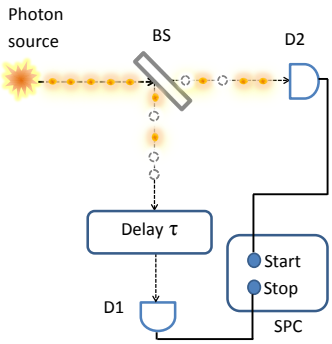

Figure 2.11. *The photon stream is split into two paths by a 50/50 beam splitter. Detectors D1 and D2 record the photons arriving by each path. The pulse resulting from a single photon is registered by a single photon counting board, allowing a histogram of the events when both detectors are triggered to be constructed as a function the time delay τ between the two paths.*

splitter divides the incoming stream of photons into two parts, which are directed to two different detectors, D1 and D2. The resulting electric pulses representing a single photon are registered in a single-photon counting board, where the pulse from D2 starts the trigger and the pulse from D1 stops the trigger. A histogram of events defined by both detectors can be constructed as a function of the time interval between the trigger pulses, which is in principle the $g^{(2)}$ function. The characterization of single emitter emission in terms of $g^{(2)}$ has been demonstrated experimentally [21, 46, 47].

For a comparison, a qualitative description on $g^{(2)}$ for different light sources is presented below.

(i) For a single emitter $g^{(2)}(0) = 0$, which is natural as only one photon can be emitted at a time. The fact that the probability of detecting two photons increases with the time separation τ indicates that $g^{(2)}(\tau) > g^{(2)}(0)$. For an extremely long time delay ($\tau \to \infty$), $g^{(2)}$ approaches unity.

(ii) For a thermal light or a discharge lamp with a constant average intensity $\langle I(t)\rangle = I$ and time-dependent intensity fluctuations $\Delta I(t)$, it is easy to show that

$$\begin{aligned} \langle I(t)I(t+\tau)\rangle_{\tau=0} &= I^2 + \langle \Delta I^2(t)\rangle \\ &> I^2 \ , \end{aligned} \tag{2.20}$$

which indicates that $g^{(2)}(0) > 1$ and $g^{(2)}(t)$ decreases with time delay τ. A strict calculation shows that $g^{(2)}(0) = 2$ [48].

(iii) For a monochromatic coherent light source, the intensity is independent of time, so $\Delta I(t) = 0$, which means that $g^{(2)}(\tau) = 1$ for any delay.

Chapter 3

Rare earth ions in crystals

The rare earth elements consist of the 15 lanthanides of the periodic table plus scandium and yttrium. The electron configurations of a RE ion are the same as that of xenon plus an additional part $\mathbf{4f^x 5d^y 6s^2}$, where x ranges from 0 to 14 for the elements from lanthanum to ytterbium, and y is 1 for La, Ce and Gd, and 0 for all the others, see Figure 3.1 for an illustration. The trivalent RE ions (RE^{3+}) are formed when the two electrons in the outermost 6s subshell and one electron from the 5d subshell (if there is an electron in this subshell) or the 4f subshell (if there is no electron in the 5d subshell) are delocalized from the nucleus. As a result the number of electrons in the 4f subshell of RE^{3+} (except Sc, Y and Lu) is 0 to 13, increasing with ascending atomic number. The electrons in the 4f subshell are shielded from the crystal environment by the completely filled outer-lying 5s and 5p subshells, which greatly reduces the linewidth broadening of the intra-orbital (4f-4f) transitions by the disturbance of the crystal environment. Due to this, the properties of RE^{3+} ions in a crystal resemble those of free ions, which makes a RE^{3+} doped transparent crystal a good material for studying coherent light-matter interactions. The 5d levels, on the other hand, are more exposed to the crystal field, so the homogeneous linewidth of a 4f-5d transition is generally much broader than that of a 4f-4f transition.

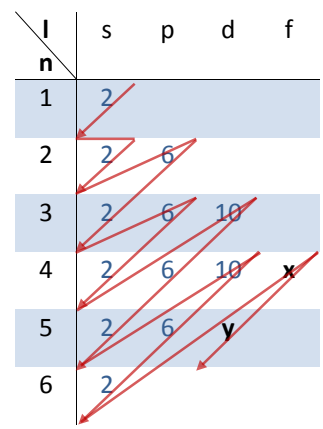

Figure 3.1. *Electron distribution of RE elements in different subshells. Arrows indicate the filling order of the electrons. More information is given in the text.*

RE^{3+} doped Y_2SiO_5 crystals are being used by our group to study the coherent interaction between light and matter, where quantum computing is one example. To understand why $RE^{3+}:Y_2SiO_5$ is a good material, it is helpful to consider two of the fundamental building blocks for a quantum computer.

One building block required to carry out a quantum algorithm is a qubit, which can be in a coherent superposition ($\alpha|0\rangle + \beta|1\rangle$) of the two states ($|0\rangle$ and $|1\rangle$) used in a conventional computing scheme. Coherence means that both the amplitude and phase relationship between these two states are well defined and can be

predicted. This coherence must be preserved throughout any series of computing operations, which is the essential difference between quantum and conventional computing. Thus, a long coherence time is a figure of merit for a good qubit. As mentioned above, the coherence property of a RE^{3+} ion 4f-4f transition is well preserved due to the shielding by the outer-lying 5s and 5p subshells.

Another building block is the multiple qubits and the qubit-qubit interactions, which means operations on one qubit will be carried out conditionally, depending on the state of another qubit. This requires a strong interaction between two qubits so that they can control each other. In a RE-ion-doped crystal, the optical transition lines are inhomogeneously broadened as a result of the random substitutions of the RE ions (qubit ions), which cause slight variations in the crystal field at the sites of the individual ions. The ratio between the inhomogeneous and homogeneous broadening in these systems can be greater than 10^6. Thus a very large number of sub-ensembles of ions can be singled out in frequency space within the inhomogeneous line. Each sub-ensemble can act as a frequency-selectively addressed qubit, which consists of many ions randomly distributed in space. The conditional gate operations in these systems can be realized via the permanent electric dipole-dipole interaction between the strong-interacting ions in each qubit (see Fig.3 and Fig.11 in [49] for more details).

This chapter provides some background information on the properties of the RE ion that are favourable for quantum computing, where single Ce ion detection is part of the work involved in developing the ability to read out the hyperfine state of a single-ion qubit in order to obtain a scalable quantum computing system.

3.1 Energy levels of RE^{3+}

The presence of multiple electrons in the 4f subshell of RE^{3+} ions makes the level structures complicated due to electron-electron interactions. Generally, the level structures of an ion embedded in a solid matrix will become even more complicated by the interaction between the ion and its crystalline surroundings. However, the 4f levels of a RE ion doped in a crystal resemble those of a free ion due to shielding by the outer-lying 5s and 5p subshells. Thus, the non-centrosymmetric crystal field acting as a perturbation breaks the symmetry of the free ion wavefunction. As a consequence, the electronic state becomes a mixture of odd parity and even parity states [50, 51]. This broken symmetry makes the forbidden 4f-4f transition weakly allowed (the oscillator strength is generally in the range of $\sim 10^{-9} - 10^{-6}$) and also gives rise to a permanent electric dipole moment of each state. The lower 4f energy levels were measured by Dieke et.al. [26] in a $LaCl_3$ crystal, as shown in Figure 3.2. The same levels in other crystal substrates may be

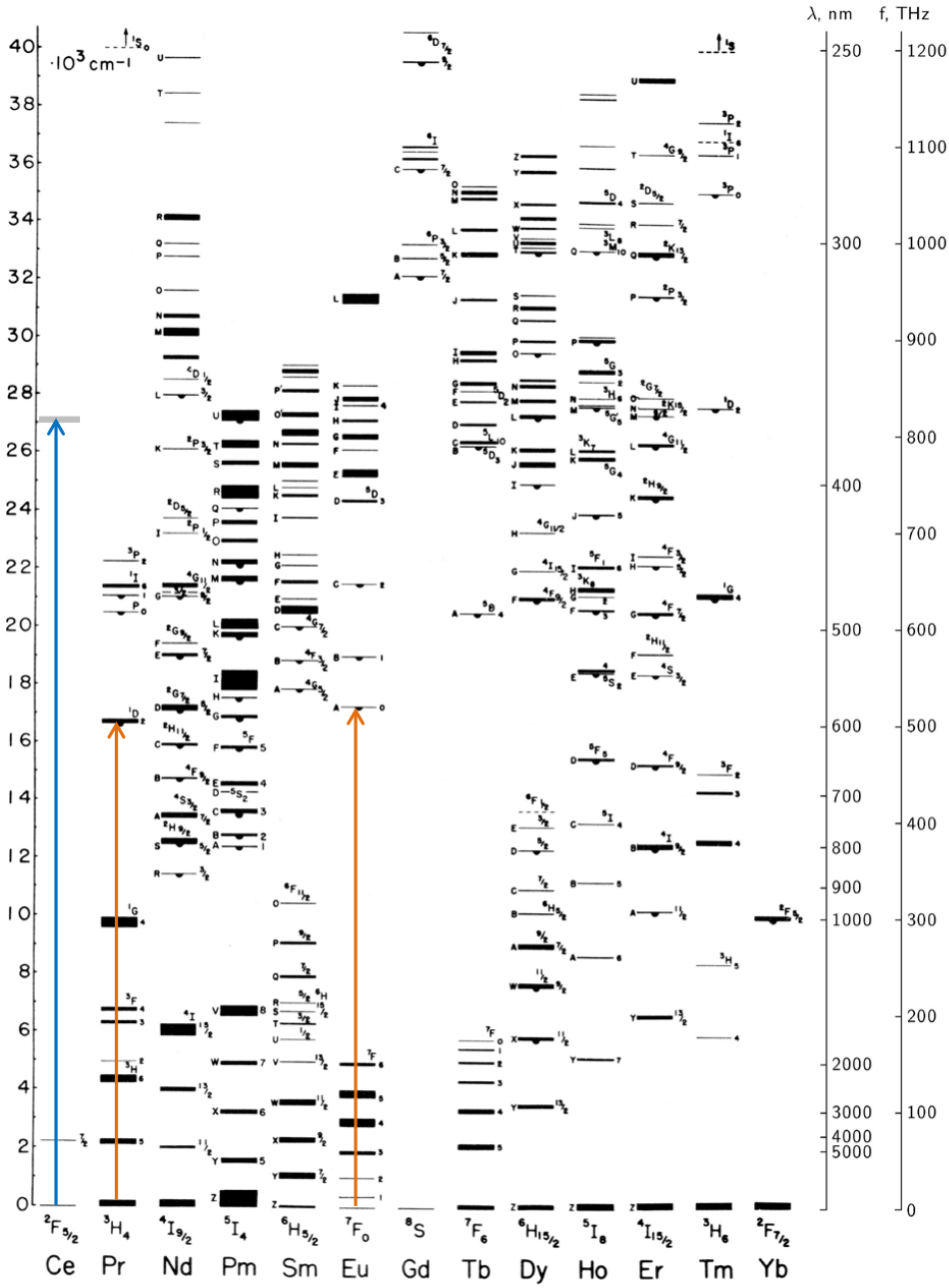

Figure 3.2. *The lower 4f levels of RE^{3+} ions in a $LaCl_3$ crystal measured by Dieke et.al (reproduced from [52]). The thickness of the line represents the crystal field splitting, and the centre of gravity shows the level of the free-ion levels. The arrows indicate the transitions of interest in the present work. The 5d level of Ce^{3+} (grey line at 27000 cm^{-1}) is included only for illustration.*

RE^{3+}	Radius (pm)
Y^{3+}	104
Ce^{3+}	115
Pr^{3+}	113
Eu^{3+}	108.7
Er^{3+}	103
Tm^{3+}	102

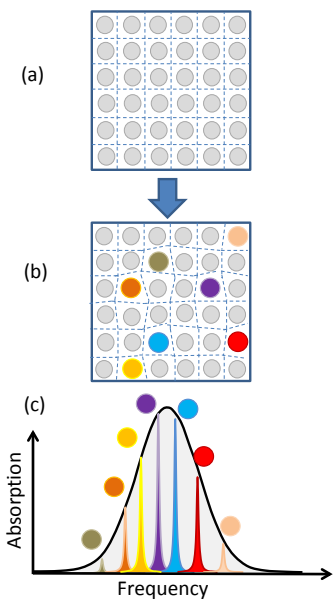

Figure 3.3. *The table gives the ionic radius of some of the RE^{3+} ions in 6-coordination [56]. (a) illustrates the regular lattice sites, that the Y ions occupy. The dashed lines illustrate the lattice strain. (b) shows the distortion in the lattice caused by the dopants, which have different radii from the Y ions. Different colours indicate that the ions belong to different subgroups with a specific transition frequency. (c) illustrates the inhomogeneous transition lines of the dopant ions, where the shaded areas represent the summed-up homogeneous absorption of the ions in an individual subgroup.*

shifted by a few hundred cm^{-1}, but the structure remains the same.

However, the inter-configurational 4f-5d transitions of a RE ion have a stronger dependence on the crystal substrate than a 4f-4f transitions because the 5d levels are much more exposed to crystal strains. Both the absorption and fluorescence spectra of a 4f-5d transition are often continuous bands and only a limited number of zero-phonon lines can be observed [53]. For a 4f-5d transition, the crystal-field induced Stark splitting of the 5d levels is generally greater than the splitting induced by the spin-orbit interaction.

The magnitudes of different interaction-induced splittings of the 4f levels of a RE ion are given in Table 3.1 [54] (Figure 3.10 shows the splitting of levels in Pr^{3+} doped Y_2SiO_5 as an example).

Interaction Mechanism	Energy (cm^{-1})
Non-central electrostatic field	10^4
Spin-orbit coupling splitting	10^3
Crystal field interaction	10^2
Ion-ion interaction	10^{-2}-10
Hyperfine splitting	10^{-3}-10^{-1}
Superhyperfine splitting	10^{-4}-10^{-2}

Table 3.1: *The energy scale of the 4f levels of a RE ion caused by different interaction mechanisms. This table is reproduced from Ref.[54].*

3.2 Inhomogeneous line broadening

The optical transition frequency of an individual RE ion in a crystal is slightly shifted (often red-shifted) compared to a free ion because of the influence of the strain in the local crystalline environment. Even in a very regular lattice, the local environment experienced by an individual ion might be slightly different from one ion to another. This difference could be the result of defects or disorders in the crystal, such as trace impurities (e.g. isotopes of host ions), different lattice sites, nearby ion-ion interactions, vacancies etc. Thus, the optical frequencies of a specific transition of of several identical RE ions are not the same, but spread out often as a Gaussian distribution. This is the so-called inhomogeneous line broadening, which has been reviewed [53, 55].

In the crystals studied in this work, the RE ions are randomly doped into an Y_2SiO_5 crystal by substituting some of the Y ions. Since the ionic radii of RE ions are different from that of Y ions, as can be seen from the Table in Figure 3.3 [56], this substitution distorts the regular lattice structure randomly (see Figure 3.3b), causing the inhomogeneous broadening (see Figure 3.3c).

3.2.1 Line shape

An ion embedded in a crystal vibrates around its equilibrium position due to the interaction with the vibrational motion of the crystal (so-called phonons in a quantum mechanical description). This interaction energy can be approximated by a harmonic potential if the vibrational amplitude is small, which often means that the sample must be at low temperature. Figure 3.4 gives an example of such harmonic potentials of a 4f-5d transition, where the excited parabola is shifted in the configurational coordinates relative to that of the ground state. Thus, a ground to excited state transition could take place from any one of the ground state phonon levels ($|g_i\rangle$, i = 0, 1, 2, 3, ...) to any one of the excited state phonon levels ($|e_i\rangle$, i = 0, 1, 2, 3, ...). This interaction between the ion and the lattice vibrational motions turns the finite linewidth atomic transition into a broad absorption/emission band, especially at high temperatures. At low temperatures (for instance around liquid helium temperature) the higher phonon energy modes are less likely to be populated, so the phonon transitions are greatly reduced. There is one transition (from $|g_0\rangle$ to $|e_0\rangle$) where phonons are not present and this is called the ZPL. At low temperature, the ZPL is usually located at the lower energy end of the absorption band, while it is found at the higher energy end in the emission spectrum, regardless of whether the ion is excited by its ZPL or higher phonon levels, because a higher phonon level in the excited state can relaxes non-radiatively to level $|e_0\rangle$, from where the ions decay to any of the ground state phonon levels radiatively (shown by the downward-pointing arrows in Figure 3.4).

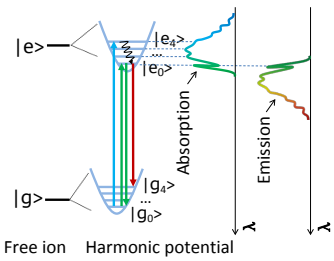

Figure 3.4. *Illustration of the harmonic potential used to describe the ion-phonon coupling in a crystal lattice. In this example, both the absorption and emission spectra are a continuous band, and will be mirror images of each other if the ground and excited state parabolas are identical.*

For RE^{3+} ions in a crystal at low temperature, ZPLs generally dominate the spectra of the 4f-4f transition [27, 57], whereas the phonon bands dominate the 4f-5d transition spectra because of the displacement of the harmonic potentials.

Line shapes of inhomogeneously broadened ZPLs caused by defects have been investigated, for example, in [58, 59], where it is shown that it is generally a Gaussian function. The position of a ZPL can be shifted with temperature. This has been investigated, for example in [60–62]. The dependence of the shift on temperature is different for different crystals, and is in the range of a few to tens of cm^{-1} for a 4f-4f transition within the temperature range of 4-300 K.

3.2.2 Linewidth

The inhomogeneous linewidth of the RE^{3+} 4f-4f transition is typically in the range of one to tens of GHz. A comprehensive review of the RE ion spectroscopy has been made by R. M. Macfarlane [63]. It is of fundamental interest to find the factors limiting the

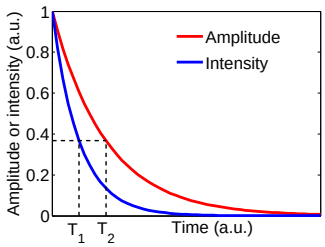

Figure 3.5. *In an optimal case, where the decay of the excited state is the only broadening mechanism, the coherence time T_2 takes its maximum value of $2T_1$. the red curve shows the field amplitude as a function of time, and the blue curve shows the corresponding dependence of intensity on time. The horizontal dashed line indicates $1/e$ of the maxima.*

linewidth, and it also provides a measure of the extent to which the crystalline structure is distorted. This limitation varies from crystal to crystal, and from ion to ion. For instance, a 10 MHz inhomogeneous linewidth has been reported in a $YLiF_4$ crystal doped with the odd isotopes ^{141}Nd and ^{143}Nd [64].

Generally inhomogeneous broadening is undesirable as it obscures the intrinsic narrow homogeneous lines of the individual ions. However, this feature could be used in quantum computing research as it offers a means of creating multiple qubits in RE-ion-doped crystals by selectively addressing subgroups of ions as individual qubits [65].

3.3 Homogeneous line broadening

Homogeneous linewidth broadening is intrinsic to all transitions and is independent of the local environment surrounding the ion, or in the other words, each individual ion experiences the same amount of broadening. This broadening typically has a Lorentzian line shape. There are two kinds of broadening mechanisms. One is the decay of the excited state (characterized by its lifetime T_1). The physical origin of this broadening can be understood from the quantum mechanical point of view in terms of the Heisenberg uncertainty principle [66], or from an analogy to the classic model of a damping oscillator [67]. The other mechanism is the pure dephasing process (described by the relaxation time T_2^*), which refers to all the processes that change the radiative transition frequency but do not affect the lifetime. Some of these processes, which are important for this research, are discussed briefly below.

The homogeneous linewidth, Γ_h, is related to the coherence time, T_2, the excited state lifetime, T_1, and the relaxation time T_2^* as follows:

$$\Gamma_h = \frac{1}{\pi T_2} = \frac{1}{2\pi T_1} + \frac{1}{\pi T_2^*} \ . \tag{3.1}$$

From the above equation it can be seen that the narrowest linewidth of a real transition is $1/2\pi T_1$, which happens in the optimal case where there is no other broadening mechanisms (meaning T_2^* is infinity) except the finite excited state lifetime decay. In such a case, the system coherence time takes its maximum value of $2T_1$. The factor of 2 between T_2 and T_1 arises from their different definitions, where T_2 and T_1 are the times that have elapsed when the amplitude and intensity have fallen to $1/e$ of their maxima, as illstrated in Figure 3.5.

The optical coherence time of the low-energy 4f-4f transitions of a RE ion in a crystal can be in the range of hundreds of microseconds to milliseconds, which makes the RE ion a competitive test bed for implementing quantum algorithms. A 50 Hz linewidth had been determined for Er ions in an Y_2SiO_5 crystal [68]. A homoge-

neous linewidth as low as 122 Hz for the Eu $^7F_0 - ^5D_0$ transition at site 1 has been reported in a photon echo experiment when a moderate magnetic field was applied [69]. When extrapolated to zero-excitation intensity, the homogeneous linewidth was 105 Hz, which is appraching the lifetime limited (1.9 ms) width of about 85 Hz.

3.3.1 Ion-phonon interaction

The energy required for a transition to occur in an ion in a solid may be higher or lower than the energy separation between the two transition states because the ion can absorb an energy corresponding to one or more phonon quanta from the lattice or phonon energies to released to the lattice. This ion-phonon interaction broadens the homogeneous transition line, and this has been investigated both theoretically and experimentally e.g. [28, 70–72].

It has been shown that in the low-temperature range ($T < 0.084\ \theta_D$), broadening has a temperature dependence of T^7, where the two-phonon Raman process is dominant [28, 71, 72], whereas at high temperatures ($T > 0.48\ \theta_D$), the dependence scales as T^2 [70]. θ_D is the Debye temperature of the host lattice, which approximately determines the maximum phonon levels which are populated and contribute to the transition.

The phonon energy of RE ions in a crystal is typically of the order of 10-100 cm^{-1} [71] and the phonon-induced dephasing becomes important above 4K [68, 73]. The electron-phonon coupling strength of a 4f-5d transition is usually one order of magnitude higher than a 4f-4f transition [50].

3.3.2 Ion-ion interaction

Ion-ion interactions constitute another dynamic process leading to homogeneous line broadening, where the transition frequencies are shifted as a result of ion-ion interactions, such as the permanent electric dipole-dipole interaction between two neighbouring dopant ions, or the electron spin-nuclear spin interaction between a dopant ion and its neighbouring host ions.

The permanent electric dipole-dipole interaction

When an ion changes its state from the ground to the excited state, or vice visa, the surrounding electric field is changed correspondingly because of the different permanent electric dipole moments of these two states. This change induces a frequency shift in the initial optical transition frequencies of the neighbouring ions. This is the dipole-dipole interaction, and the induced shift is called the excitation-induced frequency shift [74, 75], which depends on the permanent dipole moments, $\Delta\mu$, and the distance between the

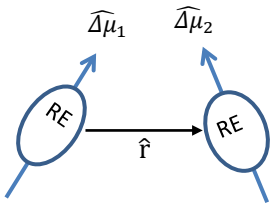

Figure 3.6. *Illustration of the dipole orientations and their displacement.*

ions, r, as

$$\Delta\nu = \frac{(\epsilon(0)+2)^2}{9\epsilon(0)} \cdot \frac{\Delta\mu_1 \cdot \Delta\mu_2}{4\pi\epsilon_0 h \cdot r^3} \cdot [\hat{\Delta\mu}_1 \cdot \hat{\Delta\mu}_2 - 3(\hat{\Delta\mu}_1 \cdot \hat{r})(\hat{\Delta\mu}_2 \cdot \hat{r})], \tag{3.2}$$

where the first factor accounts for the dielectric Lorentz local field correction [76], $\epsilon(0)$ (≈ 7) is the dielectric constant of the host medium at zero frequency, and $\hat{\Delta\mu}$ and $\hat{r}$ are the unit vectors of the dipole moment, and the displacement between one dipole and the other. The term in the square brackets describes the angle dependence of a dipole in response to the electric field generated by another dipole, and is affected by the dipole orientations and their relative positions, as illustrated in Figure 3.6. For two Pr ions (site 1) with a separation of 1 nm, the dipole-dipole interaction induced shift is about 1 GHz.

The homogeneous broadening caused by the dipole-dipole interaction can have a non-negligible effect on the linewidth measured from the decay of photon echoes. The magnitude of the broadening strongly depends on the excitation density, which has been quantitatively characterized and experimentally investigated [69, 77, 78]. The homogeneous linewidth broadening caused by the dipole-dipole interaction provides an alternative way of characterizing the change in permanent dipole moment change of a transition for a specific ion, which was the method used in the study described in Paper **III** to measure the change in dipole moment ($\Delta\mu_{Ce}$).

Electron spin-nuclear spin interaction

The electron spin-nuclear spin interaction is similar to the permanent dipole-dipole interaction described above. The nuclear spin flip of the surrounding host ions is the origin of this interaction. The magnetic field associated with the nuclear spin acts as a local field, interacting with the nearby ions (optical centre) being studied. A nucleus could have zero spin if the numbers of protons and neutrons within the nucleus are both even. One qualitative explanation is that two protons with opposite spins tend to form pairs, as do two neutrons. So the effective spin of all the pairs is zero. It is worth noting that the nuclear spins of isotopes are generally different.

Nuclear spin flips of the host ions surrounding the optical centre cause a fluctuating magnetic field. This spin flip induces a frequency shift of the optical centre's transition line. The magnitude of the shift, $\delta\nu$, depends on the magnetic moment of the nucleus, μ_n, and the electrons (of the optical centre), μ_e, as [53]

$$\delta\nu \propto \frac{\mu_e \cdot \mu_n}{r^3}. \tag{3.3}$$

The homogeneous linewidth broadening of Eu^{3+} ions caused by the nuclear spin flip of Y ions in Y_2SiO_5 has been investigated, e.g. [69]. The broadening contribution was found to be about 110 Hz (site 1) when no external magnetic field was applied, whereas the value was reduced to 20 Hz when a 100 G magnetic field was applied.

3.4 Probing the homogeneous linewidth

The narrow homogeneous 4f-4f transition lines of RE ions in a solid are concealed by the broad inhomogeneous absorption line, as can be seen in Figure 3.3c. However, methods of probing them are well developed, for instance, using the spectral hole-burning technique to directly probe the lines in the frequency domain, or recording the decay curve of a coherent emission in the time domain to measure the coherence time of the transition, by photon echoes or free induction decay. Measurement of the homogeneous linewidth using the coherent transient effect has been reviewed e.g. [63, 68]. A brief introduction to the spectral hole-burning and photon echo techniques will be provided below.

3.4.1 Spectral hole-burning

Spectral hole-burning is the most commonly used technique for high-resolution spectroscopy, especially since the advent of tunable lasers. A laser pulse (called the hole-burning pulse) selectively excites a subgroup of ions (or molecules) within the broad inhomogeneous profile. We assume that the linewidth of the laser is much narrower than the linewidth of the inhomogeneous line. As a consequence of excitation some of the ions may end up in a state other than the initial ground state from which they were excited. This state could be the excited state of the transition, which is the case in saturation spectroscopy, or other long-lived ground states, such as the Zeeman levels, the hyperfine or superhyperfine levels. In both cases, population of the initial ground state is reduced, which gives rise to decreased absorption (the so-called 'hole') at the excitation frequency relative to its surroundings. This modified absorption structure created by the hole-burning pulse is probed by the absorption of low-power radiation, scanned across the hole-burning frequency. The hole is only visible during its lifetime, which is determined by the lifetime of the ending state of the ion, and can be on the ns timescale (the lifetime of the excited state of a 4f-5d transition) or several days (the lifetime of the hyperfine level) as shown in [28].

The width of the spectral hole (Γ_{hole}) observed in a hole-burning experiment is related to the homogeneous linewidth (Γ_h)

of the transition as

$$\Gamma_{hole} = 2\ (\Gamma_h + \Gamma_{laser}), \tag{3.4}$$

where Γ_{laser} denotes the laser linewidth and both Γ_h and Γ_{laser} are assumed to be Lorentzian. The reason for the summation of the two linewidths is that the hole created by the burning pulse is a convolution between the homogeneous line and the laser line. The factor of 2 arises from the fact that this convolution takes place in both the pump and probe step.

In some cases, the spectral hole is too shallow to be 'seen' by the probe pulse. There are several possible reasons for this shallow hole: (i) the absorption of the transition is too weak, (ii) the excitation intensity is too weak because of limited laser power, or (ii) the excited state lifetime is too short.

The first hole-burning experiment on a RE system (Pr) was demonstrated in 1977 [79]. An extreme case of a spectral hole is the so-called spectral pit, where the absorption is approaching zero [80]. This will be discussed in Chapter 6.

3.4.2 Photon echoes

A photon echo is a coherent burst of light emitted by an ensemble of atoms which are in a superposition of the ground and excited states. It is an optical frequency analogue of the spin echo [81]. The first photon echo experiment was carried out in 1964 [82]. Like any kind of coherent phenomenon, the magnitude of the echo is strongly dependent on the extent to which the coherence properties survived at the time of emission. The coherence time of the system can be extracted by recording the strength of the photon echo as a function of elapsed time, then the homogeneous linewidth will be known.

The physics behind the photon echo process can be understood in the Bloch sphere representation. For simplicity, a two-pulse photon echo is considered here. Two coherent laser pulses successively interact with the medium with a time separation of t_{12} between them, see Figure 3.7a. The first pulse has a pulse area of $\pi/2$, and coherently drives a sub-ensemble of atoms, whose transition frequencies are within the Fourier frequency span of the pulse, into a superposition state. Their Bloch vectors end up in the equatorial plane, as shown in the right column in Figure 3.7b. As time progresses, these atoms experience a phase evolution at a rate determined by their own intrinsic transition frequencies, which are generally different for different atoms due to inhomogeneous broadening. This dephasing process results in a distribution of the Bloch vectors at time t_{12}, as shown in the left column in Figure 3.7c, assuming $t_{12} \ll T_2$. The second laser pulse, with a pulse area of π, flips the established phase distribution around the

u axis ($\mathbf{v} \rightarrow -\mathbf{v}$), as shown in the right column in Figure 3.7c. The phases of atoms then start to evolute again (rephasing process) at the same rate as in the dephasing step. After exactly the same time period of t_{12} after the π pulse, the Bloch vectors converge at the negative **v** axis (see Figure 3.7d). The atoms are now all in phase and combine to give macroscopic polarization, which yields a coherent emission (echo signal).

In reality, the dephasing and rephasing processes do not match perfectly since the atoms can dephase with each other within the time period $2t_{12}$. The strength of the echo signal decreases with pulse separation time t_{12} exponentially as:

$$I_{echo}(t) = I_{echo}(0) \cdot e^{-\frac{4t_{12}}{T_2}} \tag{3.5}$$

If we assume that, suppose all the atoms experience the same pulse area at a certain time separation t_{12}, the echo intensity will depend on the number of excited atoms (N), the pulse area of the first pulse (θ_1) and the area of the second pulse (θ_2) as:

$$I_{echo} \propto N^2 \sin^2\theta_1 \sin^4(\frac{\theta_2}{2}) \tag{3.6}$$

For small θ, the above equation can be written:

$$I_{echo} \propto N^2\ I_1\ {I_2}^2\ \triangle {t_1}^2\ \triangle {t_2}^4, \tag{3.7}$$

where $I_{1,2}$ and $\triangle t_{1,2}$ denote the beam intensity and the duration time of pulses 1 and 2, respectively. It can be seen from Equation (3.7) that the echo signal is maximized when the first pulse is a $\pi/2$ pulse and the second is a π pulse. However, photon echoes can be observed for an arbitrary pulse area as long as the sinusoidal functions are non-zero.

The two-pulse photon echo is essentially a third-order nonlinear process, where the phase matching condition leads to the following relation between the wave vectors [83, 84]

$$\overrightarrow{k_1} + \overrightarrow{k_e} = 2\overrightarrow{k_2}, \tag{3.8}$$

where $\overrightarrow{k_1}$, $\overrightarrow{k_e}$, and $\overrightarrow{k_2}$ are the wave vectors of the first pulse, the echo and the second pulse, respectively.

One advantage of using photon echoes to measure the homogeneous linewidth is that it is less sensitive to the laser frequency jitter provided that the Fourier frequency span of the pulses is greater than the frequency jitter. However, the observed coherence time may depend strongly on the excitation intensity due to spectral diffusion (see Section 3.3.2) and this has been investigated extensively e.g. in [69, 77, 78].

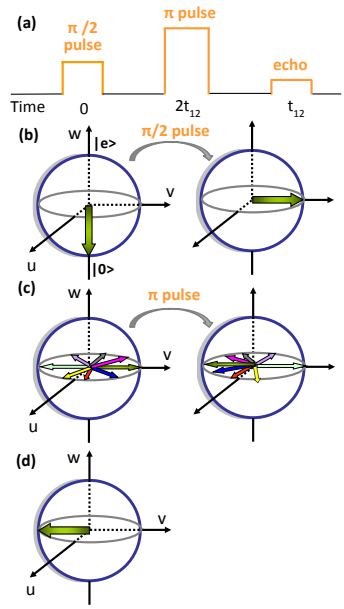

Figure 3.7. *(a) shows the two-pulse photon echo sequence. (b) and (c) shows the function of the first pulse and the second pulse in the Bloch sphere representation. (d) shows the Bloch vector at time $2t_{12}$ where the Bloch vectors of all the individual atoms meet. The transition from (b) to (c) (from (c) to (d)) is the echo dephasing (rephasing) process.*

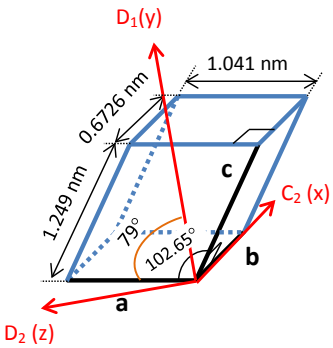

Figure 3.8. *Structure of the monoclinic cell of Y_2SiO_5 , in which 8 molecules are present.*

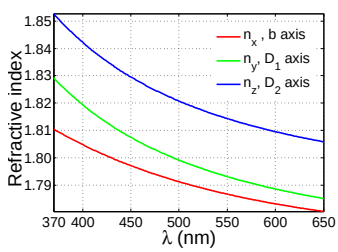

Figure 3.9. *Refractive index of Y_2SiO_5 in the wavelength range 370-650 nm.*

3.5 The Y_2SiO_5 crystal

The Y_2SiO_5 crystal has a monoclinic cell structure with C_{2h}^6 symmetry, which contains a two-fold (180°) rotation axis and one mirror plane perpendicular to the rotation axis. There are eight Y_2SiO_5 molecules within the cell. A schematic illustration of the cell is shown in Figure 3.8, where the **b** axis is perpendicular to the $\mathbf{a}-\mathbf{c}$ plane and the angle between **a** and **c** is 102.65° [85]. There are two inequivalent crystalline sites for Y ions. One is surrounded by 6 oxygen ligands and the other is surrounded by 7 oxygen ligands. The principal axes (x, y and z) are denoted C_2, D_1 and D_2. D_1 and D_2 lie in the $\mathbf{a}-\mathbf{c}$ plane. The refractive index dependence within the wavelength range of 370-650 nm is shown in Figure 3.9 [86].

Y_2SiO_5 is an interesting host for exploring the properties of RE ions for optical data storage and data processing [87], and in the fields of quantum computing and quantum memories [5–8, 88]. The attractive properties of Y_2SiO_5 for these applications are the low nuclear magnetic moments and low abundance of isotopes with non-zero nuclear magnetic moments, which limits the homogeneous linewidth broadening contribution from the spin-flip of the host ions, and enables long coherence times (up to ms timescale) for the RE ion transitions [27, 57, 69]. Table 3.2 lists the nuclear magnetic moments for each element in Y_2SiO_5 , where μ_N is the nuclear magneton, which is a constant with a value of about 0.03 μeV/T [89]. Y_2O_3 is also a low nuclear magnetic moment substrate, but it is difficult to grow as a bulk crystal as its melting temperature is higher than that of Y_2SiO_5 (∼2410° C vs. ∼2070° C) [57].

Atom	Isotopes	Abundance (%)	Nuclear spin	μ (μ_N)
Y	$^{89}_{39}$Y	100	1/2	-0.137
Si	$^{28}_{14}$Si	92.2	0	0
	$^{29}_{14}$Si	4.6	1/2	-0.55
	$^{30}_{14}$Si	3.1	0	0
O	$^{16}_{8}$O	99.7	0	0
	$^{17}_{8}$O	0.04	5/2	-1.89
	$^{18}_{8}$O	0.2	0	0

Table 3.2: *Stable isotopes and nuclear magnetic moments of Y, Si and O.*

A small fraction of Y ions is often substituted by trivalent RE ions (e.g. Ce^{3+}, Pr^{3+}, Eu^{3+} and Tm^{3+}). Substitution takes place at both sites, but the occupation of the different sites can be very different. For instance, the occupation of Pr^{3+} is roughly 87% (in site 1) and 13% (in site 2) based on the very different absorption coefficient observed in [87].

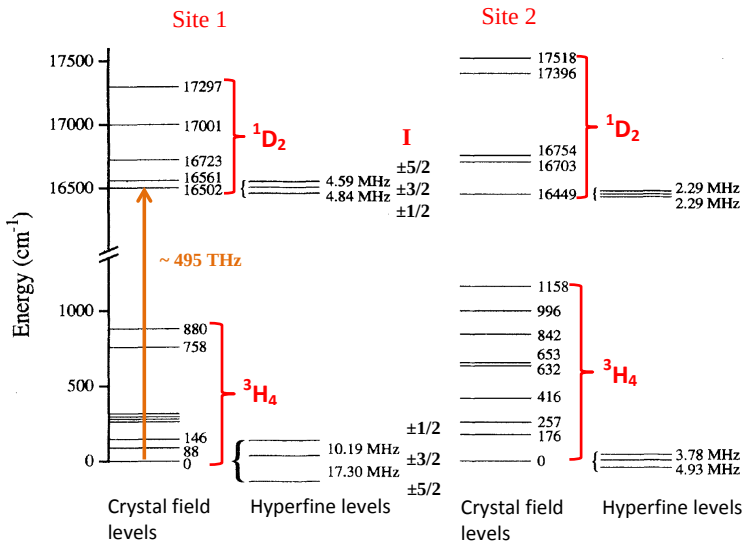

Figure 3.10. *The $^3H_4$ ground state multiplets and $^1D_2$ excited state multiplets of Pr^{3+} in Y_2SiO_5 for both sites at 1.4 K. The figure is reproduced from [27, 90].*

A short summary of the properties of Pr^{3+} and Eu^{3+} (in Y_2SiO_5) relevant for this work will be given below, based on results presented in the literature.

3.5.1 Pr^{3+}:Y_2SiO_5

There are two electrons in the 4f subshell of a Pr^{3+} ion. The projection of the total electron spin (S) can take the value 0 or 1, which is then coupled with the total angular moment (L = 0, 1, 2, ... 6), resulting in the multiple fine structure levels ($^{2S+1}L_J$) of Pr ions shown in Figure 3.2. These fine structure levels are further split by the crystal field when the ion is embedded in a lattice matrix. The $^3H_4 \rightarrow {}^1D_2$ transition within the 4f subshell is of our interest in this work, and has been very well investigated by many groups. The coupling of the nuclear spin (I = 5/2) of the Pr ion (there is only one Pr isotope ^{141}Pr) with the total electron angular momentum (J) gives rise to the hyperfine structures within each crystal filed level. The $^3H_4$ and $^1D_2$ crystal field multiplets and the hyperfine levels of the lowest crystal field levels are shown in Figure 3.10.

Some of the spectroscopic data for Pr^{3+} taken from the literature are given in Table 3.3. Further information can be found in the references given in the Table.

Parameters	Pr (site 1)	Pr (site 2)	References
λ_{vac}(nm)	605.977	607.933	[90]
T_1 (µs)	164	222	[27]
Γ_{T1} (Hz)	970	717	[27]
T_2 (H = 77 G) (µs)	152	377	[27]
Γ_h (H = 77 G) (Hz)	2100	850	[27]
f	7.7×10^{-7}	4.5×10^{-8}	[78]
μ (C · m)	2.5×10^{-32}	6.3×10^{-33}	[78]
$\Delta\mu_{ge}$ (C · m)	2.4×10^{-31}	2.0×10^{-31}	[78]

Table 3.3: *Some of the spectroscopic data for Pr^{3+} in Y_2SiO_5 taken from the literature (T_1 and T_2 stands for the excited state lifetime and coherence time of the $^3H_4$ and $^1D_2$ transition, respectively; f, μ and $\Delta\mu_{ge}$ are the oscillator strength, the transition dipole moment and the difference in permanent dipole moment in the ground and excited states.).*

The orientation of the permanent electric dipole moment of Pr^{3+} has been investigated by applying an external electric field [91], and the angle between the two inequivalent dipole moments was found to be 24.8 ° for site 1 and 11.8 ° for site 2.

3.5.2 Eu^{3+}:Y_2SiO_5

The $^7F_0 \rightarrow ^5D_0$ transition of Eu^{3+} in Y_2SiO_5 has attracted extensive attention because of its millisecond long lifetime and its narrow homogeneous linewidth (almost approaching the lifetime-limited value). The energy level structures of Eu^{3+} in Y_2SiO_5 have been reported previously [57, 92]. Some spectroscopic data are given in Table 3.4.

Parameters	Eu (site 1)	Eu (site 2)	References
λ_{vac}(nm)	579.879	580.049	[69]
T_1 (ms)	1.9	1.6	[28, 69]
Γ_{T1} (Hz)	84	99	[28, 69]
T_2 (H = 100 G) (ms)	2.6	1.9	[69]
Γ_h (H = 100 G) (Hz)	122	167	[69]
f	1.2×10^{-8}	3.1×10^{-8}	[69]
μ (C · m)	6.6×10^{-33}	-	[78]
$\Delta\mu_{ge}$ (C · m)	7.6×10^{-32}	-	[78]

Table 3.4: *Spectroscopic data for Eu^{3+} in Y_2SiO_5 taken from the literature (symbols as Table 3.3). The oscillator strength is given for the polarization under study in the literature. Γ_h is 105 Hz when extrapolated to zero excitation intensity.).*

Chapter 4

Experimental system

The experimental systems involved in the work described in this thesis are presented briefly in this chapter. Two different systems were used for different types of experiments. One system was used for the quantum control experiments on the qubit ions, and is described in Section 4.1. The other system was used for the detection of single Ce ions, and is presented in Section 4.2.

4.1 Experimental system for quantum control

The experimental system used to demonstrate quantum control of RE ions (mainly Pr^{3+} and Eu^{3+}) includes a light source (a dye laser), stabilization system for the light source, an optical pulse generation system (acousto-optical modulators, AOMs) and a cryostat where the temperature of the RE-ion-doped crystals was kept below 4 K (liquid helium temperature).

4.1.1 The light source

The quantum system being studied is the hyperfine levels (in the 4f subshell) of Pr^{3+} or Eu^{3+} ions, randomly doped into a solid crystal, (e.g. Y_2SiO_5 by the substitution of Y ions). The relevant optical transition wavelengths are ∼606 nm ($^3H_1 \rightarrow^1 D_2$ transition of Pr ions in site 1) and ∼580 nm ($^7F_0 \rightarrow^5 D_0$ transition of Eu ions in site 1). These wavelengths can not be obtained from laser diodes, which would have been preferable as they are more compact, easier to operate, and also have a relatively narrow spectral linewidth. The light source used is a ring cavity dye laser (Coherent 699-21) using the dye Rhodamine 6G as the gain medium, whose emission spectrum covers both required wavelengths [93]. The dye is dissolved in ethylene glycol and is ejected from a thin nozzle and circulates in the dye flow loop. With a dye pressure of ∼4 bar at the nozzle input and a temperature of ∼5-10°C, the laser

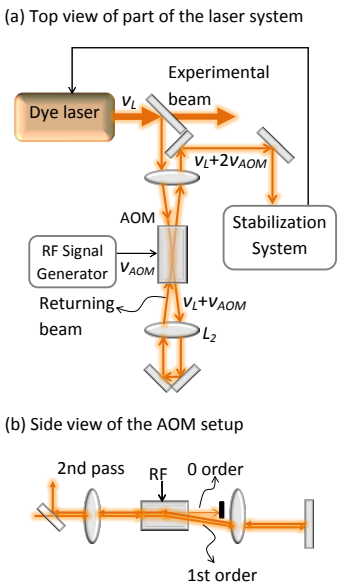

Figure 4.1. *Setup used to tuning the frequency of the experimental beam while the laser is locked onto the stable cavity. It can be tuned within 1.5 GHz continuously using the first order deflected beam from the AOM.*

output is ∼600 mW in single transverse mode. The stability of the dye flow strongly affects the stability of both the laser output frequency and the power. The dye laser has a spectral linewidth of about 1 MHz with its internal active stabilization system, which means that the coherence time of the laser is of the order of a few µs. This is more than two orders of magnitude shorter than the optical coherence times of Pr^{3+} ions (150 µs [27]) and Eu^{3+} ions (2.6 ms [69]).

4.1.2 Dye laser stabilization system

To extend the laser coherence time, a secondary frequency stabilization system was built based on a stable Fabry-Pérot cavity made of ULE glass with a finesse of 150000 and free spectral range (FSR) of 3 GHz, employing the PDH locking technique [94]. The error signal from the cavity was fed back to an intra-cavity electric-optical modulator (EOM) to compensate for the fast fluctuations, and to the tweeter and Brewster plate to compensate for slow variations. In this way, the laser linewidth could be reduced to the level of ∼10 Hz [95]. The PDH setup and principle are discussed in Chapter 5. More information on this ULE cavity can be found in [96] and the complete feedback system is presented in [97–99].

Scanning the laser frequency while it is locked

The transmission from a high-finesse Fabry-Pérot cavity consists of a series of narrow lines equally separated in frequency domain (the interval between two lines are the FRS, $\Delta\nu_{FSR}$), onto any of which the laser frequency can be locked. In order to tune the frequency of the experimental beam continuously within a certain range while the laser is locked onto a specific mode of the cavity (e.g. it is sometimes necessary to match a specific absorption line of a RE ion), the output from the laser is split into two beams. Most of the beam is directed to the experimental set-up, while a small fraction is directed towards the stabilization system, where an AOM (from Brimrose) with a centre radio frequency (RF) of 1.125 GHz and a 3dB bandwidth of 750 MHz is used, as illustrated in Figure 4.1.

An AOM contains an acoustic crystal and a transducer, that is driven by an external RF signal. The acoustic wave generated by the transducer creates a periodic change in the refractive index of the crystal, upon which the input laser beam is diffracted by different orders. The first order diffracted beam is often optimized with good efficiency. The amplitude, frequency and phase of the diffracted beam can be fully controlled by adjusting the respective parameters of the RF signal. The double-pass configuration is used in the set-up to eliminate the dependence of the output

beam position on the RF frequency. For this particular AOM, the diffraction occurs in the vertical plane, see Figure 4.1b.

The frequency of the final output beam from the AOM is $\nu_L + 2\nu_{AOM}$ (the 1st order deflected beam is used for both passes). When this beam is locked onto the transmission mode $k\Delta\nu_{FSR}$ (k is an integer), the laser frequency is $\nu_L = k\Delta\nu_{FSR} - 2\nu_{AOM}$, where $\nu_{AOM} \in [0.75, 1.5]$ GHz. The scanning range of the laser is indicated by the orange arrow in Figure 4.2 which covers half of the FSR. In a similar manner, the laser can be tuned within the other half of the FSR when the -1 order deflected beam is used ($\nu_L = k\Delta\nu_{FSR} + 2\nu_{AOM}$). The frequency of the laser can be scanned across other half FSRs when the deflected beam after the AOM is locked onto other transmission modes of the cavity.

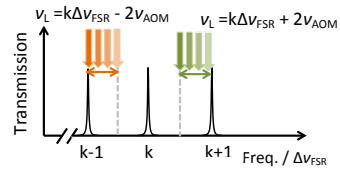

Figure 4.2. *The discrete transmission lines of the ULE cavity (FSR of 3 GHz) and an illustration of the laser scanning range using the ±1 orders of deflected beams from an AOM. One half of the FSR (indicated by the orange arrow) is covered by the +1 order deflected beam, and the other half by the −1 order deflected beam.*

Spherical aberration of the collimating lens L_2

In the double-pass AOM set-up illustrated in Figure 4.1, spherical aberration of lens L_2 presented a problem due to the large deflection angle ($\theta \in [4.2°, 7.8°]$ for radio frequencies in the range 0.75 GHz to 1.5 GHz). The deflected beams at different values of ν_{AOM} can not be collimated by lens L_2, which means that the vertical displacement of a deflected beam at near field (Δx_1) and at far field (Δx_2) will not be equal for all the AOM frequencies, as illustrated in Figure 4.3. This prevents the returning deflected beam from focusing at the same spot in the crystal at different AOM frequencies. Thus, the spatial position of the second-pass deflected beam changes with the RF frequency, making the double-pass configuration unusable. A ray-tracing simulation was performed (using FRED) to investigate how much Δx_1 and Δx_2 differ for a spherical lens and an aberration-free aspherical lens. The results are shown in the table in Figure 4.3, where the deviation is defined as $(\Delta x_2 - \Delta x_1)/\Delta x_1$. Clearly, the aspherical lens is better, and such a lens was used in the set-up.

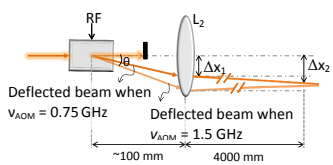

Type of lenses (L_2)	ν_{AOM} (GHz)	Δx_1 (mm)	Δx_2 (mm)	Deviation
Spherical lens	0.75	-7.27	-7.81	7.4%
	1.5	-13.35	-10.70	-18%
Aspherical lens	0.75	-7.30	-7.28	-0.3%
	1.5	-13.47	-13.47	0

Figure 4.3. *Illustration of the spherical aberration problem from lens L_2 used in the double pass AOM setup. The aspherical lens is AL50100-A purchased from Thorlabs. More information is available in the text.*

4.1.3 Optical pulse generation system

The light pulses used for the experiment are created from the continuous laser source by another AOM (from A.A. Opto-Electronics) in the experimental beam path by engineering the RF signal entering the AOM. The RF signal is generated by an arbitrary waveform generator (Tektronix AWG520) with a sampling rate of 1GS per second, which is controlled via a computer.

The variation in the laser output power from day to day causes the intenisty of the generated light pulse to vary in the same way, which can give day-to-day variations in the experimental results. To overcome this problem a feed-forward calibration system was constructed, in which the amplitude of the RF signal is adjusted in correspondence to the variation of the laser power to obtain a

light pulse with stable intensity. More information can be found in a doctoral thesis [99].

4.1.4 The helium bath cryostat

A liquid helium bath cryostat (Spectromag SM4000 from Oxford Instruments) was used for the quantum control experiments to maintain the temperature of the crystal below 4 K, to ensure a longer coherence time. Reducing the pressure in the chamber containing the liquid helium can allow the temperature to be reduced below the lambda point (2.17 K at 1 atmosphere), so the liquid helium becomes superfluid. At the lambda point temperature the specific heat capacity is at its maximal value, so it is insensitive to heating effects such as thermal radiation or laser heating. All the quantum control experiments were performed at a temperature below the lambda point.

4.2 Experimental system for the single-ion readout

The main pieces of experimental equipment for the single-ion readout project are an external cavity diode laser, which is used to excite the Ce ions, a helium-cooled microscopy cryostat, in which the crystal is mounted, and an optical system for the detection of fluorescence, based on a fluorescence microscope, a monochromator and a charge-coupled device (CCD) camera.

4.2.1 The external cavity diode laser

The 4f-5d zero phonon transition line of the Ce ions is around 371 nm, which will be discussed in Chapter 7. Laser diodes at this wavelength, with a maximum free-running output power of 20 mW, recently became available (e.g. the LD-0375-0020-2 from Toptica, manufactured by Nichia). A home-built Littrow cavity, defined by the back facet of the laser diode, and a grating (GH13-36U from Thorlabs) were used to obtain a single-frequency output with a maximum output power of about 12 mW. The output wavelength can be tuned to the Ce absorption line by adjusting the reflection angle of the grating and lowering the temperature of the laser diode to about 15 °C (the tunability coefficient is about 0.05 nm/°C).

The output beam is linearly polarized parallel to the active layer of the gain medium, see Figure 4.4a. The extinction ratio of the polarization state is about 25 dB. The spatial mode of the output beam is not good, see Figure 4.4b, and in some experiments requiring a well-defined intensity distribution, it must be cleaned by, e.g. coupling to a single-mode fibre.

The typical frequency stability of this type of external cavity diode laser is ~ 5 MHz over 10 ms [100]. Because the homogeneous

linewidth of the Ce ion was about 4 MHz which will be discussed in Chapter 7, a frequency stabilization system was built to enable the laser to interact with the same single Ce ion for a long period of time (a few hours). Further details on the stabilization system are given in Chapter 5.

4.2.2 The helium-cooled microscopy cryostat

A microscopy helium cryostat (called microstat hereafter, bought from Oxford Instruments) was used. The microstat is a liquid helium-cooled cold finger cryostat, where the lowest temperature of the heat exchanger is ∼3.4 K. This microscopy cryostat is compact, easy to operate, and is compatible with the fluorescence microscope system. It also has a fast cooling process (requires only a few minutes starting from room temperature). However, it is important to ensure good thermal contact between the cold finger, which is a nickel-plated copper plate attached to the heat exchanger, and the sample. The spherical aberration caused by the cryostat window (thickness of 1.5 mm) must be corrected to achieve a tight focus.

Thermal contact

The crystal was attached to the cold finger of the microscopy cryostat using a water-based graphite paint (its main contents are micrometer size graphite particles and deionized water) [101]. The main reason for using this paint is that, among the materials investigated, it fluoresces least under illumination of the Ce excitation source (∼371 nm) (see Section 8.2.2). When the water in the paint has evaporated, the crystal remain stuck onto the cold finger. However, this takes a few hours at room temperature, as the water molecules are confined to a thin layer between two surfaces. In an attmept to speed up the procedure, we tried firstly attaching the crystal to a silicon plate with the graphite paint, and heating the silicon plate together with the crystal in an oven at 100°C for 1-2 hours. The silicon plate was then attached to the cold finger with silver conductive paste. Although a reduction in time was achieved, the silicon plate increased the thermal load.

A thin layer of the graphite paint should be used to minimize the thermal load introduced by the graphite particles. However, the crystal surface better be completely covered by the graphite particles to ensure good thermal contact with the cold finger. Bearing in mind the above considerations, the actual temperature of the crystal may be higher than the temperature of the heat exchanger, although this was not measured.

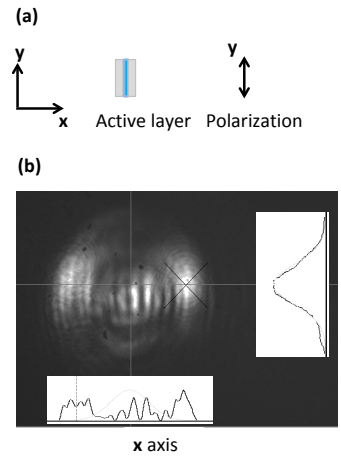

Figure 4.4. *(a): The polarization of the light relative to the orientation of the active layer. (b): Spatial mode of the free running laser diode with a centre output wavelength of 372.1 nm. The curves show the intensity distribution along two axes.*

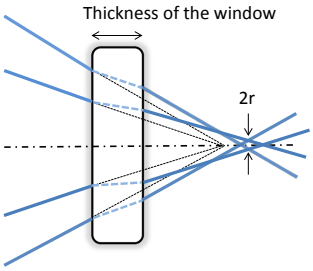

Figure 4.5. *Illustration of spherical aberration from the cryostat window.*

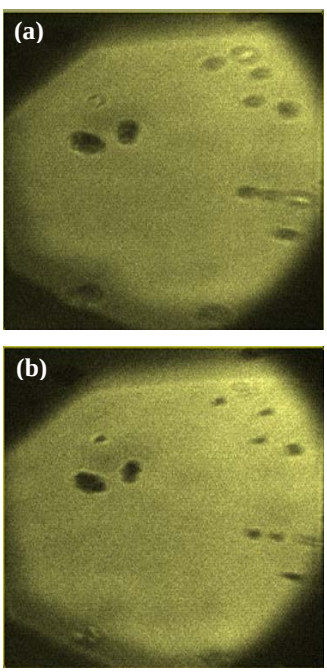

Figure 4.6. *Tests on the aberration correction function of the objective lens (LUCPLFLN 20×). (a) shows the image of some micro-spheres with no aberration correction, and (b) shows the same image with correction.*

Spherical aberration

Spherical aberration occurs when the sharply focused light rays from the objective lens pass through the cryostat window, as illustrated in Figure 4.5. For example, the radius of the focus is about 8 µm (the diffraction-limited focal radius is only about 0.5 µm) when the outer rays has an incidence angle of 26.7° (for a NA of 0.45) passing through a window with thickness of 1.5 mm.

This spherical aberration can be corrected for by adjusting the collar correction ring which is available on some objectives, which allows the distance between two groups of lenses to be changed. To test this on one of the objective lenses used in the experiments (LUCPLFLN 20× from Olympus), micrometre-sized beads with dye solutions inside a plastic shell were used as samples (TetraSpeck^{TM}, bought from Lifetechnologies). Figure 4.6 shows images of some of the spheres without (Figure 4.6a) and with correction (Figure 4.6b) for aberration. The visibility and sharpness of the sphere images (black spots in the figure) are for sure better in Figure 4.6(b), which can be clearly seen from those spheres on the right. However the images do not look like spheres, which indicates that there are still some aberrations presented possibly originating from other optics in the set-up.

4.2.3 The fluorescence detection system

All the fluorescence measurements on Ce ions described in this thesis were performed on the optical system illustrated in Figure 4.7. An objective lens in a microscope was used to focus the excitation laser into the crystal and collects the fluorescence emitted from the crystal. Then the fluorescence was directed to a monochromator, finally captured by a CCD camera.

The fluorescence microscope is an upright microscope, in which the internal lamp or an external light source can be used for illumination, and the fluorescence can be directed to the eyepiece or to the CCD camera. Two objective lenses were used: M Plan Apo NUV 50× (from Mitutoyo) and LUCPLFLN 20× (from Olympus). Both objective lenses are infinity-corrected. The lens L_f focuses the parallel fluorescence light onto the plane of the slit. This plane is the conjugate focal plane of the objective lens. By turning the angle of the grating inside the monochromator either the fluorescence spectrum (1st-order diffracted light) or the overall image (zero-order diffracted light) on the slit is directed to the CCD camera. There is no magnification of the image on the slit to the image on the CCD camera.

A monochromator (HR 460, from Instruments S.A. Jobin-Yvon/Spex) was used to analyse the fluorescence spectrum, using a grating with a groove density of 150 gr/mm blazed at 1200 nm. The slit can be adjusted in the range 0.01-2 mm via remote control.

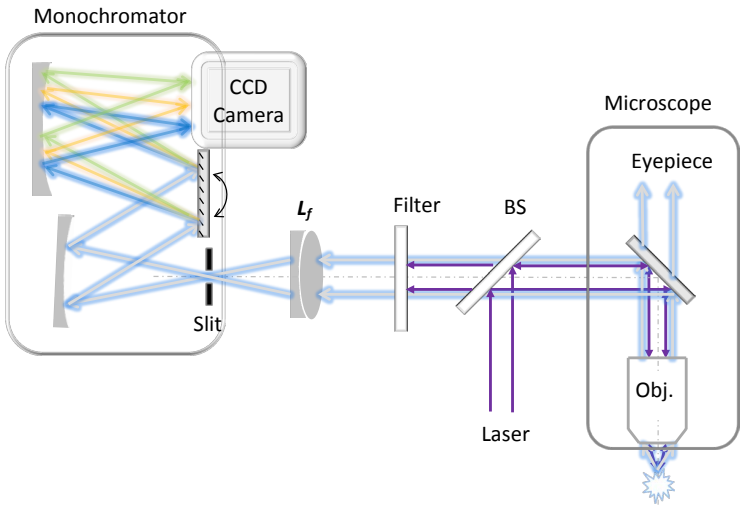

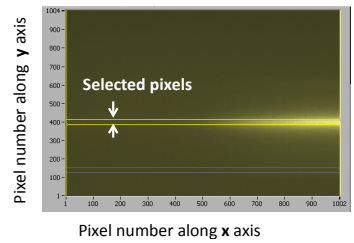

Figure 4.8. *An example of the fluorescence intensity distribution in the CCD camera (diffraction occurs along the x axis). Two cursors are used to select the area to be read out.*

Figure 4.7. *Schematic set-up for fluorescence detection.*

Different orders of diffracted beams can be selected by remotely turning the grating.

The CCD camera with a pixel size of 8 µm (iXon 885 from Andor) was used to capture the fluorescence photons. The effective readout noise of each pixel is reduced to the sub-electron level benefiting from the electron multiplication technique, and the dark current was only 0.028 electron/(pixel·s) at -70°C [102]. Figure 4.8 shows an example of the distribution of the fluorescence intensity on the CCD matrix when recording the spectrum. The number of pixels along the y axis can be selected by setting the position of two cursors, and the pixels on x axis represent different wavelengths. The fluorescence observation volume can be restricted by decreasing both the size of the slit in one dimension (along x axis) and the number of pixels in the CCD camera in the other dimension (along y axis). This combination provides a confocal geometry.

Alignment of the setup

As this set-up is not an integrated system, it is crucial to position the focusing lens L_f correctly, so that its focal point is exactly on the centre of the slit. A gold-coated plate with etched rings (diameter ∼20 µm) was used as the sample for allignment. The following procedure was used to find the correct position of lens L_f and to align the external laser beam path. The diameter of the ring is about 20 µm.

(i) The image plane of the objective lens was determined with

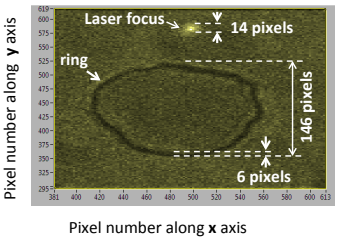

Figure 4.9. *Image of the gold-coated plate showing an etched ring. In this measurement the focal length of L_f is 500 mm and the 20× objective lens (effective focal length 9 mm) was used. Aberration correction was made.*

the aid of the eyepiece. The sample was illuminated with the microscope lamp and its position was adjusted along the beam propagation axis until the sharpest image of one etched ring was seen in the eyepiece. The sample should not be moved after this adjustment.

(ii) The correct position of lens L_f was established based on the sharpness of the image of the etched ring in the CCD camera. The grating was then turned to direct the zero-order diffracted beam onto the CCD camera.

(iii) The external laser beam was then directed into the microscope, and the divergence and direction adjusted slightly until a tight focus was achieved on the CCD camera. This step ensures that the focal plane of the laser coincides with the image plane of the objective lens.

Figure 4.9 shows the image in the CCD camera when the set-up is well aligned.

Magnification and resolution of the system

The image magnification from the focal plane of the objective lens to the CCD camera is determined by dividing the focal length of lens L_f by the effective focal length of the objective lens. In the measurement shown in Figure 4.9, the magnification is about 55 times. This was verified by comparing the size of the image of ring in the CCD camera, where the image is about 1168 µm (corresponding to ∼146 pixels), and its actual size 20 µm. The deviation is within the error margin.

The thickness of the etched line was ∼6 pixels on the CCD camera image, which means that the actual thickness of the line was at most 0.9 µm. This indicates that the resolution of the objective lens is, at worst, 0.9 µm.

The size of the laser focus at the top of Figure 4.9 (∼14 pixels) indicates that the focal diameter of the collimated incidence beam, which had a diameter of 3.3 mm, is about 2 µm.

Collection efficiency of the system

The optical collection efficiency is defined here as the probability of an emitted fluorescence photon passing through all the optics shown in Figure 4.7, and then reaching the CCD camera. The collection efficiency for the zero-order diffracted light is about 0.003%. The reflectivity or transmissivity of each component is listed in Table 4.1.

Component	Reflectivity or transmissivity
Fraction of solid angle accepted by the objective lens	1.5%
Transmission of the objective lens	64%
Mirror M_{in}	63%
Beam splitter	83%
Filter	70%
lens L_f	90%
Monochromator	1.1% (0th order), 1.5% (1st order)

Table 4.1: *The reflectivity or transmissivity of the optical components in the fluorescence detection setup. The objective lens refers to the LUCPLFLN 20×.*

Chapter 5

Diode laser frequency stabilization

The objective of the work described in this thesis was to detect the fluorescence signal from a single Ce ion in an Y_2SiO_5 crystal. The Ce ion transition frequency is ∼800 THz (371 nm) and has a homogeneous absorption linewidth of 4 MHz. To interact with a specific single Ce ion and obtain a good SNR, the laser frequency should be tuned to the centre frequency of the ion and have a relatively small frequency excursion (e.g. no more than ±50 kHz) during the signal integration time. In order to verify that the signal is indeed from a single Ce ion, the time required for a time correlation measurement (as shown in Figure 2.11) would be a few hours. This imposes a high requirement on the excitation laser source.

The source currently being used is an ECDL, which has a linewidth of typically ∼1 MHz over 1 ms, and a frequency stability of 5 MHz over 10 ms [100]. In order to meet the frequency requirements mentioned above the ECDL frequency must be stabilized. In this chapter various frequency reference options that were considered will be discussed (Section 5.1). This will be followed by a brief introduction to the PDH locking technique used for stabilization (Section 5.2). The third section in this chapter sheds some light on the design of the entire stabilization system (Section 5.3). Finally, a brief discussion about the future work on the stabilization is given (Section 5.4).

5.1 Frequency references

Various frequency references were considered for the stabilizing of the ECDL, some of which are described briefly in this section. An

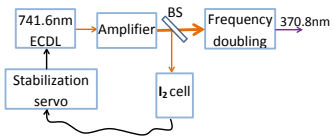

Figure 5.1. *A stable 371 nm laser can be generated by frequency doubling a 741 nm laser that is locked to an I_2 line. As a result of the frequency doubling efficiency is only a few percent, and a light amplifier is needed to increase the power.*

ULE cavity was finally chosen as the frequency reference, based on its cost and convenience.

5.1.1 Spectral lines

Some of the spectral lines of certain diatomic molecules (eg. iodine in gas phase) have been thoroughly investigated [103]. For example, the hyperfine lines of a rotational vibronic transition of the iodine molecule could have a full width at half maximum (FWHM) linewidth as narrow as 400 kHz at a pressure of 0.01 mbar, and the frequency shift can be as low as 230 kHz/mbar [104]. These features make it possible to use these lines as frequency references. For example, Kremser et.al. stabilized a diode laser at around 790 nm to a hyperfine transition of the iodine molecule [105]. The laser linewidth was found to be less than 100 kHz, and the relative frequency stability was 4×10^{-11} for 1 s.

Unfortunately, no molecular transitions have been found around the Ce ion absorption line at 370.8 nm. However there are iodine lines around 741.6 nm (twice the wavelength of the Ce absorption line). This provides the possibility to frequency double a stabilized laser at 741 nm. A schematic set-up employing a commercially available ECDL is shown in Figure 5.1. The relevant iodine lines are the hyperfine components of the P(81)(4-13) and P(106)(1-11) transitions, which are ∼14 GHz away from the desired frequency. However, these lines are rather weak (α ∼0.02 m^{-1} at 793 K), which would lead to a low SNR. The SNR, can be increased by pre-stabilizing the laser to a cavity, and then integrating the signal over a longer time [106], or by increasing the absorption, either by increasing the temperature in the iodine cell, or by placing it inside a cavity to increase the interaction length. However, these procedures increase the complexity of the system. Besides the weak absorption, this scheme has another disadvantage. The frequency doubling efficiency from 741 nm to 370.8 nm is only about 5% [107], which means that in order to obtain a power of 10 mW power on 370.8 nm (the power required for the present experiments) it would be necessary to have a power of 200 mW at 741 nm, which can only be achieved with an extra amplifier (e.g. a tapered amplifier). This makes the use of molecular lines as a frequency standard both laborious and costly.

5.1.2 Frequency combs

A frequency comb is a light source with a series of sharp, equally spaced lines. The span of the comb may be hundreds of nm (e.g. the FC1500-250-WG Er-doped frequency comb with the M-VIS extension package from Menlo Systems covers a spectrum range 530-900 nm), and the comb tooth spacing may range from tens of MHz to a few GHz. Two important parameters characterize

a frequency comb: the frequency offset (f_o) and the comb tooth spacing (f_r). Frequency combs are often generated by a femtosecond mode-locked laser [108, 109], where the phase shift between the peak of the E field envelope and the closest peak of the carrier determines f_o, and the inverse of the the round-trip time of the cavity determines f_r.

To use a frequency comb as a frequency reference for laser stabilization, both f_o and f_r must be stabilized. The stabilization of f_o is much easier for a comb that has a span of one octave [110, 111]. A illustration of this stabilization is shown in Figure 5.2. The frequency-doubled line of the n^{th} tooth at $f_o+n\cdot f_r$ beats with the $2n^{th}$ tooth line at $f_o+2n\cdot f_r$, generating an oscillation at a frequency of f_o. This oscillation can be stabilized onto a stable RF source. The stabilization of f_r is much simpler than that for f_o, since a fast photodiode can be used to directly measure the beating pattern of a femtosecond pulse, and f_r then can be locked to a stable RF source.

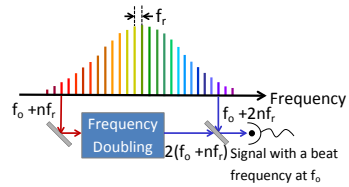

Figure 5.2. *Illustration of the stabilization of the frequency offset, f_o, in a frequency comb covering an octave.*

However, commercially available frequency combs (e.g. those supplied by Menlo Systems) only cover the visible and near-infrared range. These would have to be frequency doubled to cover the ultra-violet range, and this would involve a significant amount of work and financial investment.

5.1.3 Transfer cavity

A transfer cavity is an active cavity, in which one of the cavity mirror is mounted on a movable element, typically a piezo transducer (PZT). The cavity length can be stabilized by locking onto a pre-stabilized laser (called the reference laser) by regulating the voltage to the PZT and the temperature of the cavity. The long term stability of the transfer cavity is similar to that of the reference laser. Thus, the frequency stability of the reference laser could be transferred to another laser (called the target laser) via this transfer cavity. If a stable laser is available, this idea is easy to implement at a reasonable low cost.

It is worth noting that the cavity should be in vacuum. The reason for this is that the change in the refractive index of air in response to the change of the air pressure (δp) is dependent on the wavelength, which causes a change in the frequency of the target laser, $\delta\nu_{target}$, as follows [112]:

$$\delta\nu_{target} \approx \nu_{target} \cdot \frac{\delta p}{p} \cdot (n_{reference} - n_{target})$$

where ν_{target} is the initial target laser frequency; p is the initial air pressure; and $n_{reference}$ and n_{target} are the refractive indices of air at the reference and target laser frequencies. In our consideration, the reference laser was a 606 nm dye laser with a linewidth at the level of tens of Hz, and the target laser was a 371 nm laser.

The sensitivity of the frequency change of the 371 nm laser is 6.3 MHz/mbar.

This scheme was not chosen for two reasons. The first was related to timing, as the stabilization of the 606 nm laser had not been completed when this scheme was under consideration. The second reason was that we wanted to be able to move the 370 nm laser between different buildings for different experiments, but the 606 nm laser can not be moved for various reasons.

5.1.4 Stable cavity

A stable cavity is an optical spacer, normally made of a bulk material, such as ULE glass [113], pure silicon [114, 115] or sapphire [116], with two cavity mirrors in optical contact with the ends. Only the ULE glass cavity is considered here, as this is commercially available. ULE glass has a coefficient of thermal expansion (CTE) of the level of $\sim$10 ppb/°C in the temperature range of 5 °C to 35 °C. For comparison, the CTE of Invar and Zerodur are 1.5 ppm/°C and 20 ppb/°C, respectively. The CTE of ULE glass can be approximated to zero to the first order at a certain temperature (called the zero-crossing temperature), which varies from boule to boule, and depends strongly on the external stress in the glass [117]. The zero CTE is a valuable feature, which makes the ULE glass a usefull material for several critical elements, e.g. the mirrors in the Hubble Space Telescope, mechanical length standards, etc.

A number of factors could cause a change in the length of a passive cavity, for instance, temperature, elastic deformation induced by mechanical vibrations, acoustic vibrations, pressure variation, expansion of the mirror coating [113] and Brownian motion of the atoms in the mirror substrate [118]. Some of these can be reduced in various ways.

(i) The cavity should be operated around its zero-crossing temperature, and this temperature should be stable within a few mK.

(ii) Suitable mounting schemes can be used to minimize elastic deformation [119–123]. A very good numerical analysis of this is given in Ref.[124].

(iii) The cavity should be placed in a vacuum chamber at a pressure $<\sim 10^{-8}$ mbar for a number of reasons. The most important is that any dust or organic molecules in the air may be deposited on the inner surface of the mirror, and be combusted by the high intensity intra-cavity laser, which would destroy the highly reflectivity coating. The second reason is that the refractive index of air changes with pressure, so if the cavity is not under vacuum, pressure changes will change

the effective cavity length, leading to a corresponding change in frequency (200 MHz/mbar at atmospheric pressure) [112]. The third reason is that thermal convection between the cavity and environment makes mK temperature stabilization impossible, and the fourth reason is that acoustic waves can be transmitted to the ULE cavity very efficiently by air.

Sub-hertz diode laser linewidthes have been demonstrated by locking the laser frequency onto a passive stable ULE cavity through the PDH locking technique [119, 122, 125].

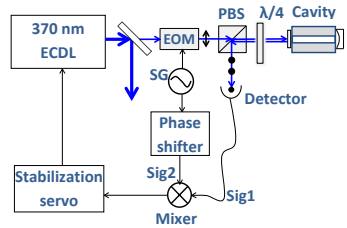

Figure 5.3. *Schematic illustration of a PDH locking set-up. The phase modulation on the light is implemented by an EOM. The reflected beam from the cavity is detected by a photodiode, then this electronic signal further goes into a mixer, where it mixes with another signal with the same frequency. With proper phase adjustment between these two signals, an error signal is produced. Then it is fed back to the laser. The symbols ↕ and • indicate the light polarizations.*

5.2 Pound-Drever-Hall locking

Pound-Drever-Hall locking is one of the techniques available for laser phase and frequency stabilization. It has been widely used for laser stabilization since it was proposed in 1983 [94]. The technique has been described in detail by M. Zhu et.al., and E. D. Black [126, 127]. The keywords describing the essential parts of this technique are **phase modulation** and **the beam reflected from the cavity**. A brief review of the generation of the error signal is given in this section from a mathematic point of view, considering a lossless cavity and equal reflectivity of the cavity mirrors.

The basic idea behind the PDH locking is the same as in all other frequency stabilization techniques, i.e., comparison of the target laser frequency with a frequency reference, e.g. a spectral line or a transmission line of a cavity, then feeding the resulting error signal back to the laser, and starting the active regulation system. A schematic illustration of a PDH locking set-up is shown in Figure 5.3. For an ECDL, the feedback signals are generally directed to both the driving current to the laser diode (fast control on µs timescale) and the PZT (slow control on the ms scale), which are both used to tune the length of the external cavity.

There are two significant advantages of the PDH locking scheme compared with other laser stabilization techniques.

(i) A phase modulation is implemented onto the incidence beam to the cavity. This beam contains three frequency components (the carrier and two sidebands located symmetrically on either side of the carrier), and these maintain a certain phase relationship. This phase relationship helps identify the direction in which the laser frequency is drifting away from the resonance line. This information can not be obtained if there is no phase modulation as the intensity of the reflected or transmitted beam from the cavity are symmetric around the resonance line. This technique is very similar to an older technique developed in 1946 [128] for stabilizing a microwave oscillator. It is also very similar to the frequency modulation spectroscopy technique used in atomic physics.

(ii) The error signal is extracted from the beam reflected by the cavity. The reason for not detecting the transmitted beam is that transmission can not be established until the intracavity field has been built up. This means that there is a time delay between the instantaneous laser status and the error signal. The idea of detecting the reflected beam instead of the transmitted beam was first proposed in 1978 by Yu V Troitskiĭ [129], who showed that the SNR could be improved by at least 10 dB. Apart from the improvement in SNR, detecting the reflected beam allows not only frequency stabilization but also phase stabilization of the laser.

It is interesting to note that although similar improvements were demonstrated before PDH locking was proposed, it took five years before the combination of techniques (i) and (ii) was suggested. This led to an important step forward in the laser stabilization.

5.2.1 Generation of sidebands

Sidebands are generated by phase modulation, which is implemented by applying an RF signal to an EOM. The electric field leaving the EOM is:

$$E_{in} = E_0 e^{i(\omega t + \beta \sin(\Omega t))} \tag{5.1}$$

where E_0 and ω are the amplitude and frequency of the unmodulated beam, respectively, and β and Ω are the modulation depth and modulation frequency (often in the range of tens of MHz). This expression can be expanded using the Bessel function of the first kind as:

$$\begin{aligned} E_{in} &\approx E_0[J_0(\beta) + 2iJ_1(\beta)\sin(\Omega t)]e^{i\omega t} \\ &= E_c e^{i\omega t} + E_s e^{i(\omega+\Omega)t} - E_s e^{i(\omega-\Omega)t} \end{aligned} \tag{5.2}$$

where $E_c = E_0 J_0(\beta)$, and $E_s = E_0 J_1(\beta)$ are the amplitudes of the carrier (at frequency ω) and sidebands (at $\omega \pm \Omega$), respectively.

It is worth noting that although there are three frequency components in the beam, to a first order approximation, there is no net intensity modulation at the modulation frequency (Ω). This can be understood as the interference between the carrier and the left and right side bands cancel each other out exactly, due to the opposite phases of the sidebands. The modulation frequency is often chosen to be much higher than the cavity resonance linewidth in order to maximize the SNR, so the two sidebands have no interaction with the cavity.

5.2.2 The beam reflected from the cavity

The reflected beam is separated from the input beam by a polarizing beam splitter cube, as shown in Figure 5.3, and can be seen as a coherent superposition of two beams. One is the direct reflection of the input beam, which provides an instantaneous response to the laser status, while the other one is the leakage from the cavity after the intra-cavity field has been built up. This leakage beam shows a delayed response (determined by the cavity lifetime) with respect to the instantaneous change in laser frequency or phase. The interference between these two beams results in a complex amplitude reflection coefficient [127]

$$F(\omega) = E_{ref}/E_{in} = \frac{r(\ e^{\ i\omega/\Delta\nu_{fsr}} - 1\ )}{1 - r^2 e^{\ i\omega/\Delta\nu_{fsr}}}, \tag{5.3}$$

where r is the amplitude of the reflectivity of the mirrors and $\Delta\nu_{fsr}$ is the FSR of the cavity. The real and imaginary parts of $F(\omega)$ are:

$$Re(F) = \frac{r\ (1+r^2)\ (\cos(\frac{\omega}{\Delta\nu_{fsr}}) - 1)}{1 + r^4 - 2r^2 \cdot \cos(\frac{\omega}{\Delta\nu_{fsr}})}, \tag{5.4}$$

and

$$Im(F) = \frac{r\ (1-r^2) \cdot \sin(\frac{\omega}{\Delta\nu_{fsr}})}{1 + r^4 - 2r^2 \cdot \cos(\frac{\omega}{\Delta\nu_{fsr}})}. \tag{5.5}$$

The power of the reflected beam contains a DC term and an AC term (neglecting the 2Ω terms) [127]. Only the AC term (P_{AC}) is of interest here since this causes the error signal.

$$P_{AC} \approx 2\sqrt{P_c P_s}\ [Re(B_{\omega,\Omega})\ \cos(\Omega t) + Im(B_{\omega,\Omega})\ \sin(\Omega t)], \tag{5.6}$$

where P_c and P_s represent the power of the carrier and sidebands, and $B_{\omega,\Omega}$ contains information on the interaction between the light fields and the cavity.

$$B_{\omega,\Omega} = F(\omega)F^*(\omega+\Omega) - F^*(\omega)F(\omega-\Omega) \tag{5.7}$$

Equation (5.6) shows that there is an modulation signal at frequency of Ω on the reflected beam. The amplitude of this modulation depends on the interaction between the light fields and the cavity. If we consider the case where the carrier is near the cavity resonance line, then the sidebands are totally reflected and $F_{\omega+\Omega} = F_{\omega-\Omega} = -1$. Equation (5.7) is then reduced to:

$$B_{\omega,\Omega} = -2i \cdot Im(F(\omega)). \tag{5.8}$$

Correspondingly, the reflected power depends only on $Im(F(\omega))$ as

$$P_{ac} = -4\sqrt{P_c P_s}\ Im(F(\omega)) \cdot \sin(\Omega t), \tag{5.9}$$

where $Im(F(\omega))$ is defined in Equation (5.5). Below it will be shown how P_{AC} [Equation (5.9)] reflects a frequency error or phase error.

Frequency error

When the laser frequency is near resonance with a small deviation ($\delta\omega$), $\omega = 2\pi N \cdot \Delta\nu_{fsr} + \delta\omega$, N is an integer. Using the first order approximation, Equation (5.9) will then be

$$\begin{aligned} P_{ac} &\approx -\frac{4}{\pi}\sqrt{P_c P_s}\ F \cdot \frac{\delta\omega}{\Delta\nu_{fsr}} \cdot \sin(\Omega t) \\ &= -\frac{4}{\pi}\sqrt{P_c P_s}\ \frac{\delta\omega}{\delta\nu} \cdot \sin(\Omega t). \end{aligned} \tag{5.10}$$

where F is the finesse of the cavity and $\delta\nu$ is the linewidth of the cavity.

It is now clear that the amplitude of the intensity modulation is proportional to the magnitude of the frequency drift, and if the laser frequency drifts across the resonance line there will be a 180° phase change. If this signal is processed with phase sensitive detection, it will be possible to identify the direction of the frequency drift. This can also be explained by the interference of the fields. Since the laser frequency does not perfectly match the cavity resonance frequency, the leakage field is smaller than in the perfect matching situation, so it will not completely cancel the direct reflected beam. The interference between this residual carrier beam and the sidebands leads to intensity modulation at the frequency of Ω. A very good description of this field interference has been given by L. Rippe [97].

Phase error

Since the instantaneous phase change only affects the direct-reflected beam and not the light leaking out from the cavity in a timescale shorter than the cavity lifetime, it is necessary to define the relation of between P_{AC} and $F(\omega)$ from the beginning. $F(\omega)$ can be rewritten in terms of the sum of the direct reflection and the leakage (F_{leak}) from the cavity as

$$F(\omega) = -r + F_{leak}, \tag{5.11}$$

where

$$F_{leak} = \frac{r(1-r^2)\cdot e^{i\frac{\omega}{\Delta\nu_{fsr}}}}{1-r^2\cdot e^{i\frac{\omega}{\Delta\nu_{fsr}}}} \tag{5.12}$$

The complex electric field (E_r) of the reflected beam with a phase change of $\delta\varphi$ is

$$\begin{aligned} E_{rfl} = {} & E_c e^{i\omega t}(-r\ e^{i\delta\varphi} + F_{leak}) - E_s e^{i(\omega+\Omega)t} e^{i\delta\varphi} \\ & + E_s e^{i(\omega-\Omega)t} e^{i\delta\varphi}. \end{aligned} \tag{5.13}$$

The AC term (P_{AC}) of the reflected beam power ($E_{rfl}\cdot E^*_{rfl}$) is

$$P_{AC} = 4\sqrt{P_c P_s}\ [\ Im(e^{i\delta\varphi}F_{leak})\ ]\cdot\sin(\Omega t), \tag{5.14}$$

For simplicity, we will consider the case where the laser frequency is exactly on resonance, and there is a small phase change ($\delta\varphi \ll 1$). Equation (5.14) then becomes:

$$P_{ac} \approx 4\sqrt{P_c P_s}\ (\ r\delta\varphi\ )\cdot\sin(\Omega t) \tag{5.15}$$

There is also a modulation at frequency Ω. The amplitude of this modulation reflects the phase error in a similar manner to the frequency error. Detecting the phase-modulated beam allows not only frequency locking but also phase locking, and the feedback bandwidth is not limited by the lifetime of the cavity.

5.2.3 Error signal

As discussed above, whenever there is a frequency or a phase error a beat pattern will be seen on the reflected beam at frequency Ω. In this section, it will be shown how the error signal is related to this beat pattern and what the error signal would be when the laser is scanned across the sidebands. The reflected beam is detected by a photodiode with a bandwidth larger than 2Ω, as shown in Figure 5.3. The photocurrent generated in this photodiode (called Sig1) is fed to one input of a mixer, where it is multiplied by a reference signal (called Sig2) at the same frequency, see Figure 5.3 for an illustration. With the correct phase relationship between these two inputs (a phase shifter is usually needed for adjustment), the output from the mixer is a DC signal, and its amplitude is proportional to the amplitude of the beat pattern. This DC signal is then passed through a low-pass filter and fed back to the regulation system.

The error signals in different cases are:

- Exactly on resonance: $E_r = 0$.
- A small frequency error: $E_r = -8\sqrt{P_c P_s}\ \delta f/\delta\nu$.
- A small phase error: $E_r = 4r\sqrt{P_c P_s}\ \delta\varphi$.

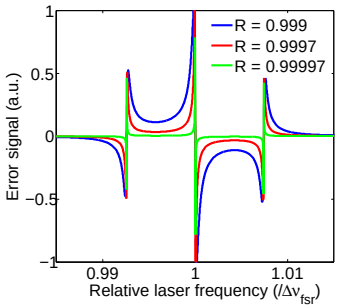

Figure 5.4. *Error signal when the laser is scanned across the sidebands. The relative laser frequency in unit of the FSR of the cavity is shown on the x axis.*

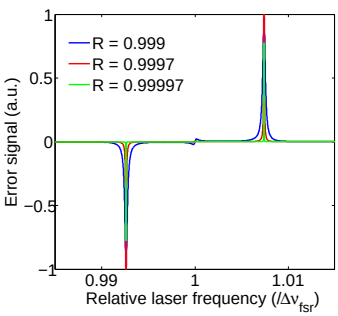

Figure 5.5. *Error signal similar to Figure 5.4, but for an extra 90° phase shift in Sig2.*

Error signal when the laser is scanning

If the other input signal to the mixer (Sig2) is in phase with $\sin(\Omega t)$, the error signal for a frequency scanned laser (over a range greater than 2Ω across the resonance line) is given by:

$$E_r = 2\sqrt{P_c P_s}\ Im(B_{\omega,\Omega}), \tag{5.16}$$

while it is

$$E_r = 2\sqrt{P_c P_s}\ Re(B_{\omega,\Omega}) \tag{5.17}$$

when Sig2 is phase shifted by 90°. Since $Im(B_{\omega,\Omega})$ provides a much steeper and larger error signal when the carrier is near resonance, it was chosen as the error signal. $Im(B_{\omega,\Omega})$ in various cases are:

- $Im(B_{\omega,\Omega}) = Im[F(\delta\omega)]$ when the left sideband is near resonance,
- $Im(B_{\omega,\Omega}) = -2Im[F(\delta\omega)]$ when the carrier is near resonance,
- $Im(B_{\omega,\Omega}) = Im[F(\delta\omega)]$ when the right sideband is near resonance.

A few conclusions can be drawn from the above expressions for $Im(B_{\omega,\Omega})$: (i) The error signal is anti-symmetric around the resonance line regardless of whether the carrier or sideband is on resonance. (ii) The error signal is the same for both sidebands. (iii) The slope of the error signal of the carrier is opposite to that of the sidebands.

A plot of this error signal is shown in Figure 5.4 for cavities with a finesse of 3140, 10000 and 100000. The linewidth of the cavity is about 0.7% of the FSR. One can see that the higher the finesse, the sharper the slope. The error signal with an extra 90° phase shift in Sig2 is shown in Figure 5.5.

5.3 System design

The plan for the laser stabilization was to actively stabilize the length of the laser cavity by locking onto a stable ULE cavity via a feedback signal to both the laser driving current and the PZT mounted on the grating. Two specific considerations must be kept in mind when designing such a system. One is that the wavelength of the laser to be stabilized is around 371 nm, i.e. in the ultra-violet range, where many materials absorb strongly. Optics are commercially available for this spectral range, but they are not as common as those in the visible range, and tend to be rather expensive. Another consideration is that we wanted the whole stabilization system to fit onto an optical table measuring

75 cm × 90 cm to allow the system to be transported between different labs. This places a size restriction on some elements, for instance, the vacuum chamber and the focal length of the lens used in the double-pass AOM set-up. The electronics considerations for a PDH locking system have been described previously [97].

The next section provides a brief description of the custom-ordered ULE cavity and radiation shield used in this set-up, since the other components are more common. The objective is to share our experience with others who are considering the construction of similar stabilization systems.

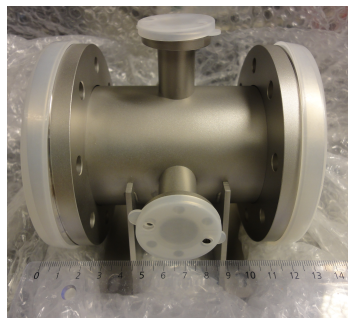

Figure 5.6. *Steel vacuum chamber for the cavity spacer.*

5.3.1 ULE cavity spacer

In order to keep the laser frequency at around 800 THz with a maximum excursion of ±50 kHz within a few hours, the fractional change in the cavity length ($\triangle L/L$) should be kept below 1.2×10^{-10}. This means that the change in length should be smaller than 6 pm for a 5 cm-long cavity. This is not a very stringent requirement, and stabilization of the cavity length within the size of a proton (a few fm) or even less has been demonstrated previously [113, 123].

In order to ensure that the length of the cavity does not change by more than 6 pm, the cavity temperature should be stabilized within 0.3 K around the zero-crossing temperature, and it should be evacuated to 10^{-8} mbar (the reasons were described in Section 5.1.4.

Other important factors are the cavity configuration and the mounting scheme, as the set-up should be insensitive to mechanical vibrations. Various mounting schemes have been investigate previously, e.g. [119–124], where the acceleration sensitivities of the fractional change in length ($\triangle L/L$) are all below 3×10^{-10}/ ms^{-2}. Considering that the typical acceleration in the lab is $\sim1\times10^{-4}$ ms^{-2} [120], any one of the mounting schemes can be used for the purpose. We eventually chose the spring wire suspension configuration described by T. Nazarova et.al. [120] because it can be reasonably easily installed in a 12 cm-long cylindrical vacuum chamber (as shown in Figure 5.6) with reasonable effort.

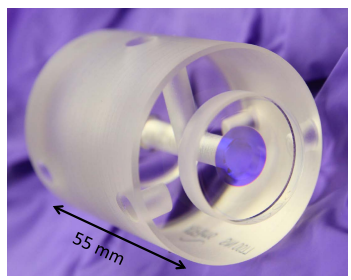

Figure 5.7. *ULE cavity spacer with a length of 55mm and a diameter of 44mm. For the evacuation purpose, a hole with a diameter of 6 mm were drilled from the top downwards into the center, and another hole with the same diameter was drilled along the cavity length direction.*

A photograph of the cavity spacer is shown in Figure 5.7. The length of the cavity is 55 mm, and the diameter is 44 mm. Detail of the structure is shown in Schematic 1. The mirror substrate is also ULE glass to obtain a zero-crossing temperature slightly below room temperature. The mirror coating has a reflectivity of 99.97% in the wavelength range 365 nm to 370 nm, and 99.997% from 575 nm to 615 nm.

The positions of the mounting holes were determined from a finite-element simulation written by Professor Uwe Sterr's group in Physikalisch-Technische Bundesanstalt, Germany. The cavity is suspended from the radiation shield by spring wires with Viton

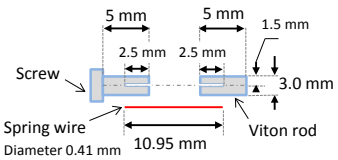

Figure 5.8. *Illustration of the screw, Viton rod and spring wire. The spring wire is inserted into the holes, connecting the screw and Viton rod together.*

Figure 5.9. *The connections between the viton rod, spring wire and screws.*

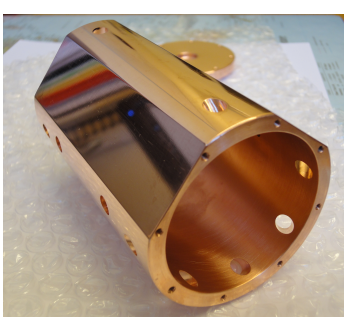

Figure 5.10. *Gold coated cylindrical radiation shield with two cutting edges and two lids.*

rods and screws on each end, in the same way as shown in their article [120]. The stainless steel spring wires were bought from a guitar shop. The screws and Viton rods were cut to a length of 5.0 mm and the spring wire was 10.95 mm long, see an illustration in Figure 5.8. Holes with a diameter of 0.43 mm were drilled at the centre of the screw and Viton rods to a depth of 2.5 mm by Drill Service in England. A photograph of the connection between the screw, spring wire and Viton rod is shown in Figure 5.9.

5.3.2 Radiation shield

A gold-coated copper radiation shield was designed. It is cylindrical with two edges cut, shown by the photograph in Figure 5.10. The drawing is given in Schematic 2. It has four threaded holes for mounting of the cavity spacer. Two planar surfaces ensure good thermal contact with the thermoelectric coolers (TECs). 12 inclined holes were drilled at an angle of $\sim 45°$ to the axis of the cylinder, which serve as venting holes for the evacuation of the cavity spacer. The angle should be chosen so that the area of the surface exposed to radiation is not increased, while not decreasing the pumping speed too much.

5.3.3 Vacuum chamber assembly

Four TECs were used in the assembly. These are mounted on the copper adaptors which were glued onto the inner wall of the vacuum chamber. The radiation shield is placed on top of the TECs with one TEC at each end. The distance between the chamber and the radiation shield, and the distance between the shield and the cavity spacer is only 3 mm. A photograph of the whole vacuum chamber assembly is shown in Figure 5.11. As the design is compact it is necessary to ensure that every step is carried out correctly before moving on to the next as it is rather difficult to correct errors without removing the radiation shield from the chamber. Gluing the TECs is one of the more difficult parts of the work. One has to be extremely careful because the TECs are very fragile and damage may go unseen. They can only be checked by running a small current through them and measuring the resistance via the four-wire measurement method. Detailed information on the assembly and installation were given in Ref. [130].

A photograph of the system platform is shown in Figure 5.12. The initial test on the stabilization system showed that the laser can be locked for $\sim$3 hours, but the transmitted intensity showed fluctuations on the µs timescale, which must be investigated.

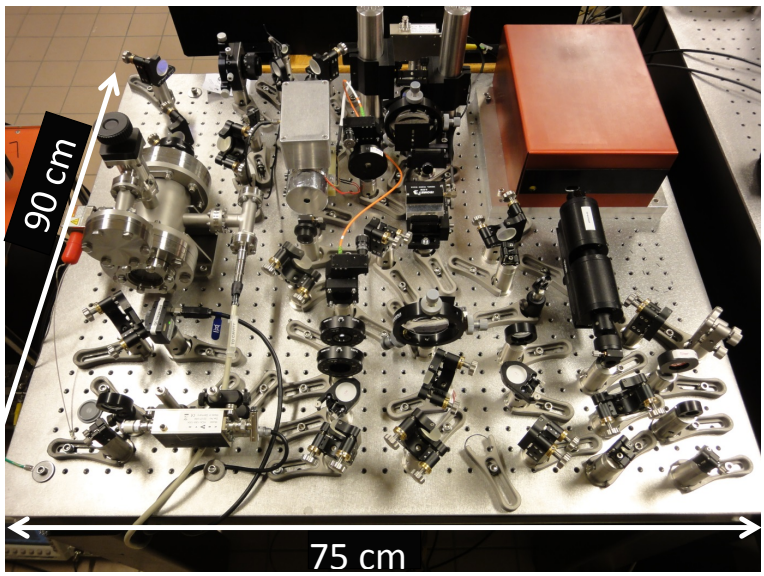

Figure 5.12. *The 371 nm laser stabilization platform measuring 75 cm × 90 cm.*

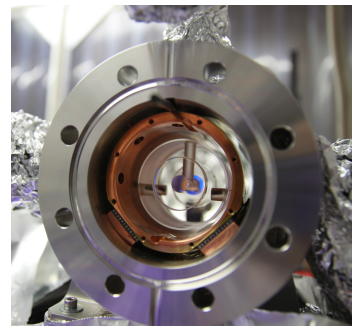

Figure 5.11. *Vacuum chamber assembly after the cavity spacer, TECs and radiation shield have been installed.*

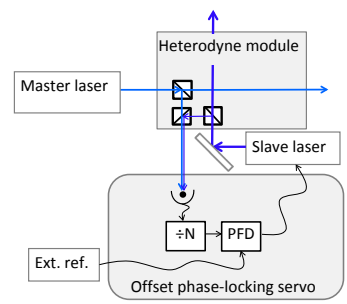

Figure 5.13. *Schematic diagram of the offset phase-locking scheme.*

5.4 Future work

In the long term, the laser should have the capability of scanning a frequency of about tens of GHz while being stabilized. This capability would allow selective switching between addressing different individual Ce ions within the inhomogeneous line, characterized by sitting so close to a single qubit ion that they can detect the qubit state through the permanent dipole-dipole interaction, which will be described in detail in Section 6.2.1.

One way of developing frequency scanning is to use the offset phase-locking scheme[131], as illustrated in Figure 5.13. In this scheme two laser sources with almost the same frequency (maximum allowed difference ~ 80 GHz) are required. One is a stabilized laser (denoted the Master laser), which is the frequency reference. The other is the laser to be stabilized and used for the frequency scanning (the Slave laser). It is first necessary to carry out a heterodyne detection of the two sources, then perform frequency division on the beat nodes and compare this signal with an external frequency reference. The comparison provides the error signal to the slave laser. The heterodyne module and the offset phase locker both are available commercially from Vescent Photonics.

Chapter 6

Quantum computing using rare-earth ions

Quantum computing has attracted extensive attention in the past few decades [1–3, 132]. Although there is currently no experimental demonstration of a quantum computer that can outperform a classical computer, it is of fundamental interest to study the nature of quantum mechanical computing. Also, Moore's law predicts that the density of transistors on an integrated circuit doubles every two years [133]. However, there is a limit on the minimum size of a transistor, and it will soon be necessary to move into the microscopic world, where classical physics fails to describe the system, and quantum mechanics takes over. Thus, it is necessary to learn how to control quantum systems.

This chapter describes how the electron populations in the hyperfine levels of the RE ions (in this case Pr^{3+}) in a crystal (Y_2SiO_5) were manipulated and controlled in the frame of quantum computing. Part of the work is presented in Paper **I**. Two quantum computing approaches were investigated: the ensemble qubit approach [8, 65] (Section 6.1) and the single-ion qubit approach [134] (Section 6.2). The description of each approach will be based on the five criteria for the realization of quantum computation established by D. P. DiVincenzo in 2000 [135]. These can be summarized briefly as following: (1) a well defined qubit and qubit initialization, (2) a much longer coherence time than the gate operation time, (3) a universal set of quantum gates, (4) qubit state readout capability, and (5) the possibility of scaling to a large number of qubits.

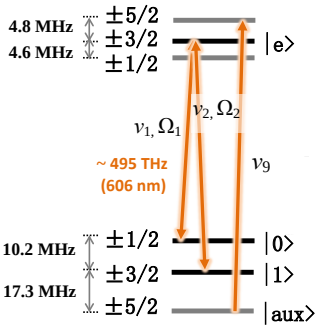

|g>/|e>	±1/2	±3/2	±5/2
±1/2	0.56	0.38	0.06
±3/2	0.39	0.60	0.01
±5/2	0.05	0.02	0.93

Figure 6.1. *Hyperfine levels of the lowest crystal field level in the $^3H_4$ and $^1D_2$ terms of Pr^{3+} (site 1) in Y_2SiO_5 . ±1/2, ±3/2 and ±5/2 refer to the projection value of the nuclear spin. The table gives the relative oscillator strength of each transition.*

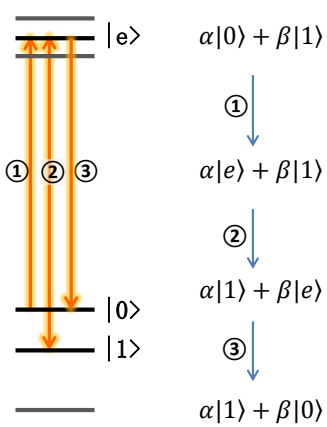

Figure 6.2. *Scheme of a NOT gate for a qubit, showing the implementation of three consecutive optical pulses.*

6.1 Ensemble qubit quantum computing

Our group has been working with Pr^{3+} ions doped in an Y_2SiO_5 crystal for quantum computing. In this system, the qubit is defined as two of the hyperfine levels ($|0\rangle$ and $|1\rangle$) of the lowest crystal field level in the $^3H_4$ term, which is illustrated in Figure 6.1. The lifetime and coherence time of the qubit levels can be as long as a few minutes [90, 136] and ∼30 s [137], respectively.

The optical transition lines of Pr ions are inhomogeneously broadened up to a few GHz, depending on dopant concentrations, due to local lattice distortion, as discussed in Section 3.2. This broadening provides the option of using a subgroup of Pr ions in a much narrower frequency range (e.g. 170 kHz [8]) as a qubit, by addressing them via their optical transition frequencies (e.g. $|0\rangle \rightarrow |e\rangle$), and subgroups of ions with different frequencies can serve as different qubits [65]. The time duration of the pulses for the qubit gate operations must be considerably shorter than the coherence time of the optical transitions, which is ∼152 µs for Pr ions in site 1 (Table 3.3), otherwise decoherence of the optical transition will destroy the qubit. Figure 6.2 shows an example of a NOT operation, which is realized via three optical pulses ①, ② and pulse ③ with a pulse area of π. Experimental realization of arbitrary single qubit rotations and state characterization (quantum state tomography) will be described in Section 6.1.2 and Section 6.1.3, respectively.

The qubit-qubit interaction in these systems can be realized via the permanent electric dipole-dipole interaction (discussed in Section 3.3.2) between strongly-interacting ions in each qubit [49]. The scheme for a conditional not (CNOT) gate operation and the initial experimental investigation (qubit distillation) will be described in Section 6.1.4.

6.1.1 Rare-earth ion qubit initialization

To ensure good control of the pulse area, an addressing frequency which corresponds to only one specific isolated transition is required (e.g. from $|0\rangle$ to $|e\rangle$). However this is not possible in a system with inhomogeneous broadening, and particularly not when the inhomogeneous broadening of each of the nine optical transitions shown in Figure 6.1 is about 3 orders of magnitude greater than the splitting of the hyperfine levels, so that all transitions are overlapping. The situation can be improved using two steps. In the first, a spectral range is created somewhere inside the inhomogeneous absorption profile, where there is minimal (close to zero) absorption (further denoted a spectral pit). In the second step, a subgroup of ions with almost the same optical transition frequencies outside the pit is selected and pumped back into the empty pit. This subgroup of ions represents one qubit. These two steps

will be described below in the example of initializing the qubit in the $|0\rangle$ state.

The spectral pit

The essential task of creating a pit inside the inhomogeneous profile is to redistribute the ion population within the ground state hyperfine levels via spectral hole-burning, in such a way that no ions absorb at the frequencies where the pit is located. A spectral hole centred at ν_1, see Figure 6.3, can be created by repeatedly sending a light pulse centred at that frequency into the crystal, as discussed in Section 3.4.1. The time separation between two consecutive pulses should be long enough to allow the excited ions to relax to their ground states. Decay to hyperfine levels other than the initial one gives rise to the spectral hole. As the lifetime of the ground state hyperfine levels is several orders of magnitude longer than the time between two consecutive hole-burning pulses and the duration of the hole-burning pulse, the population of the levels with an optical transition frequency of ν_1 will continue to decrease until no absorption is observed. A wider spectral hole can be burnt if the centre frequencies of the hole-burning pulses are scanned across a range ($\Delta\nu$). More detailed information on the creation of spectral pits can be found in previous publications [80, 99, 138].

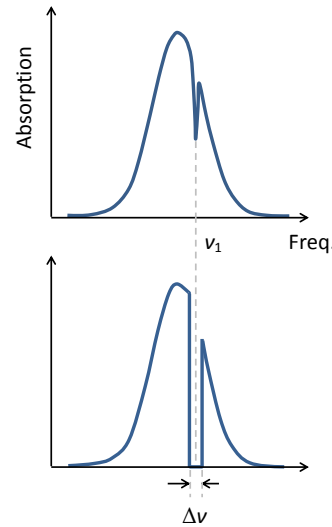

Figure 6.3. *Illustration of a spectral pit created in the inhomogeneous absorption line by scanning the centre frequency of the hole-burning pulses.*

The maximum frequency width of the pit for Pr ions is ∼18.1 MHz, which is determined by the difference in the total energy separation of the hyperfine levels between the ground state and the excited state. The reason of this determination is easier to understand by starting from the transparency frequency range of a single class of ions (class is defined by the subgroup of ions that all have the same optical transition frequencies), then to see how this range is decreased by the absorption lines from other classes of ions with different optical transition frequencies resulting from the inhomogeneous broadening. Considering one specific class of ions, see Figure 6.1, taking the frequency of the transition between the $|1/2g\rangle$ (referred to the $\pm 1/2$ ground state in Figure 6.1) and $|1/2e\rangle$ excited states as the frequency reference, the transparent range is all the frequency space except three transition lines, as an example, the lines are shown in Figure 6.4a for the ions initially in the $|5/2g\rangle$ ground state. The arrows denote the nine transition lines from each of the three ground hyperfine states (denoted as $|i/2g\rangle$, i = 1, 2, 3) to either of the three excited hyperfine state (denoted as $|ei\rangle$, i = 1, 2, 3). Taking the inhomogeneous broadening into account means that there are other classes of ions with absorption lines that have the same separation as those in Figure 6.4a, but they are distributed continuously in a few GHz. Absorption from the transitions outside the frequency range of Δf (27.5 MHz) changes the transparent range to a window, shown in

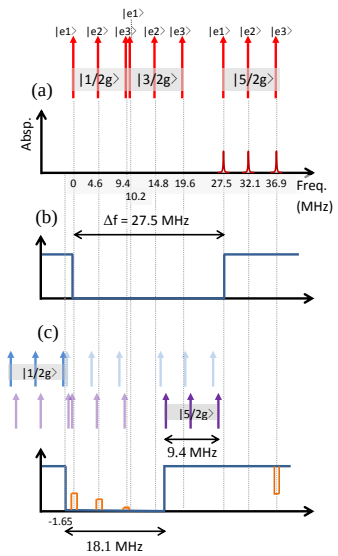

Figure 6.4. *Illustration of the maximum pit width determined by the energy structure of Pr ions. The horizontal axis shows the relative optical transition frequencies of the ions. (a) shows the absorption peaks form a single class of ions. (b) shows a reduced transparency window when the ions, with all transitions frequencies outside the range 0-36.9 MHz, are taken into account. (c) shows the pit width when the other ions, with some of the transitions lines inside the window, are also taken into account. A single class of ions with the $|5/2g\rangle \rightarrow |e3\rangle$ transition frequency at 36.9 MHz was burnt back into the pit.*

Figure 6.4b. The groups of lines inside the window can be divided into two groups depending on whether the $|1/2g\rangle \rightarrow |e3\rangle$ transition frequency is lower (type 1) or higher (type 2) than -1.65 MHz in the reference frequency frame. A margin of -1.65 MHz was used to obtain an equal distance between the edges of the pit to the nearest absorption lines of the qubit inside the pit. Type 1 lines do not affect the window as all ions can be prepared to be in the $|1/2g\rangle$ state. But part of the type 2 lines, with the $|1/2g\rangle \rightarrow |e3\rangle$ transitions frequencies higher than -1.65 MHz but smaller than 7.75 MHz (displaced by 9.4 MHz), do affect the window, regardless of in which ground state hyperfine levels the ions are prepared. This reduces the width of the window by an amount which is equal to the total energy separation of the excited state hyperfine levels, as illustrated in Figure 6.4c, e.g. all ions are prepared in their $|5/2g\rangle$.

The straight absorption edges in Figure 6.4c are undesirable, as strong transitions outside the pit but close to the edge could be activated through off-resonant excitation of pulses whose frequencies are inside the pit, as has been discussed previously [99, 139]. To minimize this influence, the ions should be prepared in a hyperfine state which is as far as possible from the pit. In the experimental implementation the ions whose $|1/2g\rangle \rightarrow |e_3\rangle$ transition frequency is lower than -1.65 MHz are pumped into their $|1/2g\rangle$ state, whereas ions with transition frequencies above -1.65 MHz are pumped into their $|5/2g\rangle$ state. This improvement leads to the pit structure shown in Figure 6.5, where the upper panel shows the result of simulation [139] and the lower panel shows the result of the experimental measurement. The experimental value of the absorption value is calculated from the transmission of a weak pulse (called the readout pulse), whose frequency changes linearly with time over a range of ±30 MHz [140]. The steps on the left and right sides of the pit correspond to transitions from the $|1/2g\rangle$ and $|5/2g\rangle$ states, respectively, to each of the excited hyperfine levels. More information on the pit-burning pulses can be found elsewhere [99, 141].

Peak creation

After the pit has been created, a laser pulse centred at 36.9 MHz (relative to the reference frequency, see Figure 6.4c), where the $|5/2g\rangle \rightarrow |e3\rangle$ transition is located for the class of ions shown in Figure 6.4a, and covering a narrow Fourier frequency span (e.g. a 170 kHz peak was created in Paper **I**) pumps a fraction of ions to their excited states. A second pulse, with centre frequency of 9.4 MHz then de-excites the ions of interest to their $|1/2g\rangle$ state. This group of ions represents a qubit.

The population of the $|1/2g\rangle$ state is shown as three absorption peaks inside the pit when it is probed by the readout pulse, see

Figure 6.6. These peaks correspond to the three transitions from the $|1/2g\rangle$ state to any of the three excited states. It is assumed here that the readout pulse is so weak that the population change caused by excitation at the resonance frequency can be neglected. The difference in height between the peaks is caused by different oscillator strengths.

The excitation and de-excitation pulses generally address several classes of ions at the same time, some of which will also fall into the pit, but at different positions. These can be spectrally removed from the pit by optical pumping.

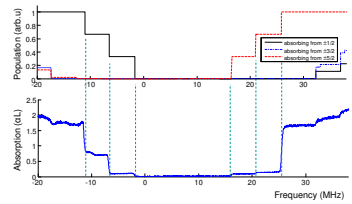

Figure 6.5. *Simulated (upper trace) and experimental (lower trace) pit structure in* Pr^{3+}*:*Y_2SiO_5 *. The y axis in the lower figure represents the absorption, which is a product of the population (y axis in the upper figure) and the respective oscillator strength.*

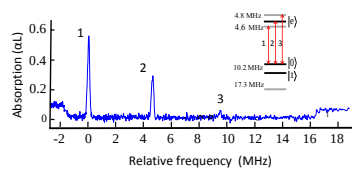

Figure 6.6. *A fraction of ions whose* $|1/2g\rangle \rightarrow |1/2e\rangle$ *transition frequency is at the selected reference frequency was burned back into the pit. The population in the* $|1/2g\rangle$ *state is shown as three absorption peaks (labeled as 1-3) when probed with a readout pulse.*

6.1.2 Single qubit rotation

A perfect qubit operation requires that the light pulse interacts with the individual ions constituting that qubit in exactly the same way, regardless of the slight inhomogeneity in the optical transition frequencies between them. The complex hyperbolic secant pulse (hereafter called the sechyp pulse) has been shown to the kind of pulse that is insensitive to the frequency detuning between the ions, and state transfer is achieved with high efficiency [49, 142]. However, the sechyp pulse can directly do the population transfer from pole to pole on the Bloch sphere, e.g. from $|0\rangle$ to $|e\rangle$, but not to a superposition state e.g. $\frac{1}{\sqrt{2}}(|0\rangle + |e\rangle)$.

An arbitrary superposition state $(\alpha|0\rangle + \beta|1\rangle)$ (where α and β are complex numbers and $|\alpha|^2 + |\beta|^2 = 1$) can be realized by the pole-to-pole transfers in a rotated base, where two sets of two-colour dark state pulses are used [8]. A set of two-colour dark state pulse refers to two sechyp pulses, one of which targets the $|0\rangle \rightarrow |e\rangle$ transition and the other the $|1\rangle \rightarrow |e\rangle$ transition, with Rabi frequencies of Ω_1 and Ω_2, respectively, as indicated in Figure 6.1.

When the two Rabi frequencies are equal, the net effect of these two pulses is that they operate on one superposition state $|B\rangle$ (this state is often called a bright state), but not the orthogonal state $|D\rangle$ (called a dark state). $|B\rangle$ and $|D\rangle$ are defined as follows (for notational simplicity the normalization factor is omitted):

$$|B\rangle = |0\rangle - e^{-i\phi}|1\rangle, \quad and \quad |D\rangle = |0\rangle + e^{-i\phi}|1\rangle, \tag{6.1}$$

where ϕ denotes the phase difference between the two pulses. $|B\rangle$ and $|D\rangle$ can be represented by two Bloch vectors on the equatorial plane of the Bloch sphere constructed on the $|0\rangle$ and $|1\rangle$ state, shown in panel Figure 6.7a.

The first set of two-colour pulses described above transfers state $|B\rangle$ to state $|e\rangle$ along route 1 (Figure 6.7b), then the second two-colour pulse transfers the population back along a different route (route 2). These two operations transform state $|B\rangle$ into $e^{i\theta}|B\rangle$, where θ is determined by the phase differences between the two sets of two-colour pulses. In the original base ($|0\rangle$ and $|1\rangle$) these

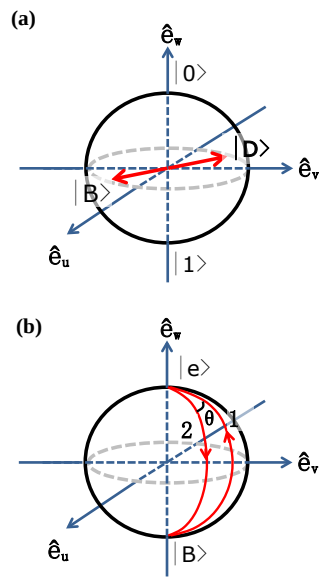

Figure 6.7. *Illustration of the bright, dark state and the two-color pulses. (a) The bright and dark state in the basis of* $|0\rangle$ *and* $|1\rangle$*. (b) Two sets of dark state pulses are used to transfer the* $|B\rangle$ *state to* $|e\rangle$ *state then back along a different route. The final state is* $e^{i\theta}|B\rangle$*.*

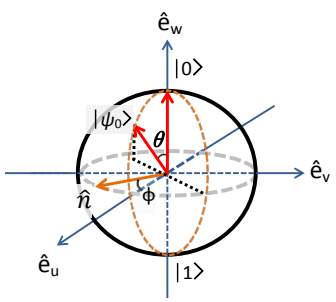

Figure 6.8. *State* ψ_0 *is achieved by rotation around a unit vector,* $\hat{n}$*, by an angle of* θ *from an initial state of* $|0\rangle$*.*

two sets of two-colour pulses create the following states in response to an initial state of $|0\rangle$ or $|1\rangle$

$$|\psi_0\rangle = e^{i\frac{\theta}{2}}[\cos\left(\frac{\theta}{2}\right)|0\rangle - i\sin\left(\frac{\theta}{2}\right)e^{-i\phi}|1\rangle], \tag{6.2}$$

or

$$|\psi_1\rangle = e^{i\frac{\theta}{2}}[-i\sin\left(\frac{\theta}{2}\right)e^{i\phi}|0\rangle + \cos\left(\frac{\theta}{2}\right)|1\rangle], \tag{6.3}$$

where one can see that θ controls the population fraction in states $|0\rangle$ and $|1\rangle$, and imposes a global phase on the states, which can be neglected for one qubit. ϕ determines the relative phase between the qubit levels.

In the matrix representation formed by states $|0\rangle$ and $|1\rangle$, the two-colour dark state operations mentioned above can be written as a unitary operator

$$U(\theta,\phi) = e^{i\frac{\theta}{2}}\begin{bmatrix}\cos(\frac{\theta}{2}) & -i\sin(\frac{\theta}{2})e^{i\phi}\\ -i\sin(\frac{\theta}{2})e^{-i\phi} & \cos(\frac{\theta}{2})\end{bmatrix}. \tag{6.4}$$

This operator describes a rotation by an angle of θ around a unit vector $(\hat{n})$ in the equatorial plane characterized by the angle ϕ [143], see Figure 6.8. For example, if one wants to create state $\frac{1}{\sqrt{2}}(|0\rangle + |1\rangle)$ from the initial state $|0\rangle$, the required U operator is

$$U(\theta,\phi) = e^{i\frac{\pi}{4}}\begin{bmatrix}1 & -1\\ 1 & 1\end{bmatrix}. \tag{6.5}$$

and corresponds to a rotation of 90° around $\hat{e}_v$.

It is worth noting that during the dark state operations a different phase factor for each ion is accumulated as their transition frequencies are slightly different, and this phase factor only happens to the $|B\rangle$ state wavefunction not to the dark state ($|D\rangle$). One way of of removing the influence of this phase factor is to let state $|D\rangle$ acquire exactly the same phase factor as the bright state, constituting a global phase that will not affect the qubit state. This can be achieved by implementing a similar dark state operation (with a π phase shift relative to the dark state operations on $|B\rangle$) on state $|D\rangle$, which is now a bright state, but along the same route ($\theta = 0$). Starting from state $|0\rangle$, an arbitrary single qubit state can be realized via four sets of two-colour pulses.

6.1.3 Quantum state tomography

An arbitrary superposition state (e.g. state ψ_0 in Figure 6.8) can be characterized by acquiring the respective projections on the three axes. The projection on $\hat{e}_w$ represents the population difference between state $|0\rangle$ and state $|1\rangle$, which can be quantified by

the absorption (calculated from the transmission of the readout pulse) at the optical transition lines from either of the states ($|0\rangle$ or $|1\rangle$) to any of the excited states.

The projections on $\hat{e}_u$ and $\hat{e}_v$ can not be measured directly in the same way as that on $\hat{e}_w$. They must first be rotated onto the $\hat{e}_w$ axis by implementing dark state operations similar to those used for single qubit rotation. They can then be probed by the readout pulses. Each measurement collapses the original qubit state, so it must be re-created after each projection measurement. Figure 6.9 shows an example of the tomography for state ($|0\rangle - |1\rangle$), which is prepared from an initial state of $|0\rangle$. Figure 6.9a, b and c shows the absorption measurements of the projections on $\hat{e}_u$, $\hat{e}_v$ and $\hat{e}_w$ axes, respectively.

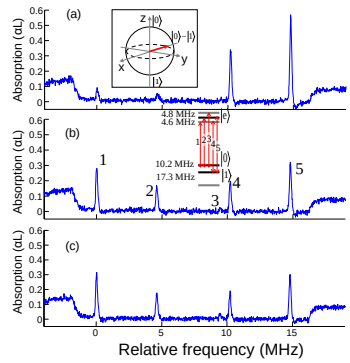

Figure 6.9. *Tomography of the state ($|0\rangle - |1\rangle$). (a), (b) and (c) shows the absorption measurement of the projection of the Bloch vector on $\hat{e}_u$, $\hat{e}_v$ and $\hat{e}_w$ axes, respectively. The number 1-5 refer to the five transitions shown in the energy diagram in (b).*

Fidelity

When all three projections are known, the quantum state experimentally created ($|\psi_{exp}\rangle$) can be reconstructed on the Bloch sphere. Fidelity is used as a measure of the extent to which the experimentally created state $|\psi_{exp}\rangle$ resembles the desired state $|\psi_{des}\rangle$, and is defined as

$$\begin{aligned} F &= |\langle\psi_{des}|\psi_{exp}\rangle|^2 \\ &= \langle\psi_{des}|\rho_{exp}|\psi_{des}\rangle, \end{aligned} \tag{6.6}$$

where ρ_{exp} denotes the density matrix constructed from the experimental state, and can be represented by Pauli matrices as [143]

$$\begin{aligned} \rho_{exp} &= 0.5[tr(\rho_{exp})I + tr(X\rho_{exp})X + tr(Y\rho_{exp})Y + tr(Z\rho_{exp})Z] \\ &= 0.5[tr(\rho_{exp})I + \mathrm{u}_{exp}X + \mathrm{v}_{exp}Y + \mathrm{w}_{exp}Z], \end{aligned} \tag{6.7}$$

where u_{exp}, v_{exp} and w_{exp} denote the measured projections of state ψ_{exp} on the $\hat{e}_u$, $\hat{e}_v$ and $\hat{e}_w$ axes, respectively. A fidelity of 90-96% was demonstrated for a single qubit rotation (Paper **I**). Details of the calculations are can be found elsewhere [99].

6.1.4 Qubit-qubit interaction scheme

A CNOT gate operation in this system can be realized through the permanent dipole-dipole interaction, as illustrated in Figure 6.10. A sequence of laser pulses with pulse area π interacts with the system. Pulse ① targets the $|0\rangle \rightarrow |e\rangle$ transition of Qubit1. Following this, the other three pulses (②, ③ and ④) implement a full NOT gate on Qubit2. When Qubit1 is initially in state $|1\rangle$ (Figure 6.10a), the dipole-dipole interaction is not initiated, so pulses ②, ③ and ④ are resonant with the transitions, and a NOT operation will be carried out on Qubit2. On the other hand, when Qubit1 is initially in state $|0\rangle$ (Figure 6.10b), it will be pumped to

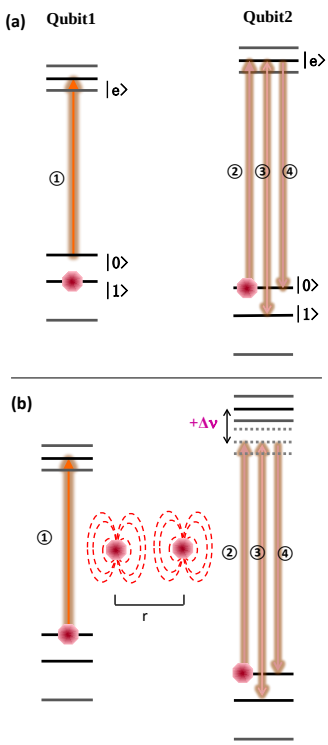

Figure 6.10. *Illustration of qubit-qubit interaction (e.g. CNOT gate). On condition of the state of Qubit1 ($|1\rangle$ or $|0\rangle$), a NOT operation will (or not) be implemented on the nearby Qubit2.*

state $|e\rangle$, which induces a frequency shift ($\Delta\nu$) of the Qubit2 transition line. If $\Delta\nu$ is large enough (e.g. much larger than the total energy separation of the excited states δe_{tot}, which is 9.4 MHz for Pr^{3+}), pulses ②, ③ and ④ are off resonant with Qubit2, and the implementation of the NOT operation is inhibited.

The interaction scheme described above requires that $\Delta\nu$ should be greater than a certain value (e.g. a few MHz for Pr ions), which means that the two qubits must be spatially close to each other, as $\Delta\nu \propto 1/r^3$ (Equation (3.2)). The consequence of this distance-dependent coupling strength and the randomness of the dopant ions in each qubit is that only those ions in one qubit that happen to be close to ions in the second qubit can control each other. The other ions in each qubit that don't have strong interactions must be spectrally removed in order to obtain an efficient qubit-qubit gate operation, which is the purpose of qubit distillation. This has been demonstrated experimentally by our group [49].

6.1.5 Scalability

In this random system, the average probability, P, of an ion in one qubit being sufficiently close to an ion in another qubit to control its state is often $\ll 1$ for weakly dopant concentrations. This means that the number of active ions in one ensemble qubit that interact strongly with one ion in each of the rest of the $m-1$ qubits scales as P^{m-1} in a m-qubit system. This exponential decrease in the number of ions in each qubit creates a problem in the qubit readout procedure, where the absorption of the ions is monitored, and limits the number of qubits which can be used in the ensemble qubit approach. Although the ion-ion distance can be more closer in a crystal which high dopant concentrations, the number density of the ions in one frequency interval, i.e. number density of qubit ions, remains the same due to the increasing inhomogeneous linewidth [134].

6.2 Single-ion qubit quantum computing

Single-ion qubit quantum computing is an approach to improve the scalability, where a qubit is represented by a single ion [134]. Simulations have shown that with a sufficient dopant concentration, for instance 0.2% for $Pr:Y_2SiO_5$, there is a high possibility of sequences of Pr ions (>50 ions) [144]. Each Pr ion on that sequence absorbs at a specific and unique optical frequency and represents one single qubit, and the distance between ions is sufficiently short for all ions to be able to control each other. This is illustrated in Figure 6.11.

6.2.1 Single-ion readout scheme

In the single-ion qubit quantum computing approach, a technique for reading out the quantum state of a single-ion qubit must be developed. Straightforward fluorescence measurements cannot be used for several reasons. Firstly, the excited state lifetimes of the transitions of the qubit ion that can discriminate the qubit states are longer than 10 µs, which provides too low an emission rate for a high SNR detection. Secondly, and more importantly, the excited qubit ions (Pr or Eu ions) have more than one ground state hyperfine level to which they can decay, and thus there is no transition that can be cycled until the number of emitted photons is sufficiently large to provide the state selective information.

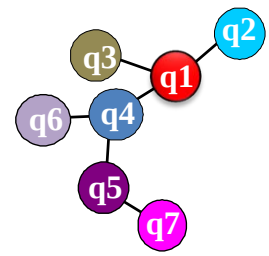

Figure 6.11. *At a sufficiently high dopant concentration, sequences of ions are highly probable, where each ion represents one qubit with a unique optical transition frequency (indicated by q1, q2, ... q7), and where all the ions can control each other via permanent dipole-dipole interactions (indicated by the solid lines connecting two ions).*

One proposal for reading out a single-ion qubit state is to co-dope the crystal with another type of ion (hereafter called a readout ion) and to use this ion as a sensor to probe the state of a nearby qubit. The dopant concentration of the readout ion must be so low that there is only one ion actively interacting with the driving laser, i.e. there is only one ion on resonance with the laser. The fluorescence signal of the readout ion, either OFF or ON, depends on whether the single qubit ion is excited or not, which depends in turn on whether its initial state is $|0\rangle$ or $|1\rangle$.

Figure 6.12 shows the readout procedure. Two lasers interact with the ions, one with the qubit ion and one with the readout ion. The qubit laser sends out a π pulse on the $|0\rangle \rightarrow |e\rangle$ transition. Following this pulse, the readout pulse is turned on and continuously excites the readout ion for certain time of period. If the qubit ion is in state $|1\rangle$ Figure 6.12a, the qubit laser is not on resonance with the ion, so it will not pump the qubit ion to state $|e\rangle$. There is no interaction between the qubit and readout ion in this case. The readout ion emits fluorescence photons (ON) upon the excitation by the readout laser. If, on the other hand, the Pr ion is initially in state $|0\rangle$ Figure 6.12b, it will be excited by the qubit laser pulse. This state change of the qubit ion induces a frequency shift ($\Delta\nu$) of the nearby readout ion transition line. If the shift is greater than the homogeneous linewidth, the readout ion will be off resonance with the readout laser, and will not be excited, so there will be no fluorescence (OFF).

For the other qubits, which are not directly coupled to the readout ion, their state can be transferred consecutively using CNOT gates between two nearby ions until the state reaches the qubit ion that is directly coupled to the readout ion. Then its state can be read out in the way described above.

In the following sections, the experimental considerations for the single-ion qubit quantum computing will be discussed.

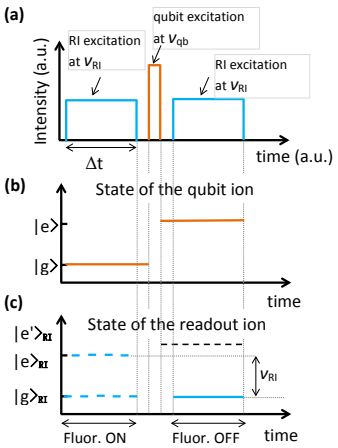

Figure 6.13. *Principle of identifying the closest qubit ions which can control the readout ion. (a) shows the pulse sequence can be used for this purpose. (b) shows the qubit state in response to the pulse sequence. (c) shows the RI state, where the excited state level is shifted from $|e\rangle_{RI}$ to $|e'\rangle_{RI}$ when the strongly interacting qubit ion being excited. If this happens, the readout ion can not be excited by the initial excitation laser at frequency of ν_{RI}, so there is no fluorescence signal.*

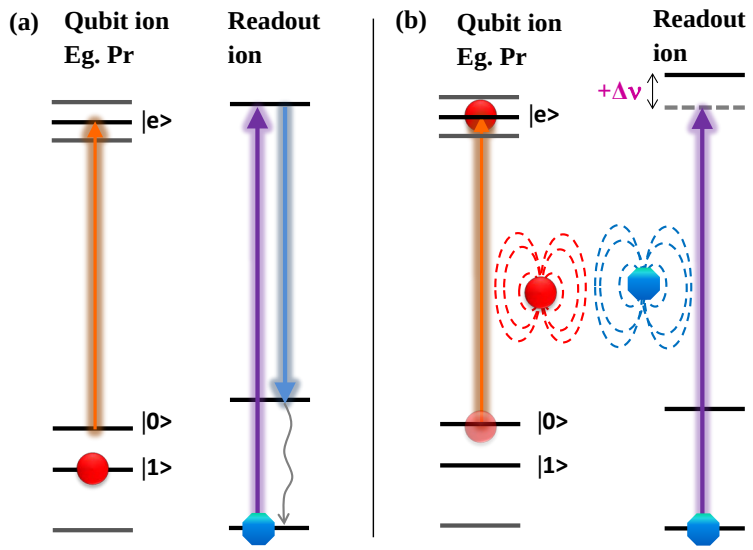

Figure 6.12. *Principle of reading out a single-ion qubit state by detecting the fluorescence of the readout ion. The scheme works for any qubit ion that has different permanent dipole moments in the ground and excited states.*

6.2.2 Searching the qubit chain around the readout ion

The strongly interacting qubit chain (e.g. the chain shown in Figure 6.11) can be experimentally identified through monitoring the fluorescence of the single readout ion. The pulse sequence shown in Figure 6.13a can be used for this purpose. The procedure is as follows.

(i) The readout ion transition at the optical frequency of ν_{RI} is cycled for a time period of $\triangle t$. During this time the readout ion emits fluorescence photons. The state of the readout ion in response to the pulses is illustrated in Figure 6.13c.

(ii) Some of the qubit ions at a random position ν_{qb} within the inhomogeneous absorption line with a certain frequency span (e.g. a few MHz for Pr ions) are excited. The qubit state in response to the pulses is illustrated in Figure 6.13b.

(iii) While the qubit ions are still in their excited states, the readout ion excitation laser is turned on again, for the same time period as the first excitation pulse. The fluorescence signal is then monitored. The signal may be the same as in step (i),

which means that the excited qubit ions does not affect the readout ion; or there maybe no signal, which indicates that a nearby strongly-interacting qubit ion has been excited.

(iv) The qubit excitation frequency of ν_{qb} is then scanned across the inhomogeneous line, and all the frequency channels of the qubit ions that can control the readout ion will be mapped out.

(v) Similar steps (i-iv) can be used to look for a second qubit, which can control the first qubit identified above.

From the above it is clear that the fluorescence collection time, $\triangle t$, should be smaller than the excited state lifetime of the qubit, as the transition frequency of the readout ion is only shifted when the qubit is in its excited states.

6.2.3 Requirements for the readout ion

The readout scheme discussed above requires that the readout ion has the following characteristics.

(i) A short excited state lifetime, in order to obtain a large difference in the number of photons emitted per unit time between the case when the qubit is in the ground state and when it is in the excited state.

(ii) A narrow homogeneous absorption linewidth such that the permanent dipole-dipole interaction with a nearby qubit shifts the readout ion resonance frequency by several homogeneous linewidths.

(iii) A large change in dipole moment between the ground and excited states again such that the shift due to the permanent dipole-dipole interaction is sufficiently large.

(iv) No fluorescence quenching mechanisms such as a long-lived trapping state or energy transfer from the readout ion to the qubit ion.

(v) Experimental detection of the fluorescence emitted from a single Ce ion.

6.2.4 Fidelity analysis of the single ion readout scheme

The probability of obtaining the correct qubit state (called the readout fidelity) from the fluorescence light emitted by the single readout ion in the scheme described in Figure 6.12 is determined by the contrast in the number of collected photons between when

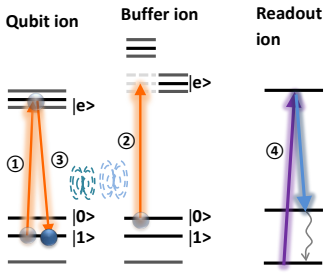

Figure 6.14. *Illustration of the single ion readout scheme including one buffer ion taking the qubit in state $|1\rangle$ as an example. Pulse ① to ④ are implemented one after another. When the qubit ion is in state $|1\rangle$, it will be excited by pulse ①, and as a consequence of the dipole-dipole interaction the energy level of the buffer ion is shifted. Thus, the buffer ion initial state is not affected by pulse ② (still in ground state). The excited qubit ion is then de-excited by pulse ③ to minimizing the possibility of state corruption. Then the readout ion is excited by pulse ④ and the fluorescence photons are collected. On the contrary if the qubit is in state $|0\rangle$, the buffer ion will be excited, and the excitation on readout ion is blocked as a result of the dipole-dipole interaction between the buffer and readout ion.*

the readout ion fluoresces (when the qubit ion is in state $|1\rangle$) and not fluoresces (when the qubit is in state $|0\rangle$). The number of photons is determined by the emission rate of the readout ion and the accumulation time of the photons, which is presumably limited by the excited state lifetime of the qubit ion.

The readout ion under investigation is the Ce ion in an Y_2SiO_5 crystal, which has an excited state lifetime of about 40 ns (more information are presented in Chapter 7). The qubit ion candidate under concern is the Eu ions, whose excited state lifetime is 1.9 ms (T_1^{qb}). A simulation presented in Paper **IV** showed that the optimal probability of detecting the correct qubit state was approximately 87%, when the signal was accumulated within a time period of one third of T_1^{qb} assuming a reasonable photon collection efficiency of 1%.

Improved fidelity by introducing the buffer ions

The readout fidelity can be improved if the accumulation time of the photons can be effectively extended, which is possible if another ion, who has strong permanent dipole-dipole interactions with both the qubit and readout ion, is used as a buffer ion. The buffer ion can be any ion with a long lifetime in the excited state. Here the same species of ion as the qubit ion is considered. The qubit state information is firstly mapped onto the buffer ion, then its state is read out by the readout ion. By repeating these two procedures, the fluorescence photons can be accumulated in a time period which is not limited by the excited state lifetime of the qubit ion.

In this scheme the buffer ion is initialized in state $|0\rangle$, then pulse ① and pulse ② with pulse area of π, illustrated in Figure 6.14, are implemented in a way that a correlation between the qubit and buffer ion is established: if the qubit ion is in state $|0\rangle$ the buffer ion will be in $|e\rangle$, and if the qubit in $|1\rangle$ the buffer ion remains in $|0\rangle$. Pulse ② is followed by pulse ③, which de-excites the qubit ion to its original ground state (if the qubit ion has been excited by pulse ①) to minimize the possibility of qubit-state corruption caused by the decay of the excited state. Then the readout laser pulses (pulse ④) is implemented, however, the readout ion can only be excited if the buffer ion is in the ground state. The fluorescence signal is then collected within $0.33T_1^{bf}$ (T_1^{bf} is the lifetime of the excited state of the buffer ion). After this signal is recorded the buffer ion is re-initialized and pulses ① to ④ are implemented again, and the fluorescence photons are accumulated for all repetition steps. As the qubit ion is only in the excited state for the time period in which pulse ② is implemented (in the microsecond timescale), the probability of the qubit state being corrupted is negligible. The simulated readout fidelity of this scheme can reach 99% when the above mentioned readout

procedures are implemented consecutively by 20 times. This work was presented in Paper **IV**.

In above scheme a number of buffer ions can be concatenated, for example, in a two-buffer-ion scheme, the state of the qubit ion is at first transferred to the first buffer ion, which is then read out by a readout system consisting of the second buffer ion and the readout ion in the same way as described above. By repeating the transfer and the readout processes by 5 times, a 99.75% fidelity was reached in the simulation, which was presented in Paper **IV**.

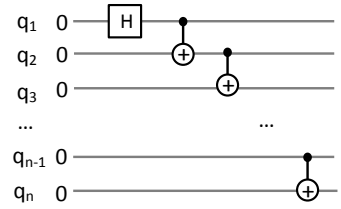

Figure 6.15. *Illustration of the procedure of creating a n-qubit GHZ state in a quantum circuit.*

Fidelity of creating and characterizing a multiple-qubit GHZ state

Greenberger-Horne-Zeilinger (GHZ) state is a type of multiple-qubit entangled state [145]. For example, a 3-qubit GHZ state is

$$|\mathrm{GHZ}\rangle_3 = \frac{1}{\sqrt{2}}(|000\rangle + |111\rangle). \tag{6.8}$$

The fidelity of creating and reading out a multiple-qubit GHZ state has been discussed in Paper **IV**. The main ideal behind this calculation is briefly described here. The quantum circuit shown Figure 6.15 describes the procedures of creating a n-qubit GHZ state, where H represents a Hadamard gate, and $\oplus$ together with the dots and the line denote a controlled-not gate [143].

The fidelity of a n-qubit GHZ state was simply estimated as:

$$F_{GHZ} = \eta_{int}^{n} \cdot \eta_H \cdot \eta_{CNOT}^{n-1}, \tag{6.9}$$

where η_{int}, η_H and η_{CNOT} denote the fidelity of qubit initialization, Hadamard gate and CNOT gate, respectively. Fidelity of creating a 10-qubit GHZ state larger than 94% was achieved based on an estimation of best experimentally achievable parameters.

The characterization of a n-qubit GHZ state is essentially a task of reading out the projections of each qubit-state on $\hat{e}_u$, $\hat{e}_v$ and $\hat{e}_w$ axes. One readout sequence includes a consecutive measurement of one of the three projections on each qubit, as done for a two-qubit entangled state [146, 147]. Then the GHZ state must be recreated and a second readout sequence is implemented to read out different projections in the qubits. Thus, a full characterization of a n-qubit GHZ state takes 3^n times of recreation and readout sequences. The projection on $\hat{e}_w$ is a straightforward measurement as it is the population difference between the ground and excited states. However, for the projection measurements on $\hat{e}_u$ and $\hat{e}_v$, tomography processes must be implemented on the qubits, as described in Section 6.1.3 before they can be read out. As an example, considering the projection measurement on $\hat{e}_u$ or $\hat{e}_v$ axes, and assuming that each qubit can be directly read out by

the two-buffer-ion readout system, the fidelity of such a recreating and readout sequence was calculated as:

$$F_{GHZ}^{drd} = F_{GHZ} \cdot \eta_{tm}^{n} \cdot \eta_{rd}^{n}, \tag{6.10}$$

where η_{tm} and η_{rd} denote the fidelity of the quantum tomography and the readout process. The fidelity of a 10-qubit GHZ state in the case of a direct readout scheme was calculated to above 92% using Equation (6.10) based on the fidelities of the initialization and gate operations obtained in a simulation.

In the case where only one qubit is directly coupled to the two-buffer-ion readout system, swap operations have to be implemented successively between the neighbouring qubits until the states of the indirectly-coupled qubits reach the nearest-neighbour-qubit of the first buffer ion in the readout system. The fidelity of creating and characterizing such a GHZ state was done as:

$$F_{GHZ}^{idrd} = F_{GHZ} \cdot \eta_{tm}^{n} \cdot \eta_{rd}^{n} \cdot \prod_{i=1}^{n-1} \eta_{swap}^{i}, \tag{6.11}$$

where η_{swap} denotes the fidelity of a swap operation, which is the cube of the fidelity for a CNOT gate. The fidelity of a 10-qubit GHZ state in this scenario is ∼43%.

6.2.5 Impact of the energy transfer on the single-ion readout scheme

In the single-ion readout scheme, the buffer ion (Pr or Eu ion) and the readout ion (Ce ion) should be spatially close so that the frequency shift induced by the permanent dipole-dipole interaction between them is large enough to block the excitation of Ce ions by the initial laser pulse, and the fluorescence signal is off as a consequence. However, they can not be too close as an energy transfer process from the Ce ion to the Pr or Eu ion may take place, which will quench the Ce fluorescence, and corrupt the qubit-state information encoded on the buffer ion resulting from the promotion to an excited state. Resonant energy transfer process can happen as the Ce (readout ion) emission spectrum is located in the range 380-540 nm, which is shown in Chapter 8, covering the transitions from $^3H_4$ to $^3P_0$, $^3P_1$, $^3P_2$ and $^1I_6$ of Pr^{3+} ions and the transitions from $^7F_0$ to $^5D_0$, $^5D_1$, $^5D_2$ and $^5D_3$ of Eu^{3+} ions, see the energy diagram presented in Figure 3.2. Furthermore, the energy transfer from Ce^{3+} to Pr^{3+} ions in an Y_2SiO_5 crystal has been recently reported [148] and also shown in Paper **V**.

However, the permanent dipole-dipole interaction and the energy transfer process scales differently with the ion-ion distance: the former is proportional to $1/r^3$ and the latter to $1/r^6$. Thus, there could be a region of the ion-ion distance where the energy

transfer dies out but the permanent dipole-dipole interaction is sufficiently strong for the readout scheme. The identification of this range and the influence of the energy transfer process on the single-ion readout scheme were analyzed in Paper **V**. The methods and important results presented in the article are briefly discussed below.

The energy transfer rate, k_{ET}, described in Section 2.2.2 between the Ce^{3+} to Pr^{3+} and Ce^{3+} to Eu^{3+} ions were calculated from the transfer microparamter, C, as follows:

$$k_{ET} = \frac{C}{r^6}, \tag{6.12}$$

where r denotes the distance between the donor (Ce^{3+}) and acceptor (Pr^{3+} or Eu^{3+}), and C is determined by the integrated spectra overlap between the emission cross section of Ce ions ($\sigma_{EM,D}$) and the absorption cross section of Pr or Eu ions ($\sigma_{Abs,A}$). Precisely, C is as follows [149]:

$$C = \frac{3c}{8\pi^4 n^2} \int \sigma_{EM,D}(\lambda)\sigma_{Abs,A}(\lambda)\ d\lambda, \tag{6.13}$$

where c is the speed of light in vacuum and n is the refractive index of the crystal. The emission and absorption cross section were obtained from the experimental spectra of the ions making use of the Fluchtbauer-Ladenburg spectroscopic method [150].

The energy transfer efficiencies of Ce^{3+} to Pr^{3+} and Ce^{3+} to Eu^{3+} ions as a function of the ion-ion distance were calculated based on the transfer rate mentioned above using Equation (2.15) described in Chapter 2, where in this case T_1 is the lifetime of Ce ions when the energy transfer process is absent. The results showed that to keep the energy transfer efficiency sufficiently low (e.g. $< 5 \times 10^{-4}$) and the frequency shift sufficiently large (e.g. > 20 MHz), the ion-ion distance should be larger than 20 Å but smaller than 90 Å for a Ce and a Eu ion, and larger than 30 Å smaller than 130 Å for the Ce-Pr pair. The probabilities of finding the ions in such a range in a crystal with dopant concentration of 2% was estimated to be about 4% in a simulation, which is doable.

6.3 Status and discussion

- Our group has been mainly working on Pr^{3+} ions in Y_2SiO_5 for quantum computing. However, Eu^{3+} ions doped in Y_2SiO_5 have more than an order of magnitude longer excited state coherence time (∼2.6 ms in site 1 [69]), and the qubit coherence time is expected to be 300 times higher [151]. Eu^{3+} ions have better properties except the fact that the

transition oscillator strength is about one order of magnitude lower (see Table 3.4). However, this weakness could be partly overcome by tight focusing.

- In the single-ion qubit quantum computing approach, the work carried out by us so far has been concentrated on developing the capability to detect a single readout ion, which is an important step towards single-ion quantum computing. Other issues related to this approach must be investigated further, e.g. experimental initialization of the qubit state of a single ion. Furthermore, since the single qubit ion is not physically isolated in this system, but surrounded by an ensemble of ions with similar optical frequencies, studies must be carried out to determine the extent to which the off-resonant excitation of these ions could destroy the single-ion readout scheme.

- If implemented with the same pulses as the ensemble qubit ions, single-ion qubit operations should, in principle, have a better fidelity, as the dephasing caused by the inhomogeneous broadening is no longer a concern. However, the question of whether the high-fidelity single qubit operations can be realized must be verified experimentally, bearing in mind the practical difficulties of single-ion detection.

Chapter 7

Investigations of Ce^{3+} as a readout ion

It was shown in Chapter 6 that single-ion quantum computing is a promising approach to achieve better scalability. In this approach the single-ion readout concept is proposed to probe the state of the neighbouring single-ion qubit. For this approach to be successful, the readout ion must have the spectroscopic properties described in Section 6.2.3. The experimental investigation of properties (ii)-(iv) will be presented in this chapter, and the study is presented in detail in Paper **III**. The candidate for the readout ion is Ce^{3+} [152]. Its lifetime in an Y_2SiO_5 crystal is known to be about 40 ns [153–155], which is three orders of magnitude shorter than that of the qubit ion candidates: i.e. ∼164 µs for Pr^{3+} and ∼2 ms for Eu. Section 7.1 presents the general properties of Ce ions relevant for this research. Measurement of the inhomogeneous and homogeneous linewidths of the 4f-5d ZPL are described in Section 7.2. Measurements of the difference in permanent dipole moment, $\triangle\mu_{Ce}$, between the ground and excited states of the Ce ion are presented in Section 7.3. Additional interesting measurements related to the topics presented in this chapter are described in Section 7.4.

7.1 Properties of the Ce ion

Cerium is the second member of the rare earths, with an atomic number of 58. The delocalization of the electrons in the outer 5d and 6s subshells results in a Ce^{3+} ion. Cerium was discovered in 1803, independently, by the chemists J. J. Berzelius and W. Hisinger at an ore field in Sweden, and by M. H. Klaproth in Germany [156].

There are four natural cerium isotopes, ^{140}Ce, ^{142}Ce, ^{138}Ce, and ^{136}Ce, with fractional abundances of 88.5%, 11%, 0.3% and

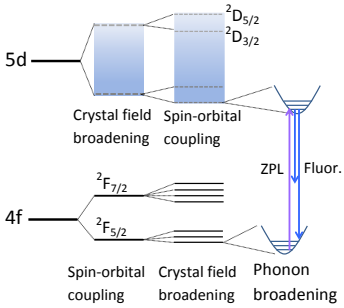

Figure 7.1. *Schematic energy structure of Ce^{3+} in a crystal. The broadening contributions are illustrated in descending order.*

0.2%, respectively [157]. All the Ce isotopes have zero nuclear spin, so they have no hyperfine levels. The ionic radius of Ce^{3+} is given in the table in Figure 3.3.

7.1.1 Energy structure of Ce^{3+} in a crystal

The 4f subshell of Ce^{3+} is well shielded from crystal field disturbance, as is the case in all the RE ions. The ground state splits into two fine structure levels due to the coupling between the electron spin (S = 1/2) and its orbital angular moment (L = 3). However, the 5d levels are more exposed to the crystal field, so the magnitude of the crystal field splitting is much greater than the fine structure splitting. On top of this splitting, the interaction with the vibrational motion of the crystal also broadens the lines. These can be described as a harmonic potential where the different phonon modes are described by discrete levels in the potential, similar to a harmonic oscillator, as shown in the schematic energy level structure in Figure 7.1. However, the configurational coordinates of the two harmonic potentials in the ground and excited states are displaced relative to each other.

The line of interest in this work is the ZPL between the two lowest Kramers' doublets in the ground and excited state. This is the longest excitation wavelength for this 4f→5d transition, as indicated in Figure 7.1. Because of the smaller wavefunction overlap between the zero-phonon levels, the transition probability of the ZPL is lower than that of phonon-assisted transitions. An excited Ce ion can decay to any of the phonon levels in the harmonic potentials in the 4f subshell, which gives rise to a continuous emission spectrum.

7.2 Linewidth measurements of Ce^{3+} in an Y_2SiO_5 crystal

The excitation and emission spectra of Ce^{3+} in an Y_2SiO_5 crystal have been investigated previously using gamma-rays, X-rays or xenon lamps as the excitation source [153, 158, 159]. The narrow ZPL was not demonstrated in these studies due to the low wavelength resolution. In the present work, the location and linewidth of the inhomogeneous ZPL, as well as the homogeneous linewidth, were measured using an ECDL as the excitation source. In these measurements the crystal was cooled to about 2 K in a helium bath cryostat.

7.2.1 Inhomogeneous linewidth

The inhomogeneous absorption ZPL of the Ce^{3+} ions was measured in an Y_2SiO_5 crystal (grown in Czochralski method) with a

Ce dopant concentration of 0.088% (nominal value) relative to the Y ions. The line center is at 370.83 nm, and the FWHM is about 50 GHz, as shown in Figure 7.2.

Line shape

The line shape of the ZPL provides information on the broadening mechanism and also reveals, to some extent, the crystalline environment of the Ce^{3+} ions. The data in Figure 7.2 were fitted with various curves and combinations of curves. Fitting a Gaussian curve to the data did not provide a good fit at the edges. In an attempt to obtain a better fit, a Gaussian and a Lorentzian function were combined, which is replotted in Figure 7.3. This combination might be explained by the inhomogeneous broadening model developed based on the point defects in the crystal [58, 59]. A multiple Gaussian functions consisting of three curves (illustrated in Figure 7.4) was also fitted to the data. Multiple Gaussian functions could result from the contributions of the satellite lines, which are not completely separated from the main line. However it is not known to us which of the two possibilities is more like.

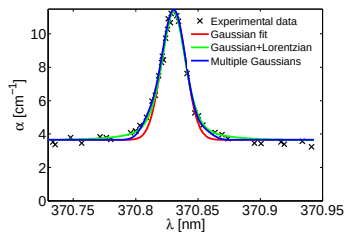

Figure 7.2. *ZPL of Ce^{3+} in an Y_2SiO_5 crystal. The symbols represent the experimental data, and the solid lines show different curves used to fit the data.*

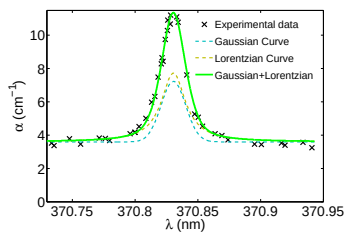

Figure 7.3. *Fitting using the sum of Gaussian and a Lorentzian curve.*

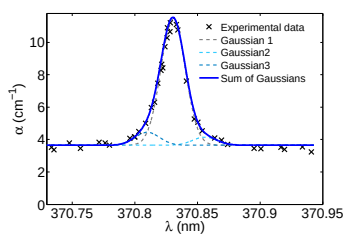

Figure 7.4. *Fitting with the sum of three Gaussian curves.*

Background absorption from Ce ions in site 2

The observed ZPL shown in Figure 7.2 is superimposed on a background with a absorption coefficient of $\sim$3.6 cm^{-1}. This probably arises from the Ce ions occupying site 2 (denoted Ce2). The two sites of Ce^{3+} in Y_2SiO_5 have been investigated previously, by analysing the excitation and fluorescence spectra [153, 158]. Existence of Ce2 will be verified by the fluorescence spectrum under an offline excitation e.g. at 371.5 nm, which will be discussed in Section 8.1.1.

Frequency-integrated absorption cross section

The frequency-integrated absorption cross section (σ_0, expressed in units of m^2rad/s) [160] is a useful parameter in the calculations presented below. It can be expressed as:

$$\sigma_0 = \frac{\int \alpha(\omega)\, d\omega}{D} \simeq 1.78 \times 10^{-11}, \tag{7.1}$$

where $\alpha(\omega)$ is represented by the Gaussian fit curve in Figure 7.2, as a function of the angular frequency (ω), and D represents the number density of Ce ions in site 1 (denoted Ce1). We assume that the probability of the Ce ions occupying site 1 is the same as that of the Pr ions, i.e. about 87% [87] since their ionic radii only differ by about 1.7%.

The oscillator strength (f) of the ZPL transition can be calculated using σ_0 as follows [50]

$$f = \frac{2m_e c\epsilon_0}{\pi e^2} \cdot \frac{9n}{(n^2+2)^2} \cdot \sigma_0 \simeq 6.2 \times 10^{-7}, \tag{7.2}$$

where m_e, c, ϵ_0, e and n denote the mass of the electron, the speed of light in vacuum, vacuum permittivity, the electron charge and the refractive index of the crystal at the Ce transition frequency, respectively. The factor $\frac{9}{(n^2+2)^2}$ is the local field correction [76].

The decay rate (A_{21}) from the upper to the lower state of the ZPL transition was also calculated from σ_0:

$$A_{21} = \frac{4\sigma_0}{\lambda_{21}^2} \simeq 519\ s^{-1}. \tag{7.3}$$

It is worth noting that A_{21} is five orders of magnitude less than $1/T_1$. This is because there are more decay channels from the excited state to a lower ground state, and the ground state of the ZPL is only one of them, as shown in Figure 7.1.

7.2.2 Homogeneous linewidth

The homogeneous linewidth was measured with the spectral-hole burning technique described in Section 3.4.1, but with intensity modulation on both the pump (modulation frequency 302 Hz) and probe beams (modulation frequency 362 Hz) to improve the SNR, as the top-hat pump beam intensity (6.5×10^4 W/m^2) for Ce1 ions is ∼0.5% of the estimated saturation intensity (assuming the homogeneous linewidth is lifetime limited). The experiment is presented in detail in Paper **III**.

A schematic of the experimental set-up is shown in Figure 7.5, where both the pump and probe beams were generated from the same ECDL via a beam splitter (70:30), and then focused onto the Ce^{3+}:Y_2SiO_5 crystal submerged in a helium bath cryostat with the common lens. The focal diameter of the probe beam was about ∼ 85 µm. As saturation is a nonlinear process, the transmitted probe beam not only has the modulation at frequency of 362 Hz, but two other modulations at the sum (664 Hz) and difference frequencies (60 Hz). The signal strength at 664 Hz was extracted from the Fourier transform of the transmitted power of the probe beam and recorded as a function of the detuning frequency between the pump and probe beams, △f.

The experimental data are shown in Figure 7.6, where the vertical axis shows the sum frequency signal normalized to the square of the input probe beam power, to compensate for the change in laser power between the data points. The signal at 664 Hz was 16 times higher than the noise floor when △f is zero, but only 1.3% of the signal strength at 362 Hz. The FWHM of the spectral hole

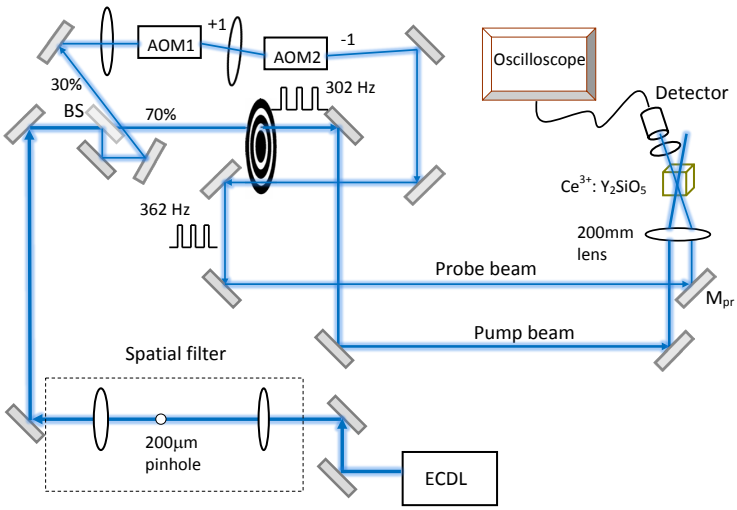

Figure 7.5. *Schematic of the experimental set-up for the homogeneous linewidth measurement of the Ce 4f-5d ZPL. Two AOMs were used in the probe beam line. The +1 order deflected beam from AOM1 was directed to AOM2, then the -1 order deflected beam was directed to the crystal. In this way the probe beam frequency could be tuned within a range of ±50 MHz relative to the pump beam frequency by adjusting the radio frequency to AOM2. Movement of the probe beam at different detuning frequencies was compensated for by slightly adjusting mirror M_{pr} by maximizing the probe beam transmission. The probe beam was propagated at an angle of ∼ 3 degrees relative to the pump beam in order to separate the two beams for detection.*

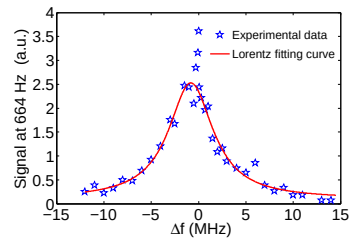

Figure 7.6. *Homogeneous linewidth of Ce ions in an Y_2SiO_5 crystal measured using saturation spectroscopy. Symbols indicate the measured data points. The solid curve is a Lorentzian fit to the points excluding the central four, which we believe are due to population trapping.*

shown in Figure 7.6 is about 5.8 MHz, which is a convolution of the laser line (Lorentzian) and the homogeneous line of the transition (Lorentzian) for both the pump and probe steps. However the contribution from the laser linewidth should be negligible, as only fast laser frequency fluctuations within the timescale of the excited state lifetime (∼ 40 ns) would affect the measurement, and the typical linewidth of such an ECDL is 300 kHz over 100 µs. Thus, the homogeneous linewidth measured in this study has an upper limit of 2.9 MHz.

The 40 ns (T_1) lifetime reported in the literature [153–155] places a lower limit on the linewidth of ∼ 4 MHz. The reason why a linewidth was measured below 4 MHz may be that the signal at positive detuning frequencies was not properly maximized by adjusting the spatial overlap between the pump and probe beams. The fact that the centre of the Lorentzian fitting curve is not at zero detuning, but slightly shifted to the left, indicates that this is a possible explanation. The measurements indicate that the homogeneous linewidth is essentially limited by the lifetime of

the excited state, which implies that the coherence time takes its optimal value of 80 ns.

Saturation intensity

The saturation intensity of the ZPL was calculated from the value of coherence time (T_2) determined above, together with the expression:

$$I_s = \frac{\hbar\omega}{2T_1\sigma(\omega)} \simeq 1.4 \times 10^7 \ W/m^2, \tag{7.4}$$

where ω is the transition frequency of the ZPL, and $\sigma(\omega)$ the absorption cross section of the Ce1 ions 'seen' by the laser at a frequency of ω. $\sigma(\omega)$ was calculated from the frequency-integrated absorption cross section (σ_0) described in Equation (7.1) [160]:

$$\begin{aligned}\sigma(\omega) &= \sigma_0 \cdot g_h(\omega) \\ &= \sigma_0 \cdot \frac{T_2}{\pi \cdot (1 + (\omega - \omega_0)T_2^2)} \simeq 4.5 \times 10^{-19} \ m^2,\end{aligned} \tag{7.5}$$

where $g_h(\omega)$ (expressed in $\mathrm{rad}^{-1}{\cdot}\mathrm{s}^1$) is the homogeneous line shape function centred at ω_0 with the normalization of $\int g_h(\omega)\, d\omega = 1$. The above value is considered to reflect the exactly on resonance case, where $\omega_0 = \omega$.

Narrow structure at the centre

The origin of the increased interaction between the beams within a narrow range ($\sim$ 400 kHz) around the line centre shown in Figure 7.6 was not investigated, but narrow resonances of this type can occur if the upper state can also decay to a third level which relaxes slowly (compared with the relaxation from the excited state) to the ground state (see e.g. [161, 162]). The linewidth of the resonance is then determined by the decay rate of this third level. In the present experiment, the third level could be one of the lowest Kramer's doublet in the $^2F_{5/2}$ (4f) ground state (see e.g. [22]).

Making use of the saturation intensity in Equation (7.4) and the Beer-Lambert law, the signal at the sum frequency (664 Hz) was estimated to be about 0.4% of the signal at 362 Hz at zero detuning frequency, based on the excitation parameters. However, a value of 0.8% was observed in the experiment, despite the narrow structure. The existence of a third level may gives rise not only to the narrow structure mentioned above, but also to a higher saturation effect due to the trapping of ions in this level.

7.3 Ce-Pr ion-ion interaction

Ce^{3+} and Pr^{3+} ions doped in an Y_2SiO_5 crystal have different permanent electric dipole moments (this difference is denoted $\Delta\mu_{Ce}$

and $\Delta\mu_{Pr}$, respectively) in their ground and excited states, as they are located in non-centrosymmetric sites. The precise value of $\Delta\mu_{Ce}$ is not known, but could be determined, for example, by measuring the Stark shift caused by the interaction between the ions and an external electric field [91]. In the present work an Y_2SiO_5 crystal co-doped with Ce^{3+} and Pr^{3+} at concentrations of 0.027% (Pr) and 0.012% (Ce) (grown at Shanghai Institute of Ceramics in China) was used in a two-pulse photon echo experiment (described in Section 3.4.2) on Pr ions. The Ce ions were excited during the dephasing period of the Pr ions, and a reduction in the echo intensity was observed [72]. This work is presented in detail in Paper **III**.

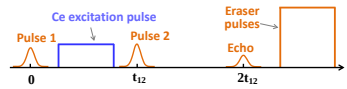

Figure 7.7. *Pulses sequence for the Ce-Pr interaction measurement.*

The echo reduction is caused by the fact that a subgroup of Pr ions experiences a frequency shift (see Equation (3.2)) induced by the excitation of nearby Ce ions, due to the permanent dipole-dipole interactions between them. Since the shift arises from the change in the permanent dipole moment, and not the transition dipole interactions, the frequency shifts are the same, regardless of which of the two ions is excited. When this happens the phases of the Pr superposition states evolve at a different rate in the dephasing period from that in the rephasing period, which results in only a fraction of the Bloch vectors shown in Figure 3.7d converging. Thus, the Ce-Pr ion-ion interaction introduces an additional dephasing channel to the excited Pr ions, which broadens the homogeneous linewidth of the Pr ions. $\Delta\mu_{Ce}$ can then be calculated from this extra broadening using the model presented by F. R. Graf et.al. [78].

7.3.1 Photon echo experiments

The pulse sequence used in the experiment is shown in Figure 7.7. Two weak Gaussian pulses, both with powers of ∼0.5 mW and 0.15 µs duration, were created with an AOM from the frequency-stabilized dye laser described in Section 4.1.2, and used to excite the Pr $^3H_4 \rightarrow {}^1D_2$ transition at ∼606 nm. The excitation pulse for the Ce ions (excitation power of ∼0.5 mW) was created by another AOM from the ECDL. After the echo pulse, several frequency scanning pulses at 606 nm (referred to as eraser pulses) were applied for the purpose of shuffling the Pr ions between the hyperfine states to prevent the spectral hole burning that would otherwise be created by the two Gaussian pulses (Pulse 1 and Pulse 2) over time.

The echo intensity from Pr ions was recorded as a function of the pulse separation time (t_{12}) in two situations: Ce ions being excited and not being excited (the Ce laser was blocked during this period). Ce excitation was implemented at either an 'online' wavelength (370.83 nm) or an 'offline' wavelength (371.54 nm). Online and offline mean that the excitation laser frequency is on

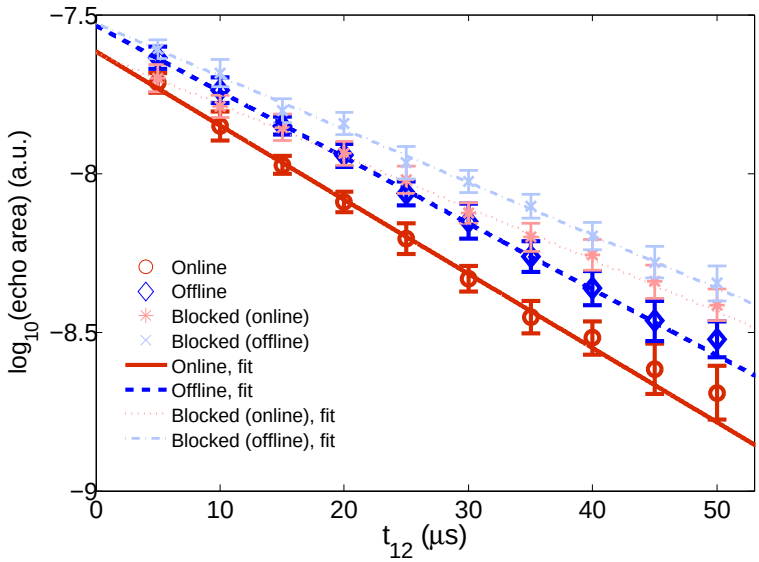

Figure 7.8. *Decay curve of the echo from the Pr ions in the Pr:Ce:Y_2SiO_5 crystal. Details are given in the text.*

or off the ZPL of Ce1 ions. So four series of data were recorded in total, as shown in Figure 7.8. Each point is an average value of $\sim$ 30 shots, and the error bars show the standard deviation. The circles represent the echo signals when Ce ions were excited online. Each online data point was followed by a complimentary offline data point (recorded with the Ce excitation laser blocked). After the data points had been recorded at each value of t_{12}, the Ce laser was tuned to the offline wavelength, and similar sets of data were recorded [shown by the diamonds (Ce laser offline) and crosses (Ce laser blocked)]. The two blocked cases are equivalent, but show an offset in the echo signal, possibly caused by laser power drift. However, the slopes are the same within the margin of error. The lines are logarithmic fits of each set of data.

Based on the dependence of the echo intensity (I_{echo}) on the pulse separation time (t_{12}), see Equation (3.5), the coherence time (T_2) of Pr ions of each measurement was calculated from the fitting lines with a 70% confidence interval, and from this the homogeneous linewidth (Γ_{hom}) was calculated. The results are given in Table 7.1.

As can be seen in Table 7.1, the homogeneous linewidth broadening caused by the Ce online excitation is 1.3 $\pm$ 0.14 kHz, while for Ce offline excitation the broadening is $\sim$ 0.7 kHz ($\pm$0.11 kHz). The difference between these two values is the broadening contri-

Measured values (Pr)	Ce Online		Ce Offline	
	Laser on	Laser off	Laser on	Laser off
T_2 (μs)	74±2	107±3	83±1	104±3
Γ_{hom} (kHz)	4.3±0.1	3.0±0.1	3.83±0.05	3.1±0.1

Table 7.1: *Measured homogeneous linewidths of the $^3H_4 \rightarrow ^1 D_2$ transition of Pr ions with Ce excitation laser at the online wavelength, and offline wavelength with the Ce laser turned on and off.*

bution from the Ce1 ions alone, which is ∼0.6 (±0.18) kHz (Γ_{br}). This value was used to calculate $\Delta\mu_{Ce}$ as described below.

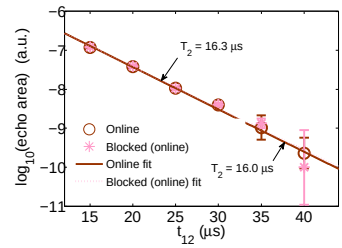

Figure 7.9. *Echo decay curve on the Pr ions in an Y_2SiO_5 crystal.*

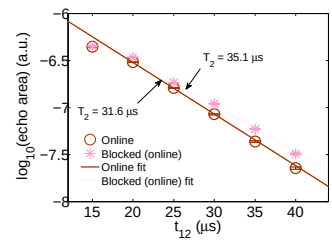

Figure 7.10. *Echo decay curve from the Pr:Ce:Y_2SiO_5 crystal.*

7.3.2 Other mechanisms than the frequency shift?

The reduction in the echo intensity could conceivably be caused by mechanisms other than a frequency shift caused by the permanent dipole-dipole interaction. The Pr ions may directly absorb photons from the Ce excitation laser, leading to processes then shorten the coherence time, which would cause a decrease in the echo intensity, although this is unlikely according to a previous work [163]. The energy may also be transferred from the excited Ce ions to the Pr ions in the photon echo process, causing the Pr ions to be excited to a higher level, which could also cause a reduction in the echo. Measurements performed to investigate these possibilities are described below.

Direct photon absorption

To establish whether direct photon absorption was taking place, the same experiment as that described above was carried out on an Y_2SiO_5 crystal with a dopant concentration of 0.05% of the Pr ions but no Ce ions. The results are shown in Figure 7.9, where it can be seen that the coherence time of Pr line in the cases with and without Ce online excitation are the same, within the errors. Under exactly the same experimental conditions, the same measurements in the Pr and Ce co-doped crystal showed a 10% difference in the coherence time, as shown in Figure 7.10. The same type of measurements when the Ce ions were excited at the offline wavelength in the two crystals show the same trend as the online excitation cases. The shorter coherence time measured in the Pr:YSO crystal than that in the co-doped crystal is partly caused by the spectral diffusion resulting from the higher dopant concentration of the Pr ions. These measurements showed that the linewidth broadening seen in Figure 7.8 does not result from direct photon absorption by the Pr ions. It is worth noting that the shorter coherence time shown in Figure 7.10 than in Figure 7.8 is caused by the higher excitation power (1.02 mW).

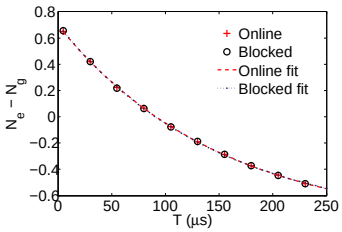

Figure 7.11. *Population difference between the excited and ground state of Pr ions in the same Pr:Ce:Y_2SiO_5 crystal as a function of time with Ce Online excitation (+) and Ce laser blocked (◯). The standard deviation of the data points is ∼2%.*

Energy transfer

If energy is transferred to the Pr ions, the population decay rate of Pr ions will be different from the case when Ce ions are not excited (laser blocked). An excited state population decay measurement was therefore carried out on Pr ions in the same Pr:Ce:Y_2SiO_5 crystal as follows:

The procedures are as follows:

A pit structure was first created centred around the $|5/2g\rangle \rightarrow |5/2e\rangle$ transition (indicated by frequency ν_9 in Figure 6.1), and a peak was burnt back at ν_9 as described in Section 6.1.1.

A pulse with an area of π was then used to excite these ions to their $|\pm 5/2e\rangle$ state with an efficiency greater than 85%.

The crystal was then excited with a Ce excitation pulse with a duration T. If there is any energy transfer between the Ce and Pr ions, or state changing interactions other than the excitation-induced frequency shifts, the Pr ions population in the excited state should change.

Finally, after time T, the transmission of a frequency scanning pulse (denoted a readout pulse) across ν_9 was used to determine the population difference between the $|\pm 5/2e\rangle$ and $|\pm 5/2g\rangle$ states.

This population difference $(N_e - N_g)$, normalized to the initial population of the $|\pm 5/2g\rangle$ state, was recorded as a function of the time (T) between the π pulse and the readout pulse for the two cases in which Ce ions were excited online or not excited during the time T. The results are plotted in Figure 7.11. Each data point is an average of about 10 shots. The fitted lines agreed within 3%. Similar measurements for the Ce offline excitation and with the Ce laser blocked show similar results. It was therefore concluded that there was no energy transfer between the Ce and Pr ions in this measurement.

7.3.3 Calculation of $\Delta\mu_{Ce}$

Based on the measurements presented above, the homogeneous broadening shown in Figure 7.8 should be caused by the permanent dipole-dipole interaction between the Pr and Ce ions. The relation between the change in the permanent dipole moments of Ce ions ($\Delta\mu_{Ce}$) and the Pr homogeneous linewidth broadening (Γ_{br}) induced by the Ce-Pr ion-ion interaction can be expressed as follows [78]

$$\Delta\mu_{Ce} \propto \frac{\Gamma_{br}}{p \cdot \langle|\kappa|\rangle \cdot \langle W_{Ce}\rangle}, \tag{7.6}$$

where, for the sake of simplicity, only the important experimental parameters are included (see Equations (4), (5) and (6) in Paper **III** for details).

In the above equation, p is the probability that a lattice spot in the crystal will be occupied by a Ce1 ion. For the Ce dopant concentration mentioned above (0.012% relative to Y ions) $p = 2.6 \times 10^{-5}$, again assuming that the probability that site 1 is occupied is 87%. κ is a dimensionless quantity of the order of 1, which describes the angular dependence of the dipole-dipole interaction (see Equation (3.2)) [72]. $\langle|\kappa|\rangle$ is the average value of κ over all angles defining the relative dipole orientations and their orientations with respect to the displacement between two dipoles, as shown in Figure 3.6. $\langle W_{Ce}\rangle$ is the average excitation probability of the Ce ions contributing to the interaction during the dephasing time. The calculation of $\langle W_{Ce}\rangle$ is presented in detail below.

Ce excitation probability

$\langle W_{Ce}\rangle$ can be calculated in a steady-state approximation since the duration time of the Ce excitation pulse (∼µs) is two orders of magnitude longer than the excited state lifetime (∼40 ns) of Ce1 ions. The calculation is given below.

$\langle W_{Ce}\rangle$ was calculated from the number of absorbed photons as follows:

$$\langle W_{Ce}\rangle = \frac{D_{ex}}{D_0}, \tag{7.7}$$

where D_{ex} and D_0 denote the excitation and physically available number density of Ce1 ions.

D_{ex} was estimated from the following equation

$$\begin{aligned} D_{ex} &= \frac{N_{ex}}{V_{ex}} \\ &= \frac{P \cdot e^{-\alpha_2 L} \cdot (1 - e^{-\alpha_1 L}) \cdot T_1/h\nu}{\pi w_0^2 L}, \end{aligned} \tag{7.8}$$

where N_{ex} is the average number of photons absorbed by Ce1 ions over the period of the Ce lifetime, T_1 (40 ns), and V_{ex} is the excitation volume, which is approximated by the cylindrical volume defined by the focal diameter of the Ce excitation laser (w_0) and the thickness of the crystal (L). P, α_1 and α_2 denote the Ce excitation laser power, and the absorption coefficients of Ce1 and Ce2 ions, respectively.

The result of Equation (7.7) in this calculation is $\sim 1.3 \times 10^{-6}$.

Result of the change in permanent dipole moment of Ce ions

Using the complete equation resembled by Equation (7.6) the difference in dipole moments between the ground and excited states of Ce1 ions was calculated to be $\sim 9.6 \times 10^{-30}$ C·m . The error bar was determined to be $\pm$ 5.3 $\times 10^{-30}$ C·m, taking the following

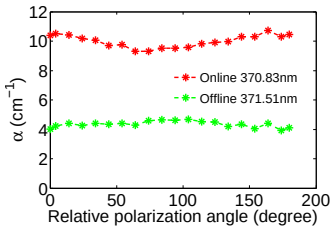

Figure 7.12. *Absorption coefficient of Ce^{3+} in the Pr:Ce:Y_2SiO_5 crystal as a function of the light polarization relative to the vertical direction, at two excitation wavelengths: 370.83 nm (line centre of Ce1 ions) and 371.53 nm (offline for Ce1 ions.*

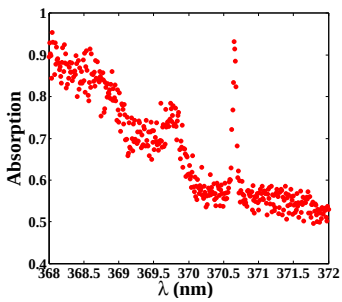

Figure 7.13. *A relatively broad absorption spectrum was shown around the ZPL, where the the narrow peak at about 370 nm indicates the ZPL.*

error sources into consideration: linewidth broadening Γ_{br} (30% error), occupation probability p (assuming a 20% error), and the excitation probability W_{Ce} (39% error).

Based on the measured value of $\Delta\mu_{Ce}$ the transition line of a Ce1 ion will be shifted by more than 300 MHz due to the change in states of a neighbouring Pr ion with an 5 nm distance from the Ce ion (it is the average ion-ion distance of a crystal with a dopant concentration of 0.05%). This shift is clearly large enough to force the Ce ions in site 1 out of resonance with the laser frequency which is initially on resonance.

7.4 Other measurements

Other measurements related to the topics presented in this chapter are given in this section.

Polarization dependence of the absorption

No significant dependence of the Ce1 ion absorption on polarization was found for the ZPL transition. Figure 7.12 shows the measured absorption coefficient of Ce ions (from both sites) in the co-doped crystal mentioned above, as a function of the laser polarization orientation relative to the vertical axis. The beam was propagating along the b axis of the crystal (see Figure 3.8). The absorption coefficients were measured at an excitation wavelength of 370.83 nm (line centre of Ce1 ions) and 371.53 nm (offline for Ce1 ions). The variation in the absorption coefficient relative to the mean value is about 7% for online excitation and 10% for offline excitation.

The absorption spectrum around the ZPL

A relatively broad absorption spectrum was obtained using a tungsten lamp as an excitation source by our collaborator Professor Philippe Goldner's group in Chimie Paris Tech in Paris using the same Ce:Y_2SiO_5 crystal (nominal dopant concentration of 0.088%) at 10 K, as shown in Figure 7.13. The line centre is at about 370.7 nm. There is a strong phonon band at shorter wavelengths, of which only the low frequency wing can be seen. The exact FWHM of the absorption line can not be accurately determined in this measurement due to limited spectral resolution.

Chapter 8

Towards single Ce ion detection

The experiments performed in an attempt to detect the fluorescence emitted by a single Ce ion in a bulk Ce:Y_2SiO_5 crystal are presented in this chapter.

Section 8.1 shows the work on detecting the fluorescence signal of a high Ce dopant concentration crystal (nominal value is 8.8×10^{-4} relative to the Y ions, hence forth called crystal1), in which there are about ten millions of Ce ions within one 1 µm^3.

The studies proceeded with the fluorescence detection from a crystal with a low nominal concentration of 1×10^{-7} of Ce ions (called crystal2), in which the number density of Ce ions is about 2000 ions/µm^3 (Section 8.2).

However as the Ce excitation source (the ECDL) has a linewidth (∼1 MHz over 1 ms) narrower than the homogeneous linewidth of the Ce ion (4 MHz), only a fraction of the illuminated Ce ions that are on resonance with the laser frequency are actively interacting with the laser. This fraction is, on average, the ratio between the homogeneous and inhomogeneous linewidths. This 4 MHz frequency interval, centred around the laser frequency, is hereafter called a frequency channel. Due to this fact the effective number density of Ce ions is reduced to approximately 1 ion within 4.6 µm^3. The number of ions detected was further decreased by restricting the observation volume via making use of the confocal geometry. The number of ions contributing to the observed signal was estimated, shown in Section 8.3.

The trial experiment to determine whether the observed signal originated from a single Ce ion in crystal2 is presented in Section 8.4.

Finally, the problems encountered in these experiments and possible improvements in future studies are discussed in Section 8.5.

All the Ce fluorescence spectra presented in this thesis were recorded in the system described in Section 4.2, in which a mi-

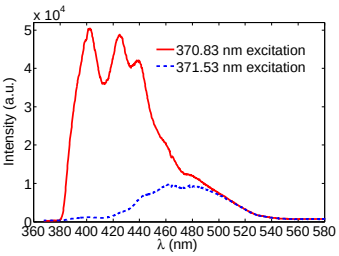

Figure 8.1. *Fluorescence spectrum from Ce^{3+} ions doped in an Y_2SiO_5 crystal (dopant concentration 0.088% relative to Y ions, the crystal was from Scientific material) with 370.83 nm excitation (centre of the ZPL) and 371.53 nm excitation (outside the ZPL).*

croscopy helium cryostat was used to cool down the temperature of the crystal. The temperature of the heat exchanger is ∼4 K and the exact temperature of the crystal is unknown. All the spectra were obtained with an excitation wavelength within or close to the ZPL, which is in principle not required for the single Ce ion detection. However, the homogeneous linewidth of the ZPL was measured and found to be ∼4 MHz. This narrow linewidth provides us with the convenience of identifying the single ion emission by just tuning the ECDL frequency across the homogeneous line in the tens of MHz range. This tuning range can be easily obtained in the lab. The narrow homogeneous line is also one important requirement for the single-ion readout scheme described in Section 6.2.1. None of the spectra presented in this thesis was corrected for the transmission or diffraction efficiencies of the optical components (e.g. objective lens, bandpass filters etc.), however, this will not affect the main features of the spectra.

8.1 Fluorescence detection of a large number of Ce ions

8.1.1 Fluorescence spectrum

Figure 8.1 shows the spectrum obtained from Ce ions in crystal1 using the optical set-up shown in Figure 4.7, where the objective lens was an M Plan Apo NUV 50×, the optical filter was a bandpass filter (range 380-550 nm, (HQ465/170m-2p from Chroma), the focal length of the lens before the monochromator is 150 mm, the slit size is 0.2 mm, and the number of pixels along the y axis (perpendicular to the slit) was 25.

The solid curve in Figure 8.1 shows the emission spectrum obtained at an excitation wavelength of 370.83 nm, which is the centre of the ZPL. This spectrum is called the online spectrum hereafter. Three peaks were presented in the online spectrum, where the energy separation between the first and the second peak is ∼1321 cm^{-1}, and the separation between the first and the third peak ∼2035 cm^{-1}. The Ce spectrum in various crystals has been previously investigated [153, 154, 159], where only two peaks were observed and they were attributed to the emission from the excited state to the two fine structure levels ($^2F_{5/2}$ and $^2F_{7/2}$) in the 4f ground state. The energy separations in an Y_2SiO_5 crystal were reported about 1900 cm^{-1}. The reason why one extra peak presented in the spectra in Figure 8.1 was not investigated. It appears in all the spectra from Ce ions regardless of the dopant concentration and the manufacturer of the crystal. It can also be seen from the online spectrum in Figure 8.1 that the Stokes shift is about ∼2000 cm^{-1}.

The dashed curve in Figure 8.1 shows the emission spectrum

at an excitation wavelength of 371.53 nm, which is outside the ZPL (linewidth is only 50 GHz), with the same excitation power. This spectrum is called the offline spectrum hereafter. In order to figure out the origin of the offline spectrum, the spectra are re-scaled in Figure 8.2b, where they are compared with the spectrum recorded following site-selective excitation (Figure 8.2a), reported by W. Drozdowski et.al. [159]. The solid curve in Figure 8.2a represents the spectrum from a Ce1 excitation and the dashed curve the spectrum from a Ce2 excitation. The online and offline spectra in Figure 8.2b highly resemble the spectra from Ce1 and Ce2 excitation in Figure 8.2a. However there is one difference apart from the number of peaks mentioned above. The spectrum in Figure 8.2b can not be shown below 380 nm or above 550 nm as it is blocked by the bandpass filter mentioned above. Therefore, when comparing it with the spectrum in Figure 8.2a the offline spectrum appears to originate from the emission of Ce2 ions, while the online spectrum contains contributions from ions at both sites, as we believe that the ZPL of Ce1 ions is superimposed on the broad Ce2 ion absorption band.

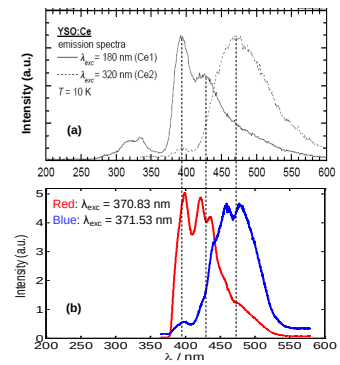

Figure 8.2. *Comparison of the Ce spectra measured in this work (b) with those presented in Ref. [159] from a site-selective excitation (a). The offline spectrum in panel (b) is magnified for the purpose of comparison.*

Checking the online and offline spectrum is a good way of identifying if the observed fluorescence signal is originating from the Ce ions or from any other substances. This identification is important especially for detecting a single Ce ion because most material fluoresces under excitation of ultra-violet photons. However most likely only Ce ions are sensitive for the change of the excitation wavelength in the level of 0.7 nm.

8.1.2 The spectrum at room temperature

The difference in intensity between the first and second peaks varies with temperature, as can be seen in Figure 8.3 (note that the intensity of the spectrum at room temperature has been re-scaled to facilitate comparison.). At low temperature, the first peak is higher than the second, but the reverse is seen at room temperature. No significant change in intensity between the second and third peaks has been observed between at low and room temperature.

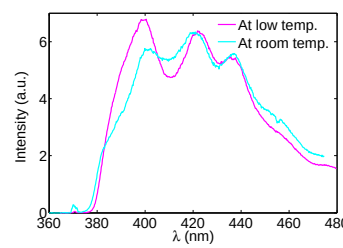

Figure 8.3. *Comparison of the spectra of Ce emission between at low temperature (magenta) and at room temperature (cyan). The intensity of the spectrum at room temperature is re-scaled for a better comparison. All the other conditions are the same.*

As the actual temperature of the crystal is not known, the relative strengths of the two peaks provide a rough indication of the thermal contact between the crystal and the cold finger of the microstat. However a more reliable way of checking the thermal contact is to compare the spectra from an online excitation and offline excitation. Figure 8.4 shows the spectra obtained with poor thermal contact, at online and offline excitation. Both spectra resemble that obtained at room temperature shown in Figure 8.3. The fact that the spectra obtained with an online and offline excitation are the same, apart from a difference in intensity, can be explained as follows. At high temperature, the homogeneous

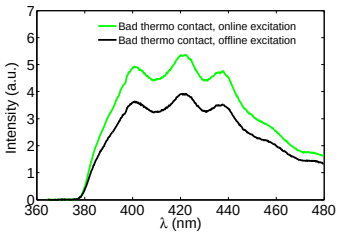

Figure 8.4. *The emission spectrum of Ce ions in the same crystal as in Figure 8.1. The relative strength between the first two shoulders indicates that the actual temperature of the crystal is more close the room temperature, which is potentially caused by a bad thermal contact. More information is given in the text.*

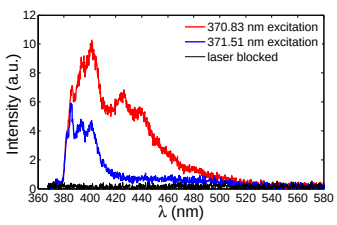

Figure 8.5. *Fluorescence signal from a Ce:Y_2SiO_5 crystal with a dopant concentration of $\sim 1\times10^{-7}$. The signal was obtained with a slit size (along x axis) of 0.2 mm and the number of pixels along y axis of 25. More information is given in the text.*

linewidth of the Ce ion transition is broadened so much by the ion-phonon interaction (discussed in Section 3.3.1) that its width is greater than the spread in the absorption frequencies caused by inhomogeneous broadening. In this case, both the online and offline excitation wavelengths are still inside the (broadened) absorption line of the Ce1 ions, so the spectra are the same.

8.2 Detecting the signal from fewer Ce ions

As an intermediate step towards the detection of a single Ce ion, the fluorescence signal from Ce ions was detected in crystal2, which has a nominal relative Ce dopant concentration of a level of 1×10^{-7}. This crystal was provided by Professor Philippe Goldner's group in Chimie Paris Tech in Paris. There are $\sim$2000 Ce ions per 1 µm^3. Assuming an inhomogeneous linewidth of 37 GHz (based on the measurement described in Section 8.4.3), there is on average about 1 Ce ion within 4.6 µm^3 in one frequency channel.

8.2.1 Signal from a less doped crystal

The spectra obtained from crystal2 under the same experimental conditions as Figure 8.1 (online excitation at 370.83 nm and offline excitation at 371.51 nm) is shown in Figure 8.5. It is clear that the first peak in the spectra are not exactly the same as that in Figure 8.5, though they should be if they are indeed the spectra from Ce ions. Two questions must be answered: (1) Is the spectrum only attributable to the Ce ions, especially the structure in the range 380-420 nm in the offline spectrum? (2) Is the signal strength reduced by the factor that could be expected from the reduction in the the dopant concentration?

The fluorescence in the wavelength range 380-420 nm in the offline spectrum should originate mainly from sources other than Ce ions, because if it was from the Ce ions, it should have been visible in the spectrum shown in Figure 8.1, which it was not. If this is the case, then this background fluorescence should be present in all the spectra shown in Figure 8.1 and Figure 8.5, regardless of the dopant concentration or excitation wavelength. However, the Ce signal shown in Figure 8.1 is several orders of magnitude higher, so the influence of this background signal is negligible. The exact origin of this background fluorescence will be discussed below.

It is unreasonable to directly compare the strength of the signal in Figure 8.1 with that in Figure 8.5 because of the significant disturbance of the fluorescence signal shown in Figure 8.5 due to this background. However, subtracting the offline spectrum from the offline spectrum will remove the background, leaving the signal from the Ce1 ions, which should scale linearly with the change in

the dopant concentration. The results of this subtraction for the two spectra in Figure 8.1 and Figure 8.5 are shown in Figure 8.6. The ratio between the doping concentrations is 8800, and it can be seen that there is good agreement between the two spectra within the error margin when the subtracted signal from Figure 8.5 is multiplied by 8500.

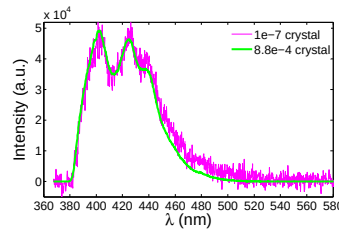

Figure 8.6. *Subtraction of the offline spectrum from the online spectrum, from two crystals with different Ce dopant concentrations. Note that the resulting signal from Figure 8.5 has been multiplied by a factor 8500.*

8.2.2 Background fluorescence

To investigate the origin of the background fluorescence shown in Figure 8.5, the Ce excitation laser was focused onto the surfaces of different materials in the experimental set-up: the cold finger of the microstat, a silicon plate, an optical mirror with aluminium coating, the quartz window of the microstat, and the graphite paint, and their fluorescence signals were observed. The spectra obtained are shown in Figure 8.7, where it can be seen that they all exhibit the same features, but differ in intensity. This shows that the background fluorescence could be due to one substance on the surfaces of all the components mentioned above, or components in the fluorescence detection path.

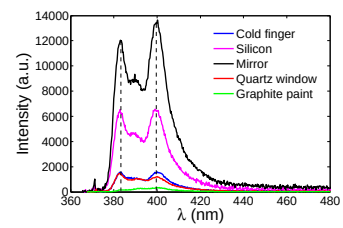

Figure 8.7. *The background signals due to the fluorescence from the surfaces of different components in the experimental set-up resulting from illumination by the Ce excitation laser. Note that the intensities in this figure are not the same as the intensity in Figure 8.5 as the measurement conditions were different.*

The strength of this background fluorescence scales linearly with the intensity of the Ce excitation laser, see Figure 8.8. The experimental data points show the relative signals obtained from the window of the cryostat under illumination of the Ce excitation laser at various laser intensities which were achieved by attenuating the laser power via neutral density filters. The value in y axis of each point is an integration of the spectrum of the background fluorescence. The dashed line denotes a linear fitting of the data points.

The signal strength also decreases dramatically with increasing distance from the focal point to the surface of the material under study, as can be seen in Figure 8.9, where the signal falls to ∼35% when the focal point is below the surface by about five Rayleigh lengths. To reduce the influence of this background signal on the signal from the Ce ions, all the spectra presented in the next section were obtained with the laser focus about 100 µm below the surface of the crystal under study, which is about 12 times the Rayleigh length (∼8 µm) of a beam with a focal diameter of 2 µm.

All the measurements described above are helpful, but do not provide conclusive evidence of the origin of the background fluorescence. We believe that the background is due to the surface enhanced Raman scattering from water vapour molecules on the surfaces. If this is the case, the energy loss in the scattering process in water vapour should be about 1700 cm^{-1}, which is half of the energy loss in liquid water, according to the relation between the emission and excitation wavelength presented by A. J. Lawaetz [164].

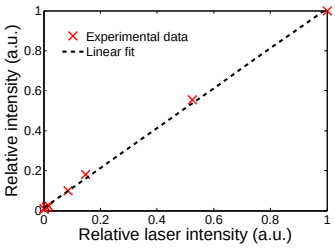

Figure 8.8. *The background fluorescence signal decreases linearly with the laser intensity. Detail is given in the text.*

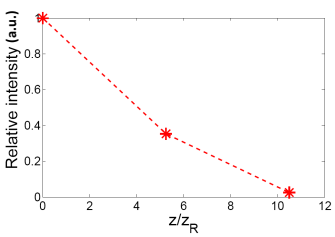

Figure 8.9. *The background fluorescence signal decreases with distance from the focal point to the surface of the material under study. z_R is the Rayleigh length of the focused beam.*

8.2.3 Restricting the observation volume

The background fluorescence in the spectra obtained later from the same crystal was much lower than in Figure 8.5. The spectra are shown in Figure 8.10. The difference in intensity between the upper and lower panels originates from the different observation volume, which will be explained below. The reduction in the background signal was achieved by making two main changes to the experimental set-up: (i) a new microstat window, and (ii) improvement of the spatial mode of the Ce excitation laser by coupling the laser through a single mode optical fibre, which led to a tighter focus but with retained intensity as the fibre coupling efficiency is about 20%.

As mentioned in Section 4.2.3 the microscope set-up is a confocal microscope through controlling both the size of the slit in one dimension (x axis) and the number of pixels in the perpendicular dimension (y axis), as illustrated in Figure 8.11. The signal observation volume in the sample can be reduced by decreasing the slit size and the number of pixels, until the radius of the observation area on the sample approaches to the resolution of the objective lens, which is ∼0.9 µm as described in Section 4.2.3. This determines the effective minimum slit size to be about 67 µm and the number of pixels along the y axis to be about 8, considering the system magnification factor of 37.5.

Figure 8.12 shows the integrated values of the online fluorescence spectrum recorded with a fixed number of pixels (93 pixels) and varying slit sizes. It can be seen that the signal decreases linearly as the size of the slit is reduced. Measurements with a fixed slit size (50 µm) and varying numbers of pixels are shown in Figure 8.13. The signal also decreases linearly with the number of pixels. The explanation for this linear dependence is not exactly clear to us. The reduction in the fluorescence intensity, collected from the focal plane, is expected to be greater at smaller slit sizes than that at larger sizes, considering the Gaussian distribution of the excitation intensity. However, the size of slit also affects the collection volume along the beam propagation direction, where the dependence of the reduction in fluorescence intensity on slit sizes is not transparent to us.

8.3 Estimation of the number of ions contributing to the observed signal

In order to obtain an idea of how close or far away we were from detecting a single ion, rough estimate of the number of excited Ce ions being detected were made as follows, based on the signal shown in the lower panel in Figure 8.10.

How many excited ions is the observed signal from?

The number of excited Ce ions (N_1) that provide such a signal can be calculated as follows, from the observed signal and the estimated collection efficiency of the optical system described in Section 4.2.3.

$$N_1 = \frac{P_c \cdot CF}{QE \cdot \triangle t \cdot CE \cdot R_{em}} \simeq 6, \tag{8.1}$$

where P_c denotes the total number of counts (150) in the fluorescence spectrum within an integration time of $\triangle t$ (0.3 s) resulting from the Ce1 ions. CF is the conversion factor used to convert the number of electrons into counts (5 eletrons/count); QE is an average value of the quantum efficiency of the CCD camera over the spectral range 370-460 nm, and is set to 0.4 electrons/photon; CE, is the collection efficiency of the system (0.004%), and R_{em} is the photon emission rate from one excited Ce ion (2.5×10^7 photons/s).

The result obtained from Equation (8.1) shows that the signal observed in the lower panel of Figure 8.10 is equivalent to the emission from six excited Ce ions, assuming each of the emitted photons has a 0.004% probability of reaching the CCD camera.

The following assumptions were used in the calculation:

- The collection efficiency is constant regardless of the ion's position. This is in fact not true: the average distance between two Ce ions in the same frequency channel is about 2 µm in crystal2 assuming a homogeneous (Γ_h) and inhomogeneous (Γ_{inh}) linewidth of 4 MHz and 37 GHz, respectively. Thus, the collection efficiency of the photons emitted from each ion will differ from the estimated value depending on position, especially when confocal geometry is used.
- The photon emission rate of an excited Ce ion was estimated to be 2.5×10^7 photons/s, based on its 40 ns-long lifetime [153, 154].

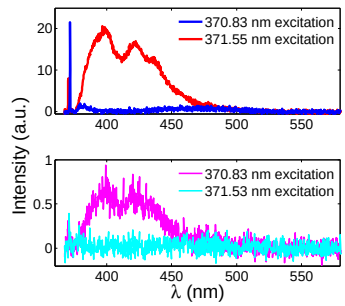

Figure 8.10. *Fluorescence signal from the crystal containing $1{\times}10^{-7}$ Ce ions relative to Y ions recorded with a 50 µm slit and 96 pixels along the y axis (upper figure), and a 20 µm slit and 10 pixels along the y axis (lower figure).*

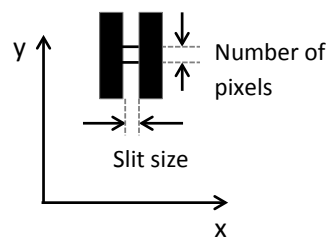

Figure 8.11. *The size of the slit can be controlled along x axis, and the number of pixels in the CCD camera can be controlled in y axis.*

How many ions were excited/observed?

In contrast to previous estimate, another estimate from the excitation point of view, will give the number of excited Ce1 ions under observation for a particular slit size and numbers of pixels in the CCD camera. The value obtained will vary with the experimental conditions, such as the excitation beam diameter (D), Rayleigh length of the focus (Z_R) and the laser power (52 µW). Estimates were made as described below.

(i) A rough estimate

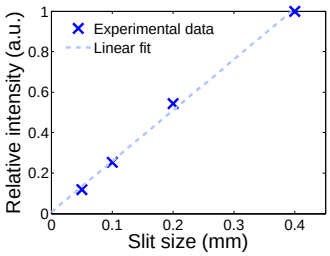

Figure 8.12. *The integrated signal of the online spectrum with a fixed number of pixels (93) changes linearly with the size of the slit.*

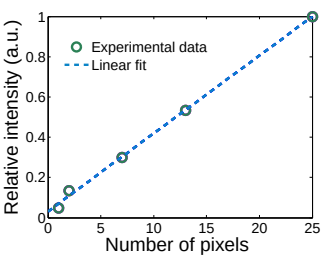

Figure 8.13. *The integrated signal of the online spectrum with a fixed slit size of 50 µm changes linearly with the number of pixels selected in the CCD camera.*

A very rough estimate of the number of excited ions (N_2) can be made based on the product of the number density of Ce ions in the laser frequency channel, the excitation volume (V_{ex}), and the excitation probability of each ion.

The excitation volume (V_{ex}) was estimated to be:

$$V_{ex} \simeq \pi \cdot (D/2)^2 \cdot 2Z_R = 53\ \mu m^3. \tag{8.2}$$

where D $\simeq$ 2 µm (measured value) and Z_R = 8.5 µm.

The number of ions (N_V) within the 4 MHz frequency channel, on average, within this excitation volume is approximated as:

$$N_V = D_Y \cdot Conc \cdot \Gamma_h/\Gamma_{inh} \cdot V_{ex} \simeq 11, \tag{8.3}$$

where D_Y represents the number density ($1.87\times10^{10}/\mu m^3$) of yttrium ions [85]; $Conc$ is the concentration of Ce1 ions relative to yttrium ions (0.87×10^{-7}), where it is assumed that the occupation probability of Ce ions at site 1 is the same as that of Pr ions (87%); Γ_h is the homogeneous linewidth (4 MHz) and Γ_{inh} (assuming 37 GHz) the inhomogeneous linewidth (assumed to be 37 GHz).

The number of excited ions (N_2) within the excitation volume is given by the product of the number of ions available (N_V) and the excitation probability of each ion [24]:

$$N_2 = \frac{1}{2}(1 - \frac{1}{1 + I_{ex}/I_s}) \cdot N_V \simeq 3, \tag{8.4}$$

where I_{ex} represents the top-hat excitation intensity on the crystal surface (1.65×10^7 W/m^2) and I_s denotes the saturation intensity, which is 1.4×10^7 W/m^2, as described in Section 7.2.2.

The result of this calculation is that three Ce ions were excited.

The following assumptions were used in the above estimate.

- Excitation outside the excitation/observation volume was neglected, which leads to underestimation of the number of excited ions contributing to the signal.
- The laser used to excite the Ce ions had a top-hat intensity distribution, while in fact was a Gaussian.
- The number density of Ce1 ions per frequency channel was approximated by the ratio of the homogeneous and inhomogeneous linewidths.

(ii) A rigorous calculation

The assumptions in the previous estimate were replaced by more rigorous calculations, which are presented below. The effective number of excited ions (N_3) under observation was performed by three dimensional integration of the product of the position dependent excitation density of Ce1 ions caused by the Gaussian distribution of the excitation intensity [$I_{ex}(x,y,z)$] and the position-dependent collection efficiency [CE(x,y,z)] of the ions (caused by the confocal geometry) over the entire crystal:

$$N_3 = \int\int\int D_{ex} \cdot CE(x,y,z)\ dx\ dy\ dz \simeq 2, \tag{8.5}$$

where D_{ex} represents the excitation density of Ce1 ions (unit: number of excited ions/m^3). D_{ex} can be determined as a function of the excitation intensity:

$$D_{ex} = \frac{1}{2}(1 - \frac{1}{1 + I_{ex}(x,y,z)/I_s}) \cdot D, \tag{8.6}$$

where D is the number density of Ce1 ions per frequency channel. It was calculated based on the linewidths of the homogeneous and inhomogeneous line:

$$D = D_Y \cdot Conc \cdot \frac{\int L_h(f)\,df}{\int G_{inh}(f)\,df} \simeq 4.8 \times 10^{17}\ ions/m^3, \tag{8.7}$$

where $L_h(f)$ and $G_{inh}(f)$ represents the homogeneous (Lorentzian) and inhomogeneous (Gaussian) line profiles with a linewidths of 4 MHz and 37 GHz, respectively.

We assume that $CE(x,y,z)$ has a Gaussian distribution with a characteristic radius of w_0, which is determined by the size of the images of the slit and the pixels on the sample.

$$CE(x,y,z) = (\frac{w_0}{w_z})^2 \cdot e^{\frac{-2(x^2+y^2)}{{w_z}^2}}, \tag{8.8}$$

where $w_0 = \frac{1}{2} \cdot \frac{\sqrt{SS \cdot N_{px} \cdot 8}}{Mag}$ is the effective radius; $w_z = w_0 \cdot \sqrt{1 + (\frac{z}{z_0})^2}$ denotes the beam radius at position z, and z_0 is the Rayleigh length of the Gaussian distribution function.

This calculation gives the result that 2 excited Ce ions which are observed.

It is worth noting that the influence of the aberration caused by the microstat window on the fluorescence observation volume was not taken into account in above calculations. This causes an underestimation on the number of excited Ce1 ions observed.

Regardless of the variations between the above estimates, the calculations indicate that if the excitation laser frequency is tuned to the wing of the inhomogeneous absorption line, where the Ce1 number density is significantly lower than the averaged value, it should be possible ensure that the laser only interacts with a single Ce ion.

8.4 Attempt to detect a single Ce ion

In this section, experiments in which where the number of detected Ce ions was reduced further by addressing the Ce ions whose transition frequencies are on the wing of the inhomogeneous absorption line, and experiments intended to verify whether the observed signal originates from the emission of a single Ce ion are described. All the signals described in this section were obtained from crystal2.

Improvements to the experimental set-up

A few improvements to the system were made, regarding both the light source and on the optical set-up.

- Two improvements were made to the laser source. (i) The linewidth of the excitation laser (ECDL) was reduced to about ±50 kHz (the design value) for a few hours with active frequency stabilization centred around a stable optical cavity, as described in Chapter 5. This ensures that the laser can interact with the same ion for a few hours. (ii) The laser frequency can be scanned within ±100 MHz while remaining locked to the cavity. This was achieved by scanning the frequency of the electric field which drives a double-pass AOM, in the same manner as described in Section 4.1.2.

- The aberration caused by the microstat window was overcome by using a different objective lens (LUCPLFLN 20×) with a collar correction ring. The laser focal diameter was measured and found to be about 2 µm.

- The beam splitter (BS in Figure 4.7) was changed to obtain higher transmission of the fluorescence signal (83%). In some experiments, the zero-order diffracted beam of the grating inside the monochromator was used to reduce the number of pixels used, so that both the dark counts and the readout noise could be minimized. The filter in Figure 4.7 was replaced by a bandpass filter (NC217171-ET405/40m from Chroma) to select only the part of spectrum that has the highest contrast between the online and an offline spectra (385-425 nm).

- The lens L_f in Figure 4.7 was changed to a focal length of 500 mm. The magnification of the system was increased from 37.5 to 55.5.

8.4.1 Gradual movement of the excitation wavelength to the wing of the inhomogeneous absorption line

At the wing of the ZPL, the number density of Ce ions per frequency channel is lower than the average value (1 ion within 4.6 μm^3). Thus, by tuning the excitation laser wavelength far enough away from the line centre, it should be possible to find some frequency channels where the number density of Ce1 ions is so low that there is only 1 ion within the observation volume. However, as explained in Section 8.1.1, the absorption by the Ce ions at site 2 does not change over the wavelength interval of interest, which means that the number density of Ce2 ions remains the same, regardless of the change in wavelength over a few nm. As mentioned previously, the fluorescence signal from a single Ce1 ion is superimposed on the signal from all the Ce2 ions within the same observation volume. A single ion can only be observed if the signal from the single Ce1 ion is above the noise resulting from the signal from the Ce2 ions.

The fluorescence spectra (below 485 nm) at different excitation wavelengths (370.82 nm, 370.85 nm, 370.87 nm and 371.55 nm), but with the same laser power are shown in Figure 8.14, where the observation area is approximately 2.5 µm × 2.9 µm. The spectrum observed with excitation at 370.82 nm, 370.85 nm and 370.87 nm contain contributions from the ions at both sites, but the spectrum excited at 371.55 nm can be almost purely attributed to the Ce2 ions, as this excitation wavelength is far from line centre of the ZPL.

The bandpass filter was used to select part of the spectrum to obtain higher contrast between the online and offline signals. The spectra obtained at different excitation wavelengths are shown in Figure 8.15. The integrated intensity of the spectrum obtained with an excitation frequency at the absorption line centre (at 370.83 nm) is about 45 times higher than the signal obtained with an excitation at at wavelength at the edge of the line (371.51).

The reduction in intensity of each spectrum towards the spectrum obtained with an excitation wavelength of 371.51 nm is caused by the reduction in the number density of Ce1 ions. The number densities at different excitation wavelengths are shown relative to the density at excitation wavelength 370.83 nm in Figure 8.16. The number density is 2% at excitation of 370.9 nm. Figure 8.16 also shows that the absorption linewidth (FWHM) is

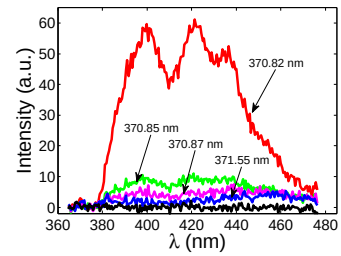

Figure 8.14. *The fluorescence spectra recorded at different excitation wavelengths as indicated in the figure. The black curve is the background signal when the excitation laser is blocked.*

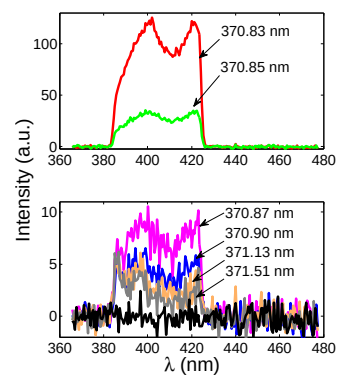

Figure 8.15. *Fluorescence spectra in the range 385-425 nm recorded at different excitation wavelengths, as indicated in the figure. The black curve is the background signal when the excitation laser is blocked.*

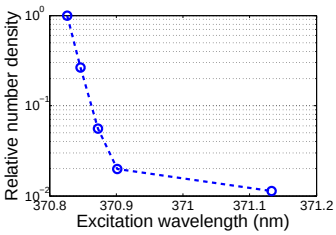

Figure 8.16. *The relative number density of Ce1 ions in different excitation wavelength channels.*

about 57 GHz if it is assumed that the line centre is at 370.82 nm.

Spectra at longer excitation wavelengths ($>$ 371.51 nm) was also recorded, but showed hardly any difference from that at 371.51 nm. As the fluorescence intensity obtained with 371.13 nm excitation is so close to that obtained with an excitation of 371.51 nm, this is probably a suitable wavelength to start searching for a single ion.

8.4.2 Turning the fluorescence signal from a single ion on/off

When only one Ce1 ion actively interacts with the frequency-stabilized excitation laser, it should be possible to turn its fluorescence signal on when the excitation laser frequency coincides with its homogeneous absorption line, and off when the laser frequency is off-resonance with the transition. Since the absorption lines of the individual single ions are discretely spaced in the frequency domain, one can search for such a single ion by scanning the excitation laser frequency over a certain range. We expect to see some discrete peaks, which have a FWHM about 4 MHz (the homogeneous linewidth of the transition), superimposed on the background fluorescence signal from Ce2 ions. These peaks would represent the signals from single Ce1 ions.

The integrated fluorescence intensities over the spectral range of 385-425 nm were recorded as a function of the laser frequency, which scanned across a 100 MHz range centred at the wavelengths on the wing of the inhomogeneous profile, such as 370.87 nm, 371 nm etc. Unfortunately no clear discrete peaks were observed. The possible reasons for this result are analyzed below.

8.4.3 Potential reasons for the failure

There are two possible explanations of why we were not able to detect a single Ce ion. The first is that the signal from a single Ce ion was below the noise of the background signal. The second explanation is that the homogeneous linewidth of the Ce ions was for some reason broader than the value we measured (described in Section 7.2.2). The evidence of this broadening will be discussed below.

Signal to noise analysis

Suppose the fluorescence emission is from a single Ce1 ion, the number of photons we should detect (R_{ph}) in one second is

$$R_{ph} = R_{em} \cdot CE_0 \cdot T_{bpf} \cdot QE_{bp} \simeq 19 \text{ photons/s}, \tag{8.9}$$

where $R_{em} = 6.25 \times 10^6$ photons/s is the emission rate of the Ce ion, determined by the excitation intensity (it was in the level of

the saturation intensity in above scanning measurements); CE_0 is the collection efficiency of the optical system for the zero-order diffracted beam as stated in Table 4.1 (3×10^{-5}); T_{bpf} is the fractional throughput of the bandpass filter (28%); and QE_{bp} is the average quantum efficiency of the camera chip in the spectral range of 385-425 nm (35%).

The noises of the signals in above scan measurements were measured and found to be ∼4 photons/s, which included a few contributions: the noise resulting from the signal of Ce2 ions, the electronic noises of the CCD camera, and the laser intensity variations. These noises superposed on the shot noise of the signal from Ce1 ion, leading to the total noise of 6 photons/s, which is dominated by the shot noise of the Ce1 signal.

Thus, the signal to noise ratio in the above mentioned scanning measurements should be about 3, where the error margin was very limited. Currently an optical system designed for a collection efficiency of a few percent is on the way, which will presumably increase the SNR by more than one order of magnitude.

Homogeneous linewidth is much broader?

There are two possible reasons for the homogeneous linewidth being broader than we assumed. (i) The line is intrinsically broader, which means that the measurement of the homogeneous line described in Section 7.2.2 is incorrect for a reason that is not currently clear to us. (ii) The homogeneous linewidth of the ions was broader than thought when the above scanning experiments were performed. This could be caused by the ion-phonon interaction when the crystal temperature is relatively high.

It has been shown that the homogeneous linewidth (Γ_h) as a function of the temperature (T) in the low temperature range is: $\Gamma_h(T) = 0.0072 \cdot (T^7 - 2^7) + \Gamma_h(2)$ [28]. The coefficient (0.072) was verified experimentally for a 4f-4f transition and describes the ion-phone coupling strength. If we assume that the phonon coupling strength of a 4f-5d transition is one order of magnitude higher than that of a 4f-4f transition, the homogeneous linewidth would be 48 MHz at 18 K, and 4.6 GHz at 35 K. As discussed in Section 8.1.2, in some cases the thermal contact between the cold finger of the microstat and the crystal was poor.

In the experiments described in Section 8.4.2, the temperature of the crystal appears to reasonably low, as the online and offline spectra differ significantly. However, since the exact temperature is not known, it is impossible to say whether the intrinsic homogeneous linewidth is broadened at this temperature. One way of investigating the broadening is to record the fluorescence intensity as a function of the excitation wavelengths, which is another way of measuring the total width of the absorption line. This line is a convolution of the inhomogeneous and homogeneous line. As only the

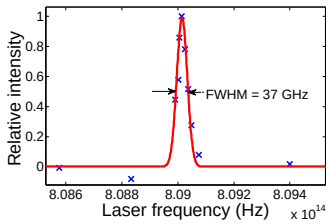

Figure 8.17. *The integrated fluorescence intensity of Ce1 ions as a function of the excitation laser frequency. The symbols show the experimental data and the solid curve is a Gaussian fit, which gives a FWHM of 37 GHz.*

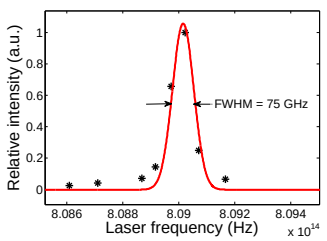

Figure 8.18. *Another measurement of the integrated fluorescence intensity of Ce1 ions as a function of the excitation laser frequency. The symbols show the experimental data, and the solid curve is a Gaussian fit, which reveals a FWHM of 75 GHz.*

homogeneous linewidth varies with temperature, the width of this curve will be greater if the homogeneous line is significantly broadened. This measurement was carried out a number of times using the same crystal (crystal2), and the results are presented in Figure 8.17, Figure 8.18 and Figure 8.16 (the number density shown on the y axis is proportional to the fluorescence signal strength). Their FWHM widths are about 37 GHz (according to Gaussian fitting), 75 GHz (Gaussian fitting) and 57 GHz (indicated by the 50% decrease), respectively. These variations should be the result of broadening of the homogeneous line due to differences in the temperature of the crystal. The larger broadening in Figure 8.18 could be attributed to more layers of thermal conducting surfaces, as the crystal was first 'glued' onto a silicon plate with graphite paint, and the silicon plate was then attached to the cold finger using silver paint. However, the results shown in Figure 8.17 and Figure 8.16 were obtained with the crystal directly attached to the cold finger with graphite paint.

8.5 Discussion

Suggested improvements in future single Ce ion detection experiments and the experimental difficulties encountered are discussed in this section.

8.5.1 Suggestions for improvements

The following improvements are suggested for future experiments.

- Monitoring of the crystal temperature
  One temperature sensor should be mounted on the cold finger of the microscopy cryostat and another on the crystal surface. This would help to determine whether the homogeneous line broadening as a result of high temperatures is one of the reasons it was not possible to detect a single Ce ion.

- Improvement of the collection efficiency
  This improvement will increase the SNR and provide us a larger margin of error.

- Removing the background fluorescence signal from Ce2 ions.
  A significant improvement could be achieved in the fidelity of the single ion readout process (described in Section 6.2.4) if the background fluorescence signal from Ce2 ions could be eliminated in some way, e.g. by site-selective excitation, or by using a crystal in which only one Ce ion is physically available within the observation volume.

8.5.2 Experimental difficulties

The detection of single Ce ions in a YAG ($Y_3Al_5O_{12}$) crystal was recently demonstrated [22]. However, this experiment differed from the one described in this thesis. Firstly, the experiment was performed at room temperature, thus avoiding the problems associated with thermal contact, and aberrations caused by the cryostat window, etc. Secondly, Ce excitation was performed by two-photon excitation at 920 nm and the fluorescence was recorded in the 485-630 nm range, which is free from background fluorescence. Thirdly, there appeared to be only one Ce occupation site in the YAG crystal, so there was no background fluorescence signal from Ce2 ions in their experiment. Finally, the detection was performed on the surface of an ultra pure YAG crystal, where a higher collection efficiency can be achieved due to the absence of the light refraction upon the crystal surface.

In the experiments described in this thesis, using a single Ce ion as a probe to read out the quantum state of the neighbouring single qubit ion, detection must be carried at about the liquid helium temperature as the coherence time of the qubit ions must be preserved. Furthmore, the Ce ions must be doped in an Y_2SiO_5 crystal (the advantages of Y_2SiO_5 were described in Section 3.5), in which there are two crystalline sites that the Ce ions can occupy. At last, the single ion detection must be performed below the crystal surface, as the coherence time of the qubit ions closer to the crystal surface decreases non-negligibly. Two main experimental difficulties in this set-up are discussed below.

Thermal contact

Though the background fluorescence of graphite is low, it might not be best choice considering the following two disadvantages: (i) the thermal conductivity of graphite is likely low, and (ii) it appears that the graphite paint deteriorates after it has been reduced from room temperature to the low temperature once.

Background signal

There are two kinds of background signal in our measurements. The first is background fluorescence from the substances on the optical surfaces. As the Ce excitation frequency ($\sim$371 nm) lies in the ultra-violet range, the high photon energy can excite many substances producing a fluorescence signal. To minimize this signal, all the optical surfaces that can be illuminated by the laser (e.g. the window of the cryostat, objective lenses and the crystal itself) must be as clean as possible. The crystal was cleaned in an ultrasonic cleaner using chemicals (acetone and isopropanol) in the experiments described here, although the optical components were not. The second kind of background is fluorescence from the

Ce2 ions. This background can be reduced by restricting the excitation volume, or by using a crystal with an even lower dopant concentration. It is not clear whether this kind of background can be completely eliminated.

Summary of the thesis work

The work presented in this thesis can be divided into two parts: one is the quantum control of an ensemble of RE ions randomly positioned in an Y_2SiO_5 crystal for quantum computing, and the other is the spectroscopic investigations on the readout ion candidate (Ce^{3+}) to develop the capability of reading out the qubit state encoded on a single RE ion.

It was shown that an arbitrary superposition state for a single qubit can be created experimentally with fidelity above 90%, and the quantum tomography procedures were implemented to characterize the qubit state created. The fidelity of the single ion readout scheme was investigated and the impact of the energy transfer on the single-ion quantum computing concept was analyzed.

The major part of the time was spent on the single ion readout project. In response to the spectroscopic requirements of the single-ion readout scheme on the readout ion, the position of the ZPL of the Ce^{3+} 4f-5d transition was found, the inhomogeneous and homogeneous linewidths of the transition were measured, the change in dipole moment between the ground and excited states was characterized. Among this work the biggest effort was given to the single Ce ion detection (thesis Chapter 8). A laser stabilization system for the Ce excitation source was designed and put into operation. On the way towards detecting the fluorescence emission from a single Ce ion, a number of problems such as background fluorescence emission from the substances on the surfaces, thermal contact between the crystal and the cold finger of the cryostat, and the background fluorescence emission from the ions in site 2 etc. were identified and the possible ways to reduce/eliminate their influences were discussed. Estimations on the number of Ce ions detected were performed, which shows that we are approaching the single ion level. Measurements of verifying whether the detected signal originates from a single Ce ion were implemented. Unfortunately the single ion detection was not successful. The potential reasons were analyzed. With the aid of a new fluorescence detection system recently being built, we are very optimistic about achieving single ion detection in near future, which will be

a significant step forward to the single-ion quantum computing approach.

Comments on the papers

I **Experimental quantum state tomography of a solid state qubit**

Arbitrary single qubit rotations encoded into two hyperfine levels of Pr ions doped in a crystal were experimentally demonstrated, and the fidelities of the rotations were characterized by quantum state tomography. 90-95% fidelities were achieved.

I contributed to the calibration procedure to create the two-colour pulses used for the experiment, I measured the coherence lifetime and analysed the residual population in the excited state as complimentary data to the article. I also prepared the figures for the article.

II **Extracting high fidelity quantum computer hardware from random systems**

This paper provides an overview of the status of and progress in rare-earth-ion based quantum computing (mainly concerning the work our group did). Qubit initialization, gate operations, the single ion readout concept and investigations of the concept, as well as different ways of creating a remote entanglement between two crystals were discussed.

I contributed to some of the experimental results presented in the article and wrote part of the manuscript.

III **Measurement of linewidths and permanent electric dipole moment change of the Ce 4f-5d transition in Y_2SiO_5 for qubit readout scheme in rare-earth ion based quantum computing**

The relevant spectroscopic properties of Ce ions as a candidate for readout ions were investigated. The inhomogeneous and homogeneous linewidths of the zero phonon line were measured, from which the absorption cross section and saturation intensity of the transition were calculated. The difference in permanent dipole moment between the ground and excited states of Ce ions was measured via a photon echo experiment, in which the Ce-Pr ion-ion interaction was demonstrated.

I took part in the planning of the experiments, carried out the different linewidth measurements mainly by myself, and performed the Ce-Pr interaction experiment together with Jenny Karlsson. I performed the calculations, and wrote and finalized the manuscript.

IV **High fidelity readout scheme for rare-earth solid state quantum computing**

A readout scheme involving one or two of the qubit ions closest to the readout ion as buffer ions was proposed, the readout fidelities were simulated, and the fidelity of creating and reading out a full CNOT gate was investigated using density matrixes. The fidelity of generating and characterizing an n-qubit GHz state was calculated in a simplified formulation.

I participated in all the planning meetings and performed the calculation of the fidelity of creating an n-qubit GHZ state.

V **Energy transfer mechanisms in Ce^{3+}-Pr^{3+} and Ce^{3+}-Eu^{3+} codoped Y_2SiO_5 and their impact on single-ion based quantum computing**

Energy transfer efficiencies between Ce and Pr/Eu ions were analyzed theoretically based on the microparameters calculated from the overlap between the emission spectrum of Ce ions and the absorption spectrum of Pr/Eu ions. Energy transfer was also experimentally observed. The influence of the energy transfer process on single rare-earth-ion quantum computing was discussed.

I took part in the planning of the experiments and helped to carry out the experiments.

Unpublished work

Detection of a single Ce ion in a bulk crystal for a single-ion qubit readout scheme

The largest part of the time during my PhD education has been devoted developing the capability of detecting a single Ce ion in a bulk crystal at liquid helium temperature using an external cavity diode laser at 371 nm (thesis Chapter 8). Several experiments using gradually lower Ce dopant concentration crystals were carried out. Finally the fluorescence signal of Ce ions in a crystal where there is on average 1 ion within 4.6 μm^3 interacting with the excitation laser was studied in a microscope setup. A frequency stabilization system on the diode laser centered around an ULE cavity has been constructed designed for a frequency stability of ± 50 kHz over a few hours (thesis Chapter 5). Using the frequency-stabilized laser, trial experiments aiming for turning on/off the fluorescence signal of a single Ce ion by scanning the excitation frequency across its resonance line were carried out. The single ion detection was unsuccessful. Possible reasons for not being able to detect a single Ce ion were analyzed.

Acknowledgements

I would first like to thank my supervisor, Professor Stefan Kröll, for his inspiration, for always being available for discussions, for his persistent encouragement, and for his kindness.

I would also like to thank my co-supervisor, Assistant Professor Zhongshan Li, for his instructions on scientific problems, as well as other problems of life. My sincere thanks also go to my other co-supervisor, Dr. Lars Rippe, for his generous help with all kinds of problems in the lab, for his enthusiasm at coffee breaks, raising interesting discussion topics varying from science to politics. I also thank my mentor, Professor Hongqi Xu, for taking the time to discuss my career plans after this PhD studies.

Thank you to all the members of the quantum information group: Andreas Walther, Jenny Karlsson, Diana Sirrano, Mahmood Sabooni, and Qian Li, for the help you gave me, for all the happy lunch-times we spent together, and for creating such a free and comfortable research environment in the group. I am also grateful to the former Master's student, Xingqiu Zhao for his hard work on setting up the 370 nm laser stabilization system.

My thanks also go to Leif Magnusson at the Kryolab for supplying as much the liquid helium as I need, even if at weekends. I acknowledge Anne Petersson Jungbeck, Harriett Lindahl, and our former secretary Camilla Nilsson, for their kind help with the administrative matters; Åke Johansson and Bertil Hermansson for their help in solving problems with computers, and for supplying the electronic equipment etc.; and Anders Persson and Hans Lundberg for their generous help, despite the fact that we were not in the same research group. Moreover, I would like to express my appreciation of the current and former Heads of the Atomic Physics Division, Professor Claes-Göran Wahlström and Professor Sune Svanberg, for creating such a free, friendly and lively working environment.

I would like to thank everyone at the Atomic Physics Division. Your kindness and help made me feel at home, and I cherished being part of the Divison.

I would also thank all the my collaborators, particularly Professor Mats-Erik Pistol's group at Solid State Physics Division,

Associate Professor Ivan Scheblykin's group at the Department of Chemical Physics, Professor Philippe Goldner's group at Université Pierre et Marie Curie in Paris, and Professor Jun Xu's group at the Shanghai Institute of Ceramics, for their important help with the experiments in different ways.

I would like to extend my deepest gratitude to my family: my parents, for their courage in conquering great difficulties to provide me with the opportunity of the higher education, and for their unconditional support whenever I needed it; my parents-in-law, for their kind considerations and valuable support over the past few years; my husband, for his help even when I woke him up at midnight, for his forgiveness for not being able to travel with him as much as we planned, and for his patience, waiting for me so that we could have dinner together. My last and most grateful thanks go to my daughter, Lufei. You are the star in my sky. Your smile has been and will continue to be the best encouragement for me to overcome my difficulties and move on.

References

1. T. D. Ladd, F. Jelezko, R. Laflamme, Y. Nakamura, C. Monroe and J. L. O′Brien. *Quantum computers.* Nature **464**, 45 (2010).

2. C. Monroe and J. Kim. *Scaling the ion trap quantum processor.* Scicence **339**, 1164 (2013).

3. C. H. Bennett and D. P. DiVincenzo. *Quantum information and computation.* Nature **404**, 247 (2000).

4. S. E. Beavan, E. Fraval, M. J. Sellars and J. J. Longdell. *Demonstration of the reduction of decoherent errors in a solid-state qubit using dynamic decoupling techniques.* Phys. Rev. A **80**, 032308 (2009).

5. I. Usmani, C. Clausen, F. Bussiéres, N. Sangouard, M. Afzelius and N. Gisin. *Heralded quantum entanglement between two crystals.* Nat. Photon. **6**, 234 (2012).

6. E. Saglamyurek, N. Sinclair, J. Jin, J. A. Slater, D. Oblak, F. Bussiéres, M. George, R. Ricken, W. Sohler and W. Tittel. *Broadband waveguide quantum memory for entangled photons.* Nautre **469**, 512 (2011).

7. J. J. Longdell and M. J. Sellars. *Experimental demonstration of quantum-state tomography and qubit-qubit interactions for rare-earth-metal-ion-based solid-state qubits.* Phys. Rev. A **69**, 032307 (2004).

8. L. Rippe, B. Julsgaard, A. Walther, Y. Ying and S. Kröll. *Experimental quantum-state tomography of a solid-state qubit.* Phys. Rev. A **77**, 022307 (2008).

9. W. E. Moerner and M. Orrit. *Illuminating single molecules in condensed matter.* Science **283**, 1670 (1999).

10. W. E. Moerner. *Single molecule spectroscopy in chemistry, physics and biology* volume 96. Springer (2010).

11. J. K. Gimzewski and C. Joachim. *Nanoscale science of single molecules using local probes.* Science **283**, 1683 (1999).

12. T. Hirschfeld. *Optical microscopic observation of single small molecules.* Appl. Opt. **15**, 2965 (1976).

13. K. Peck, A. N. Glazer L. Stryer and R. A. Mathies. *Single-molecule fluorescence detection: Autocorrelation criterion and experimental realization with phycoerythrin.* Proc. Nadl. Acad. Sci. USA **86**, 4087 (1989).

14. E. B. Shera, N. K. Seitzinger, L. M. Davis, R. A. Keller and S. A. Soper. *Detection of single fluorescent molecules.* Chem. Phys. Lett. **174**, 553 (1990).

15. W. Nagourney, G. Janik and H. Dehmelt. *Linewidth of single laser-cooled $^{24}Mg^{+}$ ion in radiofrequency trap.* Proc. Natl. Acad. Sci. USA **80**, 643 (1983).

16. J. C. Bergquist, R. G. Hulet, W. M. Itano and D. J. Wineland. *Observation of Quantum Jumps in a Single Atom.* Phys. Rev. Lett. **57**, 1699 (1986).

17. F. Diedrich and H. Walther. *Nonclassical Radiation of a Single Stored Ion.* Phys. Rev. Lett. **58**, 203 (1987).

18. W. E. Moerner and L. Kador. *Optical Detection and Spectroscopy of Single Molecules in a Solid.* Phys. Rev. Lett. **62**, 2535 (1989).

19. A. P. Bartko, L. A. Peyser, R. M. Dickson, A. Mehta, T. Thundat, R. Bhargava and M.D. Barnes. *Observation of dipolar emission patterns from isolated Eu^{3+}:Y_2O_3 doped nanocrystals: new evidence for single ion luminescence.* Chem. Phys. Lett. **358**, 459 (2002).

20. A. Gruber, A. Dräbenstedt, C. Tietz, L. Fleury, J. Wrachtrup and C. von Borczyskowski. *Scanning confocal optical microscopy and magnetic resonance on single defect centers.* Science **276**, 2012 (1997).

21. R. Kolesov, K. Xia, R. Reuter, R. Stöhr, A. Zappe, J. Meijer, P.R. Hemmer and J. Wrachtrup1. *Optical detection of a single rare-earth ion in a crystal.* Nature communications **3**, 1029 (2012).

22. R. Kolesov, K.Xia, R. Reuter, R. Stöhr, T. Inal, P. Siyushev and J. Wrachtrup. *Mapping spin coherence of a single rare-earth ion in a crystal onto a single photon polarization state.* arXiv **1301.5215v1** (2013).

23. F. Bloch. *Nuclear induction.* Phys. rev. **70**, 460 (1946).

24. C. J. Foot. *Atomic physcis.* Oxford University Press (2006).

25. M. O. Scully and M. S. Zubairy. *Quantum optics.* Cambridge University Press (1997).

26. G. H. Dieke and H. M. Crosswhite. *The spectra of the doubly and triply ionized rare earths.* Appl. Opt. **2**, 675 (1963).

27. R. W. Equall, R. L. Cone and R. M. Macfarlane. *Homogeneous broadening and hyperfine structure of optical transitions in Pr^{3+}:Y_2SiO_5.* Phys. Rev. B **52**, 3963 (1995).

28. F. Könz, Y. Sun, C. W. Thiel and R. L. Cone. *Temperature and concentration dependence of optical dephasing, spectral-hole lifetime, and anisotropic absorption in Eu^{3+}: Y_2SiO_5.* Phys. Rev. B **68**, 085109 (2003).

29. R. M. Clegg. *Fluorescence resonance energy trnasfer.* in Fluorescence imaging spectroscopy and microscopy. John Willey & Sons (1996).

30. J. R. Lakowicz. *Principles of fluorescence spectroscopy.* Springer (2010).

31. J. B. Pawley, editor. *Handbook of biological confocal microscopy.* Springer (2006).

32. E. H. K. Stelzer. *Practical limits to resolution in fluorescence light micorscopy.* Imaging Neurons: A Laboratory Manual. New York: Cold Spring Harbor Press. (2000).

33. J. Murray. *Confocal micorscopy, deconvolution, and structured illumination methords.* Live Cell Imaging: A Laboratory Manual. New York: Cold Spring Harbor Press. (2005).

34. S. Inoué. *Handbook of biological confocal microscopy.* Springer (2006).

35. S. W. Hell, E. H. K. Stelzer, S. Lindek and Ch. Cremer. *Confocal microscopy with an increased dedection aperture: type B 4Pi confocal microscopy.* Opt. Lett. **19**, 222 (1994).

36. A. Egner, S. Jakobs and S.W. Hell. *Fast 100-nm resolution three-dimensional microscope reveals structural plasticity of mitochondria in live yeast.* PNAS **99**, 3370 (2002).

37. M. Born and E. Wolf. *Principles of optics.* Cambridge University Press (1999).

38. W. Kaiser and C. G. B. Garrett. *Two-photon excitation in CaF_2:Eu^{2+}.* Phys. Rev. Lett. **7**, 229 (1961).

39. I. D. Abella. *Optical double-photon absorption in cesium vapor.* Phys. Rev. Lett. **9**, 453 (1962).

40. M. Oheim, D. J. Michael, M. Geisbauer, D. Madsen and R. H. Chow. *Principles of two-photon exciation fluorescence microscopy and other nonlinear imaging approaches.* Adv. Drug Deliv. Rev. **58**, 788 (2006).

41. M. Dyba and S. W. Hell. *Fcoal spot of size λ/23 open up far-field fluorescence microscopy at 33 nm axial resolution.* Phy. Rev. Lett. **88**, 163901 (2002).

42. S. W. Hell. *Toward fluorescence nanoscopy.* Nat. Biotechnol. **21**, 1347 (2003).

43. V. Westphal, S. O. Rizzoli, M. A. Lauterbach D. Kamin, R. Jahn and S. W. Hell. *Video-ratefFar-field optical nanoscopy dissects synaptic vesicle movement.* Science **320**, 246 (2008).

44. M. Orrit and J. Bernard. *Single pentacene moleucles detected by fluorescence excitation in a p-terphenyl crystal.* Phy. Rev. Lett. **65**, 2716 (1990).

45. M. Fox. *Quantum optics - an Introduction.* Oxford University Press (2006).

46. H. J. Kimble, M. Dagenais and L. Mandel. *Photon antibunching in resonance fluorescence.* Phys. Rev. Lett. **39**, 691 (1977).

47. A. Beveratos, R. Brouri, T. Gacoin, J.-P. Poizat and P. Grangier. *Non-classical radiation from diamond nanocrystals.* Phys. Rev. A **64**, 061802 (2001).

48. R. Loudon. *The quantum theory of light.* Oxford University Press third edition (2000).

49. L. Rippe, M. Nilsson, R. Klieber S. Kröll and D. Seuter. *Experimental demonstration of efficient and selective populaiton transfer and qubit distillation in a rare-earth-metal-ion-doped crystal.* Phys. Rev. B **71**, 062328 (2005).

50. B. Henderson and G. F. Imbusch. *Optical spectroscopy of inorganic solids.* Oxford Science Publications (1989).

51. A. A. Kaplyanskii. *Linear Stark effect in spectroscopy and luminescence of doped inorganic insulating crystals.* J. Lummin. **100**, 21 (2002).

52. W. M. Yen, Selzer P. M., G. F. Imbush, R. Kopelman, T. Holstein, S. K. Lyo, R. Orbach, D. L. Kuber, M. J. Weber and A. H. Francis. *Laser spectroscopy of solids.* Springer-Verlag Berlin (1981).

53. R. S. Meltzer. *Line broadening mechanisms and their measurement.* in Spectroscopic properites of rare earths in optical materials. Springer-Verlag Berlin (2005).

54. G. Liu. *Electronic energy level structure.* in Spectroscopic properites of rare earths in optical materials. Springer (2005).

55. R. M. Macfarlane. *Inhomogeneous broadening of spectral lines in doped insulators.* J. Lumin. **45**, 1 (1990).

56. Wikepedia. Ionic radius (2013). URL http://en.wikipedia.org/wiki/Ionic_radius.

57. R. Yano, M. Mitsunaga and N. Uesugi. *Ultralong optical dephasing time in Eu^{3+}:Y_2SiO_5.* Opt. lett. **16**, 1884 (1991).

58. D. L. Orth, R. J. Mash and J. L. Skinner. *Optical lineshapes of impurities in crystals: a lattice model of inhomogeneous broadening by point defects.* J. Phys.: Condens. Matter **5**, 2533 (1993).

59. D. L. Orth and J. L. Skinner. *Lattice model of inhomogeneous broadening in crystals: correlation of frequency distributions for different transitions.* J. Phys. Chem. **98**, 7342 (1994).

60. Z. J. Kiss. *Energy levels of divalent thulium in CaF_2.* Phys. Rev. **127**, 718 (1962).

61. D. K. Sardar and S. C. Stubblefield. *Phonon effects on sharp spectral lines for inter-Stark transitions of trivalent neodymium ions in strontium fluorovanadate.* Phys. Rev. B **60**, 14724 (1999).

62. F. Pellé, N. Gardant, R. Pelletier and N. Pelletier-Allard. *Spectroscopic analysis of Pr^{3+}-doped $CsCdCl_3$.* Opt. Material **14**, 49 (2000).

63. R. M. Macfarlane. *High-resolution laser spectroscopy of rare-earth doped insulators: a personal perspective.* J. Lumin. **100**, 1 (2002).

64. R. M. Macfarlane, R. S. Meltzer and B. Z. Malkin. *Optical measurement of the isotope shifts and hyperfine and superhyperfine interactions of Nd in the solid state.* Phys. Rev. B **58**, 5692 (1998).

65. N. Ohlsson, R. K. Mohan and S. Kröll. *Quantum computer hardware based on rare-earth-ion-doped inorganic crystals.* Opt. Commun. **201**, 71 (2002).

66. S. Svanberg. *Atomic and molecular spectroscopy.* Springer (2004).

67. W. Demtröder. *Laser spectroscopy, basic concepts and instrumentation.* Springer (2003).

68. Y. Sun, C. W. Thiel, R. L. Cone, R. W. Equall and R. L. Hutcheson. *Recent progress in developing new rare earth materials for hole burning and coherent transient applications.* J. Lumin. **98**, 281 (2002).

69. R. W. Equall, Y. Sun and R. L. Cone. *Ultraslow optical dephasing in Eu^{3+} : Y_2SiO_5.* Phys. Rev. Lett. **72**, 2179 (1994).

70. D. E. McCumber and M. D. Sturge. *Linewidth and temperature shift of the R Lines in ruby.* J. App. Phys. **34**, 1682 (1963).

71. W. M. Yen, C. Scott and A. L. Schaylow. *Phonon-induced relaxation in excited optical states of trivalent praseodymium in LaF3.* Phys. Rev. A **136**, A271 (1964).

72. S. B. Altner, G. Zumofen, U. P. Wild and M. Mitsunaga. *Photon-echo attenuation in rare-earth-ion-doped crystals.* Phys. Rev. B **54**, 17493 (1996).

73. W. R. Babbitt, A. Lezama and T. W. Mossberg. *Optical dephasing, hyperfine structure, and hyperfine relaxation associated with the 580.8-nm $^7F_0$-$^5D_0$ transition of europium in Eu^{3+}:Y_2O_3.* Phys. Rev. B **39**, 1987 (1989).

74. J. Huang, J. M. Zhang, A. Lezama and T. W. Mossberg. *Excess dephasing in photon-echo experiments arising from excitation-induced electronic level shifts.* Phys. Rev. Lett. **63**, 78 (1989).

75. S. B. Altner, M. Mitsunaga, G. Zumofen and U. P. Wild. *Dephasing-rephasing balancing in photon echoes by excitation induced frequency*

shifts. Phys. Rev. Lett. **76**, 1747 (1996).

76. J. D. Jackson. *Classical electrodynamics*. John Wiley & Sons, Inc. (1962).

77. R. M. Macfarlane and R. M. Shelby. *Sub-kilohertz optical linewidths of the* $^7F_0 \leftrightarrow 5D_0$ *transition in* $Y_2O_3{:}Eu^{3+}$. Opt. Commun. **39**, 169 (1981).

78. F. R. Graf, A. Renn, G. Zumofen and Urs P. Wild. *Photon-echo attenuation by dynamical processes in rare-earth-ion-doped crystals*. Phys. Rev. B **58**, 5462 (1998).

79. L. E. Erickson. *Optical measurement of the hyperfine splitting of the* $^1D_2$ *metastable state of* Pr^{3+} *in* LaF_3 *by enhanced and saturated absorption spectroscopy*. Phys. Rev. B **16**, 4731 (1977).

80. M. Nilsson, L. Rippe and S. Kröll. *Hole-burning techniques for isolation and study of individual hyperfine transitions in inhomogeneously broadened solids demonstrated in* $Pr^{3+}{:}\ Y_2SiO_5$. Phys. Rev. B **70**, 214116 (2004).

81. E. L. Hahn. *Spin echoes*. Phys. Rev. B **80**, 580 (1950).

82. N. A. Kurnit, I. D. Abella and S. R. Hartmann. *Observation of a photon echo*. Phys. Rev. Lett. **13**, 567 (1964).

83. R. Beach, S. R. Hartmann and R. Friedberg. *Billiard-ball echo model*. Phys. Rev. A **25**, 2658 (1982).

84. M. Mitsunaga and R. G. Brewer. *Generalization perturbation theory of coherent optical emission*. Phys. Rev. A **32**, 1605 (1985).

85. B. A. Moksimov, V. V. Ilyukhin, Y. A. Kharitonov and N. V. Belov. *Crystal structure of Yttrium oxyorthosilicate* $Y_2O_3{\cdot}SiO_2 = Y_2SiO_5$. *dual function of Yttrium*. Soviet physics-Crystallography **15**, 806 (1971).

86. R. Beach, M. D. Shinn, L. Davis, R. W. Solarz and W. F. Krupke. *Optical absorption and stimulated emission of neodymium in yttrium orthosilicate*. IEEE J. Quant. Elect. **26**, 1405 (1990).

87. Y. C. Sun. *Rare earth materials in optical storage and data processing applications*. in Spectroscopic properites of rare earths in optical materials. Springer (2005).

88. M. P. Hedges, J. J. Longdell, Y. Li and M. J. Sellars. *Efficient quantum memory for light*. Nature **465**, 1052 (2010).

89. Wikipedia (2013). URL http://en.wikipedia.org/wiki/Nuclear_magneton.

90. K. Holliday, M. Croci. E. Vauthey and Urs P. Wild. *Spectral hole burning and holography in an* $Y_2SiO_5{:}Pr^{3+}$ *crystal*. Phys. Rev. B **47**, 14741 (1993).

91. F. R. Graf, A. Renn and M. Mitsunaga Urs P. Wild. *Site interference in Stark-mojulated photon echoes*. Phys. Rev. B **55**, 11225 (1997).

92. X. A. Shen and R. Kachru. $^7F_0$-$^5D_1$ *Transition in* $Eu^{3+}{:}Y_2SiO_5$. J. Opt. Soc. Am. B **11**, 591 (1994).

93. R. F. Kubin and A. N. Flectcher. *Fluorescence quantum yields of some Rhodamine dyes*. J. Lumin. **27**, 455 (1982).

94. R. W. P. Drever, J. L. Hall, F. V. Kowalski, J. Hough, G. M. Ford, A. J. Munley and H. Ward. *Laser phase and frequency stabilization using an optical resonator*. Appl. Phys. B **31**, 97 (1983).

95. It has not been measured upon the time when the thesis was written. (2013).

96. A. Wiman. Laser stabilization to a low-expansion Fabry-Pérot cavity.

Master's thesis Lund University (2011).

97. L. Rippe. *Quantum computing with naturally trapped sub-nanometre-spaced Ions.* PhD thesis Lund University (2006).

98. B. Julsgaard, A. Walther, S. Kröll and L. Rippe. *Understanding laser stabilization using spectral hole burning.* Opt. Express **15**, 11444 (2007).

99. A. Walther. *Coherent processes in rare-earth-ion-doped solids.* PhD thesis Lund University (2009).

100. L. Levin. *Mode-hop-free electro-optically tuned diode laser.* Opt. Lett. **27**, 237 (2002).

101. M. E. Taylor Engineering Inc. (2013).

102. Datasheet of iXon 885 from Andor (2013).

103. J. Verges S. Gerstenkorn and J. Chevillard. *ATLAS du spectre d'absorption de la molecure d'iode.* Laboratoire Aime Cotton, C. N. R. S. II, 91405 (1978).

104. C. J. Bordé, G. Camy, B. Decomps, J.-P. Descoubes and J. Vigué. *High precision saturation spectroscopy of $^{127}I_2$ with argon lasers at 5145 Å and 5017 Å : I - Main resonances.* J. Physique **42**, 1393 (1981).

105. S. Kremser, B. Bedermann, H. Knöckel and E. Tiemann. *Frequency stabilization of diode-laser to hyperfine transitions of the iodine molecule.* Opt. Commun. **110**, 708 (1994).

106. S. Olmschenk, K. C. Younge, D. L. Moehring, D. N. Matsukevich, P. Maunz and C. Monroe. *Manipulation and detection of a trapped Yb^+ hyperfine qubit.* Phys. Rev. A **76**, 052314 (2007).

107. Communication with commercial companies. (2012).

108. S. T. Cundiff and J. Ye. *Femtosecond optical frequency combs.* Rev. Mod. Phys. **75**, 325 (2003).

109. J. Ye and S. T. Cundiff. *Femtosecond optical frequency comb: principle, operation, and applications.* Kluwer Academic Publishers / Springer (2004).

110. Th. Udem, J. Reichert, R. Holzwarth and T. W. Hänsch. *Absolute optical frequency measurement of the cesium D_1 Line with a modelLocked laser.* Phys. Rev. Lett. **82**, 3568 (1999).

111. D. J. Jones, S. A. Diddams, J. K. Ranka, A. Stentz, R. S. Windeler, J. L. Hall and S. T. Cundiff. *Carrier-envelope phase control of femtosecond mode-locked lasers and direct optical frequency synthesis.* Science **28**, 635 (2000).

112. E. Riedle, S. H. Ashworth, J. T. Farrell and D. J. Nesbitt. *Stabilization and precise calibration of a continuous wave difference frequency spectrometer by use of a simple transfer cavity.* Rev. Sci. Instrum. **65**, 42 (1994).

113. B. C. Young, F. C. Cruz, W. M. Itano and J. C. Bergquist. *Visible lasers with subhertz linewidths.* Phys. Rev. Lett. **82**, 3799 (1999).

114. T. Kessler, C. Hagemann, C. Grebing, T. Legero, U. Sterr, F. Riehle, M. J. Martin, L. Chen and J. Ye. *A sub-40-mHz-linewidth laser based on a silicon single-crystal optical cavity.* Nature Photonics **6**, 687 (2012).

115. J. P. Richard and J. J. Hamilton. *Cryogenic monocrystalline silicon FabryPerot cavity for the stabilization of laser frequency.* Rev. Sci. Instrum. **62**, 2375 (1991).

116. R. Storz, C. Braxmaier, K. Jack, O. Pradl and S. Schiller. *Ultrahigh*

long-term dimensional stability of a sapphire cryogenic optical resonator. Opt. Lett. **23**, 1031 (1998).

117. T. Legero, T. Kessler and Uwe Sterr. *Tuning the thermal expansion properites of optical reference cavities with fused silica mirrors*. J. Opo. Soc. Am. B **27**, 914 (2010).

118. K. Numata, A. Kemery and J. Camp. *Thermal-noise limit in the frequency stabilization of lasers with rigid cavities*. Phys. Rev. Lett. **93**, 250602 (2004).

119. H. Stoehr, F. Mensing, J. Helmcke and U. Sterr. *Diode laser with 1 Hz linewidth*. Opt. Lett. **31**, 736 (2006).

120. T. Nazarova, F. Riehle and U. Sterr. *Vibration-insensitive reference cavity for an ultra-narrow-linewidth laser*. Appl. Phy. B **83**, 531 (2006).

121. S. A. Webster, M. Oxborrow and P. Gill. *Vibration insensitive optical cavity*. Phys. Rev. A **75**, 011801 (2007).

122. A. D. Ludlow, X. Huang, M. Notcutt, T. Zanon-Willette, S. M. Foreman, M. M. Boyd, S. Blatty and J. Ye. *Compact, thermal-noise-limited optical cavity for diode laser stabilization at* 1×10^{-15}. Opt. Lett. **32**, 641 (2007).

123. D. R. Leibrandt, M. J. Thorpe, M. Notcutt, R. E. Drullinger, T. Rosenband and J. C. Bergquist. *Spherical reference cavities for frequency stabilization of lasers in non-laboratory environments*. Opt. Express **19**, 3471 (2011).

124. L. Chen, J. L. Hall, Jun Ye, Tao Yang, E. Zang and T. Li. *Vibration-induced elastic deformation of Fabry-Perot cavities*. Phys. Rev. A **74**, 053801 (2006).

125. J. Alnis, A. Matveev, N. Kolachevsky, Th. Udem and T. W. Hansch. *Subhertz linewidth diode lasers by stabilization to vibrationally and thermally compensated ultralow-expansion glass Fabry-Perot cavities*. Phys. Rev. A **77**, 053809 (2008).

126. M. Zhu and J. L. Hall. *Stabilization of optical phase/frequency of a laser system: application to a commercial dye laser with an external stabilizer*. J. Opt. Soc. Am. B **10**, 802 (1993).

127. E. D. Black. *An introduction to Pound-Drever-Hall laser frequency stabilization*. Am. J. Phys. **69**, 79 (2001).

128. R. V. Pound. *Electronic frequency stabilization of microwave oscillators*. Rev. Sci. Instrum. **17**, 490 (1946).

129. Yu V Troitskiĭ. *Optimization and comparison of the characteristics of optical interference discriminators*. J. Quant. Electron **8**, 628 (1978).

130. X. Q. Zhao. Diode laser frequency stabilization onto an optical cavity. Master's thesis Lund University (2013).

131. E. N. Ivanov, F.-X. Esnault and E. A. Donley. *Offest phse locking of noisy diode lasers aided by frequency division*. Rev. Sci. Instrum. **82**, 083110 (2011).

132. A. Steane. *Qauntum computing*. Rep. Prog. Phys. **61**, 117 (1998).

133. G. E. Moore. *Progress in digital integrated electronics*. IEEE **1**, 11 (1975).

134. J. H. Wesenberg, K. Mølmer, L. Rippe and S. Kröll. *Scalable design for quantum computing with rare-earth-ion-doped crystals*. Phys. Rev. A **75**, 012304 (2007).

135. D. P. Divincenzo. *The physical implementation of quantum computation*. Fortschritte der physik-progress of physics **48**, 771 (2000).

136. N. Ohlsson, M. Nilsson and Stefan Kröll. *Experimental investigation of delayed self-interference for single photons.* Phys. Rev. B **68**, 063812 (2003).

137. E. Fraval, M. J. Sellars and J. J. Longdell. *Dynamic decoherence control of a solid-state nuclear-quadrupole qubit.* Phys. Rev. Lett. **95**, 030506 (2005).

138. M. Nilsson, L. Rippe, N. Ohlsson, T. Christinansson and S. Kröll. *Initial experiments concerning quantum information processing in rare-rarth-ion doped crystals.* Phys. Scripta **T102**, 178 (2002).

139. M. Nilsson. *Coherent interactions in rare-earth-ion-doped crystals for application in quantum information science.* PhD thesis Lund University (2004).

140. V. V. Khodos, D. A. Ryndyk and V. L. Vaks. *Fast-passage microwave molecular spectroscopy with frequency sweeping.* Eur. Phys. J.: Appl. Phys. **25**, 203 (2004).

141. A. Amari, A. Walther, M. Sabooni, M. Huang, S. Kröll, M. Afzelius, I. Usmani, B. Lauritzen, N. Sangouard, H. de Riedmatten and N. Gisin. *Toward an efficient atomic frequency comb quantum memory.* J. lumin. **130**, 1579 (2010).

142. I. Roos and K. Mølmer. *Quantum computing with an inhomogeneously broadened ensemble of ions: Suppression of errors from detuning variations by specially adapted pulses and coherent population trapping.* Phys. Rev. A **69**, 022321 (2004).

143. M. A. Nielsen and I. L. Chuang. *Quantum computation and quantum information.* Cambridge University Press (2000).

144. S. Bengtsson. Simulation and modeling of Rare earth ion based quantum gate operations. Master's thesis Lund University (2012).

145. D. M. Greenberger, M. A. Horne, A. Shimony and A. Zeilinger. *Bells theorem without inequalities.* Am. J. Phys. **58**, 1131 (1990).

146. C. F. Roos, G. P. T. Lancaster, M. Riebe, H. Häffner, W. Hänsel, S. Gulde, C. Becher, J. Eschner, F. Schmidit-Kaler and R. Blatt. *Tomography of entangled massive particles.* arXiv:quant-ph/ page 0307210 (2003).

147. C. F. Roos, G. P. T. Lancaster, M. Riebe, H. Häffner, W. Hänsel, S. Gulde, C. Becher, J. Eschner, F. Schmidit-Kaler and R. Blatt. *Bell States of Atoms with Ultralong Lifetimes and Their Tomographic State Analysis.* Phy. Rev. Lett **92**, 220402 (2004).

148. L. Zheng, R. Lisiecki, W. Ryba-Romanowski, G. Aka, J. Di, D. Li, X. Xu and Jun Xu. *Crystal growth and spectroscopic properties of Praseodymium and Cerium co-doped* Y_2SiO_5. J. Lumin. (2013).

149. J. A. Caird, A. J. Ramponi and P. R. Staver. *Quantum efficiency and excited-state relaxation dynamics in neodymium-doped phosphate laser glasses.* J. Opt. Soc. Am. B **8**, 1391 (1991).

150. P. L. Pernas and E Cantelar. *Emission and absorption cross-section calculation of rare earth doped materials for applications to integrated optic devices.* Phys. Scr. **T118**, 93 (2005).

151. J. J. Longdell, A. L. Alexander and M. J. Sellars. *Characterization of the hyperne interaction in europium-doped yttrium orthosilicate and europium chloride hexahydrate.* Phys. Rev. B **74**, 195101 (2006).

152. Suggested by Olivier Guillot-Noël in the European Quantum Information Processing and Computing workshop. Rome (2004).

153. H. Suzuki, T. A. Tombrelloa, C. L. Melcherb and J. S. Schweitzerb. *UV and gamma-ray excited luminescence of cerium-doped rare-earth oxyorthosilicates*. Nuclear Instrumetns and Methods in Physcs Research Section A **320**, 263 (1992).

154. T. Aitasalo, J. Hölsä, M. Lastusaari, J. Legendziewicz, J. Niittykoski and F. Pellé. *Delayed luminescence of Ce3 doped Y2SiO5*. Opt. Materials **26**, 107 (2004).

155. J. E. Hernandez. Spectroscopy in Ce Y_2SiO_5: A preliminary investigation for a single ion readout scheme for quantum computation with rare-earth ion doped crystals. Master's thesis Lund University (2006).

156. Wikepedia. Cerium (2013). URL http://en.wikipedia.org/wiki/Cerium#Physical_proper.

157. J. Emsley, editor. *Nature's building blocks: An A-Z guide to the elements*. Oxford University Press (2011).

158. J. Choi, S. A. Basun, L. Lu, W. M. Yen and U. Happek. *Excited state impurity band conductivity in $Y_2(SiO_4)O$: Ce^{3+}*. J. Lummin. **461**, 83 (1999).

159. W. Drozdowski, A. J. Wojtowicz, D. Wiśniewski, P. Szupryczyński, S. Janus, J. Lefaucheur and Z. Goub. *VUV spectroscopy and low temperature thermoluminescence of LSO:Ce and YSO:Ce*. J. Alloy. Compd. **380**, 146 (2004).

160. R. C. Hilborn. *Einstein coefficients, cross sections, f values, dipole moments, and all that*. Am. J. Phys. **50**, 982 (1982).

161. D. G. Steel and S. C. Rand. *Ultranarrow nonlinear optical resonances in solids*. Phys. Rev. Lett. **55**, 2285 (1985).

162. M. Mitsunaga, N. Uesugi and K. Sugiyama. *Kilohertz-resolution pump-probe spectroscopy in Pr^{3+}:$YAlO_3$*. Opt. Lett. **18**, 1256 (1993).

163. N. V. Kuleshov, V. G. Shcherbitsky, A. A. Lagatskya, V. P. Mikhailov, B. I. Minkov, T. Danger, T. Sandrock and G. Huber. *Spectroscopy, excited-state absorption and stimulated emission in Pr^{3+}-doped Gd_2SiO_5 and Y_2SiO_5 crystals*. J. Lumin. **71**, 27 (1997).

164. A. J. Lawaetz and C. A. Stedmon. *Fluorescence Intensity Calibration Using the Raman Scatter Peak of Water*. Appl. Spectroscopy **63**, 936 (2009).

Schematics

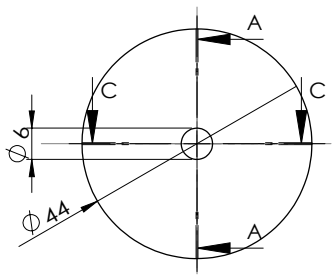

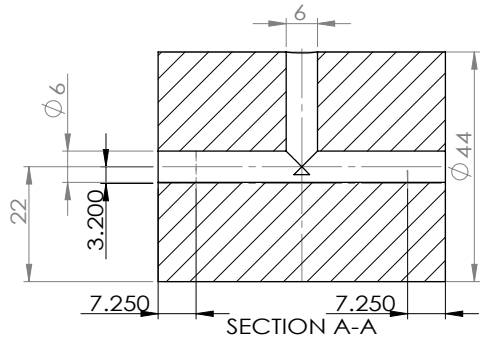

SECTION A-A

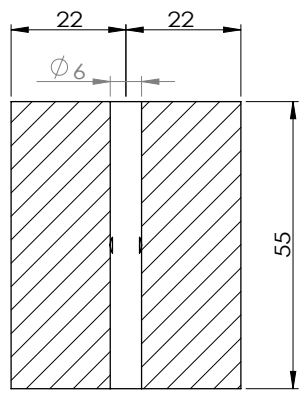

SECTION C-C

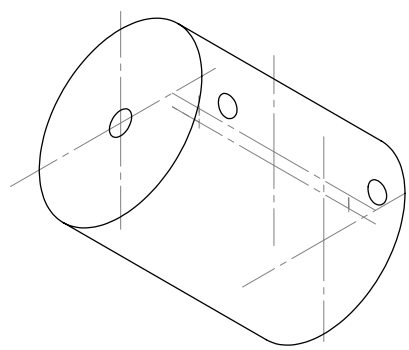

UNLESS OTHERWISE SPECIFIED: DIMENSIONS ARE IN MILLIMETERS SURFACE FINISH: TOLERANCES: LINEAR: ANGULAR:			FINISH:			DEBUR AND BREAK SHARP EDGES	DO NOT SCALE DRAWING	REVISION
	NAME	SIGNATURE	DATE				TITLE:	
DRAWN								
CHK'D								
APPV'D								
MFG								
Q.A				MATERIAL:			DWG NO. Cavity_spacer	A4
				WEIGHT:			SCALE:1:1	SHEET 1 OF 1

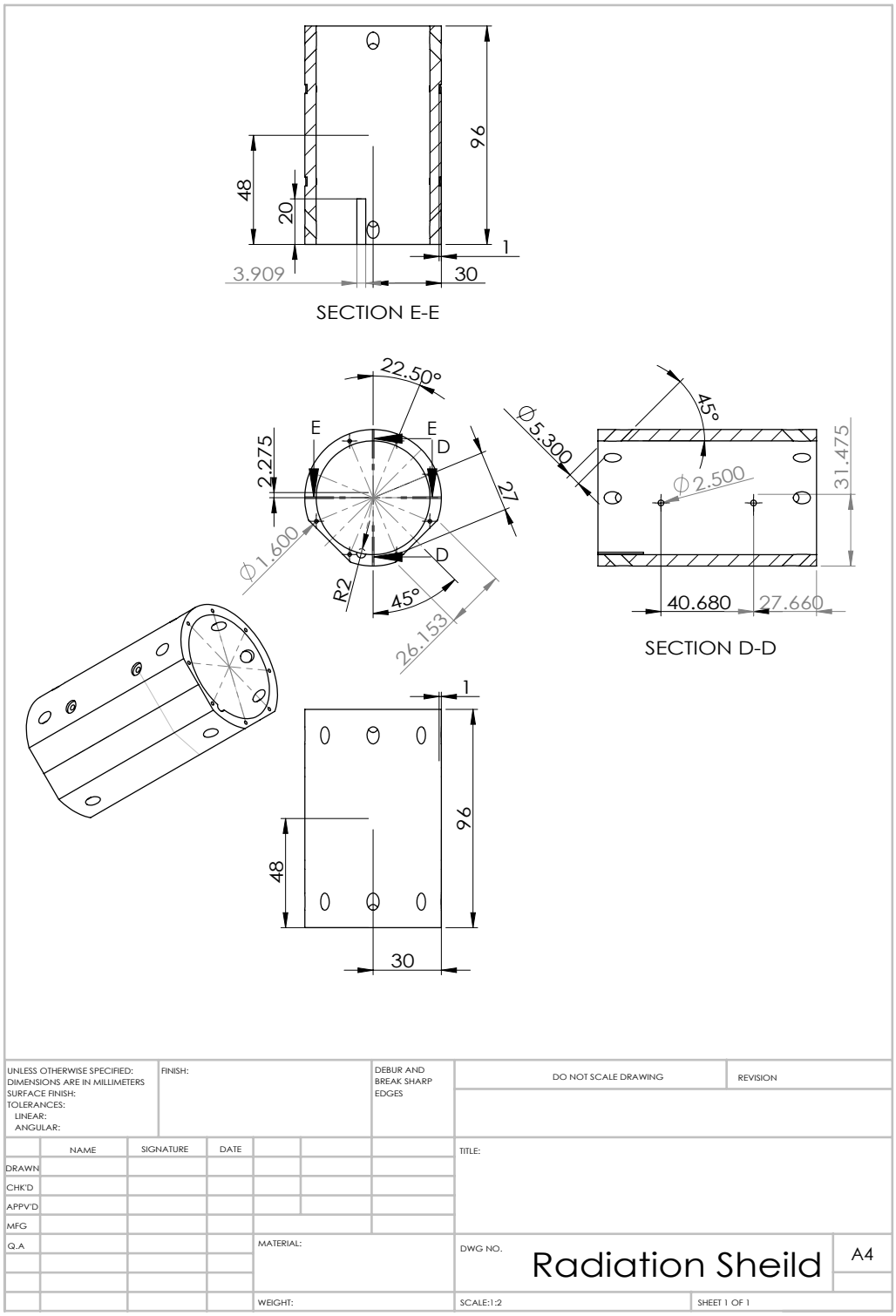
96
48
20
1
3.909
30
SECTION E-E
22.50°
E
E
D
D
2.275
27
Ø1.600
R2
45°
26.153
45°
Ø5.300
Ø2.500
31.475
40.680
27.660
SECTION D-D
1
96
48
30
UNLESS OTHERWISE SPECIFIED:
DIMENSIONS ARE IN MILLIMETERS
SURFACE FINISH:
TOLERANCES:
LINEAR:
ANGULAR:
FINISH:
DEBUR AND BREAK SHARP EDGES
DO NOT SCALE DRAWING
REVISION
NAME
SIGNATURE
DATE
TITLE:
DRAWN
CHK'D
APPV'D
MFG
Q.A
MATERIAL:
DWG NO.
Radiation Sheild
A4
WEIGHT:
SCALE:1:2
SHEET 1 OF 1

Papers

Paper I

Experimental quantum state tomography of a solid state qubit

L. Rippe, B. Julsgaard, A. Walther, Y. Ying and S. Kröll.
Phys. Rev. A **77**, 022307 (2008).

PHYSICAL REVIEW A **77**, 022307 (2008)

Experimental quantum-state tomography of a solid-state qubit

L. Rippe, B. Julsgaard, A. Walther, Yan Ying, and S. Kröll
Department of Physics, Lund Institute of Technology, P.O. Box 118, SE-22100 Lund, Sweden
(Received 25 July 2007; published 7 February 2008)

Quantum-state tomography is used to characterize the state of an ensemble based qubit implemented through two hyperfine levels in Pr^{3+} ions, doped into a Y_2SiO_5 crystal. We experimentally verify that single-qubit rotation errors due to inhomogeneities of the ensemble can be suppressed using the Roos-Mølmer dark-state scheme [Roos and Mølmer, Phys. Rev. A **69**, 022321 (2004)] Fidelities above >90%, presumably limited by excited state decoherence, were achieved. Although not explicitly taken care of in the Roos-Mølmer scheme, it appears that also decoherence due to inhomogeneous broadening on the hyperfine transition is largely suppressed.

DOI: 10.1103/PhysRevA.77.022307 PACS number(s): 03.65.Wj, 03.67.Lx, 42.50.Md, 42.50.Dv

I. INTRODUCTION

A large variety of systems are presently investigated in order to find out whether they can be used as hardware for quantum computers. The present work is carried out on a solid-state based system, rare-earth ions doped into inorganic crystals. As in several other solid-state systems the qubits are encoded in nuclear spin states, which for rare earths can have coherence times of seconds and where much longer coherence times are predicted [1]. For being a solid-state system the rare-earth ions are unusual because their optical transitions can have coherence times as long as several ms [2,3]. Quantum-state tomography has previously been carried out to characterize the fidelity by which superpositions on an optical transition can be manipulated [4]. However, since coherence times for the hyperfine states are several orders of magnitude longer, it is highly relevant to also investigate the fidelity of arbitrary qubit rotations using hyperfine qubits. Multiqubit gate operations can readily be implemented in the system because optical excitation of an ion will induce frequency shifts >100 MHz ($>10^4$ linewidths) of the optical transitions of nearby ions [5]. The large frequency shift of the optical transition makes it possible to entangle two nearby ions using operations with a duration of just a few ns [6]. A scalable implementation of the ensemble rare-earth ion scheme has been described by Wesenbeg *et al.* [6]. Scalability can also be achieved using a short lifetime readout ion. This ion acts as a state sensitive probe for the local environment [6] in a manner similar to how the electronic spin of a nitrogen-vacancy (N-V) center can probe the nuclear spin states of surrounding [13] C ions [7]. However, because of the hour-long lifetimes of the rare-earth-metal spin states [8,9], it is possible to also create qubits consisting of an ensemble of ions, all in a specific quantum state. A qubit can then be selectively manipulated by optical pulses [5,10–12] or by rf pulses directly [13], but in the latter case the possibility to have multiple qubits is reduced due to a much smaller range of spectral addressing.

These ensemble qubits, which give strong readout signals, can be used to investigate general properties of the system. Here, techniques are presented which enable arbitrary high fidelity single qubit operations even though the exact resonance and Rabi frequencies vary among the ions in the ensemble; but the techniques could also be very useful for single instance systems, in cases where parameters (e.g., Rabi or resonance frequencies) are uncertain or unknown to some degree, such as for quantum dots where fabrication techniques are not always 100% accurate. In this work ensemble qubits are used to experimentally carry out arbitrary rotations on the qubit Bloch sphere and the results are characterized by quantum-state tomography. The ability to have full qubit control represents an important advancement for these systems compared to more basic coherent effects like Raman echoes [14]. It can also be stressed that to just demonstrate basic coherent effects, there are actually fairly low requirements on pulse shape accuracy, laser stability, and ion homogeneity, etc., making the increase of the level of sophistication quite considerable when moving towards high fidelity operations, utilizing the full Bloch sphere.

II. MATERIALS AND METHODS

The relevant part of the $Pr^{3+}:Y_2SiO_5$ energy level diagram is shown in Fig. 1.

The qubit states $|0\rangle$ or $|1\rangle$ are represented by two of the three ground state hyperfine levels and the qubits can also be optically excited to the $|e\rangle$ state, which has a lifetime of 164 μs and a radiative lifetime of approximately 10 ms. Even if all ions in a specific qubit can be prepared in the $|0\rangle$ or $|1\rangle$ states using optical pumping, the ensemble approach brings additional problems because it has to be ascertained that all ions in a qubit have the same wave function. This is

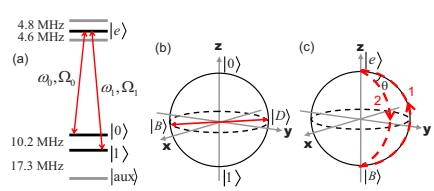

FIG. 1. (Color online) (a) Energy level diagram. (b) Qubit Bloch sphere, dark, $|D\rangle$, and bright states, $|B\rangle$, have been indicated. (c) Indicating the state transfer along paths 1 and 2 yielding an $e^{i\theta}$ phase shift of the bright state

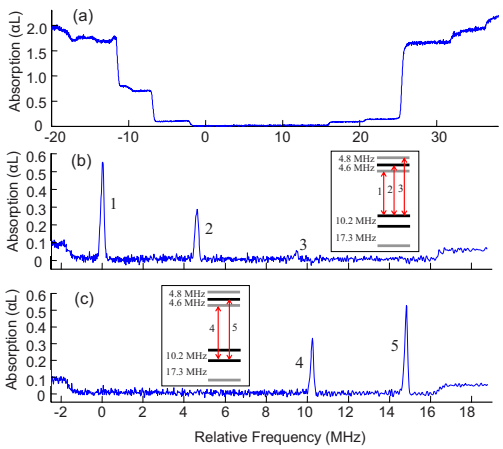

FIG. 2. (Color online) (a) Tailoring of the absorption profile, all ions within a 18 MHz spectral interval have been removed by optical pumping. b) A qubit is created by returning ions, which have their $|0\rangle$-$|e\rangle$ transition within 100 kHz from relative frequency 0, to the optically pumped region. (c) The qubit has been transferred from the $|0\rangle$ to the $|1\rangle$ state. The transfer efficiency is about 96%. The difference in peak height is caused by the difference in oscillator strengths for the involved transitions [17].

complicated by the facts that different ions within the qubit will (1) have slightly different optical transition frequencies, leading to both a different response to excitation pulses because some ions will be slightly off resonance and dephasing on the optical transition, (2) have slight differences in hyperfine transition frequencies, leading to a different response to excitation pulses as well as dephasing on the qubit transition, (3) experience different optical field strengths and have different Rabi frequencies, due to the spatial profile of the beam, which could result in different ions experiencing different pulse areas, and finally, (4) when implementing, e.g., two-qubit gates the interaction between an ion in the first qubit and the nearby ion in the second qubit will be different for different instances. However, the scheme for two-qubit gates is designed such that it compensates for the inhomogeneity of the ion-ion interaction [5] and complications 1 and 3 have been solved by employing the techniques described in [15]. Inhomogeneities in optical transition frequency and differences in Rabi frequency are compensated for by using complex hyperbolic secant pulses (abbreviated as compsech *pulses* through the rest of the text). These pulses efficiently transfer states on the Bloch sphere from one pole to the other, provided the Rabi frequencies of the individual ions are above a certain lower limit. This was experimentally verified in Ref. [10] and traces (b) and (c) in Fig. 2 also show a transfer from the $|0\rangle$ state to the $|1\rangle$ state with about 96% transfer efficiency. However, to demonstrate arbitrary operations on the qubit Bloch sphere, it is also necessary to address complication 2, the inhomogeneous broadening on the qubit transition. Therefore Roos-Mølmer [15] introduced a basis change such that operations from an arbitrary point on the qubit Bloch sphere [Fig. 1(b)] could be implemented as pole-to-pole transfers in the new base. The concept is schematically pictured in Fig. 1 and briefly described below. Two fields with optical frequencies ω_0 and ω_1 and Rabi frequencies Ω_0 and Ω_1 are driving the $|0\rangle$-$|e\rangle$ and $|1\rangle$-$|e\rangle$ transitions, respectively. Adjusting the field amplitudes such that $\Omega_0 = \Omega_1$ creates one bright state, $|B\rangle$, and one dark state, $|D\rangle$,

$$|B\rangle = |0\rangle - e^{-i\phi}|1\rangle, \quad |D\rangle = |0\rangle + e^{-i\phi}|1\rangle \tag{1}$$

depicted in the qubit Bloch sphere in Fig. 1(b). ϕ is the relative phase difference between the two fields. The dark state wave function is not changed by the driving fields, however, the interaction between the driving field and the ions will drive the bright state along, e.g., path 1, on the $|B\rangle$-$|e\rangle$ Bloch sphere [Fig. 1(c)]. If the fields Ω_0 and Ω_1 are compsech *pulses*, they will compensate for detunings on the optical transition frequency for the $|B\rangle \rightarrow |e\rangle$ transfer. If now the $|e\rangle \rightarrow |B\rangle$ transfer is carried out along a different path on the Bloch sphere, path 2, separated an angle θ from path 1, the bright state will have undergone the operation $|B\rangle = e^{i\theta}|B\rangle$. In the qubit basis ($|0\rangle$, $|1\rangle$), this is equivalent to the operation

$$U = e^{i\theta/2}\begin{pmatrix} \cos\frac{\theta}{2} & ie^{i\phi}\sin\frac{\theta}{2} \\ ie^{-i\phi}\sin\frac{\theta}{2} & \cos\frac{\theta}{2} \end{pmatrix}. \tag{2}$$

This matrix describes a unitary rotation about any axis on the equator of the Bloch sphere representing the qubit basis.

III. EXPERIMENTS

A. Setup and preperation

A Coherent 699-21 dye laser frequency stabilized against a spectral hole in a $Pr^{3+}:Y_2SiO_5$ crystal yielding a coherence time >100 μs and a frequency drift <1 kHz/s was used for the experiments [16]. The light passed twice through an 200 MHz acousto-optic modulator (AOM). This allows light pulses with arbitrarily chosen phase, amplitude, and frequency patterns to be created without any spatial displacement of the output beam. These pulses were then sent through a 350 MHz AOM driven by two rf frequencies separated by 10.2 MHz, which is the splitting between the qubit levels. In this way the first AOM produced the compsech *pulses* and the second AOM distributed them at frequencies ω_0 and ω_1, ascertaining that the pulses at the two frequencies had identical frequency chirp and amplitude envelope variations (but different overall amplitude, phase and center frequency). In these experiments exactly the same wave form was used in the first AOM for all the compsech *pulses*. The phase was controlled by the second AOM, where the voltage of the wave form feed to the AOM, for the ith pulse, is given by

$$U_i = U_{|0\rangle}\sin(\omega_{2,|0\rangle}t + 2\omega_1 t_{pc,i} + \tilde{\theta}_i) + U_{|1\rangle}\sin(\omega_{2,|1\rangle}t + 2\omega_1 t_{pc,i} + \tilde{\theta}_i + \phi_i), \tag{3}$$

where $U_{|0\rangle}$ and $U_{|0\rangle}$ are calibrated to give the same Rabi

frequency for the two transitions, and $\omega_{2,|0\rangle}$ and $\omega_{2,|1\rangle}$ are the frequencies for the second AOM that drives the $|0\rangle \rightarrow |e\rangle$ and $|1\rangle \rightarrow |e\rangle$ transitions, respectively. ω_1 is the center frequency for the first AOM compsech *pulses*, $t_{pc,i}$ is the time from the start of the sequence to the center of the ith pulse, while ϕ_i for the ith pulse and $\theta_{ij}=\tilde{\theta}_j-\tilde{\theta}_i$ for the ijth pulse pair are the two phase angles, ϕ and θ, as given by the dark state operation matrix, Eq. (2). After the AOMs the light was passed through a single-mode fiber to clean up the spatial mode. A few percent of the light was split off after the fiber and used as a reference. The rest of the light (about 50 mW) was focused onto a 0.5 mm thick Y_2SiO_5 crystal where 0.05% of the Y ions had been substituted by Pr^{3+} to a $1/e^2$ spot diameter of ~ 100 μm, yielding a Rabi frequency of maximum 2 MHz for the strongest transitions. The light transmitted through the crystal was imaged onto a 50 μm pinhole only transmitting light from the center of the laser spot in the sample. Within this region the intensity varied by less than 30%. Reference and signal beams were detected by two Thorlabs PDB150A detectors and the signals from the two detectors were divided to reduce the effect of laser amplitude fluctuations. The two-color compsech *pulses* used in the experiment had a duration of 4.4 μs and a full width at half maximum of 1.2 μs.

The qubits are created as in Refs. [10,17]. Figure 2(a) shows a part of the inhomogeneously broadened Pr^{3+} absorption line where all ions absorbing within an 18 MHz frequency interval have been transferred to other hyperfine states through optical pumping by repeatedly scanning the laser back and forth in frequency. The fraction of ions not removed is believed to be small but there will be a remaining absorption of a fraction of a percent, due to off resonant absorption by ions outside the burned pit. Ions within a narrow frequency range are transferred back into the emptied frequency interval and placed in the $|0\rangle$ state, creating a peak with an inhomogeneous width of about 170 kHz [Fig. 2(b)]. Because of the upper state hyperfine splitting, the presence of ions in the $|0\rangle$ state shows up in the absorption spectrum as three peaks separated by the upper state splittings, 4.6 and 4.8 MHz. All spectra in Figs. 2 and 3 are recorded using the rapid chirp techniques developed in Refs. [18,19]. Figure 2(c) shows the absorption spectrum after first applying one compsech *pulse* at the ω_0 frequency to the $|0\rangle$-$|e\rangle$ transition, bringing the entire population to the excited state, and then applying a second compsech *pulse* at the ω_1 frequency on the $|1\rangle$-$|e\rangle$ transition, transferring the population to the $|1\rangle$ state. The total transfer efficiency is about 96%. The homogeneous dephasing time, T_2, for the optical transitions generally depends on the density of excited state ions [20]. With a dopant concentration of 0.05% the density of excited ions for one excited, 170 kHz wide qubit is about $3\times10^{14}/\mathrm{cm}^3$, which corresponds to approximately 10^9 excited ions. From Ref. [21] this excited state density would give an excited state dephasing time of about 50 μs. This is consistent with our own photon echo measurements of the dephasing time when exciting one qubit. Simulating the state-to-state transfers with the compsech pulses used and a T_2 of 50 μs using a Bloch equation model, gives a maximum transfer efficiency of about 96%. It is consequently reasonable to assume that excited state dephasing is the main limiting factor for the transfer efficiency in Fig. 2(c).

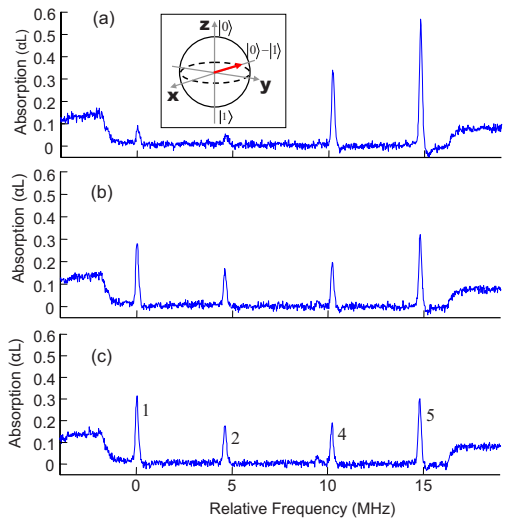

FIG. 3. (Color online) State tomography of the $|0\rangle$-$|1\rangle$ state. Traces (a)–(c) show the projection of the state on the x, y, and z axes, respectively. Numbers 1, 2, 4, and 5 in trace (c) refer to the numbering of the transitions in Fig. 2. Further explanation is given in the text.

B. Quantum-state tomography

We are now ready to use the two-color compsech *pulses*, employing the scheme outlined in Fig. 1 for performing arbitrary single qubit operations on qubits like the one shown in Fig. 2(b). Starting from state $|0\rangle$ [Fig. 2(b)] five different states on the Bloch sphere were prepared $|1\rangle$, $(|0\rangle+|1\rangle)$, $(|0\rangle-|1\rangle)$, $(|0\rangle+i|1\rangle)$, and $(|0\rangle-i|1\rangle)$ (normalization factors have been omitted for notational simplicity). To characterize the created state we calculate the fidelity, F, as $F=\langle\Psi_{\mathrm{theory}}|\rho_{\mathrm{expt}}|\Psi_{\mathrm{theory}}\rangle$, where Ψ_{theory} is the desired state and ρ_{expt} is given by [22]

$$\rho_{\mathrm{expt}}=0.5[\mathrm{tr}(\rho)I+\mathrm{tr}(X\rho)X+\mathrm{tr}(Y\rho)Y+\mathrm{tr}(Z\rho)Z]. \quad (4)$$

I is the identity matrix, X, Y, and Z are the Pauli matrices, and $\mathrm{tr}(X\rho)$, $\mathrm{tr}(Y\rho)$, and $\mathrm{tr}(Z\rho)$ are the experimental results from measurements of the projection of the prepared qubit state on the x, y, and z axes and $\mathrm{tr}(\rho)$ is set equal to unity. [It is here assumed that decay to the $|\mathrm{aux}\rangle$ state, Fig. 1(a), can be neglected and indeed the branching ratio to this state is small [17].]

In Fig. 3 the arrow in the direction of the negative x axis in the Bloch sphere schematically illustrates that the $(|0\rangle-|1\rangle)$ state has been prepared. Traces (a)–(c) show the results from the measurements of the projections of the $(|0\rangle-|1\rangle)$ state on the x, y, and z axes. The only experimental measurement at hand is to measure the z axis, i.e., a frequency re-

solved absorption measurement, telling the fraction of ions in the $|0\rangle$ and the $|1\rangle$ states. To measure the state projection on the x and y axes it is then necessary to carry out operations on the Bloch sphere rotating these axes to the z axis. However, rotating the x axis to the z-axis requires exactly the same pulses as creating the $(|0\rangle-|1\rangle)$ state from the $|0\rangle$ state and rotating the y axis to the z axis requires exactly the same pulses as creating the $(|0\rangle-i|1\rangle)$ state from the $|0\rangle$ state. Thus there is now sufficient information to carry out the single-qubit operation and the state tomography. First a qubit is prepared as in Fig. 2(b), then an operation on the $|B\rangle$-$|e\rangle$ Bloch sphere is done following the procedure in Fig. 1(c) where the angles ϕ and θ are chosen according to Eq. (2) in order to carry out the desired operation. The qubit preparation and the qubit rotation are carried out three times. The first time the rotation is followed by a second operation, rotating the x axis to the z axis [followed by an absorption measurement, compare Fig. 3(a)]. The second time, the rotation is followed by a rotation of the y axis to the z axis, [compare Fig. 3(b)], and finally the rotation is followed by a rotation of the z axis to itself by choosing θ in Fig. 1(c) equal to zero, bringing the bright state up and down along the same path (to make all three projection measurements equal). However, using only the pulses above the fidelity would be very low. The action of the two-color compsech *pulses* are to first promote the bright state to the excited state. In the general case the ions will then be in a superposition of the dark state and the excited state. Because of the inhomogeneous broadening of the optical transition, different qubit ions will acquire different phase factors while being in this superposition. However, a phase factor can be considered as global, and thus disregarded, if it appears in front of all qubit states. After the excited state has been returned to the bright state along path 2 in Fig. 1(c), the detuning dependent phase factor accumulated in the excited state can now also be accumulated on the dark state. By sending in two new two-color compsech *pulses*, identical with the previous pair except that, first, the phase ϕ [see Eq. (1)] now is increased by an amount π (this means the new pulses will act on the dark state), and second, θ is set equal to zero, which means the dark state is taken up and down on the $|D\rangle$-$|e\rangle$ Bloch sphere along the same route. Consequently U in Eq. (2) will (apart from an overall phase factor) for this second compsech *pulse* pair, be an identity operation. However, the dark state part of the wave function will still have acquired the excited state phase factor due to inhomogeneous broadening. Dephasing due to inhomogeneous broadening on the optical transition is now eliminated. A further discussion of this issue can be found in [15].

C. Results

As has been described, each single-qubit rotation as well as each tomography operation consists of four two-color compsech *pulses*. Two on the bright state and two on the dark state. In the present experiment each trace in Figs. 3(a)–3(c) is the result after applying eight two-color compsech *pulses*, where each such pulse is 4.4 μs long. The total sequence for each trace then is 35.2 μs. The fidelities obtained are given in Table I.

TABLE I. Fidelities for the single qubit rotation, F_{QR}, and single qubit rotation+quantum state tomography, $F_{\mathrm{QR+QST}}$, for five different states. A quantum-state tomography for the starting state, $|0\rangle-$, gives unity fidelity (within one standard deviation).

	$\|0\rangle-$	$\|1\rangle$	$\|0\rangle+\|1\rangle$	$\|0\rangle-\|1\rangle$	$\|0\rangle+i\|1\rangle$	$\|0\rangle-i\|1\rangle$
F_{QR}		0.96(2)	0.93(1)	0.93(1)	0.92(2)	0.91(2)
$F_{\mathrm{QR+QST}}$	1.02(2)	0.92(3)	0.87(1)	0.87(2)	0.85(4)	0.84(4)

Two different fidelities are given, $F_{\mathrm{QR+QST}}$ is the fidelity calculated according to Eq. (4), where indices QR and QST stand for qubit rotation and quantum-state tomography, respectively. However, since the QR+QST operation just is two consecutive QR operations, it is reasonable to state the fidelity for a single qubit rotation, F_{QR}, as $(F_{\mathrm{QR+QST}})^{1/2}$. Thus the fidelities for the single qubit operations are estimated to lie between 0.9 and 0.96, giving an average single operation fidelity of 0.93.

The fidelities obtained are remarkably good considering the dephasing times of the system. The average time spent in the upper state during the QR+QST operation is $t_u=8.8$ μs. The gives $e^{-t_u/T_2}=0.84$, which, assuming $\rho=0.84\rho(\text{prepared state})+0.16\rho(\text{mixed state})$, would give a best case fidelity of 0.92. Another potential contribution to lower fidelity comes from the dephasing time on the hyperfine (hf) qubit transition, $T_{2,\mathrm{hf}}$. To estimate this contribution, optically detected free induction decay (FID) at the qubit transition was used. A two-color dark state pulse was used to put the qubit in a superposition state between the qubit levels. This hyperfine coherence was then probed by a pulse resonant with one of the excited state levels. The result will be 10.2 MHz beating on the probe, and experiments with different delays for the probe pulse can be made. The strength of the beat signal as a function of probe delay will give the decay of the hyperfine coherence. The complete QR+QST sequence is 35.2 μs. From the FID measurement only about 20% of the qubit coherence remained after 35 μs. The decoherence is reversible and caused by the inhomogeneous broadening of the qubit transition.

IV. CONCLUSIONS

We have experimentally demonstrated a full solid-state hyperfine qubit in an inhomogeneously broadened ensamble system, using only optical techniques. The inhomogeneities on the optical transition, as described in Sec. II, were compensated for by the use of specially shaped compsech pulses, which are also robust against errors in, e.g., the Rabi frequency. The efficiency of the pulse techniques, described in [15], were demonstrated by performing arbitrary single qubit operations with more than 90% fidelity.

However, due to the inhomogeneity of the hyperfine levels, as demonstrated above, only about 20% of the the qubit coherence remains after the full experiment, which may make the fidelities obtained seem rather remarkable. Possibly, this could be explained by the results in Ref. [23], where it has been shown that dynamical Stark shift occurring dur-

ing qubit rotation can suppress errors due to inhomogeneous shifts of the qubit levels by as much as a factor of 10. It could also be a Zeno effect, which has been encountered previously in similar systems, such as N-*V* centers [24]. Still it would definitely be interesting to further investigate the effect of the inhomogeneous broadening on the QR fidelity.

The single qubit rotation fidelities could be improved (1) by using pulses of shorter duration developed by optimal control theory [25,26], (2) by using the single instance scheme [6] which eliminates errors due to inhomogeneous broadening on the hyperfine and optical transitions, or (3) by instead of the Pr ion use the Eu ion, where the upper state dephasing time is an order of magnitude longer. Assuming the fidelities in this work are limited by T_2 and $T_{2,\mathrm{hf}}$, one or several of these changes should enable fidelities above 0.99. To get fidelities significantly beyond this value, harder focusing of the light beam to increase the Rabi frequencies and/or dark state schemes not populating the excited state [27,28] would probably need to be used.

ACKNOWLEDGMENTS

This work was supported by the European Commission through the ESQUIRE project and the integrated project QAP under the IST directorate, by the Knut and Alice Wallenberg Foundation, and the Swedish Research Council. B. Julsgaard was partly supported by the Carlsberg Foundation.

[1] J. J. Longdell, A. L. Alexander, and M. J. Sellars, Phys. Rev. B **74**, 195101 (2006).
[2] R. W. Equall, Y. Sun, R. L. Cone, and R. M. Macfarlane, Phys. Rev. Lett. **72**, 2179 (1994).
[3] Y. Sun *et al.*, J. Lumin. **98**, 281 (2002).
[4] J. J. Longdell and M. J. Sellars, Phys. Rev. A **69**, 032307 (2004).
[5] N. Ohlsson, R. K. Mohan, and S. Kröll, Opt. Commun. **201**, 71 (2002).
[6] J. H. Wesenberg, K. Molmer, L. Rippe, and S. Kroll, Phys. Rev. A **75**, 012304 (2007).
[7] L. Childress *et al.*, Science **314**, 281 (2006).
[8] F. Könz, Y. Sun, C. W. Thiel, R. L. Cone, R. W. Equall, R. L. Hutcheson, and R. M. Macfarlane, Phys. Rev. B **68**, 085109 (2003).
[9] N. Ohlsson, M. Nilsson, and S. Kröll, Phys. Rev. A **68**, 063812 (2003).
[10] L. Rippe, M. Nilsson, S. Kroll, R. Klieber, and D. Suter, Phys. Rev. A **71**, 062328 (2005).
[11] F. de Seze *et al.*, Eur. Phys. J. D **33**, 343 (2005).
[12] M. Tian, Z. W. Barber, J. A. Fischer, and Wm. Randall Babbitt, Phys. Rev. A **69**, 050301(R) (2004).
[13] E. Fraval, M. J. Sellars, and J. J. Longdell, Phys. Rev. Lett. **95**, 030506 (2005).
[14] B. S. Ham, M. S. Shahriar, M. K. Kim, and P. R. Hemmer, Phys. Rev. B **58**, R11825 (1998).
[15] I. Roos and K. Mølmer, Phys. Rev. A **69**, 022321 (2004).
[16] B. Julsgaard, L. Rippe, A. Walther, and S. Kröll, Opt. Express **15**, 11444 (2007).
[17] M. Nilsson, L. Rippe, S. Kroll, R. Klieber, and D. Suter, Phys. Rev. B **70**, 214116 (2004).
[18] T. Chang *et al.*, Opt. Lett. **30**, 1129 (2005).
[19] F. Wolf, J. Phys. D **27**, 1774 (1994).
[20] J. Huang, J. M. Zhang, A. Lezama, and T. W. Mossberg, Phys. Rev. Lett. **63**, 78 (1989).
[21] R. W. Equall, R. L. Cone, and R. M. Macfarlane, Phys. Rev. B **52**, 3963 (1995).
[22] M. A. Nielsen and I. L. Chuang, *Quantum Computation and Quantum Information* (Cambridge University Press, Cambridge UK, 2000), Chap. 8.4.2, Eq. 8.148.
[23] K. Tordrup and K. Mølmer, Phys. Rev. A **75**, 022316 (2007).
[24] J. Wratchrup and F. Jelezko, J. Phys.: Condens. Matter **18**, 807 (2006).
[25] J. H. Wesenberg, Phys. Rev. A **69**, 042323 (2004).
[26] A. Sporl, T. Schulte-Herbruggen, S. J. Glaser, V. Bergholm, M. J. Storcz, J. Ferber, and F. K. Wilhelm, Phys. Rev. A **75**, 012302 (2007).
[27] H. Goto and K. Ichimura, Phys. Rev. A **74**, 053410 (2006).
[28] H. Goto and K. Ichimura, Phys. Rev. A **75**, 033404 (2007).

Paper II

Extracting high fidelity quantum computer hardware from random systems

A. Walther, B. Julsgaard, L. Rippe, Y. Ying, S. Kröll, R. Fisher and S. Glaser.

Phys. Scr. **T137**, 014009 (2009).

IOP PUBLISHING PHYSICA SCRIPTA
Phys. Scr. **T137** (2009) 014009 (10pp) doi:10.1088/0031-8949/2009/T137/014009

Extracting high fidelity quantum computer hardware from random systems

A Walther[1], B Julsgaard[1,3], L Rippe[1,4], Yan Ying[1], S Kröll[1], R Fisher[2] and S Glaser[2]

[1] Department of Physics, Lund University, PO Box 118, SE-22100 Lund, Sweden
[2] Department Chemie, Technische Universität München, Lichtenbergstrasse 4, 85747 Garching, Germany

E-mail: Stefan.Kroll@fysik.lth.se

Received 16 October 2009
Accepted for publication 23 October 2009
Published 14 December 2009
Online at stacks.iop.org/PhysScr/T137/014009

Abstract
An overview of current status and prospects of the development of quantum computer hardware based on inorganic crystals doped with rare-earth ions are presented. Major parts of the experimental work in this area have been done in two places, Canberra, Australia and Lund, Sweden, and the present description follows more closely the Lund work. Techniques will be described that include optimal filtering of the initially inhomogeneously broadened profile down to well separated and narrow ensembles, as well as the use of advanced pulse-shaping in order to achieve robust arbitrary single-qubit operations with fidelities above 90%, as characterized by quantum state tomography. It is expected that full scalability of these systems will require the ability to determine the state of single rare-earth ions. It has been proposed that this can be done using special readout ions doped into the crystal and an update is given on the work to find and characterize such ions. Finally, a few aspects on possibilities for remote entanglement of ions in separate rare-earth-ion-doped crystals are considered.

PACS numbers: 03.65.Wj, 03.67.Hk, 42.50.Md

(Some figures in this article are in colour only in the electronic version.)

1. Introduction

Many solid state quantum computing systems rely on a top down approach with carefully crafted systems, where parameters are designed during the manufacturing or growth process, for instance, superconducting qubits [1, 2], quantum dots [3] and the Kane model [4]. At the other end of the scale there are bottom up approaches, where useful hardware can be extracted out of random materials that intrinsically have very favorable properties, such as nitrogen vacancy (NV)-centers [5] and rare-earth-ion-doped inorganic crystals [6]. In this paper, we will discuss the development of quantum computer hardware based on inorganic crystals doped with rare earth ions. Such crystals are used extensively in current technology, e.g. as active laser materials or as scintillating materials in x-ray detectors. They are manufactured in single crystal growth processes where a dopant material is added during the growth such that the dopant ions replace host ions in the regular crystal lattice at concentrations that may range between 0.01 and 10% depending on application. Although the average concentration is defined by the dopant concentration in the crystal melt, the relative positions of the dopant ions are largely random. However, randomness and less precise control of construction and growth parameters can be compensated for by using suitable quantum computing schemes and by developing robust pulses enabling high fidelity qubit operations.

The next section (section 2) will describe basic properties of rare-earth-ion-doped crystals relevant for quantum information. This includes coherence times which can be several seconds [7] and ion–ion interactions as a mechanism for gate operations. For a laser beam passing through a rare-earth-ion-doped crystal there may be 10^{15} ions within the laser focal region. However, qubits can still be

[3] Now with Department of Physics and Astronomy, Aarhus University, Ny Munkegade 120, DK-8000, Aarhus C, Denmark.
[4] Now with National Center for Atmospheric Research, NCAR Boulder, CO, USA.

Phys. Scr. **T137** (2009) 014009

created and prepared in well-defined states and arbitrary qubit operations, characterized by full quantum state tomography, give fidelities, F, in the range $0.91 < F < 0.96$ [8]. A brief description of the experimental set-up, including the pulse-shaping system, will be given in section 3, while section 4 describes how to efficiently initialize the system into well-defined qubits, which are inhomogeneous subgroups out of these 10^{15} ions. In section 5, we show experimental data on qubits prepared in arbitrary superposition states and characterized by quantum state tomography. The high fidelity results are all based on qubit operations that are robust against individual differences between the ions [9, 10]. We will also present data from the development and use of optimal pulse sequences [11] for operation fidelities >0.96. Section 6 starts with a description of how to, in contrast to the experiments mentioned above, create qubits in these crystals that each consist of just a single ion, which offers better scalability. The single ion qubit scheme [12] is based on co-doping the crystals with 'readout ions'. Such readout ions should have a short upper state lifetime in order to enable repeated cycling. One such candidate is the 4f to 5d transition in Ce^{3+} and experimental data to characterize this transition are also presented in section 6. The last section before the summary contains a discussion on entanglement of remote qubits and further scalability.

2. Rare-earth-ion-doped crystals

A major strength of using rare-earth ions as qubits the long coherence times. In these ions, transitions within unfilled electron shells are partially shielded from environmental dephasing mechanisms by energetically lower, but outer-lying, filled shells. The present results were obtained using the $^3H_4 \rightarrow {}^1D_2$ transition in Pr^{3+}:Y_2SiO_5 at 606 nm [13]. For temperatures below 4 K, the Pr^{3+} ions in this material has an electronic state lifetime of 164 μs, and a coherence time, T_2, of about 100 μs (somewhat depending on the density of excited states in the material). By applying magnetic fields, however, this time can be increased, and there are also other rare-earth ions, which have even longer coherence times, for example Er, where a T_2 of 6.4 ms has been measured [14].

The qubit states are not represented by electronically excited states though, but rather by ground state hyperfine levels, shown in the level diagram of Pr^{3+} in figure 1. For Pr^{3+}:Y_2SiO_5, the hyperfine lifetime is about 90 s and the coherence time about 500 μs. The hyperfine T_2 can also be increased by magnetic fields, and up to 860 ms has been demonstrated [15]. In addition, dynamic decoupling sequences (bang–bang pulses) can also be applied to further increase the coherence time to more than 30 s [7].

The rare-earth ions are randomly doped into the host crystals, replacing one of the host ions in the lattice. This replacement causes changes to the crystal electric field which then causes each rare-earth ion to pick up a shift in its resonance frequency. This amounts to a large inhomogeneous broadening of the absorption line. For Pr^{3+}, the inhomogeneous linewidth is about 5 GHz, which can be compared to the homogeneous linewidth of about 3 kHz, given by the optical T_2, mentioned above.

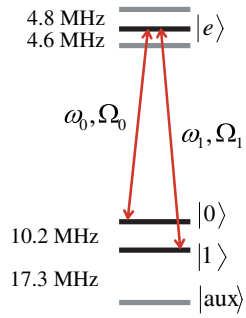

Figure 1. Relevant energy level structure for the Pr^{3+} ion transition utilized in the present work.

In the rare-earth quantum computing scheme, the inhomogeneous structure is of significant importance, as multiple qubits are addressed in the frequency domain, each qubit having a different resonance frequency. From above, the ratio of inhomogeneous over homogeneous linewidth is about 10^6 for Pr^{3+}:Y_2SiO_5, but since ions do not have only a single transition frequency, the number of frequency channels is in practice much smaller. Figure 1 shows that the lowest and the highest transition frequency for a given ion differ by $4.8 + 4.6 + 10.2 + 17.3 = 36.9$ MHz. Thus, about 100 individual frequency channels is a more realistic value. The Pr^{3+} ion sits in a non-centrosymmetric site, and thus has a permanent electric dipole moment. The value of this dipole moment depends on the electron configuration and the value of the dipole moment of an electronically excited state is therefore different from that of the ground state. Qubit–qubit gates can then be executed through dipole–dipole interactions. Since the dipole moment changes when the ion becomes excited, exciting an ion will shift the transition frequency of all near-lying ions. An ion belonging to one qubit can then be controlled by the excitation of an another ion, belonging to another qubit, if they are spatially sufficiently close to each other. This effect is used as the control mechanism for conditional gates, and the basis for this was demonstrated in [10].

3. Experimental set-up

The experimental system is based around a Coherent 699-21 ring dye laser, stabilized to 1 kHz linewidth, by locking to a spectral hole in a Pr^{3+}:Y_2SiO_5 crystal [16]. The rare-earth crystal used in the experiments is a 0.5 mm thick Pr^{3+}:Y_2SiO_5 crystal with a Pr^{3+} doping concentration of 0.05%, which gives a maximum optical density of about 2–3. In order to get rid of phonon interactions, the crystal is submerged in liquid helium and cooled to 2 K. The available laser power is of the order of 100 mW before the cryostat, which translates into maximum Rabi frequencies of about 1–3 MHz, depending on which transition is targeted, given a laser focus of 100 μm.

High fidelity gates require a high-performance pulse-shaping system, as will be further discussed in section 5. Two acousto-optic modulators (AOMs) are used to create the

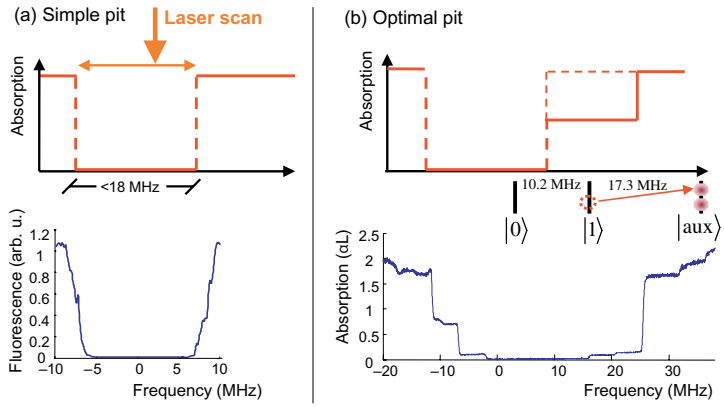

Figure 2. Panel (a) shows a simple pit created by repeated scanning across an interval less than 18 MHz. Panel (b) displays an improved pit, where scans on multiple intervals have been iteratively repeated in order to shuffle all ions outside the pit as far out as possible, thereby creating an optimal pit. Also note that the scales in the two experimental figures are different.

desired pulses. The incoming continuous wave (CW) photons are deflected by an RF acoustic wave in the AOMs. By varying the power of the acoustic wave, the amplitude of the deflected light is controlled. By virtue of energy and momentum conservation, the deflected photons must increase their frequency by an amount equal to that of the phonons. Thus, by varying the frequency of the acoustic wave we directly control the frequency of the light pulse, and furthermore, by changing the phase of the acoustic wave we also gain control over the optical phase of the light, which is necessary for controlling the coherent interaction with the ions. For these modulators, the power conversion from RF wave to light amplitude is quite nonlinear. In order to achieve high accuracy of the pulse amplitude envelopes over as much as six orders of magnitude in dynamic range, an elaborate calibration system that also includes the power dependence on RF frequency was setup. The first AOM has a center frequency of 200 MHz and is aligned in a double pass configuration, in order to cancel out spatial movement of the deflected beam. After both passes the AOM has a total deflection range of 200 MHz. The second AOM has a 360 MHz center frequency, and is used only to split a pulse at a single frequency into two frequencies, such that an excitation pulse can be resonant with the $|0\rangle \rightarrow |e\rangle$ and $|1\rangle \rightarrow |e\rangle$ transitions at the same time, as further discussed in section 5.1.

4. Qubit initialization

Starting from the inhomogeneous distribution, we employ advanced optical hole-burning sequences in order to extract a useful qubit system. Initially, the ions occupy all three ground states, and the absorption at any given frequency within the absorption profile, contains contributions from all nine possible transitions (see figure 1). The goal of the hole-burning is to initialize a narrow controlled ensemble of ions into the $|0\rangle$ state, well separated in frequency from any other ion.

First, a wide spectral hole, henceforth called a *pit*, is created. The hyperfine level splittings set the limit for the maximum frequency range of such a pit. Since the ions must be in one of the ground states, it cannot be larger than 27.5 MHz, as can be seen in figure 1. This maximum width is then further reduced by the excited state splitting down to 18.1 MHz. Scanned laser pulses target specific transitions inside this 18 MHz region, and are repeated in order to create a spectral pit where all ions have been removed within an interval of maximum 18 MHz. Such a simple pit is shown in figure 2(a).

Eventually, qubit operation pulses will be used inside the pit structure, and it then becomes important to minimize the interactions between the tails of such pulses and the edges of the pit. The pit shown in figure 2(a) displays non-optimal edges that are a bit rounded and also go up to the maximum αL immediately. In order to improve on this, a more elaborate pit-burning scheme was introduced. In this scheme, pulses that target specific levels of Pr^{3+} outside the pit are used in order to burn them even further out, as illustrated by the top part of figure 2(b). For an ion having a particular frequency relative to the pit, as the ion illustrated in this figure, level $|0\rangle$ and $|1\rangle$ are targeted in an optical pumping process that eventually transfers them to their $|\text{aux}\rangle$ state. After this, ions of other frequency ranges might fall back down inside the pit, and the initial pit-burning pulses will have to be repeated iteratively together with the secondary pulses to keep the center of the pit empty. A similar procedure is then also repeated on the left side of the pit in order to achieve an optimal result, shown in the lower part of panel (b). A more extensive description of the burning procedure can be found in [17] and a detailed list of the exact pulses used to burn such an optimal pit can be found in [18].

After an empty spectral pit has been created, a qubit ensemble can be initialized inside the pit by a *'burnback'* pulse sequence. These pulses can with benefits be coherent pulses that transfer ions from outside the pit, say at higher frequencies, first to the excited state, and from there down to one of the ground states in a controlled manner. Figure 3(a) shows the system initialized to one of the ground states, in this case the $|0\rangle$ state.

Phys. Scr. **T137** (2009) 014009

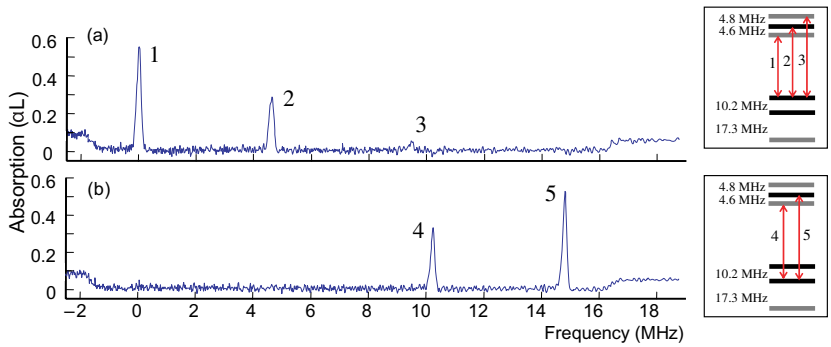

Figure 3. Panel (a) shows the rare-earth qubit system initialized to the $|0\rangle$ state, visible through the three absorption peaks from this state. Panel (b) shows the system after a coherent transfer over to the $|1\rangle$ state.

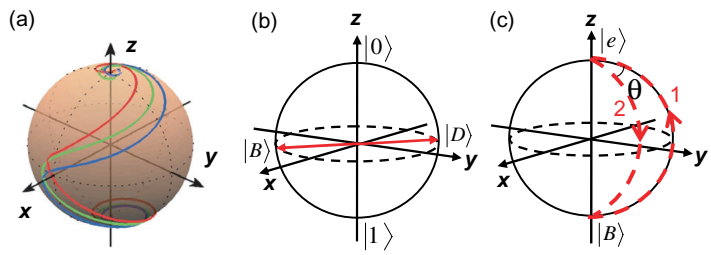

Figure 4. Panel (a) shows the paths taken by three ions with different resonance frequencies, while being transferred to the excited state by a coherent sechyp pulse. Panel (b) illustrates the dark and the bright states on the Bloch sphere, relevant for the gate operations, and panel (c) shows a full qubit gate operation by means of two consecutive dark state pulses (two-color pulses). Note that the transfer in (c) is going from and to the *bright* state.

5. Qubit gate operations

The ensemble qubit is now initialized to the $|0\rangle$ state. In order to be able to perform high fidelity gate operations, we must now find pulses that compensate for the inhomogeneous broadening of the ensemble, which would otherwise cause dephasing during the excitation. One type of pulses that are robust against such dephasing are the complex hyperbolic secant pulses, or *sechyp* for short. The amplitude envelope of these follow a hyperbolic secant shape, while at the same time the pulse is chirped according to a hyperbolic tangent function, centered around the mean ensemble transition frequency. Such pulses can efficiently transfer an inhomogeneous ensemble between the two poles on a Bloch sphere, as illustrated in figure 4(a). The different lines correspond to ions with different atomic resonance frequencies, which can all be seen to converge at the top. The robustness of these pulses has been verified experimentally by transfer efficiencies of 97% for ensembles inhomogeneously broadened more than 100 linewidths. Figure 3(b) shows the system after such a sechyp transfer from $|0\rangle \rightarrow |e\rangle$ immediately followed by a transfer from $|e\rangle \rightarrow |1\rangle$. In addition to this, the sechyp pulses also have the good property that they are robust against fluctuations in laser power. While normal square- or Gaussian-shaped pulses need to have very well tuned values of laser intensity and duration in order to get the correct pulse area, the sechyp pulses simply need to be above a certain threshold Rabi frequency, above which they always work with high efficiency. This independence of the light intensity can be intuitively perceived from the Bloch sphere in figure 4(a), where we see that as the different components approach their final state, they circle around the top pole, and a higher Rabi frequency would just make them circle around the z-axis faster, not take them away from the desired state. These pulses were investigated more carefully in [9].

5.1. Dark state gates

The sechyp pulse-shapes solve the problem of inhomogeneous dephasing as well as offer a robustness with respect to fluctuating experimental parameters, but can only perform pole-to-pole transfers, not create arbitrary superposition states. The qubit is the two hyperfine levels denoted $|0\rangle$ and $|1\rangle$ in figure 1, and to perform operations between these states, two-color fields, which are resonant with $|0\rangle \rightarrow |e\rangle$ and $|1\rangle \rightarrow |e\rangle$ at the same time, are employed [9]. Determined by the phase relation, ϕ, between the two fields, two superposition states, shown in figure 4(b), the bright and the dark state:

$$\begin{cases} |B\rangle = \frac{1}{\sqrt{2}}\left(|0\rangle - \mathrm{e}^{-\mathrm{i}\phi}|1\rangle\right), \\ |D\rangle = \frac{1}{\sqrt{2}}\left(|0\rangle + \mathrm{e}^{-\mathrm{i}\phi}|1\rangle\right), \end{cases} \tag{1}$$

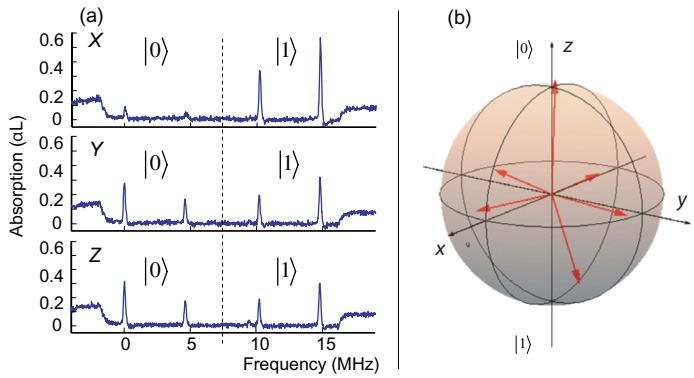

Figure 5. Panel (a) shows the projective measurements on the x-, y- and z-axes, respectively. The two left peaks are both transitions from the $|0\rangle$ state and correspond to a +1 measurement value, while the two right peaks similarly are transitions from the $|1\rangle$ state and correspond to a -1 value with respect to the current axis. Panel (b) shows the result of a quantum state tomography of the six states along the positive and negative axes.

can be defined. Similarly to electromagnetically induced transparency (EIT), the dark state does not interact with the light. Thus, the two-color pulse will only target the bright state, and two consecutive transfers, first from $|B\rangle \rightarrow |e\rangle$ and then from $|e\rangle \rightarrow |B\rangle$, but going down along a different path as illustrated in figure 4(c), will add a phase angle enclosed by the rotation, θ, to the bright state: $|B\rangle \rightarrow e^{i\theta}|B\rangle$. This operation can be rewritten in the computational basis ($|0\rangle$,$|1\rangle$), and then becomes

$$U_{\text{dark}} = e^{i\theta/2} \begin{bmatrix} \cos(\theta/2) & i\,e^{i\phi}\sin(\theta/2) \\ i\,e^{-i\phi}\sin(\theta/2) & \cos(\theta/2) \end{bmatrix}, \qquad (2)$$

which is a matrix describing an arbitrary rotation around any vector on the equator of the Bloch sphere. By picking suitable phase angles, one can thus perform any qubit gate operation [9].

These dark state gates were implemented, and the qubit superposition states that were created as a result of the rotations were characterized using quantum state tomography. In figure 5(a), the readout of a particular superposition state, $\frac{1}{\sqrt{2}}(|0\rangle - |1\rangle)$ is shown as an example. The three curves correspond to projection measurements on the x-, y- and z-axes, respectively. As expected, we see that both the y and the z measurements contain equal contributions from either state, but the x measurement gives a projection onto one of the states. States corresponding to the six different (positive and negative) axes on the Bloch sphere were prepared and characterized, and the resulting state vectors inscribed in a Bloch sphere are displayed in figure 5(b).

The z-projection was done through an absorption measurement, where the two leftmost peaks in figure 5 correspond to transitions from the $|0\rangle$ state and the two rightmost peaks correspond to transitions from the $|1\rangle$ state. In order to do the x- and y-measurements, suitable rotations were first performed to rotate those axes onto the z-axis, such that an absorption measurement now gives the same result as a direct x- or y-measurement would have, in the original basis. From those measurements the density matrix can then be calculated through (see e.g. [19])

$$\rho = \frac{\text{tr}(\rho)I + \text{tr}(X\rho)X + \text{tr}(Y\rho)Y + \text{tr}(Z\rho)Z}{2}, \qquad (3)$$

where X, Y and Z correspond to the Pauli matrices, which together with the identity, I, span the 2×2 qubit space in the density matrix representation. The above equation is useful because the traces correspond to actual physical measurements. For example, $\text{tr}(Z\rho)$ means measuring the projection of the unknown state onto the Z axis, which will yield a value between -1 and +1, and the same for the other axes. The fidelity of the entire procedure can then be calculated from

$$F_{\text{tot}} = \langle\psi_{\text{theor}}|\rho_{\text{exp}}|\psi_{\text{theor}}\rangle, \qquad (4)$$

i.e. the overlap between the theoretical and the experimental representations. For the six states displayed in figure 5(b), the total fidelities were all between 0.84 and 0.92. As mentioned above the total procedure consists of two rotations, first one to create the state, then another one to perform the measurement on the right basis. Thus, the fidelity for a single qubit gate can be expressed as $F_{\text{gate}} = \sqrt{F_{\text{tot}}}$, and we see that the qubit gate fidelities are in the range of $0.91 < F_{\text{gate}} < 0.96$. More information and discussion regarding these results can be found in [8, 18].

5.2. *Optimal control pulses*

Even though the dark state qubit gates were realized with good fidelity there are still reasons to search for further improvements. The total duration of the dark state pulses that perform one arbitrary qubit rotation is close to 18 μs. The employed laser power on the other hand, typically provides Rabi frequencies of the order of 1 MHz, which indicates that the qubit rotations could probably be performed an order of magnitude faster, with an optimal scheme. To reduce the operation time, pulses obtained through optimal control theory calculations are currently investigated.

Phys. Scr. **T137** (2009) 014009

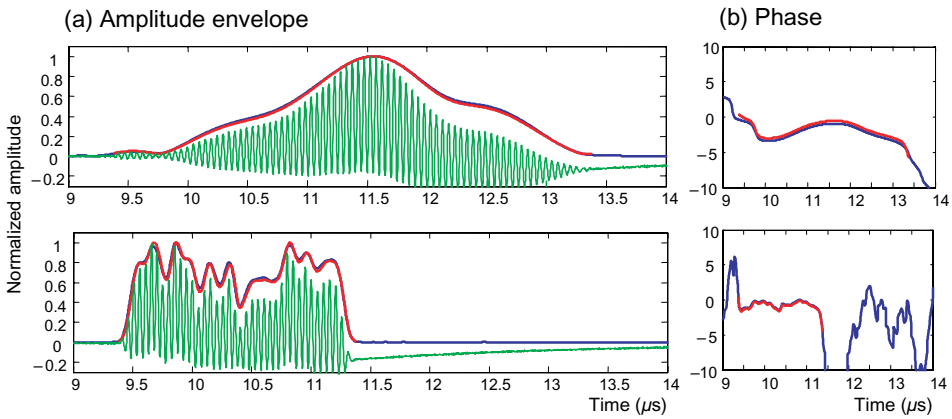

Figure 6. Two pulse shapes with different bandwidths, both designed by optimal control algorithms to perform efficient state-to-state transfers. The left side shows the detected beating and the amplitude envelope, while the right side shows the phase evolution. In both cases the red line is the theoretically desired shape, while the blue line is the experimentally detected shape, and in both cases they match very well. Note that in the phase plot, the phase does not have any meaning outside the pulse envelope (since the amplitude there is zero).

Optimal control theory provides a framework for finding the best set of controls to steer a system so that a desired target state or unitary gate is implemented. In some special cases these controls can be determined analytically, see for example [20–22]. In addition, powerful numerical methods [23] are available that make it possible to explore the physical limits of time-optimal control experiments in cases where no analytical solutions are known. These methods have so far been successfully applied to spin systems [24–26], superconducting qubits [27] and trapped ions [28]. Optimized pulses can be designed to account for experimental errors, and, if a realistic model is available, can include multiple system levels and transitions.

The basic idea of optimal control algorithms is to minimize a cost function, which is determined by the physical system at hand. In the present case, this is given by the light-field interaction with the Pr^{3+} ion, and in addition to this, a number of experimental limitations, such as AOM maximum bandwidth or laser power fluctuations, are enforced as well. The algorithm then finds a pulse shape that performs a particular operation to a specified minimum fidelity, while staying within the restrictions. It can be noted that the solution is not necessarily unique, or even at the global maximum, and the shapes that come out of the calculations are then often strange-looking, without obvious intuitive explanations. In order to characterize how well the AOM system could reproduce these strange shapes, an interference experiment was set up, where the AOM pulse-shaping system is put in one arm and the light passing through this part then interferes with the light from an undisturbed part of the laser. The result is a beating, from which both the amplitude envelope and the phase evolution of the pulses can be obtained via a Fourier transform. Figure 6 shows two examples of such pulses. In panel (a) of this figure, the green, oscillating curve is the detected beating, the blue line is the amplitude envelope of the beating, which is almost perfectly overlapping with the red line, which is the theoretically desired shape (may be hard to see if not in color).

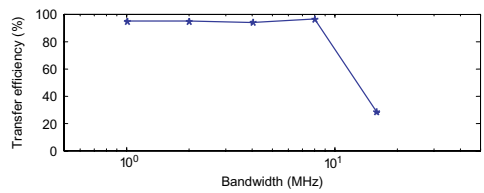

Figure 7. Transfer efficiency of $|0\rangle \rightarrow |e\rangle$ by means of optimal control pulses as a function of bandwidth.

The upper and lower pulses differ in the allowed bandwidth. The lower pulse has a bandwidth of about 16 MHz, while the upper pulse has been restricted to work with a bandwidth of only 2 MHz. Ideally, one would want as high bandwidth as possible, since this enables pulses with shorter duration. The right side of figure 6 displays the phase evolution of the detected pulses as well as the desired phase chirp, and again, there is almost perfect overlap. In order to test the optimal control results, a series of five pulses were designed, each one with the same objective, to do a state-to-state transfer from $|0\rangle$ to $|e\rangle$, but with different bandwidths. The resulting efficiency as a function of bandwidth is shown in figure 7. As can be seen, the efficiency is very good for all bandwidths except the highest (16 MHz). The reason for this is not yet fully known, but is believed to be related to complications that arise when multiple levels are involved. From the level diagram (figure 1) we see that any pulse that centers around the $|0\rangle \rightarrow |e\rangle$ transition and has a bandwidth less than $2 \times 4.6 = 9.2$ MHz will only involve those two levels and nothing else, but any pulse with a higher bandwidth will automatically involve at least the two other excited states as well, which creates a much more complicated situation. For two-level schemes, other groups have also obtained very good results, for example in ion traps [11]. But clearly, there should also be suitable optimal

pulses for three-level configurations. Thus, the good results for the simpler pulses together with the potential of an order of magnitude faster pulses make the optimal control technique seem promising for the future.

6. Single-ion qubits

6.1. Scalability of the ensemble qubit approach

Scaling to large number of qubits is a key issue for a quantum computer. In the present system, the qubit–qubit operation is achieved by the dipole–dipole interaction between two neighboring ions. As stated in section 2 they must physically sit close enough to each other so that when the state of one ion is changed, e.g. from the ground state to the excited state, and the electric field from the static dipole moment changes, this will shift the neighboring ion out of resonance with its original transition frequency. In this way, closely lying ions can control each other. For an ion absorbing at a selected frequency, ν_i, there will be several ions in the vicinity that can control this ion. In the ensemble approach, for two qubits, i and j, at transition frequencies ν_i and ν_j, there is a probability, p, that for an arbitrary ion, a_i, in qubit i, there will be an ion in qubit j that can control a_i. For n qubits, if N denotes the number of ions in a qubit that can be controlled by ions in the other $n-1$ qubits, we obtain that $N \propto p^{n-1}$. For the materials studied so far p is of the order of 1%, which means that for a five-qubit quantum register there will only be 1 out of 10^8 ions that are useful in each qubit.

Several remedies were pointed out to improve the scaling property by pushing $p > 1$, e.g. choosing ions with large static dipole moment, increasing the dopant concentration [29], constructing the qubit–qubit interaction by using a mediator bus ion [12] or adding a specially selected readout ion to detect the state of single ions, thereby enabling the use of single ions instead of an ensemble of ions for each qubit. Considering both advantages and disadvantages in each scheme the single ion readout approach is believed to be the easiest way to achieve the scalability.

6.2. The readout-ion approach

Inside any small volume within a rare-earth-ion-doped crystal there is a high probability to find several strongly interacting ions which can control each other and each of them can represent one qubit. A readout scheme has been suggested for detecting the qubit state in such a single ion qubit system through the dipole–dipole interaction [12]. The dopant concentration of the readout ion should be very low to make sure there is on average only one readout ion interacting with the laser field. To fulfill its role, the readout ion is supposed to meet several requirements: (i) the absorption spectrum should be well separated from that of the qubit ion so that the readout procedure does not affect the qubit state. (ii) The excited state lifetime should be short and there should not be any trapping state. Thus, the excitation may be cycled many times producing many photons and giving a strong detection signal. (iii) The homogeneous linewidth should be narrow so that when a nearby qubit ion is transferred between the ground and excited states, the dipole–dipole interaction is able to shift the readout ion in or out of resonance with the readout beam

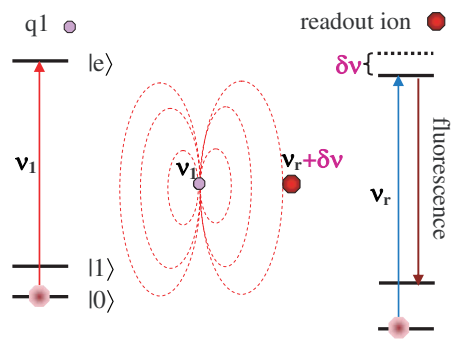

Figure 8. The dipole–dipole interaction between a qubit ion and a near-lying readout ion. If the qubit ion $q1$ is excited from the $|0\rangle$ state to the $|e\rangle$ state at frequency ν_1, the electric field generated by the dipole will shift the transition frequency of the readout ion by an amount $\delta\nu$, after which excitation at frequency ν_r will have no effect and the readout ion fluorescence will be turned off.

frequency, which consequently turns the fluorescence on or off. (iv) The inhomogeneous linewidth should be large, which provides a larger number of frequency channels.

6.3. Find and search schemes

Provided the spectral information of the readout ion is characterized, the nearest qubit, $q1$, and further qubit chain structures in the vicinity of the readout ion, can be mapped out using the fluorescence signal from the readout ion. After detecting the readout ion fluorescence at a certain excitation frequency, ν_r, one would keep the readout laser working at ν_r, while scanning the qubit laser across the inhomogeneous qubit transition frequency to find a frequency, ν_1, where the fluorescence signal stops. This would mean that a qubit ion with the addressing frequency ν_1 can control the readout ion, as illustrated in figure 8. With the qubit and readout laser working at ν_1 and ν_r respectively, the presence or absence of fluorescence tells whether $q1$ is in the $|1\rangle$ or the $|0\rangle$ state. The general case is that the qubit is in a superposition state, then one has to do the quantum state tomography measurements as described in section 5.1, then execute the above readout procedure to characterize the probability distribution between the $|0\rangle$ and $|1\rangle$ state for each projection. After the excitation frequency of $q1$ is known one can then extend the readout scheme to find out which qubit, $q2$, can control $q1$ through the qubit–qubit interaction and further, consecutively map out the whole interacting qubit chain and read out all qubits.

6.4. Investigation for a readout ion

So far Ce^{3+} is believed to be the most promising candidate for the readout ion. The excitation wavelength for the 4f–5d zero-phonon-line (ZPL) of Ce^{3+} ion randomly doped in the YSO crystal is around 371 nm, which is well separated from the qubit ion transition frequency 606 nm (Pr) or 580 nm (Eu). The Ce^{3+} homogeneous linewidth is determined by detecting the sum frequency signal from a saturation spectroscopy

experiment with different amplitude modulation frequencies on the pump and probe beams. The measured homogeneous linewidth was as narrow as 3 MHz. This is a very encouraging result, because based on a reasonable assumption about the Ce dipole moment, the Pr ion should be able to shift the Ce transition line by 30 MHz when they are separated by 7 nm [30]. With a 50 ns lifetime [31, 32] this also means that the homogeneous linewidth is lifetime-limited, which is the ideal case for this readout ion concept.

The inhomogeneous linewidth of the ZPL in a crystal with 0.08% cerium concentration is measured to be 80 GHz at 4 K. However, the fluorescence at the center of the ZPL is only twice the background signal outside the ZPL. The exact origin of this background is unknown, but it could for example be phonon sideband transitions, which are stronger for 4f–5d transitions than for 4f–4f transitions. Clearly this will affect the readout fidelity. Assume the detector quantum efficiency is 10% and the fluorescence collection efficiency is 30% [33] and a π-pulse is applied on the $|0\rangle \rightarrow |e\rangle$ qubit transition. As the readout laser is turned on, there will then be about 100 fluorescence photons detected during the optical lifetime (150 μs) of the Pr^{3+} ion, if the qubit was in its $|1\rangle$ state. On the other hand, if the Pr^{3+} ion was in its $|0\rangle$ state, the ZPL background fluorescence might still give around 50 photons due to off-resonant excitations (the background signal). However, the difference in the number of photons is certainly still sufficient for separating the two cases. One way to reduce the background signal, would be to decrease the number of Ce ions within the laser focus.

7. Scalability

When the single-ion readout system is scaled up by adding new qubits to the (possibly branched) qubit ion chain there will, although there are many frequency channels available within the inhomogeneously broadened qubit transition line, eventually be a new qubit ion (Q_{new}) that has the same frequency as one of the qubit ions (Q_{old}) already in the chain. In this situation, the two ions (Q_{old} and Q_{new}) cannot any longer be individually addressed in frequency space. It is conceivable that there are algorithmic solutions to this problem, where single qubit operations could be replaced by two-qubit operations, so that operations are applied to 'the qubit with frequency ν_i, sitting next to a qubit with frequency ν_j'. As an alternative, the problem of coinciding transition frequencies can be removed by mounting (closely spaced) electrodes onto the crystal. The part of the qubit chain on which the operations are carried out is selected by applying a voltage on the appropriate electrode. Eu in Y_2SiO_5 has a Stark coefficient of 35 kHz V^{-1} cm^{-1} [34], and ions close to the electrode can be shifted to resonance with the excitation pulse. A 1 MV cm^{-1} field would shift the transition frequency 35 GHz, a detuning much larger than the inhomogeneous transition linewidth. Simulations show that 20 nm long electrodes separated by 40 nm on a surface may give shifts of the order of 30 GHz within a 60 nm region, while ions 20 nm further away would shift less than 10 GHz [12]. However, still smaller electrodes and electrode separations would be favorable and while this is in line with the current technological development we will also now analyze the possibility of entangling spatially remote few-qubit systems.

Thus, we consider spatially separated qubit chains, each containing a not too large number of qubits. There are several schemes for entangling spatially remote few-qubit systems. To optically entangle a qubit in one system with a qubit in another system the key point is to configure the photon detection (or absorption) process such that when a photon is detected (absorbed) it cannot, in principle, be determined which of the two systems emitted (absorbed) the photon [35, 36]. If the set-up is appropriately configured, the photon detection/absorption entangles the two qubits.

Scalable quantum computing is then achievable also with errors in the remote entanglement of the order of several per cent, provided that the error probability for operation within each of the qubit chain is below 10^{-4} [37]. Remote entanglement processes often correspond to a probabilistic event, which is repeated until it succeeds. Clearly, schemes with very high probability to succeed in a single try are preferable. Such schemes can, for example, be devised using optical micro-cavities [38], e.g. toroidal micro-resonators [39, 40], and can also be improved by the use of cluster states [41].

We consider a rare earth crystal with a Ce readout ion, close to the surface facing a toroidal microcavity. Around this readout ion there will be a number of qubit ions that interact and can be read out, as described in section 6. One of these qubit ions is selected as the *entangler ion*. The purpose is now to entangle *entangler ions* in different rare-earth crystals. Such a scheme requires that also rare-earth ions close to the crystal surface retain their favorable coherence properties, and preliminary data indicate that this indeed is the case [42].

Consider figure 9, the interaction between the cavity and the ion is adjusted such that a single photon corresponds to a π-pulse [43]. Using tapered fibers, a single photon can be coupled into the toroidal microcavity with an efficiency (ideality) >99.98% [44]. The entangler ion in the first crystal, A, is prepared in the superposition state $(|0\rangle + |1\rangle)_A$ and the entangler ion in the second crystal, B, is prepared in state $|1\rangle_B$. As experimentally demonstrated [45], the ion transition frequencies to an excited state, $|e\rangle$, can readily be tuned by an electric field. Thus, by tuning the $|0\rangle \rightarrow |e\rangle$ transition for the ion in A to the same frequency as the $|1\rangle \rightarrow |e\rangle$ transition for the ion in B using electric fields (see right-hand side of figure 9) and sending a photon in the tapered fiber at this frequency in the direction indicated in the figure, the two ions will be prepared in the state $(|e\rangle_A|1\rangle_B + |1\rangle_A|e\rangle_B)$. Applying local π-pulses on each of $|e\rangle_A \rightarrow |0\rangle_A$ and $|e\rangle_B \rightarrow |0\rangle$ at the respective input ports for the qubit and the readout ion, then creates the Bell state $|01\rangle + |10\rangle$.

In a more complete version of the approach in figure 9, there would be a large number of microresonators (with their corresponding crystals) along the tapered fiber. Which two crystals that are selected for any specific entanglement process can be controlled by e.g. adjusting the distance between the tapered fiber and the resonator (cavity) using e.g. micro-actuators. Alternatively, the cavity can be tuned off resonance with the transition and photon frequency. Tuning the cavity can be carried out using expansion due to temperature. For example, electrodes can be connected to the

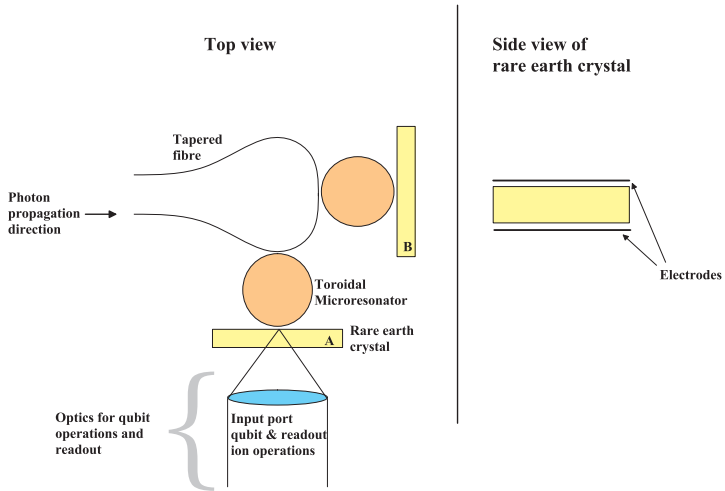

Figure 9. Schematic view of an approach to entangle spatially separate few qubit processors.

toroid and the substrate. The temperature and thereby also the frequency change will then be proportional to the dissipated power [46]. In general, the system could be quite flexible and versatile, as an example, ions can be tuned in and out of resonance with the cavity using an electric field across the crystal.

As earlier stated, the qubit coherence times can be 30 s for Pr ions [7] and for Eu ions coherence times of the order of an hour have been predicted [47]. A strength of the scheme outlined above is therefore that there is ample time both to create entanglement and to carry out operations once the systems have been entangled.

To compare with some existing data, free Cs atoms can have a single photon Rabi frequency of 100 MHz for Cs atoms 45 nm from the toroidal surface [48]. Pr^{3+}:Y_2SiO_5, which has an oscillator strength almost six orders of magnitude lower than free Cs atoms [34], would then yield a Rabi frequency of about 150 kHz. This value is too low for a single photon to act as a π-pulse and we are therefore looking at techniques for enhancing the interaction between an ion just below the surface and an evanescent field.

8. Concluding remarks

To summarize, single-qubit operation fidelities above 90% are obtained for ensemble qubits and >99% single qubit operation fidelity should be readily obtained with single-ion qubits. However, the single ion qubit scheme is contingent upon the ability to read out the hyperfine state of single rare-earth ions and work to develop this capacity is still ongoing. Although, based on current data in the investigation of using Ce^{3+} as a readout ion for such a scheme, there is reason to be quite optimistic about the possibilities to succeed. Finally, it may be pointed out that while quantum state storage in rare-earth-ion-doped materials is pursued vigorously by several groups and now demonstrates excellent progress [49] including storage efficiencies above 30% [50], only two groups [8, 51] have published experimental efforts on quantum computing in rare earth crystals and considering the limited efforts, substantial progress has been made.

Acknowledgments

This work was supported by the Swedish Research Council, the Knut and Alice Wallenberg Foundation, the European Commission through the integrated project QAP and the Crafoord Foundation.

References

[1] Nakamura Y, Pashkin Y A and Tsai J S 1999 Coherent control of macroscopic quantum states in a single-Cooper-pair box *Nature* **398** 786–8
[2] Plantenberg J H, de Groot P C, Harmans C J P M and Mooij J E 2007 Demonstration of controlled-not quantum gates on a pair of superconducting quantum bits *Nature* **447** 836
[3] Loss D and DiVincenzo D P 1998 Quantum computation with quantum dots *Phys. Rev.* A **57** 120–6
[4] Kane B E 1998 A silicon-based nuclear spin quantum computer *Nature* **393** 133–7
[5] Jelezko F, Gaebel T, Popa I, Domhan M, Gruber A and Wrachtrup J 2004 Observation of coherent oscillation of a single nuclear spin and realization of a two-qubit conditional quantum gate *Phys. Rev. Lett.* **93** 130501
[6] Ohlsson N, Mohan R K and Kröll S 2002 Quantum computer hardware based on rare-earth-ion-doped inorganic crystals *Opt. Commun.* **201** 71–7
[7] Fraval E, Sellars M J and Longdell J J 2005 Dynamic decoherence control of a solid-state nuclear-quadrupole qubit *Phys. Rev. Lett.* **95** 030506
[8] Rippe L, Julsgaard B, Walther A, Ying Y and Kröll S 2008 Experimental quantum state tomography of a solid state qubit *Phys. Rev.* A **77** 022307
[9] Roos I and Mølmer K 2004 Quantum computing with an inhomogeneously broadened ensemble of ions: suppression of errors from detuning variations by specially adapted pulses and coherent population trapping *Phys. Rev.* A **69** 022321

[10] Rippe L, Nilsson M, Klieber R, Suter D and Kröll S 2005 Experimental demonstration of efficient and selective population transfer and qubit distillation in a rare-earth-metal-ion-doped crystal *Phys. Rev.* A **71** 062328

[11] Timoney N, Elman V, Glaser S, Weiss C, Johanning M, Neuhauser W and Wunderlich C 2008 Error-resistant single-qubit gates with trapped ions *Phys. Rev.* A **77** 052334

[12] Wesenberg J H, Molmer K, Rippe L and Kroll S 2007 Scalable designs for quantum computing with rare-earth-ion-doped crystals *Phys. Rev.* A **75** 012304

[13] Equall R W, Cone R L and Macfarlane R M 1995 Homogeneous broadening and hyperfine structure of optical transitions in Pr^{3+}:Y_2SiO_5 *Phys. Rev.* B **52** 3963–9

[14] Sun Y, Thiel C W, Cone R L, Equall R W and Hutcheson R L 2002 Recent progress in developing new rare earth materials for hole burning and coherent transient applications *J. Lumin.* **98** 281–7

[15] Fraval E, Sellars M J and Longdell J J 2004 Method of extending hyperfine coherence times in Pr^{3+}:Y_2SiO_5 *Phys. Rev. Lett.* **92** 077601

[16] Julsgaard B, Rippe L, Walther A and Kröll S 2007 Understanding laser stabilization using spectral hole burning *Opt. Express* **15** 11444–65

[17] Guillot-Noël O, Goldner Ph, Beaudoux F, Le Du Y, Lejay J, Amari A, Walther A, Rippe L and Kröll S 2009 Hyperfine structure and hyperfine coherent properties of praseodymium in single-crystalline $La_2(WO_4)_3$ by hole-burning and photon-echo techniques *Phys. Rev.* B **79** 155119

[18] Walther A 2009 Coherent processes in rare-earth-ion-doped solids *PhD Thesis* Lund University http://www-atom.fysik.lth.se/QI/publications/Theses/Thesis-AW.pdf

[19] Nielsen M A and Chuang I L 2000 *Quantum Computation and Quantum Information* (Cambridge: Cambridge University Press) Equation (8.148) chapter 8.4.2

[20] Khaneja N, Brockett R and Glaser S J 2001 Time optimal control in spin systems *Phys. Rev.* A **63** 032308

[21] Khaneja N, Luy B and Glaser S J 2003 Boundary of quantum evolution under decoherence *Proc. Nat. Acad. Sci. USA* **100** 13162–6

[22] Fisher R, Yuan H, Spörl A and Glaser S 2009 Time-optimal generation of cluster states *Phys. Rev.* A **79** 042304

[23] Khaneja N, Reiss T, Kehlet C, Schulte-Herbrüggen T and Glaser S J 2005 Optimal control of coupled spin dynamics: design of NMR pulse sequences by gradient ascent algorithms *J. Magn. Reson.* **172** 296–305

[24] Skinner T E, Reiss T O, Luy B, Khaneja N and Glaser S J 2003 Application of optimal control theory to the design of broadband excitation pulses for high-resolution NMR *J. Magn. Reson.* **163** 8–15

[25] Kobzar K, Skinner T E, Khaneja N, Glaser S J and Luy B 2004 Exploring the limits of broadband excitation and inversion pulses *J. Magn. Reson.* **170** 236–43

[26] Kobzar K, Luy B, Khaneja N and Glaser S J 2005 Pattern pulses: design of arbitrary excitation profiles as a function of pulse amplitude and offset *J. Magn. Reson.* **173** 229–35

[27] Spörl A, Schulte-Herbrüggen T, Glaser S J, Bergholm V, Storcz M J, Ferber J and Wilhelm F K 2007 Optimal control of coupled Josephson qubits *Phys. Rev.* A **75** 012302

[28] Nebendahl V, Häffner H and Roos C F 2009 Optimal control of entangling operations for trapped-ion quantum computing *Phys. Rev.* A **79** 012312

[29] Nilsson M 2004 Coherent interactions in rare-earth-ion-doped crystals for applications in quantum information science *PhD Thesis* Division of Atomic Physics, LTH

[30] Ahlholm C 2008 Simulation of the single ion readout concept *Master's Thesis* Lund University *Lund Reports on Atomic Physics* LRAP-402

[31] Hernandez J E 2006 Spectroscopy in Ce^{3+}:Y_2SiO_5. a preliminary investigation for a single ion readout scheme for quantum computation with rare-earth ion doped crystals *Master's Thesis* Lund University, Lund Reports on Atomic Physics, LRAP-356

[32] Aitasalo T, Hölsä J, Lastusaari M, Legendziewicz J, Niittykoski J and Pellé F 2004 Delayed luminescence of Ce^{3+} doped Y_2SiO_5 *Opt. Mater.* **26** 107–112
Aitasalo T, Hölsä J, Lastusaari M, Legendziewicz J, Niittykoski J and Pellé F 2003 *Proc. 2nd Int. Conf. on Sol–Gel Materials. Research, Technology, Applications (SGM'03)*

[33] Palm V 1999 Compact simplified design of optical cell for single-molecule spectroscopy *Rev. Sci. Instrum.* **70** 2957

[34] Graf F R, Renn A, Zumofen G and Wild U P 1998 Photon-echo attenuation by dynamical processes in rare-earth-ion-doped crystals *Phys. Rev.* B **58** 5462–78

[35] Duan L-M and Kimble H J 2003 Efficient engineering of multiatom entanglement through single-photon detections *Phys. Rev. Lett.* **90** 253601

[36] Barett S D and Kok P 2005 Efficient high-fidelity quantum computation using matter qubits and linear optics *Phys. Rev.* A **71** 060310

[37] Jiang L, Taylor J M, Sørenssen A S and Lukin M D 2007 Distributed quantum computation based on small quantum registers *Phys. Rev.* A **76** 062323

[38] Cirac J I, Zoller P, Kimble H J and Mabuchi H 1997 Quantum state transfer and entanglement distribution among distant nodes in a quantum network *Phys. Rev. Lett.* **78** 3221–4

[39] Vahala K J 2003 Optical microcavities *Nature* **424** 839

[40] Spillane S M, Kippenberg T J, Vahala K J, Goh K W, Wilcut E and Kimble H J 2005 Ultrahigh-*q* toroidal microresonators for cavity quantum electrodynamics *Phys. Rev.* A **71** 013817

[41] Raussendorf R and Briegel H J 2001 A one-way quantum computer *Phys. Rev. Lett.* **86** 5188

[42] Longdell J *et al* 2008 Cavity QED with rare earths *Workshop in Bozeman, Montana*

[43] Xiao Y-F, Han Z-F, Yang Y and Gou G-C 2004 Quantum cpf gates between rare earth ions through measurement *Phys. Lett.* A **330** 137

[44] Spillane S M, Kippenberg T J, Painter O J and Vahala K J 2003 Ideality in a fiber-taper-coupled microresonator system for application to cavity quantum electrodynamics *Phys. Rev. Lett.* **91** 043902

[45] Macfarlane R M and Meixner A J 1994 Electric-field-modulated photon echoes in Pr^{3+}:$YAlO_3$ *Opt. Lett.* **19** 987

[46] Armani D, Min B, Martin A and Vahala K J 2004 Electrical thermo-optic tuning of ultrahigh-*q* microtoroid resonators *Appl. Phys. Lett.* **85** 5439

[47] Longdell J J, Alexander A L and Sellars M J 2006 Characterization of the hyperfine interaction in europium-doped yttrium orthosilicate and europium chloride hexahydrate *Phys. Rev.* B **74** 195101

[48] Aoki T, Dayan B, Wilcut E, Bowen W P, Parkins A S, Kippenberg T J, Vahala K J and Kimble H J 2006 Observation of strong coupling between one atom and a monolithic microresonator *Nature* **443** 671

[49] Riedmatten H, Afzelius M, Staudt M U, Simon C and Gisin N 2008 A solid-state light–matter interface at the single-photon level *Nature* **456** 773

[50] Amari A, Walther A, Sabooni M, Huang M, Kröll S, Afzelius M, Usmani I, Sangouard N, de Riedmatten H and Gisin N 2009 Towards an effective atomic frequency comb quantum memory arXiv:0911.2145

[51] Longdell J J and Sellars M J 2004 Experimental demonstration of quantum-state tomography and qubit–qubit interactions for rare-earth-metal-ion-based solid-state qubits *Phys. Rev.* A **69** 032307

Paper III

Measurement of linewidths and permanent electric dipole moment change of the Ce 4f-5d transition in Y_2SiO_5 for qubit readout scheme in rare-earth ion based quantum computing

Y. Yan, J. Karlsson, L. Rippe, A. Walther, D. Serrano, D. Lindgren, M. E. Pistol, S. Kröll, Ph. Goldner, L. Zheng and Jun Xu.

Phys. Rev. B **87**, 184205 (2013).

PHYSICAL REVIEW B **87**, 184205 (2013)

Measurement of linewidths and permanent electric dipole moment change of the Ce $4f$-$5d$ transition in Y_2SiO_5 for qubit readout scheme in rare-earth ion based quantum computing

Ying Yan,* Jenny Karlsson, Lars Rippe, Andreas Walther, Diana Serrano, David Lindgren, Mats-erik Pistol, and Stefan Kröll
Department of Physics, Lund University, P.O. Box 118, SE-22100 Lund, Sweden

Philippe Goldner
Chimie ParisTech, Laboratoire de Chimie de la Matière Condensée de Paris, CNRS-UMR 7574, UPMC Université Paris 06, 11 rue Pierre et Marie Curie 75005 Paris, France

Lihe Zheng and Jun Xu
Key Laboratory of Transparent and Opto-Functional Inorganic Materials, Shanghai Institute of Ceramics, Chinese Academy of Sciences, Shanghai 201800, China

(Received 18 February 2013; revised manuscript received 2 May 2013; published 30 May 2013)

In this work the inhomogeneous (zero-phonon line) and homogeneous linewidths and the permanent electric dipole moment change (averaged value of all dipole orientations) for the Ce $4f$-$5d$ transition in Y_2SiO_5 were measured in order to investigate the possibility for using Ce as a sensor to detect the hyperfine state of a spatially close-lying Pr or Eu ion. The experiments were carried out on Ce doped or Ce-Pr co-doped single Y_2SiO_5 crystals. The homogeneous linewidth is essentially limited by the excited state lifetime. Based on the linewidth measurements, the oscillator strength, absorption cross section, and saturation intensity were calculated to be about $6.2(\pm1.7) \times 10^{-7}$, $4.5(\pm1.3) \times 10^{-19}$ m^2, and $1.4(\pm0.4) \times 10^7$ W/m^2, respectively. The difference in permanent dipole moment, $\triangle\mu_{Ce}$, between the ground and excited states of the Ce ion was measured as $9.6(\pm5.3) \times 10^{-30}$ C m. These measurements indicate that Ce is a promising readout ion to probe a single-ion qubit state for the quantum computing scheme using rare-earth ions.

DOI: 10.1103/PhysRevB.87.184205 PACS number(s): 33.70.Jg, 78.47.jh, 42.50.Md

I. INTRODUCTION

The quantum computing research field has attracted extensive interest for its potential to give a tremendous boost in computational ability for certain types of problems. Many physical systems have been investigated as test beds for quantum computing:[1] trapped ions,[2] nuclei in molecules,[3] Josephson junctions in superconductors,[4] nitrogen vacancy centers in diamond,[5] rare-earth ions in inorganic crystals,[6] etc. Regardless of the physical system, one of the necessary criteria for a quantum computing scheme is that it should be scalable. In this paper rare-earth ions based quantum computing (REIQC) is under concern, and the results in this paper are a part of the work to develop an ability to read out the hyperfine state of single ions in a rare-earth crystal in order to obtain a scalable system. In REIQC qubit-qubit interaction and arbitrary single qubit rotations have been carried out.[7,8] In these experiments each qubit, where the qubit states ($|0\rangle$ and $|1\rangle$) are two ground-state hyperfine levels of the ion, was represented by an ensemble of ions and addressed via their optical transition frequencies.[8] The optical transition lines of rare-earth ions in a crystal are inhomogeneously broadened as a result of the random substitutions of the rare-earth ions (qubit ions) in the solid matrix, which causes slight crystal-field variations for the sites of the individual ions. The ratio between the inhomogeneous and homogeneous broadening in these systems can be larger than 10^6. Thus a very large number of subensembles of ions can be singled out in frequency space within the inhomogeneous line. Each subensemble can then act as a frequency-selectively addressed qubit although they consist of many ions randomly distributed in space. The conditional gate operations in these systems can be realized via the permanent electric dipole-dipole interaction between the strong-interacting ions in each qubit (see Figs. 3 and 11 in Ref. 9 for details). The strength of the dipole-dipole interaction between two ions depends on the spatial distance between them, r, as $1/r^3$. Because of this spatially dependent coupling and the random spatial distribution of the ions in each qubit, the average probability P of an ion in one qubit being sufficiently close to an ion in another qubit to control its state is often $\ll 1$ for reasonable dopant concentrations. This means that the number of active ions in one ensemble qubit that interact strongly with one ion in each of the rest of the $n-1$ qubits scales as P^{n-1}. In order to improve this poor scalability, Wesenberg *et al.* proposed several schemes.[10] One approach is to discard the ensemble qubits and instead let each single ion represent a qubit. With sufficient dopant concentration, for instance 0.2% for Pr:Y_2SiO_5, there is a large possibility to find sequences of ions which sit $\sim$3 nm (on average) away from each other and where each of these absorbs at a specific and unique optical frequency and represents one single qubit. With that separation the dipole-dipole interaction between the qubits are strong enough for carrying out gate operations.[11]

However, in this single instance quantum computing approach a technique to read out the quantum state of a single-ion qubit needs to be developed. The straightforward typical fluorescence measurement for detecting a single molecule does not work because, first, the transitions of the qubit ion (in Ref. 8 this has been a Pr ion), which can discriminate the qubit states, have excited state lifetimes of more than 10 μs, which provides too low an emission rate for a high signal-to-noise detection; second, and more importantly, the qubit ion candidates have

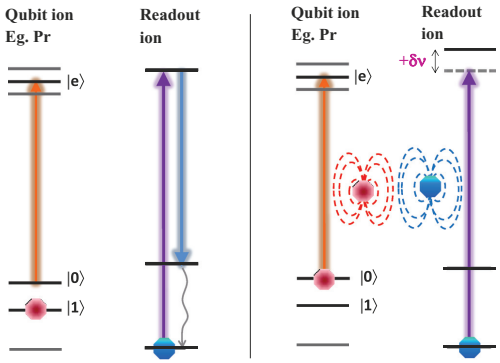

FIG. 1. (Color online) Permanent dipole-dipole interaction between a qubit ion and a readout ion that sits spatially close to this qubit ion. Two lasers interact with the ions, one for the qubit ion and one for the readout ion. The qubit laser sends out a pulse with pulse area of π on the $|0\rangle \rightarrow |e\rangle$ transition and following this pulse the readout laser is turned on and continuously excites the readout ion. If the Pr ion is in state $|1\rangle$ (left panel), the qubit laser is not on resonance with the Pr ion transition so it will not pump the Pr ion to state $|e\rangle$. There is no interaction between the qubit and readout ion in this case. The readout ion continuously sends out fluorescence photons (ON). On the other hand, if the Pr ion is initially in state $|0\rangle$ (right panel), it will be excited by the qubit laser pulse. Since the permanent dipole moment of the Pr ion in state $|e\rangle$ is different from that in state $|0\rangle$, the change of this local electric field induces a frequency shift ($\delta\nu$) of the nearby readout ion transition line. If the shift is larger than the homogeneous linewidth, the readout ion will be out of resonance with the readout laser and never excited so there is no fluorescence (OFF).

more than one ground-state hyperfine level to which they can decay, thus there is no transition that can be cycled until the number of emitted photons is sufficiently large to provide state selective information. A single-ion readout idea was proposed in Ref. 10 to accomplish single-qubit ion detection: an additional ion (hereafter called a readout ion) can be co-doped into the crystal, with such low concentration that there is only one readout ion fluorescing within the laser focal volume. This ion serves as a sensor for reading out the state of nearby qubit ions through the interaction between the qubit and readout ion, illustrated in Fig. 1. As a result the fluorescence signal from the single readout ion, either ON or OFF, depends on whether the single qubit ion is in state $|1\rangle$ or in $|0\rangle$.[12] For the other qubits, which are not directly coupled to the readout ion, their state can be transferred consecutively to its nearby ions through conditional gate operations until the qubit, which is directly coupled to the readout ion, is reached. Then its state can be read out in the way described above (see Sec. III B in Ref. 10 for details).

The readout scheme above requires that the readout ion has the following characteristics: (i) short excited-state lifetime in order to obtain a large contrast in photon emission number per unit time between when the qubit is in the ground state and when it is in the excited state; (ii) narrow homogeneous absorption linewidth such that the permanent dipole-dipole interaction with a nearby qubit shifts the readout ion resonance frequency by several homogeneous linewidths; (iii) large dipole moment change between ground and excited state (again such that the shift due to the permanent dipole-dipole interaction is sufficiently large); (iv) no fluorescence quenching mechanisms, e.g., a long-lived trapping state or energy transfer from the readout ion to the qubit ion. In this work Ce^{3+} (doped in an Y_2SiO_5 crystal) is considered as a readout ion.[13] Ce ions in Y_2SiO_5 have a short excited-state lifetime of about 40 ns,[14–16] to be compared with an excited-state lifetime of possible qubit ions as, e.g., Pr and Eu which are about 0.2 and 2 ms, respectively. The $4f$-$5d$ zero-phonon absorption line of Ce^{3+} doped in Y_2SiO_5 lies around 370.83 nm, which is well separated from the qubit transition frequencies (e.g., 606 nm for Pr ions in site 1). However, other than the excited-state lifetime, the spectroscopic parameters relevant for the readout scheme are not known. In this paper, the second and third spectroscopic requirements, (ii) and (iii) above, for a readout ion were measured for Ce ions in Y_2SiO_5 crystals. The inhomogeneous zero-phonon line (ZPL) measurement is described in Sec. II A, the homogeneous linewidth measurement is discussed in Sec. II B, and the measurement (based on the Ce-Pr interaction) of the Ce permanent dipole moment difference between the ground and excited state is described in Sec. II C. The work is concluded in Sec. III.

II. DETERMINATION OF SPECTROSCOPIC PARAMETERS OF Ce IONS

We focused on the parameters that are of special interest to the single-ion readout scheme in REIQC.

A. Zero-phonon line (ZPL) of Ce ions in an Y_2SiO_5 crystal

The absorption line of interest is the $4f$-$5d$ transition of Ce ions as illustrated in Fig. 2(a). Since the $5d$ levels are less shielded from the environment than the $4f$ levels, the $4f$-$5d$ transitions are often largely broadened by the external perturbations, for instance, defects in the crystal or electron-phonon coupling to the crystal lattice. The experiments were carried out at 2 K to greatly reduce the phonon broadening influence. In this and the following experiments, an external cavity diode laser in a Littrow configuration was used as an excitation source.

The inhomogeneous ZPL of Ce^{3+} was measured on a $Ce:Y_2SiO_5$ crystal with a nominal dopant concentration of 0.088 at.% relative to the yttrium ions. The result is shown in Fig. 3. Crosses are the experimental data and the solid curve is a Gaussian fit. The measured inhomogeneous linewidth is about 50 GHz (full width at half maximum of the absorption coefficient) with the line center at 370.83 nm. No significant polarization dependence was observed for the absorption. Based on the data shown in Fig. 3, the oscillator strength of the zero-phonon transition was calculated to be $\sim 6.2(\pm 1.7) \times 10^{-7}$ using the relations shown in Refs. 17 and 18.

The ZPL shown in Fig. 3 sits on a background absorption with $\alpha \simeq 3.6\ \mathrm{cm}^{-1}$, which most likely comes from the absorption by Ce ions in site 2. More information about this is provided by a fluorescence spectrum with an online excitation

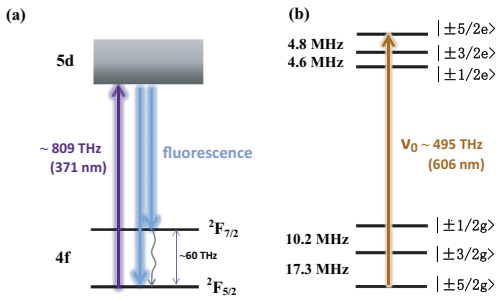

FIG. 2. (Color online) (a) Schematic level structure of Ce^{3+} in Y_2SiO_5 . (b) Schematic level structure for the $^3H_4 \rightarrow {}^1D_2$ transition of Pr^{3+} in Y_2SiO_5.

(at 370.83 nm) and an offline exciation (at 371.53 nm), shown as the solid and dashed curves in Fig. 4. The solid (dashed) curve matches reasonably well with the spectrum from a site 1 (site 2) excitation, shown in Refs. 19 and 14. However, the solid curve contains an extra shoulder sitting around 440 nm, the origin of which is unknown to us. In the rest of the paper, all calculations on Ce^{3+} refer to the ions in site 1, with the site 2 contribution being subtracted as a background.

B. Homogeneous linewidth of the ZPL

The homogeneous linewidth was measured by intensity modulated saturation spectroscopy, where both the pump and probe beams were generated from the external cavity diode laser by a beam splitter (70 : 30). Both beams were focused by a 200 mm focal length lens (focal diameter ~85 μm) onto the Ce:Y_2SiO_5 crystal, which was immersed in liquid helium. The probe beam propagated at an angle of ~3° relative to the pump beam in order to separate the two beams for the detection. Two acousto-optical modulators (AOMs) were used in series in the probe beam line. The +1 order deflected beam from the first AOM was used and followed by the −1 order deflected beam from the second AOM. In this way the probe beam frequency could be tuned within a ±50-MHz range relative to the pump

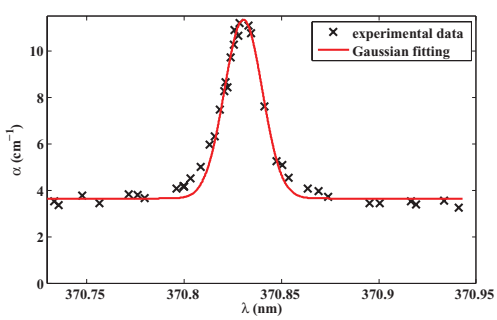

FIG. 3. (Color online) The inhomogeneous ZPL of Ce^{3+} (site 1) in an Y_2SiO_5 crystal. The linewidth is about 50 GHz. α is the absorption coefficient.

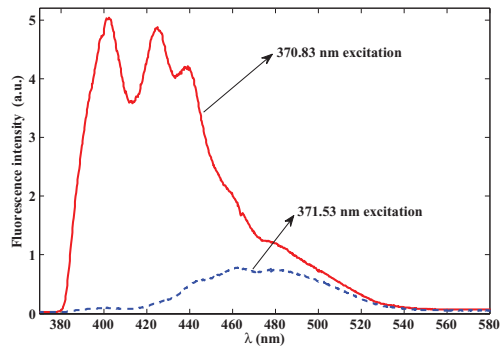

FIG. 4. (Color online) Fluorescence spectrum of Ce^{3+} in a Ce:Y_2SiO_5 crystal with 370.83-nm excitation (online of site 1) (solid line) and 371.53-nm excitation (offline of site 1) (dashed line).

beam frequency by adjusting the radio frequency of the second AOM. The probe beam position movement caused by the AOM at different detuning frequencies was compensated by slightly adjusting the mirror in front of the cryostat to overlap the two beams by maximizing the probe beam transmission. The probe beam was monitored by a photodiode after the cryostat. However, it is hard to directly detect an increase of the transmitted power caused by the saturation of the pump beam, since the top-hat pump beam intensity is only of the level of 1% of the estimated saturation intensity. To improve the signal-to-noise ratio, a chopper wheel was used to modulate the intensities of the pump and probe beam with modulation frequencies of 302 and 362 Hz, respectively. Due to the nonlinear interaction, the transmitted probe beam not only has the primary frequency modulation but also has an intensity modulation at the sum (664 Hz) and difference frequency (60 Hz). The signal strength at 664 Hz was extracted from the Fourier transform of the transmitted power of the probe beam and recorded as a function of the detuning frequencies between the pump and probe beams, Δf.

In the experiment, the observed signal at 664 Hz was 16 times as high as the noise floor when Δf is zero but only 1.3% of the signal strength at 362 Hz. The measurement data are shown in Fig. 5, where the vertical axis shows the sum frequency signal normalized by the square of the input probe beam power to compensate for the change in laser power between the data points. Figure 5 reveals a spectral hole width (full width at half maximum) of about 5.8 MHz, which results from a convolution of the laser line (Lorentzian) with the homogeneous line of the transition (Lorentzian) for both the pump step and probe step.[20] However, only fast laser frequency fluctuations within the time scale of the excited-state lifetime (~40 ns) would affect the measurement. This contribution should be negligible considering that the typical linewidth of an external cavity diode laser is 300 kHz over 100 μs. So the homogeneous linewidth we measured has an upper bound of 2.9 MHz. The 40-ns lifetime stated in the literature[14–16] poses a lower limit on the linewidth of ~4 MHz. The reason for measuring a linewidth <4 MHz might be that the signal at positive detuning frequencies was not properly maximized

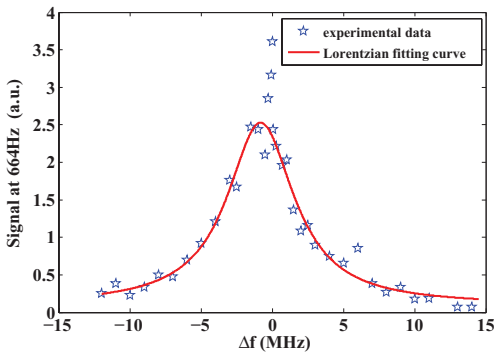

FIG. 5. (Color online) Ce ion homogeneous linewidth measured using saturation spectroscopy. The pentagrams are the measured data points. The solid curve is a Lorentzian fitting of the points excluding the central four which we believe are affected by population trapping.

by adjusting the spatial overlap between the pump and probe beam. While in principle we have no reason to suspect this, the fact that the center of the Lorentzian fitting curve is not at zero detuning but shifted to the left would indicate this as a possible explanation.

Based on the coherence time (lifetime limited value) and the frequency integrated absorption cross section (in m^2 rad/s) calculated from the inhomogeneous line,[21] the absorption cross section of the Ce ion in site 1 and the corresponding saturation intensity were calculated to be $\sim 4.5(\pm 1.3) \times 10^{-19}$ m^2 and $\sim 1.4(\pm 0.4) \times 10^7$ W/m^2, respectively.

The experimental data indicate an increased interaction between the beams within a narrow range ($\sim$400 kHz) of frequency detuning close to the line center. The origin of this resonance was not investigated but narrow resonances of this type can occur if the upper state can also decay to a third level which (compared with the relaxation from the excited state) relaxes slowly to the ground state; see, e.g., Refs. 22 and 23. The linewidth of the resonance is then determined by the decay rate of this third level. In the present experiment the third level could possibly be one of the lowest Kramer's doublets on the $^2F_{5/2}$ $(4f)$ ground state, compared with, e.g., Ref. 24, and the intrinsic width of the narrow resonance would then be given by the spin-lattice relaxation rate of the ground state. Using the calculated saturation intensity, the signal at the sum frequency (664 Hz) should be about 0.1% of the signal at 362 Hz at zero detuning frequency. However, the actual sum frequency signal is a factor of 8 higher than expected. The existence of a third level may not only give rise to the narrow structure mentioned above but also could provide a larger saturation effect due to the trapping of ions in this level. This could be part of the reason why the signal at 664 Hz (0.8% of the signal at 362 Hz) is larger than expected.

C. Ce-Pr interaction

The Ce and Pr ions in Y_2SiO_5 have different permanent electric dipole moments in their ground and excited states as they sit in noncentrosymmetric sites. This difference in the ground- and excited-state permanent dipole moment is denoted as $\Delta\mu$. When one ion is changing its state from ground to excited state or vice versa, the surrounding electric field is changed. This permanent dipole-dipole interaction causes a frequency shift Δf of the transition lines of the nearby ions, which depends on the spatial distance r between those two ions and $\Delta\mu$ of both ions as[25]

$$\Delta f \propto \frac{\Delta\mu_{\mathrm{Ce}}\Delta\mu_{\mathrm{Pr}}}{r^3}\kappa(\Delta\hat{\mu}_{\mathrm{Pr}},\Delta\hat{\mu}_{\mathrm{Ce}},\hat{r}), \tag{1}$$

where

$$\kappa(\Delta\hat{\mu}_{\mathrm{Pr}},\Delta\hat{\mu}_{\mathrm{Ce}},\hat{r}) = \Delta\hat{\mu}_{\mathrm{Ce}}\cdot\Delta\hat{\mu}_{\mathrm{Pr}} - 3(\hat{r}\cdot\Delta\hat{\mu}_{\mathrm{Ce}})(\hat{r}\cdot\Delta\hat{\mu}_{\mathrm{Pr}}) \tag{2}$$

stands for dependence of the interaction on the dipole orientations and displacement. $\Delta\hat{\mu}_{\mathrm{Pr,Ce}}$ and $\hat{r}$ are the unit vectors of the permanent dipole moment change and the displacement between these two dipoles (in our case they are a Pr dipole and a Ce dipole). Since the shift arises from the permanent dipole moment changes and not the transition dipole interactions, the shifts are the same regardless of which ion is excited for two ions with a specific distance. The value of $\Delta\mu_{\mathrm{Ce}}$ of the Ce^{3+} $4f$-$5d$ transition in Y_2SiO_5 is not previously known. It can, e.g., be determined by measuring the Stark shift caused by the interaction between the ions and an external electric field.[26] Here we instead used a sample doped with both Ce^{3+} and Pr^{3+} and implemented a two-pulse photon echo experiment on Pr ions, where Ce ions were excited during the dephasing period of the Pr ions, and the reduction of the echo intensity was observed.[25] The reduction is caused by the fact that a subgroup of Pr ions experience a frequency shift induced by the excitation of nearby Ce ions. When this happens the phases of the Pr superposition states evolve at different rates in the dephasing and rephasing periods, which causes an echo intensity decrease which depends on the magnitude of the shift and the evolution time. Thus the Pr-Ce ion-ion interaction introduces an additional dephasing channel for the excited Pr ions, which broadens the Pr homogeneous linewidth. From this extra broadening $\Delta\mu_{\mathrm{Ce}}$ can be calculated.[27]

In this experiment, an actively stabilized dye laser with a linewidth of less than 1 kHz was used to excite the Pr $^3H_4 \rightarrow {}^1D_2$ transition at 606 nm. Two weak Gaussian pulses with power of $\sim$0.5 mW (0.15-μs duration time) were created with an AOM and the photon echo from the Pr ions was recorded. Ce ions were excited during the dephasing time of the Pr ions using an external cavity diode laser and another AOM. The pulse sequence is shown in Fig. 6, where eraser pulses refer to several frequency scanning pulses at 606 nm. These were applied to shuffle the Pr ions between the hyperfine states and prevent persistent hole burning that would otherwise be created by the two Gaussian pulses (pulse 1 and pulse 2) over

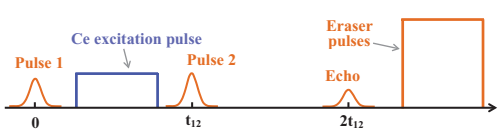

FIG. 6. (Color online) Pulses sequence for the Ce-Pr interaction measurement.

time. Each laser beam was coupled into a single mode fiber for spatial mode cleaning, and the collimated output beams from the fibers were coupled together by a dichroic mirror with 90% transmission (reflection) for 606 nm (371 nm). Those two beams were focused onto the crystal with focal diameters of about 130 and 170 μm, respectively, by a low dispersion CaF_2 lens. The spatial mode overlap between the two beams within the crystal was ascertained by using a beam profiler to ensure that the center of the two beam profiles overlapped with each other within 10 μm over the 40-cm distance between the dichroic mirror and the common focusing lens. The echo signal was deflected by a third AOM into a photomultiplier tube (PMT). Right before the PMT an electronic shutter with 100-μs rise time was used to prevent the strong frequency scanning pulses from reaching the PMT after the echo was recorded.

The intensity of the echo from the Pr ions was recorded as a function of the separation time t_{12} in two situations: Ce ions being excited or not excited (Ce laser blocked) in between the two Pr excitation pulses. The excitation of Ce ions was implemented at wavelengths of either 370.83 nm (hereafter referred to as online) or 371.54 nm (referred to as offline). Here online (offline) refers to the fact that the excitation wavelength is on (off) the ZPL of Ce ions in site 1. It is worthwhile to note that even at the offline wavelength there is still considerable background absorption as can be seen in the absorption spectrum in Fig. 3. We believe that this comes from ions in site 2, and they will also cause a reduction of the photon echo from Pr ions, by the interaction shown in Eq. (1). The experimental data from a Pr:Ce:Y_2SiO_5 crystal (grown by Shanghai Institute of Ceramics in China) with 0.05% of Pr and 0.088% of Ce dopant concentration relative to the Y ions are shown in Fig. 7.

Four series of data were recorded. The circles are the echo signals from the Pr ions when Ce ions were excited online (excitation power ~0.5 mW) during the dephasing time t_{12}. Each point is an average value of ~30 shots, and the error bar shows the standard deviation. To verify the experimental data, a complimentary data point corresponding to each circle, shown as a star, was recorded as well with the Ce excitation laser blocked. At each value of t_{12} in Fig. 7, all shots of the circle point were recorded first followed by the shots of the corresponding star point. After recording all data points at various t_{12}, the Ce laser was tuned to the offline position. The corresponding set of data was recorded, shown by the diamonds (Ce laser offline) and crosses (Ce laser blocked). The solid, dotted, dashed, and dash-dotted lines are the logarithmic fits of the experimental data for the cases when the Ce laser is online, blocked, offline, and blocked, respectively. The two blocked cases are equivalent, but show an offset on the echo signal possibly caused by laser power drift. However, the slopes are the same within the margin of error, as expected. The echo intensity as a function of the pulse separation time is

$$I_{\text{echo}} = I_0 e^{-4t_{12}/T_2}, \tag{3}$$

where I_0 is the maximum echo intensity when extrapolating the separation time to zero. Results of the measurements are shown in Table I, where T_2 and Γ_{hom} refer to the coherence time (with 70% confidence interval) and homogeneous linewidth of the Pr ions transition, respectively.

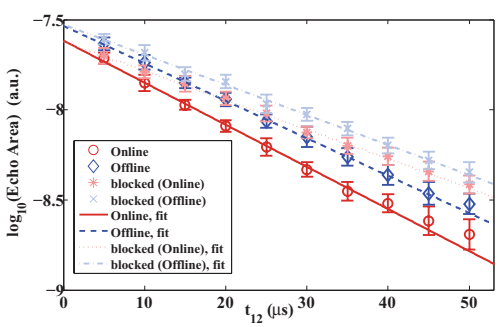

FIG. 7. (Color online) Decay curve of the echo from the Pr ions on the Pr:Ce:Y_2SiO_5 crystal. The circles (diamonds) are the experimental echo signal when the Ce ions were excited at an online (offline) wavelength. Error bar shows the standard deviation. The solid, dashed lines are logarithmic fits corresponding to those two cases. The stars (crosses) are the experimental data when the Ce excitation laser was blocked. The difference between them is explained in the text.

TABLE I. Measured homogeneous linewidths of Pr ions $^3H_4 \rightarrow {}^1D_2$ transition with Ce excitation laser being at an online wavelength, offline wavelength, and turned off.

	Ce online		Ce offline	
Measured values (Pr)	Laser on	Laser off	Laser on	Laser off
T_2 (μs)	74 ± 2	107 ± 3	83 ± 1	104 ± 3
Γ_{hom} (kHz)	4.3 ± 0.1	3.0 ± 0.1	3.83 ± 0.05	3.1 ± 0.1

Table I shows that the homogeneous linewidth broadening caused by the Ce online excitation Γ_{br} is 1.3 kHz with ±0.14 kHz for a 70% confidence interval, while for the Ce offline excitation the broadening is ~0.7 kHz (±0.11 kHz). The difference between these two values tells the broadening contribution only from the Ce ions in site 1, which is ~0.6 (±0.18) kHz. This value was used for calculating $\Delta\mu_{\text{Ce}}$ in the following passage.

However, the reduction in echo intensity could conceivably be caused by other reasons than a frequency shift resulting from the permanent dipole-dipole interaction. For instance, (1) the Pr ions directly absorb the ultraviolet (UV) photons leading to processes shortening the coherence time, which causes the echo intensity to decrease, although this is unlikely to happen, as seen from the literature.[28] (2) The energy is transferred from Ce ions to Pr ions so that Pr ions are excited to a higher level, which also can cause an echo reduction. To clarify the influence of suggestion (1) above we did exactly the same measurement as before but on an Y_2SiO_5 crystal with the same Pr dopant concentration but no Ce ions. The result is shown in Fig. 8, where the Pr homogeneous linewidths are the same when the laser pulse at the Ce absorption wavelength was present and absent, which means that the linewidth broadening shown in Fig. 7 does not result from direct UV absorption by the Pr ions. For clarifying whether the interaction can be induced by energy transfer [argument (2) above], we did an

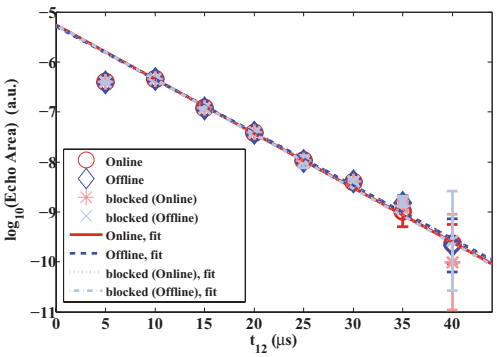

FIG. 8. (Color online) Echo decay curve on the pure Pr:Y_2SiO_5 crystal. Notation of the data symbols is the same as in Fig. 7. Circles, diamonds, stars, and crosses are for the cases when the Ce laser is online, offline, blocked (online), and blocked (offline), respectively. Deviation of the first data point from the fitting line was caused by the saturation of the PMT.

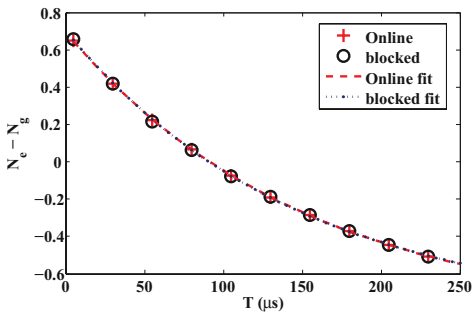

FIG. 9. (Color online) Population difference between the excited and ground state of Pr ions in a Pr:Ce:Y_2SiO_5 crystal as a function of time with Ce online excitation (+) and Ce laser blocked (◯). The dashed and dot-dashed lines are the respective exponential curve fittings. The standard deviation of the data points is ∼2%.

excited-state population decay measurement on Pr ions in the Pr:Ce:Y_2SiO_5 crystal as follows: (i) A zero absorption spectral window centered at frequency ν_0 was created using optical pumping.[29] (ii) A subset of Pr ions having their transition at frequency ν_0 is transferred to the $|\pm 5/2g\rangle$ state [the Pr ion level structure is shown in Fig. 2(b)]. (iii) A pulse with area of π excites these ions to their $|\pm 5/2e\rangle$ state with an efficiency of more than 85%. (iv) A Ce excitation pulse with duration time T was incident on the crystal. If there is Ce-Pr energy transfer or state changing interactions other than the frequency shifts due to the permanent dipole-dipole interaction, the Pr excited-state population should change. (v) After the time T the transmission of a pulse scanned in frequency around frequency ν_0 [see Fig. 2(b)] determines the population difference between the $|\pm 5/2g\rangle$ and $|\pm 5/2e\rangle$ state by measuring the absorption (this pulse is called the readout pulse in the following passage). Following the procedure above the Pr population difference (normalized to the initial population in $|\pm 5/2g\rangle$ state) between the excited and ground state, $N_e - N_g$, was recorded as a function of the separation time T between the π pulse and the readout pulse for the two cases where Ce ions were excited or not excited during the time T.

Figure 9 shows that the population differences of Pr ions when Ce ions are excited (online) and not excited (blocked) agree with each other within 3%. Similar measurements from the Ce offline excitation and Ce laser blocked cases also show the same result. Thus no effect of energy transfer between the Ce and Pr ions was observed. Based on the test on the pure Pr doped crystal (Fig. 8) and this excited-state population decay measurement of Pr ion (Fig. 9), to the best of our knowledge, the homogeneous broadening shown in Fig. 7 should be caused by the permanent dipole-dipole interaction between the Pr and Ce ions.

The homogeneous linewidth broadening induced by the permanent dipole-dipole interaction Γ_{br} relates to the $\Delta\mu$ of the interacting ions as[27]

$$\Gamma_{br} = \frac{1}{2\pi} C D_0 \langle W_{\mathrm{Ce}} \rangle, \tag{4}$$

where

$$C = \tfrac{2}{3}\pi^2 p \langle |\kappa| \rangle, \tag{5}$$

p represents the occupation probability of the Ce ions relative to the total number of ions in the crystal, and $\langle|\kappa|\rangle$ is in the order of 1,[25] representing the averaged value of κ [shown in Eq. (2)] over all angles defining the relative dipole orientations and the orientations between dipoles and the displacement.

D_0 describes the magnitude of the permanent dipole-dipole interaction with a unit distance of r_0,

$$D_0 = \eta(0)\,\frac{\Delta\mu_{\mathrm{Ce}}\Delta\mu_{\mathrm{Pr}}}{4\pi\epsilon_0\hbar r_0^3}, \tag{6}$$

where $\Delta\mu_{\mathrm{Ce}}$ and $\Delta\mu_{\mathrm{Pr}}$ is the difference of the permanent dipole moment in the ground and excited state of Ce and Pr ions, respectively. $\eta(0) = 1.28$ represents the dielectric correction factor for long-range dipole-dipole interaction.[30] ϵ_0 is the vacuum permittivity. r_0 stands for the length of the cube which one ion occupies on average. $\langle W_{\mathrm{Ce}}\rangle$ represents the average excitation probability of the Ce ions contributing to the interaction during the dephasing time.

For the crystal used in this experiment, the occupation probability $p \simeq 1.92 \times 10^{-4}$ considering a 87% occupation on site 1.[31] $\langle W_{\mathrm{Ce}}\rangle \simeq 1.8(\pm 0.7) \times 10^{-7}$, which is estimated from the saturation intensity (shown in Sec. II B) and integrated over the inhomogeneous line as in Ref. 27. The excitation intensity used for the estimation is the average value over a volume with the beam diameter of ρ_{fwhm}, the full width at half maximum of the Pr excitation laser intensity, through the crystal thickness of 1 mm. $\Delta\mu_{\mathrm{Ce}}$ (site 1) is calculated as $9.6(\pm 5.3) \times 10^{-30}$ C m using Eqs. (3)–(5) with $r_0 = 0.237$ nm, $\langle|\kappa|\rangle_\Omega \simeq 0.7$, and $\Delta\mu_{\mathrm{Pr}} = 2.43 \times 10^{-31}$ C m.[27] We also calculated $\langle W_{\mathrm{Ce}}\rangle$ from the ratio of the number of absorbed photons (equivalently number of excited Ce ions) during 40 ns over the total number of Ce ions in site 1 for a certain volume (given by the laser

beam profile). The value is $1.8(\pm 0.4) \times 10^{-7}$, which agrees with the previous value very well.

The measured value of $\Delta\mu_{Ce}$ (site 1) is an encouraging result as it indicates that the transition line of a Ce ion will be shifted by more than 300 MHz on average due to the change of states of a nearby Pr ion in a Pr:Ce:Y_2SiO_5 crystal with a dopant concentration of 0.05% (the average ion-ion distance is ∼5 nm). This shift is clearly large enough to force the Ce ions in site 1 out of resonance with the readout laser which is initially on resonance. However, this shift does not prohibit the excitation of the Ce ions in site 2 since these ions are not excited at their zero-phonon line and the absorption spectrum is much broader than the permanent dipole-dipole interaction induced shift. This gives us a background fluorescence even if the single Ce ion in site 1 is shifted out of resonance. However, based on our preliminary investigation the fluorescence contrast within the range 380–420 nm (as shown in Fig. 4) is believed to be good enough for detecting a single Ce ion in site 1 with a reasonable signal-to-noise ratio. So the fluorescence emitted from the Ce ions in site 1 can still be used as an indicator to show which state ($|0\rangle$ or $|1\rangle$) the Pr ion occupies.

III. CONCLUSION

The spectroscopic properties of Ce^{3+} doped in an Y_2SiO_5 crystal were characterized for investigating the possibility to use it as a probe for detecting which hyperfine ground state a nearby ion (e.g., Pr) is occupying. Particularly (i) the ZPL of the $4f$-$5d$ transition of Ce^{3+} doped in Y_2SiO_5 was found around 370.83 nm with a linewidth of about 50 GHz. (ii) The homogeneous linewidth was measured by intensity modulated saturation spectroscopy to be ∼3 MHz. It is essentially limited by the excited-state lifetime of that transition, which is the optimal case for using Ce^{3+} as a readout ion. In this experiment we also have not observed any signs that there is a long-lived trapping state for Ce ions, which means that the fluorescence can be cycled as many times as needed. From the linewidth measurements the oscillator strength, absorption cross section, and saturation intensity were calculated to be $\sim 6.2(\pm 1.7)\times 10^{-7}$, $\sim 4.5(\pm 1.3)\times 10^{-19}$ m^2, and $\sim 1.4(\pm 0.4)\times 10^7$ W/m^2, respectively. (iii) The Ce-Pr interaction was demonstrated through a photon echo experiment and the difference in the permanent dipole moment ($\Delta\mu_{Ce}$, averaged value of all dipole orientations) for the $4f$ ($^2F_{5/2}$) and lowest $5d$ states was measured to be $\sim 9.6(\pm 5.3) \times 10^{-30}$ C m, which is sufficiently large to provide a frequency shift much larger than the Ce homogeneous linewidth for a suitable dopant concentration of qubit ions. The data obtained so far shows that the Ce ion is a very promising readout ion candidate and a setup for single Ce ion detection by observing the $5d$-$4f$ fluorescence is currently under construction. Single Ce ion detection in a YAG ($Y_2Al_5O_{12}$) crystal was recently demonstrated.[32] The ability of state selective readout of a single rare-earth ion in inorganic crystals would be a significant step forward for quantum computing in these materials where high fidelity gate operations on ensembles have already been carried out.[7,8] It also opens the possibility to use rare-earth ions as extraordinarily sensitive probes of the local environment in these types of crystals. The ability to carry out (and read out) operations on individual ions would strongly address the scalability problem and greatly reduce the qubit operation time since fewer and simpler pulses can be used when the dephasing caused by the inhomogeneous broadening is no longer a concern. It is also quite clear that rare-earth ion doped crystals generally have excellent properties for preserving quantum states seen from the impressive quantum memory development that is taking place in these materials.[33–35]

ACKNOWLEDGMENTS

We thank M. Bettinelli for the helpful discussion. This work was supported by the Swedish Research Council (VR), the Knut and Alice Wallenberg Foundation (KAW), the Maja och Erik Lindqvists forskningsstiftelse, the Crafoord Foundation and the EC FP7 Contract No. 247743 (QuRep), (Marie Curie Action) REA Grant Agreement No. 287252 (CIPRIS), Lund Laser Center (LLC), and the Nanometer Structure Consortium at Lund University (nmC@LU).

*Corresponding author: yan.ying@fyisk.lth.se

[1] T. D. Ladd, F. Jelezko, R. Laflamme, Y. Nakamura, C. Monroe, and J. L. Obrien, Nature (London) **464**, 08812 (2010).
[2] R. Blatt and D. Wineland, Nature (London) **453**, 1008 (2008).
[3] J. A. Jones, Prog. NMR Spectrosc. **59**, 91 (2011).
[4] J. H. Plantenberg, P. C. de Groot, C. J. P. M. Harmans, and J. E. Mooij, Nature (London) **447**, 836 (2007).
[5] A. P. Nizovtsev, S. Ya. Kilin, F. Jelezko, T. Gaebal, I. Popa, A. Gruber, and J. Wrachtrup, Opt. Spectrosc. **99**, 233 (2005).
[6] N. Ohlsson, R. K. Mohan, and S. Kröll, Opt. Commun. **201**, 71 (2002).
[7] J. J. Longdell and M. J. Sellars, Phys. Rev. A **69**, 032307 (2004).
[8] L. Rippe, B. Julsgaard, A. Walther, Y. Ying, and S. Kröll, Phys. Rev. A **77**, 022307 (2008).
[9] L. Rippe, M. Nilsson, S. Kröll, R. Klieber, and D. Suter, Phys. Rev. A **71**, 062328 (2005).
[10] J. H. Wesenberg, K. Mølmer, L. Rippe, and S. Kröll, Phys. Rev. A **75**, 012304 (2007).
[11] S. Bengtsson, Master thesis, Lund University, Sweden, 2012.
[12] A. Walther, B. Julsgaard, L. Rippe, Y. Ying, S. Kröll, R. Fisher, and S. Glaser, Phys. Scr. **T137**, 014009 (2009).
[13] Suggested by Olivier Guillot-Noël in the European Quantum Information Processing and Computing workshop, Rome, 2004.
[14] H. Suzuki, T. A. Tombrello, C. L. Melcher, and J. S. Schweitzer, Nucl. Instrum. Methods Phys. Res. A **320**, 263 (1992).
[15] T. Aitasalo, J. Hlsa, M. Lastusaari, J. Legendziewicz, J. Niittykoski, and F. Pell, Opt. Mater. **26**, 107 (2004).
[16] J. E. Hernandez, Master thesis, Lund University, Sweden, 2006.
[17] B. Henderson and G. F. Imbusch, *Optical Spectroscopy of Inorganic Solids* (Oxford University Press, New York, 1989), p. 262, Eq. (6.10a).
[18] A. Smakula, Z. Phys. **59**, 603 (1930).
[19] W. Drozdowski, A. J. Wojtowicz, D. Wisniewski, P. Szupryczynski, S. Janus, J. Lefaucheur, and Z. Gou, J. Alloy. Compd. **380**, 146 (2004).
[20] S. Völker, Annu. Rev. Phys. Chem. **40**, 499 (1989).

[21]R. C. Hilborn, Am. J. Phys. **50**, 982 (1982).
[22]D. G. Steel and S. C. Rand, Phys. Rev. Lett. **55**, 2285 (1985).
[23]M. Mitsunaga, N. Uesugi, and K. Sugiyama, Opt. Lett. **18**, 1256 (1993).
[24]R. Kolesov, Phys. Rev. A **76**, 043831 (2007).
[25]S. B. Altner, G. Zumofen, U. P. Wild, and M. Mitsunaga, Phys. Rev. B **54**, 17493 (1996).
[26]F. R. Graf, A. Renn, U. P. Wild, and M. Mitsunaga, Phys. Rev. B **55**, 11225 (1997).
[27]F. R. Graf, A. Renn, G. Zumofen, and U. P. Wild, Phys. Rev. B **58**, 5462 (1998).
[28]N. V. Kuleshov, V. G. Shcherbitsky, A. A. Lagatskya, V. P. Mikhailov, B. I. Minkov, T. Danger, T. Sandrock, and G. Huber, J. Lumin. **71**, 27 (1997).
[29]M. Nilsson, L. Rippe, S. Kröll, R. Klieber, and D. Suter, Phys. Rev. B **70**, 214116 (2004).
[30]G. D. Mahan, Phys. Rev. **153**, 983 (1967).
[31]Y. C. Sun, in *Spectroscopic Properties of Rare Earths in Optical Materials*, edited by G. Liu and B. Jacquier (Springer, Berlin, 2005), Chap. 7.
[32]R. Kolesov, K. Xia, R. Reuter, R. Stöhr, T. Inal, P. Siyushev, and J. Wrachtrup, arXiv:1301.5215.
[33]M. P. Hedges, J. J. Longdell, Y. M. Li, and M. J. Sellars, Nature (London) **465**, 1052 (2010).
[34]E. Saglamyurek, N. Sinclair, J. Jin, J. A. Slater, D. Oblak, F. Bussieres, M. George, R. Ricken, W. Sohler, and W. Tittel, Nature (London) **469**, 512 (2011).
[35]I. Usmani, Ch. Clasusen, F. Bussières, N. Sangouard, M. Afzelius, and N. Gisin, Nat. Photon. **6**, 234 (2012).

Paper IV

High fidelity readout scheme for rare-earth solid state quantum computing

A. Walther, L. Rippe, Y. Yan, J. Karlsson, D. Serrano, S. Bengtsson and S. Kröll.

Manuscript in preparation , (2013).

High fidelity readout scheme for rare-earth solid state quantum computing

A. Walther,[1,*] L. Rippe,[1] Y. Yan,[1] J. Karlsson,[1] D. Serrano,[1] S. Bengtsson,[1] and S. Kröll[1]

[1] *Department of Physics, Lund Univeristy, 221 00 Lund, Sweden*

(Dated: September 13, 2013)

We propose a readout scheme for a single instance approach to quantum computing in rare-earth-ion-doped crystals. The scheme is based on using different species of qubit and readout ions, and we show that by allowing the closest qubit ion to act as a readout buffer, we can reduce the readout error by several orders of magnitude. The readout scheme is then used to predict the expected quantum fidelity of a CNOT gate in these solid state systems. In addition, we discuss the potential scalability of our protocol to larger qubit systems. The results are based on parameters which are believed to be experimentally feasible with current technology, and which can be simultaneously realized.

I. INTRODUCTION

The possibility of realizing a quantum computer is being investigated using a large variety of different expermental implementations. Currently, the largest entangled qubit systems have been realized in ion traps [1, 2] and using linear optics with single photons [3]. There is however an intrinsic value in investigating solid state systems, as they are generally regarded as having a higher potential for future scalability to larger systems. For solid state systems, the best progress has been achieved with superconducting circuits [4] and impurity-doped solids, such as NV centers in diamond [5]. Another impurity-doped system, rare-earth ions in crystals, have demonstrated very good performance in terms of quantum memories [6–8], but has yet to demonstrate reliable two-qubit gates between spin qubits or a realistic route towards larger qubit systems. A major obstacle has been that, so far, only large ensembles of rare-earth ions have been used for gate operations [9, 10], which has been shown to not scale well [11]. A promising approach to scalability in rare-earth quantum computing (REQC) is to move into the single instance regime, dealing with the particular difficulty of detecting single rare-earth ions inside their crystal hosts, something that was just recently realized [12].

In this paper, we present a readout scheme that in principle allows for an arbitrarily high readout fidelity of the quantum state of a single ion inside a macroscopic host. The readout scheme is based on using a special buffer step that can by cycled repeatedly, a scheme that is similar in nature to what has been done previously for multi-species atomic clocks [13]. We then show, that with such a readout, a full CNOT gate can be performed in these systems with fidelity of about 99 %, based on simulations that are supported by what is currently experimentally achievable. We also discuss further scaling towards larger multi-qubit systems by showing how chains of single ions can be mapped out, and we find that, including most known error sources, as discussed in Sec. IV, entangled states of 10 qubits remaining above 93 % fidelity appe feasible, as long as all ions can control each other.

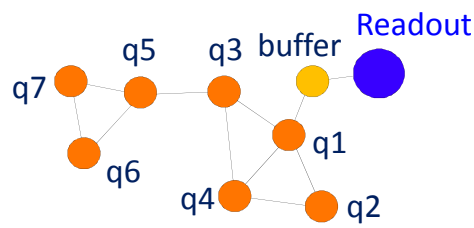

FIG. 1. (color online) A chain consisting of one readout i (Ce) surrounded by several qubit ions (Eu), where the cl est qubit ion is being used as a buffer stage (the bright on see the text for more details. The lines between the ions d plays which can interact directly via frequency shifts caus by changes to the permanent dipole moments. With a 4 doping concentration, it is expected that each Eu ion can average interact with about 5 other Eu ions surrounding it

It is interesting to note that at the single ion lev these impurity doped systems resembles the ion trap sy tems but with two major difference. The first is the a vantage that the ions are trapped by the comparative large trapping potentials of the crystal bindings. Th enables the ions to sit much closer to each other than ion traps (nanometers instead of micrometers), which turns allows the direct electrical dipole interactions b tween ions to be used as entangling mechanism. The se ond difference, is the disadvantage that the surroundi environment is not vacuum, but a crystal host that c cause additional decoherence effects as well as worsen t single ion detection possibilities through e.g. scatterin While the disadvantages may at first appear dauntin it is important to note that one of the main limitatio to scalability in ion traps is that the entangling mec anism, the common motional modes, becomes increa ingly more complex the more ions that are involved [1 The direct dipole interactions that can be used in REQ however, does not suffer from this problem, and we th expect that once the initial hurdle of establishing sing ion readout is overcome, the scaling to larger qubits w be relatively more manageable.

* andreas.walther@fysik.lth.se

The paper is organized as follows: In Sec. II the basic single instance quantum computing scheme is described together with a discussion on reasonable material parameters. Sec. III details the readout scheme, and in Sec. IV we go through a full CNOT gate from initialization to readout. Further scalability to larger qubit systems is discussed in Sec. V followed by a summary of our findings in Sec. VI.

II. OVERVIEW AND PARAMETER CONSIDERATIONS

The single instance scheme is based on using two different kinds of ions, doped into the host crystal. The first kind, the qubit ions, will have suitable ground state hyperfine levels with long coherence times and in addition long lived electronically excited states. However, because of their long life time they are not suitable for direct single ion readout, and therefore a second ion species will be used as a readout ion (see Fig. 1). Coupling between ions, both between two qubit ions for gates and between qubit ion and readout ion for detection, will be mediated via permanent dipole-dipole interactions. In both cases, when two ions are sufficiently close to each other, the change of the static dipole moment as one ion is excited is enough to shift the energy level of the neighboring ion out of resonance with a driving laser, thus giving a control mechanism.

Throughout the paper, it will be assumed that we are working with a Eu^{3+}:Y_2SiO_5 crystal, where 4 % of the Yttrium ions in the crystal host have been replaced with Europium, distributed roughly equal in each of two different sites. This is a relatively high doping concentration and simulations have shown that, given the difference between the dipole moment of the ground and excited state, any ion will on average have more than 5 other ions sufficiently close to be controlled by it. For the readout ion on the other hand, Cerium has appeared as a good candidate [15, 16], but since one readout ion is enough for an entire chain of qubits, the background trace elements of Ce is expected to be enough, no special doping is required. One potential problem with such a high doping concentration is that the fluorescence from Ce can be quenched by energy transfer to the Eu ions. This happens in particular instances where the Eu ion is very close to Ce, within 1-3 nm, and calculations show that this effect may be significant [17]. The full extent of energy transfer mechanisms still requires further study, but one mitigating factor is the fact that in practice it should be possible to avoid it by finding instances where the nearest ion is far enough away to not give energy transfer but still sufficiently close to cause a controlling shift (within ~ 14 nm corresponding to more than 10 MHz shift). Direct energy transfer between two Eu ions may also happen, but this should be less likely given that the oscillator strength of Eu is much smaller, and this has therefore not been taken into account.

Any state-to-state transfer will be done with compl hyperbolic secant (*sechyp*) pulses. These chirped puls have the advantage over simple square pulses that th are robust against certain errors, such amplitude and fr quency fluctuations, see Ref. [18] for more details. Blo simulations suggest that the Eu ions can be transferr to and from the excited state by such pulses of 400 ns d ration with an efficiency of 99.96 %, which will be us for the following calculations. It should be noted th this transfer efficiency for Eu has not been corroborat by experiments, and does not include effects such as spe tral diffusion. Preliminary calculations show that at th level of efficiency the effects from spectral diffusion m be substantial, although further studies are required. is believed however, that the effects from spectral diff sion can be strongly mitigated by holeburning sequenc that aims at keeping the total number of ions in the qu frequency channels very low. The high transfer efficien can be compared with experiments performed with t similar element Praseodymium, where the experiment transfer efficiency matches simulations rather well. F Praseodymium, the measured and calculated efficiency about 96 % [10], and the main limitations are the sho excited state life time and coherence time, as well as t fact that an ensemble was used that have not only and i homogeneous frequency spread but also sits on differe spatial parts of the beam profile, making different io experience difference Rabi frequencies. For single ion R transfers, both of those two limitations are strongly r duced.

III. READOUT SCHEME

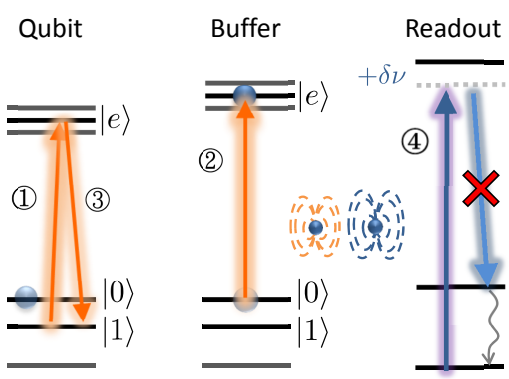

FIG. 2. (color online) Pulse sequence for reading out t state of one qubit via on buffer ion and the readout ion. the intance shown the qubit is in $|0\rangle$ state, which means t buffer ion gets excited, shifts the readout, which in turn sto fluorescing. If the ion instead was in the $|1\rangle$ state, the buf would be shifted, and would thus not become excited, and t readout would fluoresce normally.

on. First, one pulse is used to selectively excite the qubit on, then another to selectively excite the buffer ion, and a third to bring the qubit ion back to the ground state. After this selective excitation has been done the buffer is read out as described above, and the number of photons during the $T_{1,Eu}/3$ detection time is counted. The buffer ion can then be reinitialized through optical pumping and the procedure can be repeated, since the qubit ion still retains its original state, such that a total number of counted photons can be increased. Simulations show that the optimal number of times to repeat the procedure is approximately 20 times, and the threshold for distinguishing between $|0\rangle$ and $|1\rangle$ is about 550 photons, as shown in Fig. 1. Since the qubit ion now only spends a very short time in the excited state, the probability of it being corrupted is small. Using one buffer ion increases the probability of reading out the correct state to better than 99 %, and two steps of buffer ions yield 99.9 %. In principle further buffer steps could be concatenated for an exponentially decreasing error probability, however, for Eu in particular the millisecond upper state life time puts the final limit to about 99.9 %, i.e. only two buffer stages would be useful in practice.

IV. CNOT GATE FIDELITY

A full CNOT gate experiment will include the following steps:

1. Initialization
2. $\pi/2$-pulse on the control qubit
3. π-pulse doing $|0\rangle \rightarrow |e\rangle$ on control qubit
4. CNOT on target qubit
5. π-pulse reversing the excitation in step 3
6. Readout

The different steps in the list above will now be described in detail, including assumptions and expected errors for each step. The total CNOT error obtained in the end will include the error from all steps, with care taken to model the different nature of the errors. For example, any transfer pulse will cause both bit and phase flip errors, while any time spent in the excited state will be subject to lifetime decay, modeled as an amplitude damping channel (see e.g. Nielsen and Chuang [16]).

Initialization - The initialization step starts with finding a fluorescing readout ion. Next, the inhomogeneous width of the qubit ions is scanned through until the fluorescence from the readout stops, at which point an ion sufficiently close to the readout ion to shift it in frequency has been found. This will be the buffer ion. Next, the inhomogeneous width of the qubit ions is scanned from start again, in each try, exciting the buffer ion with π-pulse, and monitoring when the readout ion resumes fluorescing. This indicates that an ion that can control the buffer ion has been found. This step is repeated one mo time, such that two qubit ions that are both in the vici ity of the buffer ion is found. They will most likely al be sufficiently close to each other, but if they are nc or longer chains of ions is desired, the step is instead e tended to find ions that shift the previous qubit ion, th stopping it from controlling the buffer ion. This proce can be nested as many layers away from the readout ic as it takes, with the overhead cost of only one extra pul per layer away. After a sufficient chain of controlling io has been established, the qubit ions should be initializ to the $|0\rangle$ state, which can be done by means of optic pumping to an auxiliary state followed by a state transf back in a similar manner as the protocols used in the e semble approach [17]. The error in this step is assumed be equal to the error of the final transfer pulse (a sechyp i.e. the starting state is considered to be a mixed sta with a probability of being in the wrong level of $2 \cdot 10^$ for each qubit.

$\pi/2$-pulse on the control qubit - Since the hyperfi states cannot be directly driven, two pulses are requir to achieve a single qubit gate. This means that this st will give phase and bit flip errors for the control qubit $4 \cdot 10^{-4}$.

π-pulse doing $|0\rangle \rightarrow |e\rangle$ on control qubit - This st is a straightforward sechyp pulse, with phase and bit fl errors both considered to be $2 \cdot 10^{-4}$ for the control qub

CNOT on target qubit - Although the target qut operation is conditioned on the control ion causing frequency shift or not, this step is essentially just a pulse on the hyperfine levels, making the error on t target qubit $4 \cdot 10^{-4}$. In addition, the control qut spends two pulse durations of time in the excited stat which gives a decay probability due to limited lifetime $e^{0.8\mu s/1.9ms} \approx 4 \cdot 10^{-4}$.

π-pulse reversing the excitation in step 3 - Same o eration and errors as the excitation.

Readout - For the purpose of finding the achieva CNOT fidelity we use the scheme with two buffer ior as described above, with a readout error 10^{-3}. Note th this error is asymmetrical, i.e. it represents the probab ity that a $|0\rangle$ is counted as $|1\rangle$. The reverse error is orde of magnitude smaller and can be assumed to be negli ble. The reason for this asymmetry is that the main err is decay from the excited state which only happens in o direction.

Final experiment fidelity - In the end when all ste have been taken into account, but before the readou the system can be described by a certain density m trix, ρ. We can then compute the fidelity of the state $F = \langle\psi_{max}| \rho |\psi_{max}\rangle$, where ψ_{max} is the state we aim create, such as a maximally entangled Bell state. Wit out the readout step, the total error $\varepsilon = 1 - F$ is fou to be $\sim 2 \cdot 10^{-3}$. The readout is included by allowing t calculated density matrix to be sampled as it would du ing a real readout sequence, with projections to the fo possible two-qubit states. A quantum state tomograp sequence was then simulated, using 15 different obser

he end will include the error from all steps, with care aken to model the different nature of the errors. For example, any transfer pulse will cause both bit and phase lip errors, while any time spent in the excited state will e subject to lifetime decay, modeled as an amplitude lamping channel (see e.g. Nielsen and Chuang [19]).

Initialization - The initialization step starts with finding suitable chain of ions that can function as buffer and qubits, and can be described in 4 main steps: (i) find a fluorescing readout ion. (ii) scan through the inhomogeneous width of the qubit ions until the fluorescence rom the readout stops, at which point an ion sufficiently lose to the readout ion to shift it in frequency has been ound. This will be the buffer ion. (iii) The inhomogeneous width of the qubit ions is scanned from start again, in each try, exciting the buffer ion with π-pulse, nd monitoring when the readout ion resumes fluorescng. This indicates that an ion that can control the buffer on, and prevent it from being excited, has been found. iv) repeat the previous step one more time, such that wo qubit ions that are both in the vicinity of the buffer on is found. They will most likely also be sufficiently lose to each other, but if they are not, or longer chains f ions is desired, the step is instead extended to find ions hat shift the previous qubit ion, thus stopping it from ontrolling the buffer ion. This process can be nested as nany layers away from the readout ion as it takes, with he overhead cost of only one extra pulse per layer away.

After a sufficient chain of controlling ions has been stablished, the qubit ions should be initialized to the $|0\rangle$ state, which can be done by means of optical pumping o an auxiliary state followed by a state transfer back in a similar manner as the protocols used in the ensemble approach [10]. The error in this step is assumed to be qual to the error of the final transfer pulse (a sechyp), .e. the starting state is considered to be a mixed state with a probability of being in the wrong level of $4 \cdot 10^{-4}$ or each qubit.

$\pi/2$-pulse on the control qubit - The hyperfine states annot be directly driven by the laser. Instead, arbirary single qubit gates can be performed by two bichromatic pulses using a dark state technique (as described n Ref. [10]). These pulses have the same duration as the ransfer pulses, and thus essentially have the same error. With two pulses needed, this step will give phase and bit lip errors twice that of a transfer pulse, i.e. $8 \cdot 10^{-4}$ on he control qubit.

π-pulse doing $|0\rangle \rightarrow |e\rangle$ on control qubit - This step s a straightforward sechyp pulse, with phase and bit flip errors both considered to be $4 \cdot 10^{-4}$ for the control qubit.

NOT on target qubit - Although the target qubit operation is conditioned on the control ion causing a frequency shift or not, this step is essentially just a π-pulse on the hyperfine levels, i.e. a single qubit gate, making the error on the target qubit $8 \cdot 10^{-4}$. In addition, he control qubit spends two pulse durations of time in he excited state, which gives a decay probability due to imited lifetime of $1 - e^{-1.5\mu s/1.9\text{ms}} \approx 8 \cdot 10^{-4}$.

π-pulse reversing the excitation in step 3 - Same o eration and errors as the excitation.

Readout - For the purpose of finding the achieva CNOT fidelity we use the scheme with two buffer ion as described above, with a readout error $2.5 \cdot 10^{-3}$. No that this error is asymmetrical, i.e. it represents the pro ability that a $|0\rangle$ is counted as $|1\rangle$. The reverse error orders of magnitude smaller and can be assumed to l negligible. The reason for this asymmetry is that t main error is decay from the excited state, and state | is never excited.

Final experiment fidelity - The effects of all operatio described above is calculated from actions applied to starting density matrix. In the end when all steps ha been taken into account, but before the readout, the sy tem will be in a final density matrix, ρ_f. We can th compute the fidelity of the state as $F = \langle\psi_{max}| \rho_f |\psi_{max}$ where ψ_{max} is the state we aim to create, such as a max mally entangled Bell state. Without the readout step, t total error $\varepsilon = 1 - F$ is found to be $\sim 7 \cdot 10^{-3}$. The rea out is included by allowing the calculated density matr to be sampled as it would during a real readout sequenc with projections to the four possible two-qubit states. quantum state tomography sequence was then simulate using 15 different observables in 9 different measureme settings (see e.g. [20]). This gives a recreated densi matrix (shown in Fig. IV) that can be used obtain t fidelity, including the readout stage, and we find the t tal error to be $\sim 1.1 \cdot 10^{-2}$. This means that both t coherent operations and the readout process contribu significantly to the overall fidelity, and it emphasizes t need for using the proposed readout buffer stages.

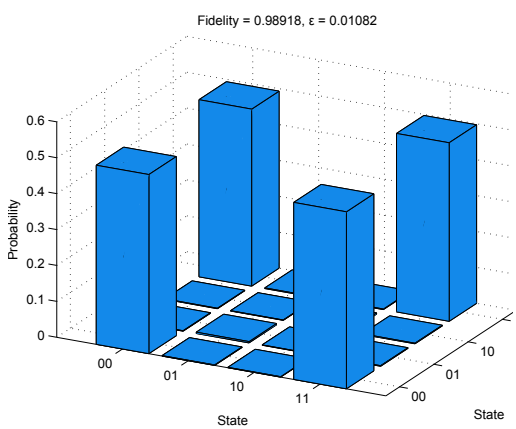

FIG. 4. (color online) Shows the (real) elements of the densi matrix of a prepared Bell state, including all error sources described in the text. The total fidelity without readout 99.3 % and with readout 98.9 %.

Note that while an effort has been made to inclu most systematic error sources, a real experiment will al include random projection noise caused by a limited nu

ber of experimental count cycles, but this has not been ncluded here. In practice, this error will be limited by he total duration of the full protocol, and since gate operations can be made in sub-microseconds, the largest ime is consumed by the readout stage. However, the luorescence detection itself is not the main culprit, as a buffer stage with 15 repetitions times a detection time $\Gamma_{1,\mathrm{Eu}}/3$ will take in the order of 5-10 ms, on par with other single ion detection rates. Instead, the main time consumption arises from the reinitialization of the buffer tep that has to be done between each repetition cycle. f simple optical pumping via the long lived excited state s used to reset the buffer state, then several life times of Eu has to be used to reset it with good fidelity, which s a few tens of ms per repetition. To circumvent this, a quenching mechanism can be used whereby the long ived excited state is excited further to a higher lying tate with short life times. For Eu, such states could be he $^5D_2$ or $^5D_3$ levels, which both have life times in the ens of µs range, much smaller than the detection time nd thus enough to eliminate the contribution from this part.

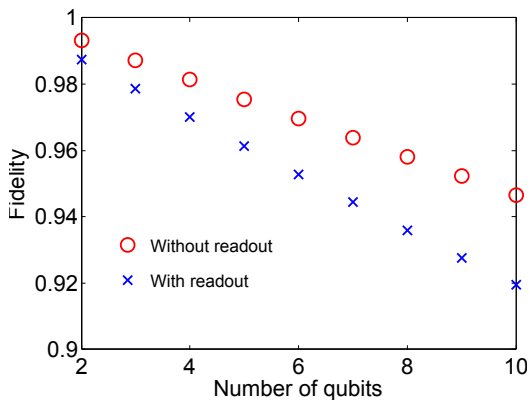

IG. 5. (color online) Predicted fidelity of n-qubit GHZ states vith and without readout. The fidelity includes pulses for omography but assumes that all ions can interact with each other, which is reasonable at least up to 5 qubits with 4 % loping concentration.

V. SCALABILITY

The previous section detailed the specific case of a two-qubit gate, where the errors were included in a careful manner in the total density matrix describing the system. This approach is difficult to extend to larger qubit systems, as the size of the Hilbert space scales exponentially with the number of qubits. In this section, we will attempt to give some figures for the scali of larger qubit states by simpler considerations, bas on the values of the CNOT gate obtained in the pre ous section. We will focus on the expected fidelity an n-qubit Greenberger-Horne-Zeilinger (GHZ) state the form $|\Psi\rangle = |0...0\rangle + |1...1\rangle$, which is a simple y useful type of entangled state. The expected fidelity this state can be fairly straightforwardly calculated l realizing that it is created by $n-1$ successive CNO gates. Moreover, this fidelity will be the same both f the case of only nearest-neighbor interactions and for t case where each ion can control each of the other ior This result is shown in Fig. 5, both with and witho readout. One limitation of the prediction is that whi the creation of the GHZ state allows situations whe only nearest neighbor interactions are possible, the rea out step is calculated with the assumption that each i can control a buffer ion directly without additional swa operations. As discussed earlier in Sec. II, this is e pected to be a reasonable case for at least up to 5 qubi for a doping concentration of 4 %.

VI. CONCLUSIONS

We have presented a readout scheme for detecti quantum states of single ions inside a crystal host. Tl scheme is based on monitoring the fluorescence from short lived rare-earth ion using another long lived rar earth ion species as a buffer stage that can be repeated cycled. Several buffer stages can in principle be concat nated to yield a very long effective detection time, su that readout errors can be reduced 2 orders of magn tude. We then used this result together with known e ror sources to obtain expected fidelities for a CNOT ga of 98.9 % and for larger GHZ states remaining abo 97 % even for 10 qubits. The main limitation of o calculations is presently that the expected increase performance for qubit rotations when switching from l to Eu has not been experimentally verified as of ye Our results are important for enabling and showing th rare-earth quantum computing is feasible in the sing instance regime.

ACKNOWLEDGEMENTS

This work was supported by the Swedish Resear Council, the Knut & Alice Wallenberg Foundation, t Crafoord Foundation. The research leading to these r sults also received funding from the People Programm (Marie Curie Actions) of the European Union's Seven Framework Programme FP7 (2007-2013) under RE grant agreement no. 287252 (CIPRIS), Lund Laser Ce ter (LLC), and the Nanometer Structure Consortium Lund University (nmC@LU).

[1] H. Häffner, W. Hänsel, C. F. Roos, J. Benhelm, D. C. al kar, M. Chwalla, T. Körber, U. D. Rapol, M. Riebe, P. O. Schmidt, C. Becher, O. Gühne, W. Dür, and R. Blatt, Nature **438**, 643 (2005).

[2] T. Monz, P. Schindler, J. T. Barreiro, M. Chwalla, D. Nigg, W. A. Coish, M. Harlander, W. Hänsel, M. Hennrich, and R. Blatt, Phys. Rev. Lett. **106**, 130506 (2011).

[3] X.-C. Yao, T.-X. Wang, P. Xu, H. Lu, G.-S. Pan, X.-H. Bao, C.-Z. Peng, C.-Y. Lu, Y.-A. Chen, and J.-W. Pan, Nat. Photon **6**, 225 (2012).

[4] M. H. Devoret and R. J. Schoelkopf, Science **339**, 1169 (2013).

[5] J. Wrachtrup and F. Jelezko, J. Phys.: Condens. Matter **18**, S807 (2006).

[6] H. Riedmatten, M. Afzelius, M. U. Staudt, C. Simon, and N. Gisin, Nature **456**, 773 (2008).

[7] M. Afzelius, I. Usmani, A. Amari, B. Lauritzen, A. Walther, C. Simon, N. Sangouard, J. c. v. Minář, H. de Riedmatten, N. Gisin, and S. Kröll, Phys. Rev. Lett. **104**, 040503 (2010).

[8] M. P. Hedges, J. J. Longdell, Y. Li, and M. J. Sellars, Nature **465**, 1052 (2010).

[9] E. Fraval, M. J. Sellars, and J. J. Longdell, Phys. Rev. Lett. **95**, 030506 (2005).

10] L. Rippe, B. Julsgaard, A. Walther, Y. Ying, and S. Kröll, Phys. Rev. A **77**, 022307 (2008).

11] J. H. Wesenberg, K. Mølmer, L. Rippe, and S. Kröll, Physical Review A **75**, 012304 (2007).

[12] R. Kolesov, K. Xia, R. Reuter, R. Stöhr, A. Zapp J. Meijer, P. Hemmer, and J. Wrachtrup, Nat. Cor mun. **3**, 1029 (2012).

[13] D. B. Hume, T. Rosenband, and D. J. Wineland, Phy Rev. Lett. **99**, 120502 (2007).

[14] D. Kielpinski, C. Monroe, and D. Wineland, Nature **41** 709 (2002).

[15] A. Walther, B. Julsgaard, L. Rippe, Y. Ying, S. Krö R. Fisher, and S. Glaser, Phys. Scr. T **137**, 0140 (2009).

[16] Y. Yan, J. Karlsson, L. Rippe, A. Walther, D. Serran D. Lindgren, M.-E. Pistol, S. Kröll, P. Goldner, L. Zhen and J. Xu, Phys. Rev. B **87**, 184205 (2013).

[17] D. Serrano, Y. Yan, J. Karlsson, L. Rippe, A. Walthe and S. Kröll, "Energy transfer mechanisms in Ce-Pr a Ce-Eu co-doped Y2SiO5 and their impact on single-i based quantum computing," Manuscript in preparatio

[18] I. Roos and K. Mølmer, Phys. Rev. A **69**, 022321 (200

[19] M. A. Nielsen and I. L. Chuang, *Quantum computati and quantum information* (Cambridge university pre 2000).

[20] C. F. Roos, G. P. T. Lancaster, M. Riebe, H. Haeffn W. Haensel, S.Gulde, C. Becher, J. Eschner, F. Schmic Kaler, and R. Blatt, "Tomography of entangled massi particles," ArXiv:quant-ph/0307210 (Paper published PRL 92, 220402 (2004), but the full sequence was list only in the arXiv version).

Paper V

Energy transfer mechanisms in Ce^{3+}-Pr^{3+} and Ce^{3+}-Eu^{3+} codoped Y_2SiO_5 and their impact on single-ion based quantum computing

D. Serrano, Y. Yan, J. Karlsson, L. Rippe, A. Walther and S. Kröll.

Manuscript in preparation , (2013).

Energy transfer mechanisms in Ce^{3+}-Pr^{3+} and Ce^{3+}-Eu^{3+} codoped Y_2SiO_5 and their impact on single-ion based quantum computing

Diana Serrano, Ying Yan, Jenny Karlsson, Lars Rippe, Andreas Walther and Stefan Kröll
Department of Physics, Lund University, P.O. Box 118, SE-22100 Lund, Sweden

Alban Ferrier and Philippe Goldner
Chimie ParisTech, Laboratoire de Chimie de la Matière Condensée de Paris, CNRS-UMR 7574, UPMC Univ Paris 06, 11 rue Pierre et Marie Curie 75005 Paris, France

(Dated: September 13, 2013)

We analyze the Ce^{3+}-Pr^{3+}:Y_2SiO_5 emission spectra obtained under selective excitation of the two Ce^{3+} sites in Y_2SiO_5 and we show clear evidence of direct energy transfer from Ce^{3+} to Pr^{3+}. Energy transfer microparameters were calculated from the experimental spectral overlap between the Ce^{3+} emission and the Pr^{3+} and Eu^{3+} absorptions from which, the transfer mechanisms $Ce^{3+}\rightarrow Pr^{3+}$ are concluded to be more efficient than the transfer mechanisms $Ce^{3+}\rightarrow Eu^{3+}$. The energy transfer processes demonstrated here are potentially detrimental for an efficient qubit readout as they lead to a quenching of the Ce^{3+} luminescence and can give rise to the unwanted change of the qubit state. The quantum computing readout scheme is based on permanent electric dipole interactions scaling as R^{-3}, where R is the distance between the Ce^{3+} and the qubit ion. The non-radiative energy transfer processes also depend on the ion-ion distances, however as R^{-6}. A discussion about the microscopic dopant distributions leading to an efficient single-ion readout quantum computing scheme is here presented, taking into account the need to limit the energy transfer processes.

PACS numbers: 42.62.Fi,78.55.-m,78.40.-q,03.67.-a,32.10.Dk

I. INTRODUCTION

The investigations pursuing the use of rare-earth doped crystals as hardware for quantum computers have led in the last decade to a number of achievements such as the possibility of qubit formation, control and the use of permanent electric dipole-dipole interactions for gate operations between qubits [1, 2]. The detection of the qubit states is planned through a so-called readout ion sitting close enough to a qubit ion so that its excited state is shifted in energy when the qubit ion is promoted from the ground state to the excited state [3]. This approach is a single instance quantum computing implementation where each qubit consist of a single ion [3, 4]. It is attractive since, in contrast to earlier work [1, 2] based on qubit ensembles, is scalable to many qubits which constitutes a fundamental requirement in terms of real quantum computation [5]. The long excited lifetimes times required for qubit operations prevent however the qubit ions themselves to carry out the readout role as it implies the detection of a single emitter. A readout ion presenting a high emission rate is thus needed for this quantum computing aproach [6]. Other approaches to build multiple qubit systems consist of rare-earth stoichiometric crystals lightly doped with another rare-earth ion [7, 8]. In these materials, the different rare-earth ions surrounding the dopant ion are targeted as independent qubits and the short distance between the qubit ions leads to a strong electric dipole-dipole coupling between them.

A number of rare-earth ions and host crystals have been so far studied for quantum information applications [9–11]. Y_2SiO_5 doped with Pr^{3+} and Eu^{3+} ions are among the most prominent. This is due to the long coherence times observed for the optical transitions at 606 nm (Pr^{3+}:$^3H_4\rightarrow{}^1D_2$) and 580 nm (Eu^{3+}:$^7F_0\rightarrow{}^5D_0$), as well as the long lifetimes and coherence times of the ground state hyperfine levels [12–14]. For instance, lifetimes of 100 seconds in the case of Pr^{3+} [15] and more than 20 days for Eu^{3+} [16] have been reported at zero magnetic field for the ground hyperfine levels. On the other hand, trivalent Cerium has been proposed to carry out the readout function [3] as its $5d\rightarrow 4f$ optical transition possesses a unity fluorescence quantum yield, no long-lived trapping states and excited state lifetime in the nanosecond scale. These features assure an emission rate high enough to collect photons from a single emitter. In addition, Ce^{3+} can be introduced into the Y_2SiO_5 lattice as a codopant so that it can eventually be found in vicinity of an interacting qubit ion. Further evidence of permanent electric dipole-dipole interaction between Ce^{3+} and Pr^{3+} ions has recently been reported in Y_2SiO_5 [6] and the succesful detection of the fluorescence of a single Ce^{3+} ion [17] has also been achieved in a YAG host. These results are very encouraging for the practical execution of the single ion quantum computing scheme.

A well-known phenomenon, often observed in rare-earth doped crystals and which has not been considered so far by the rare-earth based quantum computing approaches is the presence of energy transfer paths between the readout ion and the qubit ion. The energy transfer processes between trivalent rare-earth ions [18, 19] have been actively investigated and exploited during the last decades for the development of rare-earth based phos-

phors [20, 21], scintillators [22], luminescent solar converters [25], laser crystals [23] and in general, the study and application of upconversion phenomena [24].

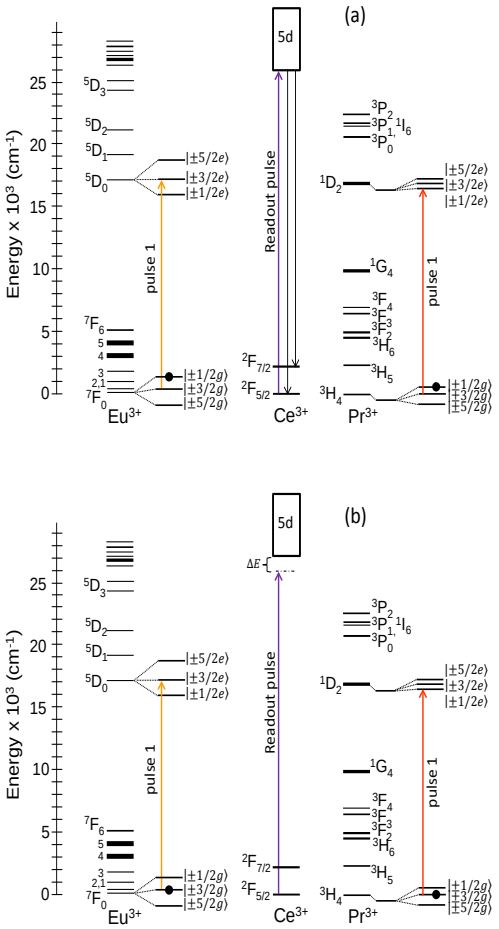

FIG. 1: Ce^{3+}-Pr^{3+}/Eu^{3+} readout scheme. Solid colored arrows represent the excitation pulses at approximately 370 nm, 606 nm and 580 nm for Ce^{3+}, Pr^{3+} and Eu^{3+} respectively. (a) Ce^{3+} emission should be detected when the qubit ion is initially found in the state $|1/2g\rangle$. (b) No emission is expected from the Ce^{3+} ion when the qubit is in the ground hyperfine state $|3/2g\rangle$. The hyperfine splitting of the $^7F_0$ and $^5D_0$ Eu^{3+} singlets and the lowest stark level of the $^3H_4$ and $^1D_1$ Pr^{3+} multiplets are not scaled in energy to the spin-orbit electronic levels as it is just several MHz (10^{-3} cm^{-1}) in the case of Pr^{3+} and hundreds of MHz for Eu^{3+} (10^{-2} cm^{-1}).

Experimental evidences of efficient energy transfer mechanisms both from Ce^{3+} to Pr^{3+} and Ce^{3+} to Eu^{3+} have been shown in host materials such as $Lu_3Al_5O_{12}$, $Y_3Al_5O_{12}$ [26, 27], YVO_4 [28] or $Y_2Zr_2O_7$ [29]. The existence of energy transfer from Ce^{3+} to Pr^{3+} has recently been reported in Ce^{3+}-Pr^{3+} codoped Y_2SiO_5 [30] and in the Ce^{3+}-Eu^{3+} case, it needs to be evaluated. The reason is that such processes can partially quench the Ce^{3+} luminescence, complicating the detection of the readout signal upcoming from a single Ce^{3+} emitter. At the same time, the qubit ion is promoted to an excited state as a consequence of the energy transfer and this would destroy the qubit state under readout.

A detailed description of the proposed readout scheme is displayed in Figure 1 for the readout-qubit pairs Ce^{3+}-Pr^{3+} and Ce^{3+}-Eu^{3+}. The scheme is essentially the same independent of the qubit center. Pr^{3+} and the two Eu^{3+} isotopes, namely ^{151}Eu and ^{153}Eu, present 5/2 nuclear spin and so, the same number of hyperfine levels. The qubit is encoded in the hyperfine levels $|1/2g\rangle$ and $|3/2g\rangle$, and the objective of the readout is to determine wether the qubit is in state $|1/2g\rangle$ or $|3/2g\rangle$ after the computations are done. Thus, a first laser pulse resonant with the qubit optical transition from the hyperfine level $|3/2g\rangle$ to one of the hyperfine levels in the excited state is sent. The qubit ion does not interact with this pulse as it is in the state $|1/2g\rangle$ (Fig. 1a). Readout pulses, resonant with the Ce^{3+} $4f \rightarrow 5d$ zero-phonon transition are next sent in resulting in the excitation of the Ce^{3+} ion and subsequent radiative decay. In Fig. 1b, the qubit ion, whose initial state is $|3/2g\rangle$, becomes excited after interaction with the first pulse. The permanent dipole moment of the excited state of the qubit ion, being different from that of the ground state, changes the energy of the Ce^{3+} excited state so that, if the energy shift $|\Delta E|$ is large enough (Fig. 1b), the new transition is no longer resonant with the readout pulses and no excitation nor luminescence can be detected from the readout ion in this case. Therefore, the detection or absence of Ce^{3+} luminescence directly probes the qubit initial state.

In this paper, we estimate the efficiency of the energy transfer processes for couples of Ce^{3+}-Pr^{3+} and Ce^{3+}-Eu^{3+} ions within Y_2SiO_5 as a function of the distance between the qubit and readout ions, and we discuss their impact on the single-ion based readout quantum computing scheme.

II. OPTICAL MEASUREMENTS

Several Czochralski grown Y_2SiO_5 singly doped Pr^{3+} and Eu^{3+} crystals with final dopant concentrations of 0.05 %at. and 0.1 %at., as well as a codoped 0.01 %at. Ce^{3+} and 0.03 at. % Pr^{3+} crystal were used in the study. Y_2SiO_5 is a biaxial monoclinic crystal with C2/c space group (number 15) and lattice parameters equal to a=14.413 Å, b=6.7190 Å, c=10.4000 Å, α=90, β=122.235 and γ=90 [31, 32]. The Y^{3+} ions occupy two inequivalent crystallographic sites within Y_2SiO_5, distinguished by their oxygen coordination (7 for site referred to as of type 1, and 6 for the site referred to as of type 2

to as of type 1, and 6 for the site referred to as of type 2 [33]). The rare-earth dopants have been found to replace the Y^{3+} ions in both sites, with site occupancies which vary depending on the rare-earth ion considered. Thus, in the case of large ions such as Pr^{3+} and Ce^{3+}, most dopants occupy the site 1 [34]. The site occupation becomes much more equilibrated in the case of Eu^{3+} since this ion is similar in size to Y^{3+} [16].

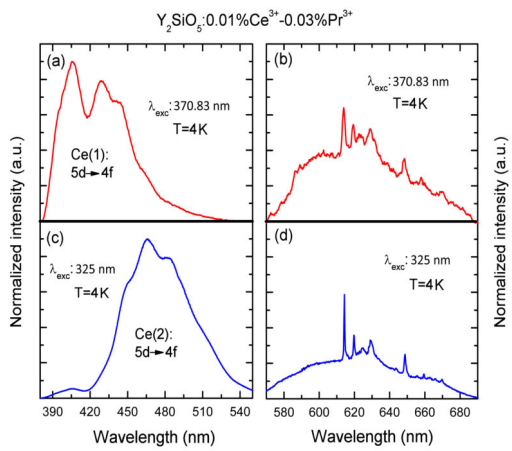

FIG. 2: (a-b) Emission spectrum obtained under Ce1 excitation at 370.83 nm. (c-d) Emission spectrum obtained under Ce2 excitation at 325 nm. The spectra were separated in two regions and normalized for the sake of clarity due to the intensity contrast between the strong Ce^{3+} bands (a) and (c), and the weak Pr^{3+} emissions (b) and (d).

Figure 2 displays the emission spectra recorded at low temperature under two different laser excitation wavelengths for the Ce^{3+}-Pr^{3+} codoped Y_2SiO_5 sample. Laser excitation at 325 nm selectively excites the Ce^{3+} ions in site 2 (Ce2) [35] while the 370.83 nm diode laser excitation is centered on the zero-phonon absorption line (ZPL) of Ce^{3+} ions in site 1 (Ce1) [6]. The excitation of the Ce1 ZPL is actually the one aimed for the readout pulses (Fig. 1) since the transition must be narrow to be shifted off resonance by the dipole-dipole interaction. Broad emission bands are observed in the 370-500 nm (Fig. 2a) and 430-550 nm (Fig. 2c) spectral regions. Those are attributed to the Ce^{3+} fluorescence in sites 1 and 2 respectively [35]. The band corresponding to Ce1 shows additional structure with a prominent peak at 400 nm and a second one around 425 nm, associated with the transitions $5d \rightarrow 4f(^2F_{5/2})$ and $5d \rightarrow 4f(^2F_{7/2})$. Besides the Ce^{3+} emissions, the appearence of a set of narrow emission peaks is observed in the 600-700 nm spectral region (Fig. 2b and d). These peaks actually correspond to Pr^{3+} emissions from the $^3P_0$ and $^1D_2$ energy levels and they are the result of an energy transfer from Ce^{3+} to Pr^{3+}. The energy transfer mechanism is therefore taking place from both Ce^{3+} sites as the Pr^{3+} emission lines are clearly observed when exciting at 370.83 nm (Fig. 2b) and 325 nm (Fig. 2d). A remarkably weak fluorescence signal was obtained for the Pr^{3+} emissions under 370.83 nm excitation. Nevertheless, a lower energy transfer efficiency Ce1 to Pr^{3+} compared to the case Ce2 to Pr^{3+} can not be derived from this result as the emission spectra were recorded under different experimental conditions for the two excitations. Thus, they can not be directly compared. In the next section, we look at the energy transfer efficiencies from Ce^{3+} to Pr^{3+} in Y_2SiO_5, with an emphasis on the microscopic point of vue of the mechanism, and we include in the study the investigation of the efficiency of the $Ce^{3+} \rightarrow Eu^{3+}$ energy transfer paths.

III. MICROSCOPIC ENERGY TRANSFER INVESTIGATION

The energy transfer rate (A_{ET}) for a resonant dipole-dipole energy transfer mechanism between two interacting ions [18, 36], usually denoted as donor and acceptor, is given by:

$$A_{ET} = \frac{C}{R^6} \tag{1}$$

where R is the distance between the two ions involved and C is

$$C = \frac{3c}{8\pi^4 n^2} \int \sigma_{Em,D}(\lambda)\sigma_{Abs,A}(\lambda)d\lambda \tag{2}$$

the so-called transfer microparameter [37], which depends on the integrated spectral overlap between the

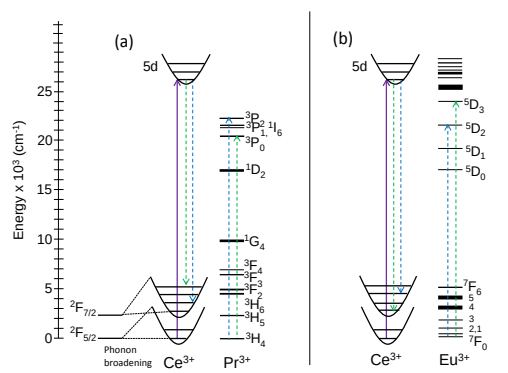

FIG. 3: (a) Ce^{3+}-Pr^{3+} and (b) Ce^{3+}-Eu^{3+} level schemes. Dashed arrows represent possible energy transfer paths after the excitation of Ce^{3+} into the 5d level. The Ce^{3+} levels are represented by a configurational coordinate diagram [38] in order to evidence the broadening of the 5d emission.

donor emission cross-section and the acceptor absorption cross-section, as well as the index of refraction of the host n and vacuum light speed c. The demonstrated existence of energy transfer mechanisms from Ce^{3+} to Pr^{3+} in Y_2SiO_5 is not really surprising as the spectral region covered by the Ce^{3+} 5d emissions (Ce1 and Ce2) overlaps several Pr^{3+} absorption lines, in particular, the ^3P_J Pr^{3+} levels (Fig. 3a). The analysis of the Eu^{3+} energy level scheme, on the other hand, also points the more than likely existence of energy transfer paths from Ce^{3+} to Eu^{3+} as displayed in Fig. 3b. Establishing the efficiency of the energy transfer processes depicted in Fig. 3 and their eventual interference within the proposed single-instance quantum computing readout scheme appears necessary for the development of quantum information hardware. Experimental methods often used to investigate energy transfer efficiencies such as the study of the dynamics of the ion acting as donor, provide a general insight into the transfer efficiency for a given rare-earth doped crystal, or in other words, they offer some idea of the behaviour of the majority of the ions in the crystal. These methods are however not really applicable to our case as they are unable to estimate the efficiency of the transfer mechanisms taking place between ions for a particular distribution of dopants within the crystal. The microscopic point of view of the transfer mechanisms has to be taken into account when discussing their influence on the single-ion based quantum computing readout scheme since this one is based on a single readout ion surrounded by qubits. In addtion, the qubit ions have to be close enough to the readout ion so that their dipolar fields can interact (Fig. 1), the strength of interaction depending on the distance as R^{-3} [6]. The inter-ionic interaction distance is so a critical parameter which must be considered carefully as it is also going to determine the efficiency of the energy transfer processes (Eq. 1).

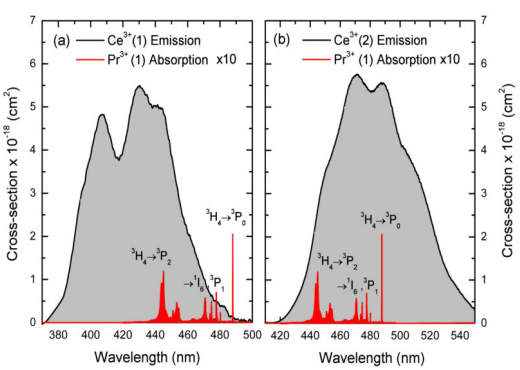

FIG. 4: Spectral overlap between the low temperature Ce^{3+} emissions (gray) and polarization averaged Pr^{3+} absorptions (red) for the cases (a) Ce1-Pr1 and (b) Ce2-Pr1.

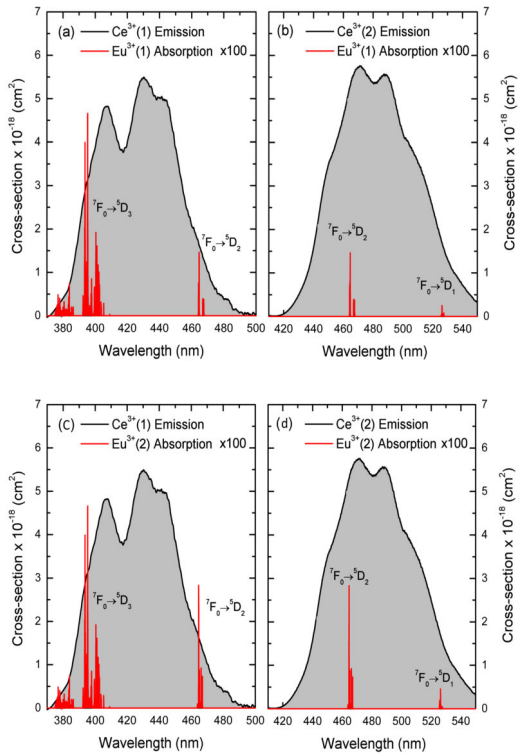

FIG. 5: Spectral overlap between the low temperature Ce^{3+} emissions (gray) and polarization averaged Eu^{3+} absorptions (red) for the cases (a) Ce1-Eu1, (b) Ce2-Eu1, (c) Ce1-Eu2 and (d) Ce2-Eu2.

The study of the energy transfer rates and efficiencies in Y_2SiO_5:Ce^{3+}-Pr^{3+} and Y_2SiO_5:Ce^{3+}-Eu^{3+} is here accomplished by the determination of transfer microparameters (Eq. 2) for resonant Ce^{3+}→Pr^{3+} and Ce^{3+}→Eu^{3+} energy transfers. Low temperature Pr^{3+} and Eu^{3+} absorption spectra were recorded in Y_2SiO_5, polarized along the principal axis of the dielectric vector, referred to as b, D_1 and D_2. The absorption of the $^3P_{0,1,2}$ and $^1I_6$ levels are observed in the Pr^{3+} absorption spectra within the 370-550 nm spectral region, and in the case of Eu^{3+}, the absorption lines corresponding to the $^5D_0$,$^5D_1$,$^5D_2$, $^5D_3$ were identified.

The analysis of the Eu^{3+} and Pr^{3+} polarized absorption spectra reveals, as expected, the presence of peaks of both crystallographic sites which could be asssigned from previous spectroscopic studies [39–41]. The polarized absorption spectra for the Pr^{3+} ions in site 1 were distinguished and separated from the site 2, not considered in the study. Pr2 is in principle not aimed to create qubits due to its lower coherence times and low site occu-

attributed to one site or the other. All the spectra were afterwards calibrated to absorption cross-section values as follows:

$$\sigma_i^{\phi} = \frac{\alpha_i^{\phi}}{N_i} \tag{3}$$

where α_i^{ϕ} and N_i are the absorption coefficient and the denstity of dopants respectively, with $i = 1, 2$ referring to the site and ϕ stating for the polarization orientation. N_i were determined by taking into account the Y^{3+} density in the host, the dopant concentration in the sample (0.05% and 0.1% for the Pr^{3+} and Eu^{3+} samples respectively), and the sites occupancies which were set to 4:1 for site 1 in Pr^{3+} and 1:1 in Eu^{3+}. Polarization averaged absorption spectra were finally calculated for the Pr^{3+} ions in site 1 (Pr1) and each one of the Eu^{3+} sites (Eu1 and Eu2). The Ce^{3+} emission spectra were calibrated in cross-section by using the Fluchtbauer-Ladenburg spectroscopic method [42]. Unlike the Eu^{3+} and Pr^{3+} absorptions, no significant differences are observed for the three polarized Ce^{3+} emissions in Y_2SiO_5 [30]. Thus, the emission spectra here presented were recorded under unpolarized light and arbitrary propagation direction. The cross-section calibrated polarization averaged absorption and emission spectra are displayed in Fig.4 and Fig.5. Spectral overlap is observed in all the cases investigated enabling resonant energy transfer paths. Transfer microparameters were afterwards derived from Eq. 2. The results are shown in Table I.

TABLE I: Calculated energy transfer microparameters (C) and critical distances.

Donor-Acceptor	C (Å^6 s^{-1})	Distance (Å)
Ce2-Pr1	10.0×10^{11}	6.1
Ce1-Pr1	8.2×10^{11}	8.3
Ce1-Eu2	5.9×10^{11}	5.4
Ce1-Eu1	5.8×10^{11}	5.3
Ce2-Eu2	5.6×10^{11}	5.2
Ce2-Eu1	0.9×10^{11}	4.1

IV. CONSEQUENCES FOR THE SINGLE-ION READOUT SQUEME

As shown in Table I, higher values were found for the two Ce^{3+}-Pr^{3+} energy transfer microparameters calculated. This is mainly due to the fact that Pr^{3+} presents larger absorption cross-section values than Eu^{3+}, which leads to stronger spectral overlaps and higher transfer rates. Critical energy transfer distances were also estimated, defined as the distance between donor and acceptor for which the energy transfer rate is identical to the radiative decay rate of the donor. The critical distances found are larger than the distance separating two dopants at nearest-neighbor positions within an yttrium orthosilicate crystal (∼3.8 Å for two ions in site 1). Thus, the Ce^{3+} emission rate will be reduced more than 50% for pairs of nearest-neighbors Ce^{3+} and Pr^{3+} or Eu^{3+} ions as a result of the energy transfer. A strong quenching of the readout ion fluorescence, symbolized by the critical distance, is not the only inconvenience which should be taken into account. Ideally, in order to avoid unwanted changes in the qubit state like its promotion to an excited state, the probability of energy transfer should be negligible during a full readout cycle. It has been estimated that the readout transition needs to be cycled a minimum of 2000 times to achieve enough photons emitted allowing to determine the qubit initial state [43]. This means that one has to find pairs of readout ions and qubit ions separated by distances so that the energy transfer probability is lower than 5×10^{-4}. The evolution of the energy transfer probability as a function of the inter-ionic distances was calculated from the ratio between the energy transfer rate, A_{ET}, given by Eq. 1, and the Ce^{3+} total desexcitation rate (A_{tot})

$$A_{tot} = \tau_{rad}^{-1} + A_{ET} \tag{4}$$

in which τ_{rad} is set to 39 ns for Ce1 and 59 ns for Ce2 [35]. The results are displayed in Fig.6:

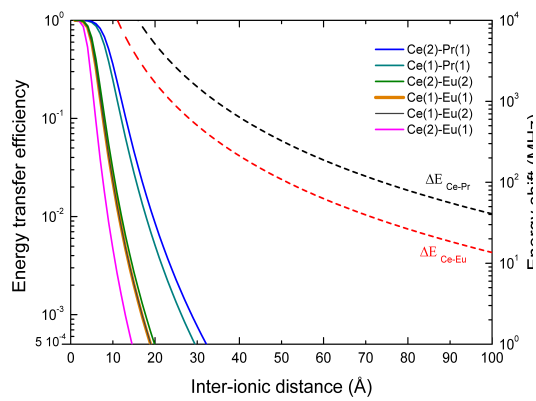

FIG. 6: Solid lines: Evolution of the energy transfer probability as a function of the inter-ionic distances for the different cases investigated (left axis). Dashed lines: Distance dependent evolution of the energy shift induced in the readout ion by a Pr^{3+} qubit ion (black) and Eu^{3+} qubit ion (red) (right axis).

In the Ce^{3+}-Pr^{3+} case, inter-ionic distances around 30 Å are needed to free the readout mechanism from energy transfer. This limit goes down to 20 Å for Ce^{3+}-Eu^{3+} due to the intrinsic lower efficiency of the energy transfer mechanisms in this codoping. The necessity to avoid distributions of dopants were the ions are sitting at distances shorter than 30 Å may seem very problematic

since, as it has been previously stated, the reaout ion needs to interact with the qubit ion so that its excited state can be shifted (Fig. 1b). Shifts of several tens of MHz are however considered sufficient as the Ce^{3+} homogeneous line has been measured to 4 MHz [6]. The evolution of the energy shift as a function of the distance can be estimated as:

$$\Delta E = \frac{1}{4\pi\epsilon_0}\frac{(\epsilon(0)+2)^2}{9\epsilon(0)}\frac{\Delta\mu_{qubit}\Delta\mu_{Ce}}{R^3} \qquad (5)$$

with $\Delta\mu_{Ce}$ and $\Delta\mu_{qubit}$ the difference between the electric dipole moment in the ground and excited state for Ce^{3+} and the qubit ion respectively, where the second factor is a local field correction. As displayed in Fig. 6, energy shifts of the order of tens of MHz can be in principle achieved for ions which are up to 100 Å away from each other. Thus, even avoiding pairs of readout and qubit ions separated by less than 30 Å for Pr^{3+} as qubit ion, and 20 Å for Eu^{3+}, any couple separated by distances between 30 and 100 Å could be eligible to carry out the readout mechanism successfully. A reduction of the doping concentration and consequent increase of the average distance between the ions is a straight forward way to limit the efficiency of the energy transfer processes. However, facing the eventual need of using relatively high doping concentrations in order to boost the qubit-qubit dipole-dipole coupling, the possibility of finding microscopic distributions of dopants fulfilling the distance criteria is small but not negligible. For instance, with a doping concentration of 2%at., the probability of finding a readout ion separated by more than 2 nm from the closest qubit ion is about 0.04 in Y_2SiO_5 (4% of the cases). It is important to note however that the detection of fluorescence arising from a single Ce^{3+} ion in such crystal would already indicate that this ion doesn't undergo a strong quenching by energy transfer. Thus, the single-ion detection required for the readout mechanism provides in addition a method to identify the microscopic dopant distributions free of energy transfer. This result, on the other hand, points at the difficulty of increasing the doping concentration beyond a certain amount. The use of stoichiometric crystals for quantum computing aims, and also, crystal hosts which tend to form pairs of dopants or any kind of clusters can be also problematic. The particular host and doping ions should however be discussed in order to state further conclusions.

The energy transfer model used here, based on electric dipole-dipole interactions, is generally considered to provide a good description of the energy transfer mechanisms [44, 45]. At the short distances range (less than 7-8 Å), the results are expected to be less accurate due to the contribution to the energy transfer rate of higher order multipolar interactions like dipole-quadrupole (scaling as R^{-8}) and quadrupole-quadrupole (scaling as R^{-10}) [45]. Exchange and superexchange mechanisms [46], on the other hand, can also appear between ions sitting very close to each other, leading to remarkably higher energy transfer rates than that expected from the dipole-dipole model. The distance region discussed for the readout mechanism (up to 10 nm) is however large enough to obtain meaningful results from a dipole-dipole description.

V. CONCLUSION

Resonant energy transfer paths have been demonstrated from Ce^{3+} to Eu^{3+} and Ce^{3+} to Pr^{3+} for the different crystallographic sites occupied by the dopants within yttrium orthosilicate. The evolution of the energy transfer probability with the distance between the ions considered indicates the need to avoid distances shorter than 3 nm in the case Ce^{3+}-Pr^{3+}, and 2 nm for Ce^{3+}-Eu^{3+} in order to succesfully use Ce^{3+} as a probe to readout the Eu^{3+} and Pr^{3+} qubit states.

Acknowledgment

This work was supported by the Swedish Research Council, the Knut & Alice Wallenberg Foundation, the Crafoord Foundation, the EC FP7 Contract No. 247743 (QuRep). The research leading to these results also received funding from the People Programme (Marie Curie Actions) of the European Union's Seventh Framework Programme FP7 (2007-2013) under REA grant agreement no. 287252(CIPRIS), Lund Laser Center (LLC), and the Nanometer Structure Consortium at Lund University (nmC@LU). We also want to thank Lihe Zheng and Jun Xu for the Y_2SiO_5:Ce^{3+}-Pr^{3+} cystal, and David Lindgren and Matts-Erik Pistol for their experimental support.

[1] J. J. Longdell and M. J. Sellars, Phys. Rev. A. **69**, 032307 (2004).
[2] L. Rippe, M. Nilsson, S. Kröll, R. Klieber and D. Suter, Phys. Rev. A. **71**, 062328 (2005).
[3] J. H. Wesenberg, K. Mølmer, L. Rippe and S. Kröll, Phys. Rev. A **75**, 012304 (2007).
[4] A. Walther, B. Julsgaard, L. Rippe, Y. Ying, S. Kröll, R Fisher and S Glaser, Phys. Scr. **T137**, 014009 (2009).
[5] D. P. Di Vincenzo, Fortschr. Phys. **48** (9-11), 771 (2000).
[6] Y. Yan, J. Karlsson, L. Rippe, A. Walther, D. Serrano, D. Lindgren, M. E. Pistol, S. Kröll, P. Goldner, L. Zheng and J. Xu, Phys. Rev. B. arXiv:1303.0877 (2013).
[7] J. J. Longdell, A. L. Alexander and M. J. Sellars, Phys. Rev. B **74**, 195101 (2006)
[8] R. L. Ahlefeldt, W. D. Hutchison and M. J. Sellars, J. Lum. **130** (9), 1594 (2010)
[9] I. Usmani, C. Clausen, F. Bussires, N. Sangouard, M. Afzelius and N. Gisin, Nature Photonics **6**, 234 (2012).
[10] E. Saglamyurek, N. Sinclair, J. Jin, J. A. Slater, D. Oblak, F. Bussires, M. George, R. Ricken, W. Sohler and W. Tittel, Nature **469**, 512 (2011).
[11] M. P. Hedges, J. J. Longdell, Y. Li and M. J. Sellars, Nature **465**, 1052 (2010).

[12] E. Fraval, M. J. Sellars and J. J. Longdell, Phys. Rev. Lett. **95** (3), 030506 (2005).
[13] M. Lovric, P. Glasenapp, D. Suter, B. Tumino, A. Ferrier, P. Goldner, M. Sabooni, L. Rippe and S. Kröll, Phys. Rev. B 84, 104417 (2011).
[14] G. Heinze, C. Hubrich and T. Halfmann, Phys. Rev. Lett **111**, 033601 (2013).
[15] M. Ohlsson, N. Nilsson and S. Kröll, Phys. Rev. A **68** (4-6), 393 (2005).
[16] F. Könz, Y. Sun, C. W. Thiel, R. L. Cone, R. W. Equall, R. L. Hutcheson and R. M. Macfarlane, Phys. Rev. B. **67** (8), 085109 (2003).
[17] R. Kolesov, K. Xia, R. Reuter, R. Stöhr, T. Inal, P. Siyushev and J. Wrachtrup, arXiv. org, arXiv: physics / 1301.5215 (2013).
[18] D. L. Dexter, J. Chem. Phys. **21** (5), 833 (1953).
[19] F. Auzel, C. R. Acad. Sci. (Paris) **262**, 1016 (1966).
[20] R. T. Wegh, H. Donker and A. Meijerink, Phys. Rev. B **56** (21), 13841 (1997).
[21] V. Sivakumar and U. V. Varadaraju, J. Electrochem. Soc. **156** (7), J179 (2009).
[22] J. M. Ogieglo, A. Zych, T. Jstel, A. Meijerink and C. R. Ronda, Opt. Mat. **35** (3), 322 (2013).
[23] H. Zellmer, P. Riedel and A. Tünnermann, Appl. Phys. B **69**, 417 (1999).
[24] F. Wang, Y. Han, C. S. Lim, Y. Lu, J. Wang, J. Xu, H. Chen, C. Zhang, M. Hong et X. Liu, Nature **463** (7284), 1061 (2010)
[25] B. M. van der Ende, L. Arts and A. Meijerink, Adv. Mat., 3073 (2009).
[26] X. Zhoua, K. Zhou, Y. Li, Z. Wang and Q. Feng, J. Lum. **132** (11), 3004 (2012).
[27] J. Zhang, L. Wang, Y. Jin, X. Zhang, Z. Hao and X.J. Wang, J. Lum. **131** (3), 429 (2011).
[28] Y. Wang, S. Wang, Z. Wu and W. Li, Journal of Alloys and Compounds **551**, 262 (2013)
[29] Q. Du, G. Zhou, H. Zhou and Z. Yang, Opt. Mat. **35** (12), 257 (2012).
[30] L. Zheng, R. Lisiecki, W. Ryba-Romanowski, G. Aka, J. Di, D. Li, X. Xu and J. Xu, J. Lum., http://dx.doi.org/10.1016/j.jlumin.2013.08.003 (2013).
[31] B. A. Maksimov, V. V. Ilyukhin, Yu. A. Kharitonov and N. V. Belov, Kristallografiya **15** (5), 926 (1970).
[32] C. Cannas, A. Musinu, G. Piccaluga, C. Deidda, F. Serra, M. Bazzoni and S. Enzo, J. Sol. State Chem. **178**, 1526 (2005).
[33] T. Aitsalo, J. Hölsä, M. Lastusaari, J. Niittykoski and F. Pellé, Opt. Mat. **27**, 1551 (2005).
[34] Y. V. Malyukin, P. N. Zhmurin, A.N. Lebedenko, M. A. Sholkina, B. V. Grinev, N. V. Znamenskii, E. A. Manykin, Y. V. Orlov, E. A. Petrenko and T. G. Yukina, Low. Temp. Phys. **28** 1, 54 (2002).
[35] H. Suzuki, T. A. Tombrello, C. L. Melcher and J. S. Schweitzer, Nuclear Instruments and Methods in Physics Research Section A: Accelerators, Spectrometers, Detectors and Associated Equipment **300** 1-2, 263 (1992).
[36] T. Förster, Annalen der Physik **437** (1-2), 55 (1948).
[37] J. A. Caird, A. J. Ramponi and P.R. Staver, J. Opt. Soc. Am. B **8** (7), 1391 (1991).
[38] R. T. Wegh and A. Meijerink, Phys. Rev. B **60** (15), 10820 (1999).
[39] R. Yano, M. Mitsunaga and N. Uesugi, J. Opt. Soc. Am. B **9** (6), 992 (1992)
[40] N. V. Kuleshov, V. G. Shcherbitsky, A. A. Lagatsky, V. P. Mikhailov, B. I. Minkov, T. Danger, T. Sandrock and G. Huber, J. Lum **71** (1), 27 (1997).
[41] R. W. Equall, R. L. Cone and R. M. Macfarlane, Phys. Rev. **52** (6), 3963 (1995).
[42] P. L. Pernas and E. Cantelar, Physica Scripta. **T118**, 93 (2005).
[43] A. Walther, L. Rippe, Y. Yan, J. Karlsson, D. Serrano, S. Bengtsson and S. Kröll, Manuscript in preparation (2013).
[44] L. G. van Uitert, E. F. Dearborn and J. J. Rubin, J. Cehm. Phys. **47**, 3653 (1967).
[45] T. Kushida, J. Phys. Soc. Jpn. **34**, 1318 (1973).
[46] W. B. Smith and R. C. Powell, J. Chem. Phys. 76 (2), 854 (1982).